

Near-Field Enhancement in Plasmonic Arrays

THÈSE N° 6114 (2014)

PRÉSENTÉE LE 14 MARS 2014

À LA FACULTÉ DES SCIENCES ET TECHNIQUES DE L'INGÉNIEUR
LABORATOIRE DE NANOPHOTONIQUE ET MÉTROLOGIE
PROGRAMME DOCTORAL EN PHOTONIQUE

ÉCOLE POLYTECHNIQUE FÉDÉRALE DE LAUSANNE

POUR L'OBTENTION DU GRADE DE DOCTEUR ÈS SCIENCES

PAR

Thomas Gerd SIEGFRIED

acceptée sur proposition du jury:

Prof. H. P. Herzig, président du jury
Prof. O. Martin, Dr H. C. Sigg, directeurs de thèse
Prof. M. Gijs, rapporteur
Prof. S.-H. Oh, rapporteur
Prof. D. Norris, rapporteur



ÉCOLE POLYTECHNIQUE
FÉDÉRALE DE LAUSANNE

Suisse
2014

Abstract

This thesis reports a detailed investigation of the near-field enhancement in plasmonic arrays of nanostructures and presents novel details on their design, fabrication, characterization and utilization. The origin to this effect is the resonant oscillation of free electrons in coinage metal nanostructures, which are called plasmons. Plasmons have the ability to localize to subwavelength regions where they produce a strongly amplified electromagnetic field at the metal surface, the plasmon near-field. Periodic arrays are chosen to obtain a dense media and homogeneously strong near-fields over large areas, as is required for cost-effective applications. Our concept is based on angular evaporation onto resist arrays that are realized using extreme ultraviolet interference lithography (EUV). By the dedicated evaporation process, sharp metal edges and sub-10 nm gap features are produced, from which near-field localization originates. Surface enhanced Raman scattering (SERS) is used to probe the plasmons near-field, since its intensity scales with the near-field amplitude to the fourth power. Ballistic simulations verify the characteristic cross section of such arrays and provide evidence for the self-controlled growth of the metal pattern leading to nanogap channels with sub-10 nm dimensions, which previously were only feasible with expensive high-resolution fabrication techniques. We demonstrate the reproducible fabrication of plasmonic arrays over a wafer-scale area, which is only limited by the exposure area of the resist array. The angular evaporation leads to high uniformity of the sharp metal edges and nanogap separations with only little defects, which is verified by electron microscopy and highly uniform SERS signals with deviations below 3%.

The use of extreme ultraviolet interference lithography enables a precise tuning of the resist array geometry and together with the well-controlled metal evaporation enables us to study the plasmon modes and near-field enhancement in great detail. We find that the arrays fabricated by angular evaporation support two plasmon modes, one Fano-type resonance and one gap plasmon mode, whereby the near-field is either localized at the sharp metal edges or in small nanogap channels. The near-field enhancement of the Fano resonant mode is maximal for thin metal layers and large array gap sizes, while the near-field of the gap plasmon mode is maximal for small gap sizes and large metal thicknesses. A dip in reflection and a peak in transmission characterize the Fano-type resonance. Its coupling to the localized plasmon mode is conveniently controlled by the array gap size which also sets the magnitude of the reflection dip and the near-field enhancement. We observe and explain that the near-field enhancement is maximal under critical coupling conditions, characterized by a reflectance value of 0.25. The resonance position is broadly tunable from the visible to the near infrared part of the spectrum by selecting the metal thickness and the array gap size. The gap plasmon mode requires gap sizes below 20 nm and nanogap channels with a minimal length of 80 nm and is thus limited to thicker evaporated metal layers. The coupling efficiency and thus the near-field enhancement are strongly increased by tapering the gap opening.

We also demonstrate a method to minimize damping of the near-field caused by adhesion layers. The concept is based on avoiding the adhesion layer to overlap with the region of highest near-field, which is called the hot spot. Together with an adhesion layer thickness as thin as 1 nm, we maintain the adhesion capability while dramatically reducing the damping. The near-field of plasmonic arrays is further improved by placing an optical cavity below the array, which consists of a reflecting layer and a transparent spacing layer. By destructive interference, almost all the incident light can be trapped in the plasmonic array, which is verified by a strong modulation of the SERS signal. We thus obtain that these crescent arrays offer numerous parameters for optimization, such as their gap size, the metal thickness, the spacing layer thickness and the angle of incidence. The latter is a particularly powerful tool for practical applications since it enables the tuning without the need to modify the plasmonic pattern.

Thanks to the large area, low cost patterning and the quality improvement of our periodic arrays, we demonstrate several promising applications. The periodic arrays are found to be extremely sensitive to Ångström changes of the gap size, when measuring the magnitude of the Fano-resonance dip. This radiance based sensing is interesting, because it can be realized by a photodiode, rather than by measuring a plasmon resonance shift requiring a spectrometer. The main application is however surface enhanced spectroscopy. We demonstrate superior SERS signal homogeneity with less than 3% deviation and calculate a local SERS enhancement factor in excess of 1×10^8 . Such plasmonic arrays are extremely robust and enable reusable SERS experiments without deteriorating the near-field enhancement, where the substrate is cleaned by UV exposure. By this, we demonstrate kinetic SERS analysis studies of the thiol layer self-assembly rate and its oxidation rate during UV exposure. We further demonstrate that the excitation from the rear side through a glass substrate increases the SERS enhancement factor and reduces the background SERS signals, which is attractive for fiber coupled SERS sensor probes.

Keywords: Plasmonics, optics, nanophotonics, plasmon resonance, Fano resonance, Fabry-Perot resonance, near-field enhancement, extreme ultraviolet interference lithography, angular deposition, periodic arrays, crescents, nanogaps, numerical simulations, ballistic simulations, surface-enhanced Raman scattering, radiance sensing, adhesion layer, cavity resonance, near-field damping.

Zusammenfassung

Edelmetall Nanostrukturen können mit einfallendem Licht wechselwirken und dieses bei einer bestimmten Resonanzwellenlänge sowohl absorbieren als auch streuen. Dieses Phänomen wurde bereits im Mittelalter bewundert und führt bei historischen Kirchenglasfenstern oder Glasgefäßen zu einer roten Farbe, ausgelöst durch Nanopartikel im Glas. Bei diesem Effekt, versetzt das einfallende Licht die freien Elektronen des Metalls in Resonanzschwingungen. Diese Plasmonen lassen sich in vielfach kleinere Bereiche fokussieren als es die Wellenlänge der zugrundeliegenden Licht-Welle normalerweise zulässt. Am Ort Fokus wird an der Oberfläche des Edelmetalls ein starkes elektromagnetisches Feld erzeugt, welches Nahfeld genannt wird. Die hohe Intensität des Nahfeldes führt zu hohen lokalen Temperaturen und kann desweiteren Moleküle verstärkt anregen und zusätzlich deren emittierende Signale verstärken. Hierdurch ist es möglich die Signale einzelner Moleküle zu detektieren und diese damit zu identifizieren. Viele Anwendungen nutzen bereits die äußerst hohe Nahfeld Verstärkung wie etwa für Spektroskopie, für in-vivo Krebstherapien, für effizientere Solarzellen oder für örtlich hoch aufgelöste Mikroskopie.

In dieser Arbeit wird die Nahfeld Verstärkung in periodisch angeordneten Nanostrukturen untersucht. Periodische Strukturen zeichnen sich durch homogenes Verhalten über große Flächen aus, was für kommerzielle Anwendungen von Vorteil ist. Mit unserer Methode können hohe Nahfeld Verstärkungen in Nanostrukturen erzielt werden, welche kostengünstig herstellbar sind. Die Methode basiert auf abgewinkelter Metallbedampfung auf periodische Photolack-Strukturen, wodurch scharfkantige Ecken im Metall sowie wenige Nanometer breite Schlitzte entstehen. Der charakteristische Querschnitte der Metallstrukturen und die selbst-limitierende Entstehung von Nanometer breiten Schlitzten wird durch ballistische Simulationen bestätigt. Wir untersuchen die Nahfeld Verstärkung mittels Oberflächen verstärkter Raman Streuung (SERS). Die abgewinkelte Metallbedampfung ermöglicht die reproduzierbare Herstellung von periodischen Nanostrukturen über große Flächen in hoher Präzision. Die geringe Defektdichte der Nanostrukturen wird durch elektronenmikroskopische Aufnahmen, sowie durch das äußerst homogene SERS Signal mit Fluktuationen von weniger als 3% über die Fläche bekräftigt.

Wir verwenden Interferenz-Lithographie bei extrem ultravioletten Wellenlängen (EUV), wodurch eine präzise Variation der periodischen Photolack-Strukturen erreicht wird. Dies ermöglicht es die Plasmonen-Resonanzen und die Nahfeld Verstärkung detailliert zu untersuchen. Es lassen sich grundsätzlich zwei verschiedene Resonanzen identifizieren, eine Fano Resonanz, deren Nahfeld an den scharfkantigen Spitzen lokalisiert, und eine Fabry-Perot Resonanz, deren Nahfeld in den Nanometer schmalen Schlitzten konzentriert ist. Die Nahfeld Intensität ändert sich stark mit der Spaltbreite der periodischen Strukturen und ist im Falle der Fano Resonanz maximal bei dünnen Metallschichten und großen Spaltbreiten, während die Nahfeld Intensität der Fabry-Perot Resonanz nur bei dickeren Metallschichten und kleinen Spaltbreiten maximal ist.

Die Fano Resonanz zeichnet sich durch ein Minimum in der Reflektion und ein Maximum in Transmission aus. Dabei kontrolliert die Spaltbreite der periodischen Struktur die Kopplung mit dem einfallenden Licht und bestimmt so den absoluten Wert des Minimums in Reflektion. Die Nahfeld Intensität wird maximal bei kritischer Kopplung an das Fern-feld, was einem Reflektionsminimum von 0.25 entspricht. Die Fano Resonanz lässt sich durch die Metalldicke und die Spaltbreite vom sichtbaren bis zum nahinfraroten Bereich positionieren. Die Fabry-Perot Resonanzposition ist ebenfalls durch die Spaltbreite und die Spalllänge, die Metalldicke, kontrolliert, und kann nur bei Metalldicken ab 80 nm existieren. Die Kopplung an das Fern-feld wird dabei durch eine konische Öffnung des Spaltes erhöht, was zu einer 10-fachen Erhöhung der gemessenen SERS Signale führt.

Die Nahfeld Intensität wird durch unabdingbare Adhäsionsschichten stark gedämpft, wodurch der Vorteil von plasmonischen Strukturen deutlich gemindert wird. Wir stellen eine Methode zur Minimierung der Dämpfung vor; diese beruht auf der Aussparung der Adhäsionsschicht in unmittelbarer Nähe zum Nahfeld-maximum. Zusammen mit einer Adhäsionslagendicke von unter einem Nanometer lassen sich damit robuste Strukturen nahezu ohne Nahfeld Dämpfung realisieren. Die Nahfeld Intensität kann zusätzlich durch eine optische Kavität unterhalb der periodischen Struktur erhöht werden. Hierbei werden Substrate mit einer reflektierenden und einer transparenten Schicht von variabler Dicke benutzt. Mittels destruktiver Interferenz kann damit nahezu das gesamte einfallende Licht in der plasmonischen Struktur eingefangen werden, was mit einer Modulierung des SERS Signals um das 20 fache einhergeht. Die Plasmonen Resonanz der periodischen Struktur lässt sich dadurch unabhängig von dessen Geometrie und allein durch die Dicke der transparenten Schicht sowie durch den Einfallswinkel des Lichts einstellen. Dies ist ein deutlicher Vorteil gegenüber anderen plasmonischen Strukturen und erlaubt eine einfache und kostengünstige Optimierung des Substrats für verschiedene Anwendungen.

Die großflächige und kostengünstige Herstellung von periodischen Strukturen mittels schräger Metallbedampfung, sowie die Homogenität der Nahfeld Verstärkung ermöglichen zahlreichen Anwendungen. Zum einen zeigen wir ein plasmonisches Längen-Messgerät. Durch Variation der Emissionsintensität in Reflektion ist es möglich, Veränderungen der Struktur Spaltbreite mit einer Genauigkeit von wenigen Ångström zu bestimmen. Solch ein Sensor kann dabei einfach über einen Photodetektor realisiert werden und benötigt kein kostenintensives Spektrometer. Die Hauptanwendung von unseren plasmonischen Strukturen liegt jedoch in der direkten Verwendung der Nahfeld Intensität, beispielsweise für Oberflächen verstärkte Spektroskopie. Wir zeigen eine überdurchschnittliche SERS Signal Homogenität mit Abweichungen von unter 3% und einem lokalen SERS Verstärkungsfaktor von 1×10^8 .

Unsere Substrate sind äußerst robust und ermöglichen eine mehrfache Wiederverwendung als SERS Sensor nach Reinigung mittels UV Bestrahlung und ohne eine messbare Abschwächung des Signal Verstärkungsfaktors. Damit zeigen wir unter anderem kinetische SERS Messungen der Selbstanordnung von organischen Thiol Molekülen auf der Edelmetalloberfläche und deren Oxidationsrate durch UV Bestrahlung. Auf der Rückseite der periodischen Struktur ist der Spalt konisch erweitert, wodurch sich die Effizienz der Einkopplung an die Plasmonenresonanz verbessert und zu höheren SERS Verstärkungsfaktoren führt. Wir zeigen zudem, dass störende Hintergrund SERS Signale bei Anregung von der Strukturrückseite durch das Glass Substrat vermindert werden. Zusammen mit der erhöhten SERS Effizienz lässt sich eine rückseitige Anregung ideal in einem Glasfaser basierten SERS Sensor realisieren.

Schlüsselwörter: Plasmonik, Optik, Nanophotonik, Plasmonenresonanz, Fano Resonanz, Fabry-Perot Resonanz, Nahfeld Verstärkung, Extreme Ultraviolett Interferenz Lithographie, Schräge Bedampfung, Periodische Strukturen, Halbmond Struktur, Nanometer Spalt, Numerische Simulationen, Ballistische Simulationen, Oberflächen verstärkte Raman Streuung, Lumineszenz Sensor, Adhäsionsschicht, Kavität Resonanz, Nahfeld Dämpfung.

Contents

Abstract	iii
Zusammenfassung	v
Chapter 1 Introduction	11
Chapter 2 State of the art	15
2.1 Near-field characterization	15
2.2 Surface enhanced spectroscopy	17
2.3 Field enhancement in individual nanoparticles and arrays	18
2.4 Field enhancement in pattern with nanogaps	20
2.5 Field enhancement with coupled plasmon modes	21
2.6 Substrate based near-field tuning	21
2.7 Damping effects of the near-field	22
Chapter 3 Materials and methods	25
3.1 Fabrication of periodic nanostructures	25
3.1.1 EUV interference lithography	25
3.1.2 Metal deposition	26
3.2 Near-field characterization	28
3.2.1 Optical characterization	28
3.2.2 Surface enhanced Raman scattering	29
3.3 Simulations	31
3.3.1 Ballistic simulations	31
3.3.2 Numerical simulations	32
3.4 Roughness contribution to SERS	33
Chapter 4 Results and discussion	35
4.1 Towards the ideal pattern by using angular evaporation	35

4.2	Controlled fabrication of crescent arrays	38
4.3	Subradiant crescent mode - the limit of larger gap sizes.....	40
4.4	Gap plasmon mode – the limit of thick crescents	42
4.5	Optimization of the near-field enhancement	45
4.5.1	Adhesion layer damping	45
4.5.2	Cavity resonance tuning.....	46
4.6	Applications arising from crescent arrays.....	47
4.6.1	Plasmon ruler based on radiance sensing.....	47
4.6.2	Surface enhanced spectroscopy	48
Chapter 5	Conclusions	51
5.1	Achieved results.....	51
5.2	Future developments	52
Chapter 6	Publications	55
(I)	Critical coupling to crescent arrays and plasmon radiance sensing.....	55
(II)	Self-limiting nanogap fabrication by angular evaporation	63
(III)	Near-field enhancement in nanogap resonators	67
(IV)	Double layer pattern with nanogap channels	79
(V)	Minimizing near-field damping by adhesion layers.....	89
(VI)	Cavity controlled SERS tuning with layered crescent arrays	101
(VII)	Reusable plasmonic substrates	113
Bibliography		125
Acknowledgements		135
Curriculum vitae		137
Publication list		139
Conference contributions		140

Chapter 1 Introduction

The ability to squeeze light into extreme subwavelength dimensions is a key feature of plasmonics. Standard optical components, such as lenses, are limited by diffraction, meaning that light at a wavelength of 633 nm can only be collimated to a spot size of around 300 nm. If combined with plasmonic materials, the light can be concentrated to spot sizes well below 20 nm [1], depending on the fabrication resolution. Such small spot sizes are interesting for many applications; including key technology fields with a huge market. For instance in optical lithography: the computational power of microchips can only increase when the components are fabricated with smaller size features. Currently, the evolution of microprocessors is stagnating due to the high technical challenges of fabricating pattern in the sub-32 nm resolution regime [2]. By combination of the lithography tool with optical components made of plasmonic materials, the resolution has been lowered to 22 nm, while keeping the same throughput as the conventional tools [3]. Moreover, small spot sizes lead to high-resolution microscopy [1], and by this they can enable enhanced sensitivity in the detection of analytes [4, 5]. Such microscopy and highly sensitive techniques are very much needed in the pharmaceutical industry to develop new treatments, for example to detect and cure cancer in early stages. Sensitive analytical techniques are also required for environmental and security screening of hazardous and toxic substances, where an open challenge is the detection of low substance concentrations. Furthermore, the extreme light concentration by plasmonic materials enables enhancing the efficiency of photovoltaic processes [6], which could boost the success of renewable energy sources.

Plasmonic materials consist of coinage metals such as gold and silver. The collimation of light in plasmonic materials is possible due to the coupling of light to the free electrons of the metals. Thanks to this coupling, the light induces collective charge oscillations at the metal to air surface, which are called plasmon resonances. These charge oscillations generate an evanescent electromagnetic field, the plasmonic near-field. In nanostructured metals, the plasmons are concentrated in very small volumes and thus form an electric near-field hot spot, with high field intensity. With the same coupling principle, light is also reemitted from such a hot spot. The localized plasmons then act as the origin of a scattered wave.

Light scattering from nanostructured plasmonic materials is the first known application dating back to the 4th century, where a Roman glass cup, the Lycurgus cup, transmits red light, but reflects green light [7]. The effect was not understood at that time, obviously. Today we know that the green color in reflection and the red color in transmission originate from scattering and absorption of plasmonic silver and gold nanoparticles that are dispersed inside the glass [8]. The transmitted color shines red, because the nanoparticles resonantly absorb and scatter light in the green and blue optical spectrum. The plasmon resonance of noble metal nanoparticles can be modified by changing the size and geometry of the nanoparticle. To understand the plasmon modes in metal nanoparticles one also needs to study the plasmon near-field. Indeed, the plasmon resonance wavelength does not hold full information on the near-field around the nanoparticle. While two nanoparticles can have similar plasmon resonance wavelengths, their

individual near-field intensity may differ due to sharper metal edges in one of them [9]. Yet, the near-field intensity is dispersed in the far field and hence cannot be reconstructed.

While the colored appearance of a surface is related to the resonance wavelength and the coupling to the far field, it is the plasmon near-field that is important for the understanding of the plasmonic mechanism. Also many of the relevant applications depend on the near-field of a localized plasmon. Such applications include:

- (i) Strong electromagnetic field enhancement, used e.g. in surface enhanced spectroscopy [10]
- (ii) Light emission from small particles, e.g. in plasmon-enhanced lithography [3]
- (iii) Generation of “hot” electron-hole pairs in electron harvesting devices [11]
- (iv) Strong heat dissipation, e.g. in cancer therapy [12] or in solar light based sterilization [13].

For most of these applications, the plasmonic nanoparticles should exhibit high near-field enhancement at a specific wavelength, which requires fabrication methods enabling to accurately tune the plasmon resonance frequency. Additionally, the fabrication should consist of potentially low cost methods to enable a widespread implementation. With the recently available fabrication techniques offering nanometer resolution, such as electron-beam lithography, many nanoparticle shapes and arrays can be realized from scratch. But the question arises, how should the ideal shape of a plasmonic particle look like? And, are there methods to implement such an optimized structure in a cost effective way for applications?

This thesis presents the use of dense arrays of dots and lines made of noble metals with a particular shape. Dense arrays are superior due to their large average near-field enhancement. We demonstrate homogeneous near-field enhancement and high control over the plasmon resonance via variations of the array gap size and the metal layer thickness. We fabricate plasmonic arrays by interference lithography combined with angular metal evaporation and obtain a broad range of specifically shaped arrays. Sub-10 nm gap features are realized in crescent shaped dots

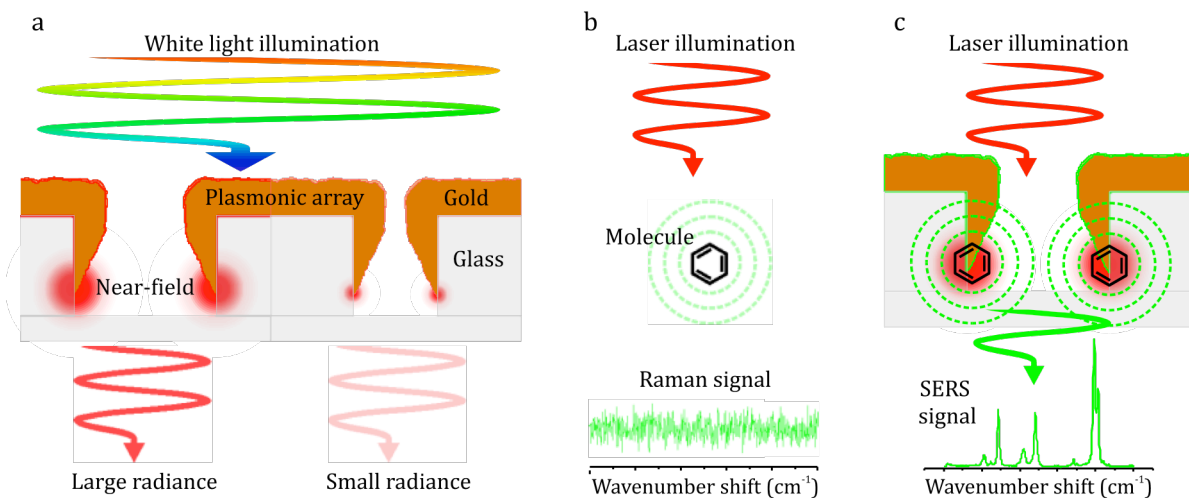


Figure 1. Introduction to radiance sensing and SERS sensing from plasmonic arrays. (a) The radiance of a plasmonic array is controlled via the gap size. (b) Raman sensing of isolated molecules and (c) SERS sensing of molecules placed in the near-field hot spot of a plasmonic array.

and lines, as illustrated in Figure 1. We demonstrate strong near-field enhancement and unlock the potential of such shaped structures to focus light to nanometer regions.

Using these arrays, we demonstrate a plasmonic sensing scheme based on plasmon radiance. Thereby, the transmission through the array is controlled by the array gap size, which is illustrated in Figure 1a. The array gap size controls the near-field amplitude and hence the light emission from the plasmonic array, which is called its radiance. We show that it is possible to measure Ångström changes of the array gap size by detecting the radiance at a single frequency. But in order to study the near-field enhancement more precisely, one needs a method that is only sensitive to the near-field of a plasmon mode.

In this thesis, we measure the near-field amplitude by surface enhanced spectroscopy, in particular surface enhanced Raman scattering (SERS). This method appears to be one of the most prominent application in sensing because it allows the identification of single analytes in an ensemble of molecules by their characteristic emission lines. Unfortunately, the efficiency of the Raman effect is extremely small and usually does not enable the measurement of small quantities, as illustrated in Figure 1b. The Raman signal can however be enhanced by the plasmon near-field, when the analyte molecule is placed close to the metal surface with a hot spot. Thereby, not only the excitation of the molecule is enhanced, but also the emission of the Raman shifted photon, leading to the well-known 4th power dependence of the Raman intensity with the field enhancement. The SERS signal thus correlates with the plasmon near-field amplitude and can lead to signal enhancement factors up to 10^9 depending on the nanoparticle shape and array [4, 5]. Vice versa, the detected SERS signal, illustrated in Figure 1c, is a measure of the near-field enhancement and it signals can assist in understanding the plasmon resonance effect in plasmonic structures.

This thesis is organized as follows. In Chapter 2, an overview of near-field characterization methods is given and techniques to enable strong near-field enhancement and to minimize damping are introduced. We aim to give a general background on near-field enhancement and on limitations arising from the existing techniques and fabrication methods. The here-applied fabrication and characterization methods are summarized in Chapter 3. We demonstrate a model to predict the shape of the crescent array fabricated by angular evaporation and we verify the homogeneous fabrication of (sub)-10 nm gap arrays by experiments and simulations.

Chapter 4 discusses the publications that form the basis for this thesis and summarizes the main results that we have obtained. The advantage of using angular evaporation is valued to obtain strong near-field enhancement in line or dot arrays. The reproducibility of the fabrication and the homogeneity of the near-field enhancement are demonstrated. We show that crescent arrays can support two regimes with different plasmon modes and opposite near-field dependence on the gap size. We will provide a detailed understanding of these plasmon modes and demonstrate promising applications. Finally, two alternative near-field optimization methods are demonstrated the first one eliminates the near-field damping from metal adhesion layers and the second one shows a way to enhance the near-field coupling by integrating the plasmonic structure into a cavity.

The conclusions are given in Chapter 5, along with propositions for further developments and applications of our crescent arrays. The publications are listed in Chapter 6 in the order of appearance in the text. This chapter offers additional details on the achieved results and adds more discussion for the interested reader.

Chapter 2 State of the art

This chapter covers important aspects of plasmon resonances and near-field enhancement in nanostructured systems. The term of near-field enhancement is explained and methods to estimate, measure and simulate the near-field are discussed. It gives an overview of the SERS technique, which is used in this thesis to measure the near-field enhancement. Different types of nanopattern are compared with their respect to their ability to generate strong near-field enhancement, and their fabrication methods are compared. Finally, methods to increase the near-field enhancement are presented that are independent from the nanopattern.

2.1 Near-field characterization

The near-field enhancement in plasmonic materials is a consequence of the collective electron charge oscillations at the metal/dielectric interface. These oscillations are caused by surface plasmons and generate a charge imbalance at the metal surface, which induces an evanescent electric field. Since the plasmon modes are bound to the surface, the electric field is maximal only at the surface and decays exponentially inside the metal and into the dielectric medium. Typical decay lengths for a gold nanoparticle are 30 nm inside the metal and roughly half of the incident wavelength, into the dielectric medium [14, 15]. Surface plasmons can either propagate along the metal surface, or localize at nanostructured metal edges [15]. The near-field amplitude is larger for localized plasmons, due to the smaller mode volume of the nanoparticle surface and the collimation of plasmons in small spot sizes [16]. Furthermore, the excitation of localized plasmon modes is largely independent of the incident angle, which allows their use in standard microscopes under normal incidence [16]. On the contrary, propagating surface plasmon modes require impedance matching with the excitation field, which is only possible under critical incident angles and thus requires specialized setups [15]. The amplitude of the near-field is limited by plasmon damping due to absorption and scattering losses, e.g. originating from ohmic losses in the metal [16, 17].

As a first impression, the near-field of plasmonic particles can be estimated from reflection spectra. Typically, the plasmon resonance of a nanoparticle is shown as a peak in the reflection spectrum [16]. The peak originates from photons scattered into the far field. The peak position indicates the wavelength of maximum near-field amplitude (or is very close to that value) and the peak width reflects the losses of the plasmon mode. As a rule of thumb, the near-field amplitude is weaker for broader plasmon resonances, due to higher intrinsic losses [18]. The plasmon resonance can however not be used to calculate an exact near-field amplitude, since the reflection is recorded in the far field, where the near-field is well dispersed [9].

To measure the near-field distribution and its amplitude in plasmonic nanopattern, different techniques can be used. A direct visualization method of the near-field distribution is scanning near-field optical microscopy (SNOM). In this method, high resolution is achieved by scanning the surface with a sharp tip moving close to the surface. A lateral resolution of 20 nm can be

achieved with this technique [1, 19]. SNOM is particularly interesting for detailed studies on single particles or particle clusters. The complicated setup and alignment make the technique however challenging and there is a high risk of artifacts [20]. Another visualization technique is electron emission loss spectroscopy (EELS). This technique excites the plasmon modes with an electron beam of variable energy and maps the scattered electrons. EELS can achieve high-resolution images of the excited plasmon modes and is used to study complex plasmon modes in single particles or few particle clusters [20-23]. The previous techniques are well suited to visualize the near-field distribution in single particles, but are limited for characterizing the near-field amplitude over large pattern arrays. One technique that is directly influenced by the near-field amplitude is surface enhanced Raman scattering (SERS). The SERS signal scales with the near-field enhancement and can thus be used to quantify near-field variations in different nanopattern. Moreover, the SERS enhancement factor can be used to estimate a near-field enhancement factor. Details of the SERS method and the near-field scaling are given in the next section 2.2.

Among all these experimental characterization methods, there is no technique that can reproducibly measure the near-field amplitude with high spatial resolution and accuracy. Simulations must therefore rigorously support the experimental results. Different simulation routines exist to simulate the electromagnetic field around metal nanoparticles based on solving Maxwell's equations. The earliest and most prominent is finite difference time domain (FDTD) [24], which calculates a full spectral field at different time steps. This technique is most valuable for far-field simulations, but is not well adapted for describing dispersive media, such as gold, since frequency dependent properties must be described in the time domain using simplified models such as the approximation by Drude [25]. Moreover, FDTD cannot discretize complex geometries with surface rounding due to the induced staircasing of the surface [26]. The finite element method (FEM) [14, 27] is a broadly applicable harmonic method, meaning it calculates each frequency individually, which can simulate inhomogeneous media properly. The FEM method can discretize complex shapes, but calculations may become extremely time-consuming, since both the metal object and the surrounding medium need to be discretized [26]. The volume integral equation method (VIE) [28] improves the calculation cost, since only the metal object needs to be discretized. The volumetric mesh cannot discretize curved surfaces however, and is limited to small objects, since the computational cost scales with the volume. The VIE method is also limited when calculating the near-field close to the metal surface, due to numerical inhomogeneities [26].

The boundary element method (BEM) [29] and the surface integral equation method (SIE) [9, 30, 31] have tremendous advantages when simulating larger objects, since the computational cost only scales with the surface of the objects and mesh size squared. Complex geometries, such as realistically shaped surfaces with curvature can be calculated with these methods. SIE is furthermore advantageous when calculating the near-field in close vicinity to the surface. While BEM calculates the field based on discrete mesh points leading to inaccurate solutions in close vicinity of the mesh points, SIE uses continuous functions that calculate a smooth field without displaying the mesh points. To calculate the near-field of periodic arrays, periodic boundary conditions were recently introduced, to allow for a simple discretization of a single array element [32]. In this thesis we use the SIE method as developed by A. Kern and B. Gallinet [32] to calculate the near-field around our crescent arrays.

2.2 Surface enhanced spectroscopy

Thanks to the strong field enhancement in the vicinity of metal nanostructures, the research on surface enhanced sensing has produced a high impact, especially since the demonstration in 1997 of sensitivities for measuring single molecules [33, 34]. The first techniques that are being used by the biopharmaceutical research and industry are surface plasmon resonance (SPR) [35] and localized surface plasmon resonance (LSPR) [36] sensing. These techniques follow the plasmon resonance shift, when molecules adsorb at the metal surface and benefit from their simple setup and ability to be combined with microfluidic systems. Their sensitivity mostly depends on the Q factor of the plasmon resonance and less on the near-field enhancement. Surface enhanced spectroscopy, can offer much higher sensitivities [37] than SPR, since their signal is determined by the near-field enhancement. Common techniques are surface enhanced Raman scattering (SERS) [38-42], surface enhanced fluorescence (SEF) [43, 44] and surface enhanced infrared absorption (SEIRA) [45, 46]. From these, SERS is the most prominent sensing technique since the detection is label-free and provides information on the adsorbed molecule via its specific Raman fingerprint.

The signal enhancement effect and the enhanced absorption originate from the amplified excitation of the analytes in the plasmon near-field, which is maximal in close proximity to the surface and decays exponentially away from the surface [47]. The possible molecule excitation enhancement factor scales with the near-field enhancement squared $(E/E_0)^2$, where E is the local near-field amplitude and E_0 is the incident field amplitude. It is unique to SERS that also the photon emission is enhanced by the same effect than the excitation, which is possible due to the spontaneous Raman effect. The total SERS signal enhancement is thus approximated by the near-field to the fourth power $(E/E_0)^4$, which leads to enhancement factors ranging between 10^4 and 10^9 [17]. The fluorescence emission, on the other hand, is time delayed, incoherent and thus decoupled from the excitation enhancement, which limits the total signal enhancement to the enhanced fluorescence excitation $(E/E_0)^2$. Moreover, the fluorescence emission can be quenched by a nonradiative decay of the excited molecule state, which is induced by an energy transfer back to the metal. This nonradiative quenching effect is typically superseding the radiative emission channel when the fluorescence molecule is less than about 5 nm away from the metal surface [17]. The typical SEF enhancement factor is thus considerably lowered to 2-100 [48, 49], which is however plentiful considering that the scattering cross-section of fluorescence is much larger than that of the Raman effect.

Apart from the electromagnetic enhancement mechanism, the molecules can also undergo chemical enhancement in SERS, when they are chemisorbed on the metal surface. The plasmons can lead to a charge transfer from the metal to the analyte molecules and additionally enhance its vibrational modes. This may lead to an additional SERS enhancement factor of 10-100 [50, 51]. Yet, SERS and SEF have not found their way into routinely used industrial applications. This is due to the complex apparatus and substrate alignment, large signal fluctuations with limited reproducibility, and high cost [52].

Surface enhanced spectroscopy requires resonance matching between the incident wavelength and the plasmon resonance [53, 54]. This resonance matching is especially crucial when the plasmon resonance is narrow [18]. Typically, the plasmon resonance should be between the excitation and the Raman-shifted detection wavelength to obtain optimal SERS enhancement. A precise control of the plasmon resonance is therefore crucial; it can be achieved by controlling the geometry of the nanopattern. A large variety of SERS-active substrates have been fabricated,

such as roughened surfaces [55], nanoparticle-based systems or lithographically patterned surfaces [42, 47, 56, 57]. However, engineering the plasmon resonance precisely to maximize the SERS enhancement for a given application can only be achieved lithographically [18, 54]. The consequence of this is that the substrates are designed for specific purposes and cannot be interchanged for multiple SERS excitation wavelengths.

An important challenge in SERS is the fabrication of substrates with a reproducible enhancement factor [52, 58] and with little signal fluctuations [57]. Many particle-based substrates have randomly distributed near-field hot spots due to fabrication defects at the nanometer scale such that these substrates frequently respond in an irreproducible way [47, 52, 59]. With highly periodic arrays of nanoparticles, the statistical signal fluctuations can be reduced, due to an averaging effect of the overall SERS signal [60]. Another limitation for applications is the high degree of expertise required for SERS sensing. Fiber sensing recently emerged for applications of SERS in chemistry and biology [61, 62]. In fiber sensors, the complicated alignment of the sensor chips is integrated in the fiber tip [63] and does not require microscopes. Moreover, the miniature fibers can also be used at remote sensing locations, which enables a wider range of applications [64, 65].

The practicability of SERS substrates is highly improved when the substrate enables long time stability [52] and reusability [58]. Organic molecules can easily adsorb on metal surfaces, which requires a cleaning procedure that does not degrade the metal surface. While silver easily oxidizes and thereby loses its SERS enhancement, the inertness of gold is ideally suited for aggressive cleaning methods. Such methods consist of acidic baths, oxygen and hydrogen plasma [66, 67] or ultraviolet/ozone (UVO) exposure [68]. Apart from an effective cleaning procedure, the SERS reusability also requires a robust substrate that does not degrade during repeated utilization cycles [69]. Substrate reusability has been reported with the use of particle based or array substrates [70, 71]. A different approach to substrate reusability is the evaporation of a thin protective oxide layer, e.g. SiO_2 , on top of the metal [72, 73]. This prevents organic molecules from chemisorbing to the gold surface. But at the same time, the SERS enhancement is strongly reduced by the weaker near-field enhancement at the distant location of the molecules away from the metal surface.

2.3 Field enhancement in individual nanoparticles and arrays

The first known example of using plasmonic nanoparticles to generate an optical effect was the famous Lycurgus cup from the 4th century AD [7]. Gold and silver nanoparticles were precipitated unintentionally during the fabrication of the colored glass cup [8]. Today, such precipitation processes from metal salts are routinely used to obtain noble metal nanoparticles at low cost. The gold nanoparticles are precipitated in solution and then grow from small seeds to form any particle size from 5 nm to over 100 nm. The plasmon resonance is thereby red-shifted for larger particle diameters. The standard particle plasmon resonance is a dipolar mode that generates a homogeneous near-field around the particle [16]. As the particle size increases, the plasmon resonance is broadened due to damping effects originating from larger scattering losses for large particles [17]. For larger particle sizes and different particle shapes, also multipolar resonances can occur, e.g. quadrupolar modes [17]. The advantage of spherical nanoparticles is their independency on the incident polarization, which increases the versatility of these particles.

Such particles have been applied for SERS sensing at remote locations, by direct deposition on the analyte surface [73].

The near-field enhancement for spherical nanoparticles is however limited due to the absence of sharp features. The precipitation can however be altered to obtain nanorods or star shaped particles with sharp edges, where the plasmon near-field localizes due to the lightning rod effect [74, 75]. This has led to strongly enhanced SERS signals, compared to smooth surfaces of particles and proves the general validity of intense near-field localization at sharp metal apexes. Asymmetrically shaped nanorod particles create an additional polarization dependency of the plasmon resonance, where the near-field enhancement is only maximal when the electric field is polarized along the long axis of the rod [16]. The advantage of suspended particles is the remote applicability, where the particles can be added to any location of analysis [73, 76]. The handling of dispersed nanoparticles and nanoparticle powder bears however a considerable environmental and health risk [77, 78] and makes a controlled dosage of particles difficult. Further disadvantage is the lack of control over the exact particle location and alignment. This is only achieved by controlled particle patterning directly on substrates.

With electron-beam lithography (EBL), the particle geometry can be altered at will to design complex nanoparticle shapes, such as antennas [79-82], split-ring resonators [83] or crescent shaped particles [84-86]. With high numerical aperture (NA) objectives, it becomes possible to examine single particles [87]. This has enabled the study of single particle plasmon resonances in full detail allowing an analysis of the electromagnetic field around such nanoparticles [16, 88-90]. For practical uses and for low magnification objectives, the particles need to be arranged at high density to increase the average emission within the illumination spot. Highly periodic arrays can also minimize the influence of defects and ensure signal reproducibility over large areas. Different arrays have been studied such as aggregated nanoparticles [47] or custom engineered nanoparticle arrays [47, 88, 91-93]. For fabrication, EBL is especially attractive due to its custom designed patterning and an ultimate lateral resolution allowing the fabrication of complex nanopatterns [94]. However, the serial writing process of EBL makes this method slow and thus economically unattractive. Alternative fabrication techniques are particle self-assembly, glancing angular deposition [95-98], nanosphere lithography [79], interference lithography [99, 100] and nanoimprint lithography [101]. These techniques have the potential for patterning full wafers, which is a prerequisite for economic applications. In particle arrays, the spacing of the particles can influence the plasmon resonance by radiative dipole coupling [36]. For smaller spacings below 100 nm, the electromagnetic field in the plane of the particle array begins to couple [36], which is shown in the next section 2.4, for gap sizes below 20 nm.

In this thesis we also discuss crescent shaped arrays. Crescents are concave, half-moon like pattern that can support multipolar resonances, which can be broadly tuned in the optical and near-infrared spectrum by the particle size and the crescent shape [102-104]. The plasmon resonances in crescents lead to strong near-field enhancement at the two crescent tips due to the lightning rod effect. This is particularly interesting for applications that require strong near-field enhancement combined with high control over the resonance position. Crescent arrays have already led to promising applications in light harvesting [104-107], LSPR sensing [84, 85, 103], extraordinary optical transmission (EOT) [108], and plasmon hybridization [86, 109]. Recently, crescent arrays were also proposed as the first broad band negative index of refraction material in the visible spectrum [110]. The fabrication of custom designed crescents usually requires high-resolution lithography due to the distinctive corner rounding and sharp edges.

However, alternative methods have been investigated, based on self-assembled nanospheres and angular evaporation [111, 112]. This technique is scalable to large areas, but strongly limits the crescent shape and thickness and cannot control the array density and array spacing.

2.4 Field enhancement in pattern with nanogaps

When noble metal nanoparticles are placed close together, their plasmon resonances begin to couple and the local electromagnetic field is enhanced in the small gap region. High attention is currently drawn to such nanogap pattern, which can benefit from near-field amplitudes that are much larger than the amplitudes produced by single particles, when the particle spacing is smaller than 20 nm [113-115]. The near-field is enhanced with decreasing gap size, due to a stronger coupling of the plasmon modes in combination with its smaller mode volume. The ultimate limit for near-field enhancement has been found at a gap of roughly 0.5 nm before charge recombination occurs through electron tunneling [114, 116]. Nanogap types of pattern are often used to design nanostructures for practical applications requiring high near-field intensity [16, 57, 81, 90, 94, 114, 115, 117-125]. Local SERS enhancement factors above $\sim 10^9$ have been reported with nanogap pattern [120, 126], which can enable single molecule detection [127].

The fabrication of nanogap arrays has been demonstrated with a variety of techniques. With electron-beam lithography (EBL), the pattern can be designed and realized with an exceptional degree of freedom. EBL is used for direct writing [94, 116, 117, 121, 128] or for the patterning of shadow masks for angular evaporation [121, 129]. Due to proximity effects of the electron beam, the control over gap sizes below 10 nm is often not reproducible and the patterning of nanogap arrays is limited to the above-16 nm gap range and to resist thicknesses below roughly 30 nm [117]. Moreover, this nanometer-precise lithographic process is extremely challenging and cost-intensive, while offering only low throughput and low nanogap filling factors. Nanosphere lithography (NSL) can offer wafer-size arrays of closely spaced nanoparticles by the self-assembly of polymer spheres and subsequent angular evaporation [57, 79]; the tuning of the particle shape, metal layer thickness and control over the gap size is however limited. Other methods yielding nanogaps involve the use of evaporation templates [130-134], electro-migration [115, 135] and shadow evaporation [121, 122].

The main challenge of nanogap fabrication is however the control over the exact gap size, which strongly influences the obtained near-field enhancement. The use of spacing layers, either by self-assembled monolayers [136, 137] or deposited layers [57, 119, 120, 126], can offer great control over the gap size. The use of molecular rulers is especially effective for gap sizes below 2 nm. Most of such patterns are however limited to horizontal gap channels, which cannot be efficiently excited under normal incidence in an optical microscope. Moreover, the gap region is filled with the spacing material, which limits the accessibility of analyte molecules for surface enhanced sensing. The use of atomic layer deposition (ALD) to fabricate the spacing layers is especially attractive for its high control of the layer thickness and versatility of the gap pattern [120, 126]. Such a gap pattern, which can be fabricated as vertically arranged slit channels, creates a standing wave Fabry-Perot mode by the lateral electromagnetic coupling between two opposing metallic surfaces. This resonance is similar to metal-insulator-metal (MIM) waveguides and is defined by the channel length and the gap size [138-140].

Overall, most patterns report strong near-field amplification frequently measured by SERS. However, the fabrication technique is often prone to complicated multistep fabrication procedures [120, 121, 130], limited geometric degrees of freedom [133-135] and a low surface density of nanogaps [120, 121, 131, 133-135]. Most of all, the inhomogeneous nanogap distribution yields strong fluctuations of the measured SERS intensities [57, 120, 121, 130, 131, 133-135], which limits the application to qualitative SERS studies.

2.5 Field enhancement with coupled plasmon modes

The coupling of closely spaced plasmonic nanoparticles can shift the plasmon resonance and result in extremely enhanced near-fields. The nanogap resonance was introduced in the previous section, where the enhanced near-field originates from the small mode volume in the gap region. But the coupling of two plasmon modes can also lead to an energy transfer between both modes, e.g. by coupling a bright, superradiant mode to a dark, subradiant mode. Such a coupled mode is known as Fano interference, and is typically found when a radiative dipole mode interferes with a nonradiative quadrupolar mode [141]. Fano interference leads to an energy transfer from the bright mode to the dark mode and vice versa. Thereby, the near-field of the quadrupolar mode can be considerably higher than the near-field of the bright mode. This originates from better energy storage in the subradiant mode due to the reduction of scattering losses [141, 142].

The strong near-field enhancement in Fano-resonant plasmonic patterns was shown by near-field simulations and by SERS measurements [142]. In the far field, Fano interferences are represented by an asymmetric lineshape in the plasmon resonance, where the dark mode suppresses radiation of the bright mode at the wavelength of their resonance overlap [141]. This leads to typically high Q factors for the Fano dip that can be used for highly sensitive refractive index sensing [141]. The isolated bright mode and the dark mode can be retraced from a fit to the Fano resonance [143-145]. The asymmetric lineshape of the Fano resonance can also lead to a mismatch between the near-field and the far field properties [146]. Typically, the near-field is maximal at the plasmon resonance position, e.g. in a bright dipole mode [54]. But in Fano resonances, the maximum near-field enhancement can be spectrally separated from the local minimum of the Fano-resonance. This near-field mismatch has impact on SERS experiments, where the excitation and detection should match with the spectral position of the highest near-field enhancement.

Typical Fano resonant pattern are found in particle clusters where the Fano interference can be tuned by a slight asymmetric alignment, such as in heptamers, non-concentric rings or dolmen structures [141]. But Fano interferences can also be induced by interface reflections when nanoparticles are excited through a glass prism at grazing incidence. Thereby, the reflected light is the broad continuum that interferes with the narrow plasmon resonance of the gold nanoparticles [147].

2.6 Substrate based near-field tuning

The nanoparticle shape and the number of nanoparticles within the illumination field mainly determine the coupling of the incident field to the plasmonic pattern. The methods to achieve

strong near-field hot spots in nanoparticles were discussed in the previous sections and are based on sharp metal edges, nanogap spacings and Fano-coupled plasmon modes. Yet, a large fraction of the incident field is often lost due to reflection, transmission and/or scattering. An effective plasmonic substrate should therefore aim to reduce such losses in order to further increase the coupling efficiency to the plasmonic pattern. This can be achieved by exploiting a critical coupling configuration where a dielectric spacer and a reflective layer are used as underlying substrate. Placing silver nanoparticles onto such a cavity substrate, it was shown that the SERS signal is influenced depending on the spacing layer thickness [148-151]. By controlling the spacing between the reflective layer and the plasmonic layer, a cavity is obtained that can lead to constructive or destructive interference of the reflected light, which causes enhanced or suppressed coupling to the plasmon mode.

Apart from critical coupling, also the scattering field of the plasmon mode is influenced by the reflective layer configuration. This was used to steer the emission of plasmonic pattern in the direction of detection, hence improving the collection of the SERS signal [152-156]. For small spacings of the patterned layer to the reflective layer, the localized plasmon mode of the patterned layer can be coupled to propagating surface plasmon modes (SPP) on the reflective layer [157]. This can be used to further increase the coupling to the incident field and has shown improved SERS signals originating from higher near-field enhancement at the excitation and the emission wavelengths [156, 158-160].

2.7 Damping effects of the near-field

Significant amount of numerical and experimental investigations have been devoted to finding the optimal pattern for near-field enhancement. Unfortunately, the plasmon mode and near-field not only depend on the metal shape, but also on its environment. Resonant plasmon modes are prone to scattering losses and absorbance by the metal itself and its surrounding, thus limiting the achievable enhancement [161]. The scattering losses can be reduced by exciting dark modes in Fano resonant systems, as shown in section 2.5, but they cannot be suppressed completely [142]. Moreover, the scattering losses can also be optimized by the grain size of the metal. Small grain sizes are obtained by high metal deposition rates and lead to higher scattering losses than large grain sizes. The grain size dependency was demonstrated by TEM and SERS studies [162] and is discussed in detail under the synonym of surface roughness in section 3.4. The light absorbance of metals is similarly influenced by the metal grain size, where small grain particles lead to higher absorbance losses inside the metal. Smooth surfaces show a clear reduction of losses, which can be achieved by stripping the metal from a smooth substrate [163]. Alternatively, the metal can be replaced with a plasmonic material that has a lower absorbance value, e.g. by switching from gold to silver [164]. But silver oxidizes quickly, which renders the material useless for near-field enhancement if the metal surface is not accessible.

The environment of the plasmonic pattern is another origin of damping. When plasmonic materials are directly patterned on silicon, the plasmon resonance and near-field enhancement is strongly influenced by its distinct permittivity. A better choice is the use of materials with a low refractive index and absorbance, such as glass. To support plasmonic materials on surfaces, adhesion layers are needed, particularly when the fabrication requires lift-off and sonication or when the applications demand high structural robustness. Typical adhesion materials are chromium and titanium, with layer thicknesses ranging between 1 and 10 nm [165-167]. Although

the existence of the adhesion layer is an important part of the plasmonic structure, its influence on the near-field and far field of the plasmonic modes is often neglected [161, 168].

The perturbation of the plasmon resonance can be derived from the real and imaginary parts of the adhesion materials permittivity, which affects refractive index locally and introduce absorption. Under such circumstances, the plasmon resonance is red-shifted and broadened, leading to reduced quality factors Q for the resonant mode [169-173]. As a consequence, techniques requiring high near-field amplitudes are strongly weakened, such as SERS and fluorescence enhancement [82, 168, 173-175] or particle trapping [176]. Simulations have shown a slight reduction of the SERS damping for decreasing adhesion layer thicknesses from 20 nm to 7 nm [82]. A route to further reduce damping is the use of less absorptive adhesion materials such as chromium oxide, titanium oxide [82, 168] and ITO [177]. The evaporation of metal oxides is however technically challenging, so that bare metals usually remain the preferred adhesion material.

Another alternative is the use of a self-assembled monolayer such as mercaptosilane. The silane-group binds to oxidic surfaces and the thiol-group binds to noble metals [178]. The dielectric environment of the noble metal is found almost unaffected by molecular adhesion layers and thus the induced plasmon resonance shift and near-field damping are minimal [161, 173]. Yet, the utilization of molecular adhesion layers has drawbacks as it requires additional fabrication steps either in wet [173] or dry [161] conditions and the layers may not withstand oxygen plasma or ultraviolet ozone (UVO) cleaning steps indispensable for substrate cleaning.

Chapter 3 Materials and methods

This chapter provides an overview of the methods used to fabricate, characterize and simulate our periodic arrays. We give a detailed overview of the fabrication process for a typical crescent array and explain the important parameters for the involved methods to ensure high quality patterns. We present detailed information on the optical characterization of our periodic arrays, and the simulation of the metal deposition process and of the electromagnetic field around the periodic array. We supplement this chapter by explaining how to obtain minimal metal roughness, which is important for the SERS experiments.

3.1 Fabrication of periodic nanostructures

3.1.1 EUV interference lithography

We choose extreme ultraviolet (EUV) interference lithography for the patterning of periodic nanostructures. This facility is available at the Paul Scherrer institute and uses coherent light from synchrotron radiation at the Swiss Light Source (SLS) [179]. Although the technique at the SLS is unique since it requires large-scale facilities and high vacuum, EUV sources are on the verge of becoming important sources for lithography, thanks to the small wavelength, which enables higher resolution nanopatterns. The method enables the combination of large area patterning known from standard photolithography, with high resolution such as that obtained for example from electron beam lithography (EBL) [180]. Because single exposures of mm^2 large areas are completed in a few seconds, the throughput is up to 10^4 times higher than with EBL. The patterns are recorded in high-resolution photoresists such as PMMA (poly methyl methacrylate) or HSQ (hydrogen silsesquioxane). By adjusting the exposure time, the duty cycle of linear or dot arrays can be modified in a large window ranging from roughly 0.2 to 0.8. Absorbance of EUV light by the photoresist leads to an undercut of the resist sidewall for negative tone resists. This undercut is later shown to favor the evaporation of double layer pattern with nanogap channels, discussed in section 4.4 and in manuscript (IV). On the other hand, the EUV absorbance limits the resist layer thickness to a maximum of roughly 120 nm.

The facility is located at the XIL beamline endstation of the SLS and is integrated in a small clean room [181]. The photons are generated in an undulator, where the electrons cycling around the storage ring are forced to oscillate and thereby emit photons at high brightness and narrow energy bandwidth [100]. The undulator is adjusted to emit photons at a wavelength of 13.5 nm. Downstream of the undulator, there is a series of filters to narrow further the emitted energy bandwidth and exclude higher harmonic wavelengths. Mirrors enable to steer the beam relative to the interference mask in the exposure station. All components and the samples under exposure need to be placed in ultra high vacuum, in order to reduce energy fluctuations and EUV absorption. The EUV beam is focused on a pinhole inside the endstation, which is located inside the clean room, to guarantee homogeneous illumination of the transmission diffraction grating, which serves as lithographic mask. These gratings are patterned on a thin silicon nitride mem-

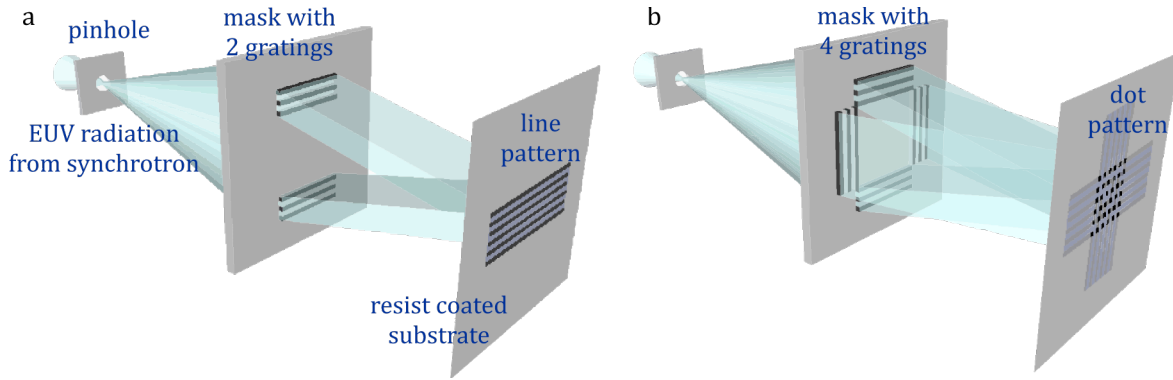


Figure 2. Schematic of the interference lithography at EUV wavelengths to obtain (a) linear gratings or (b) dot arrays, adapted from [181].

brane. The diffracted light forms the interfering beams, which lead to the intensity modulation forming the periodic pattern on the samples. The diffraction gratings are made of gold, which strongly absorbs at EUV wavelengths. Outside of the interference grating, a continuous gold film is evaporated to block the directly transmitted light, which would interfere with the diffraction pattern. The details of the fabrication process for diffraction masks are published elsewhere [100, 179]. The resist-covered substrate is placed accurately at the position of the first diffraction order, where the interference fringes are recorded in the photoresist film. A schematic of the setup is shown in Figure 2. Resulting from the first order interference, the recorded pattern has a period of half the diffraction grating mask. For a line/space type array pattern on the substrate, the mask consists of two diffraction gratings [179]. For two-dimensional dot arrays, the mask consists of 4 gratings, while 8 gratings are used for kagome-type patterns [182].

Most of the patterns used in this thesis are linear arrays with a period of 250 nm that cover an area of 0.6x1.8mm². In a typical exposure, the substrate, either silicon wafers or float glass chips, is covered with 80 nm HSQ photoresist. HSQ forms a silicon oxide network after exposure, which is resistive to most solvents and etching. Beforehand, the float glass substrates are cleaned in piranha solution. The grating mask and substrate are then fixed in the exposure chamber, where a pressure below 5x10⁻⁶ mbar is applied. Before the exposure, the EUV beam is aligned to homogeneously illuminate the grating mask, which is verified via the energy flux in front of the diffraction mask. The exposure time is controlled via a shutter, and multiple patterns are exposed with a programmed xy stage. The appropriate exposure time for varying grating line widths is found in a previous dose test experiment. The HSQ layer is developed for 60 s in a 25% tetra methyl ammonium hydroxide (TMAH) solution. After washing with millipore water and pure ethanol, the substrate is dried in a nitrogen stream. The photoresist pattern is directly used for angular evaporation.

3.1.2 Metal deposition

Usually, photoresist patterns are used either as an etching mask or as an evaporation mask and are removed after the etching or the evaporation. Here, we use the photoresist as an essential part of the nanopattern array. Using HSQ as the resist, the pattern forms a robust, glass-like crystal network. This allows us to evaporate metal onto the resist pattern without the risks of resist

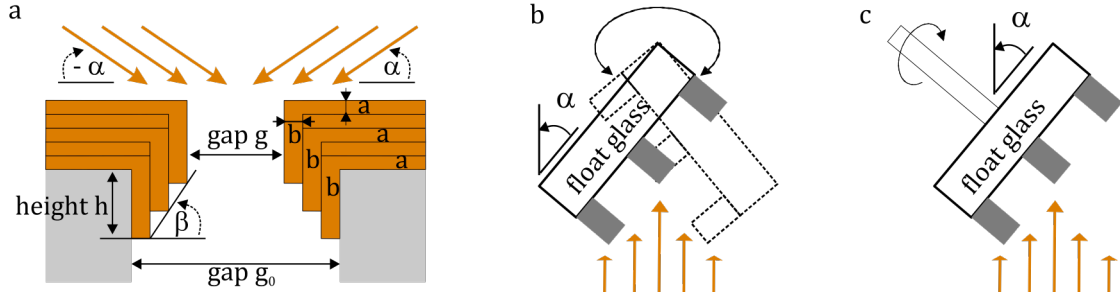


Figure 3. Angular evaporation process. (a) Schematic of the cross section geometry, (b) angular evaporation onto linear grating pattern by frequent substrate tilting and (c) angular evaporation onto dot arrays by continuous rotation.

liftoff or deformation. By application of angular metal evaporation, we tilt the substrate during the metal deposition [183]. Hence, the metal is deposited both on the top surface of the resist (layer thickness a) and on the resist sidewall (layer thickness b and layer height h). The geometry is shown schematically for a line array in Figure 3a. To obtain a uniform shape, metal is deposited at both sidewalls of the resist by tilting the substrate to the opposite side (i.e. $60^\circ/-60^\circ$ from the surface normal). After multiple layer depositions, a crescent like cross section is obtained. The resulting crescent shape is defined by the metal gap size g , the metal thickness t , the sidewall thickness s and the sidewall height h , which are illustrated in Figure 3a.

The shape is calculated with the Equations (1)-(4), by using the total evaporated thickness under normal incidence t_0 , (measured by the quartz crystal sensor of the evaporation tool), the evaporation angle α from the surface plane and the resist spacing g_0 .

$$g = g_0 - 2s = g_0 - (t_0 \cos \alpha) \quad (1)$$

$$t = \sum a = t_0 \sin \alpha \quad (2)$$

$$s = \sum b = t_0/2 \cos \alpha \quad (3)$$

$$h = g_0/\tan \alpha \quad (4)$$

The lateral spacing g between the crescents is controlled by either the initial resist gap size g_0 , which is adjusted by the exposure time, or by the total evaporated metal thickness t_0 . A linear reduction of the array spacing g is obtained by decreasing the resist gap size. However, for metal gap sizes below 20 nm, we observe a self-limitation regime, where the array spacing saturates. For continuous metal evaporation, the metal gap size is found to decrease only slowly. This regime is reached when one sidewall of the array is in the shade of the opposing sidewall, which prevents any further metal deposition inside the gap. This regime is called self-shadowing, when the metal grows merely vertically and it enables building crescent array separated by a small but extended nanogap.

We use thermal evaporation on a Balzers BAE 250 Coating System operated at a base pressure below 9×10^{-6} mbar. Gold or silver (both 99.99% purity, purchased from Balzers) is

evaporated at a rate of 2.5 Å/s. Chromium (99.99% purity, purchased from Sigma Aldrich) is evaporated between the resist and gold layer for adhesion purposes. The adhesion layer thickness is kept to a minimum of 1 nm and is evaporated under normal incidence. The deposition on resist line arrays or dot arrays differs as follows: For line arrays, substrate tilting is used, with an aligned angle of 60° from the surface normal and with an azimuthal orientation of the line pattern perpendicular to the gap extension. It is important to tilt the substrate frequently to the opposite direction (-60°), i.e. after every metal deposition of $t = 2$ nm, to obtain a homogeneous crescent shape, c.f. Figure 3b. We evaporate continuously and flip the substrate along its backside to prevent metal deposition under normal incidence. For dot arrays, we apply continuous substrate rotation at a fixed substrate angle of 60° to the surface normal, shown in Figure 3c. Each substrate contains several nanopattern arrays with different linewidths. This allows a modulation of the array gap size while keeping the metal thickness constant. Up to 9 substrate chips can be evaporated at the same time. The crescent shape is thereby found to be similar with less than 10% variations of the array gap sizes.

3.2 Near-field characterization

3.2.1 Optical characterization

Following the fabrication, the nanopattern is first characterized by its transmission and reflectance. The obtained spectra help analyze the plasmon modes and draw conclusions on the resonance matching that lead to near-field enhancement in the SERS experiments. The reflection (R) and transmission (T) spectra are recorded with a Sentech FTP spectrometer connected to a Leica microscope with a halogen lamp in the visible and near infrared range. The incident path is polarized and focused to roughly 10 μm (NA 0.2). Reflectance spectra are mostly used for optical characterization, since SERS is recorded in a backscattering configuration. The reference for reflectance measurements is taken from a continuous metal layer outside the patterned area, but on the same substrate. With this referencing method, the influence of metal roughness and metal layer thickness is reduced, enabling an accurate display of the spectral changes induced by variations in the nanopattern geometry. Usually, the near-field enhancement is closely related to the absorbance (A) in the nanopattern, which is calculated by $A=1-R-T$. Typical A, R and T spectra for a periodic nanogap pattern are shown in Figure 4 along with the wavelengths of SERS excitation at 633 nm and the detection range.

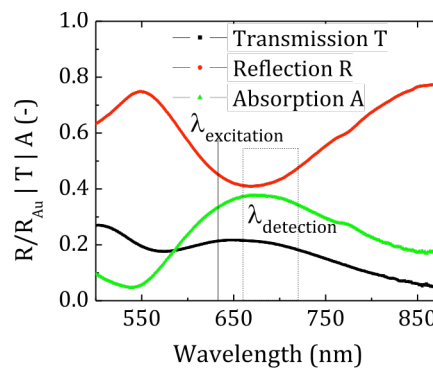


Figure 4. Optical characterization in the visible and near infrared range via the reflection R , transmission T and the calculated absorbance A .

3.2.2 Surface enhanced Raman scattering

Surface enhanced Raman scattering is performed on a confocal microscope Horiba LabRam HR with a grating resolution of 600 lines mm^{-1} . The advantage of this closed system is a fully automated set-up offering long-time stability of the measured Raman signal. The signals are thus well reproducible between multiple measurements and for several weeks. This, together with the reproducible metal covering by the analyte, ensures that the Raman signals can be used as a measure of the near-field for investigations of variations of the nanopattern geometry. As analyte, self-assembled monolayers are used to ensure a defined number of molecules contributing to the Raman effect. The SERS signal is then merely a function of the near-field enhancement and the coupling efficiency of scattered Raman signals into the detection path. We use the molecule benzene-ethane-thiol (BET), which has characteristic Raman peaks at a wavenumber shift of 1008 cm^{-1} and 1609 cm^{-1} , corresponding to carbon-carbon vibrational modes in the benzene ring. The analyte monolayer is formed on gold and silver metals during 12 h immersion in a 1 mM solution in ethanol. The substrate is then thoroughly cleaned with pure ethanol and dried under argon flow.

For excitation, a Helium-Neon laser at a wavelength of 633 nm is used, with a maximum incident power of 20 mW. The incident field is focused to a diffraction-limited spot size of roughly 1.4 μm (50x, numerical aperture NA 0.5). Automated by the system, the focus point is optimized before each measurement. This is found crucial for the signal reproducibility, since the SERS effect originates entirely from the few nm thick plasmonic layer. The incident power is controlled to minimize photobleaching of the Raman molecule, shown in Figure 5a. Generally, we use an incident power of 2 mW, which shows minimal reduction of the SERS signal by 10% after 140 s of illumination. Additionally, we rotate the laser spot in order to spread the incident power over larger areas. The laser spot is deflected automatically within an area of 10*10 μm^2 . This approach further reduces the rate of photobleaching by a factor of 2.5 compared to a fixed laser spot, as illustrated in Figure 5b.

In all measurements, the Raman signal is integrated for 3s and recorded from 16 spatially separated spots on the same nanopattern area by an automated xy-stage. The separation of the 16 grid points is chosen to cover at least 50% of the total pattern area, without using points close to the pattern edge, which can exhibit defects induced by the lithography step. Typically, the grid points cover a 300x800 μm^2 area of the crescent and nanogap-type pattern. In the analysis of the SERS signal we focus on the intensity of one peak, the 1008 cm^{-1} vibrational mode of

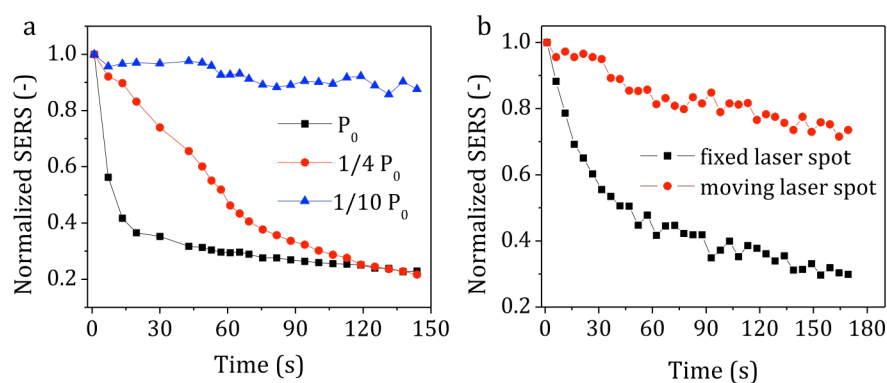


Figure 5. Photobleaching in SERS. (a) SERS signal evolution with time for varying incident power P_0 of 20 mW. (b) Influence of laser deflection on the bleaching of SERS signals.

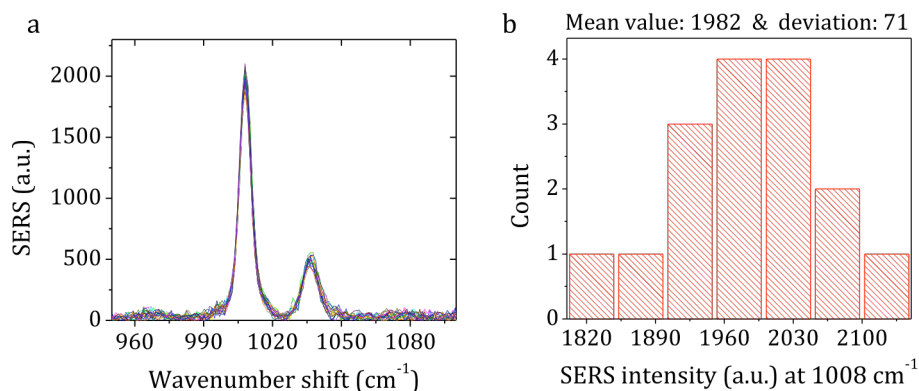


Figure 6. Statistical analysis of SERS. (a) SERS spectra and (b) SERS histogram of 16 spatially separated measurements. The histogram is shown for the Raman peak at 1008 cm⁻¹.

the BET molecule. From the multiple measurements per pattern we obtain a mean value and standard deviation, which allows a statistical evaluation free from pattern defects. The analysis of raw data is automated with matlab and a background reduction is applied to the raw signals for better visualization. Typical spectra of 16 SERS measurements and a histogram are presented in Figure 6. The spectra show excellent stability of the Raman signal across the whole nanopattern with a low standard deviation of roughly 3% and a Gaussian distribution of the signals according to the histogram.

For the Raman analysis of a multiple series of molecules, shown in manuscript (VII), some of the SERS substrates are reused. These substrates are cleaned from the previous analyte by exposure to ultraviolet light. Thereby, ozone molecules are formed that oxidize all organic compounds on the gold surface, while the inert gold is not affected. For the UV exposure, we use a UVO cleaner 42 from Jelight Company Inc and irradiate the substrate for usually 20 min with a power of 0.28 W/cm². After illumination, the substrates are thoroughly washed in THF, pure ethanol and distilled water and dried in a nitrogen stream.

SERS is strongly dependent on both the near-field enhancement and the analyte molecule density in the hot spot. The SERS signals from different patterns are thus only comparable when the number of molecules contributing to the SERS signal is constant. Due to the fact that we use self-assembled monolayers as analytes, we expect that the density of molecules is merely constant when we change the gap size or metal layer thickness of our nanopattern. The comparison of the SERS efficiency with published results is most conveniently done by calculating the average enhancement factor (EF) using Equation (5), where I is the measured signal and N is the number of molecules contributing to the signal.

$$EF = I_{SERS}/N_{SERS} \times N_{Raman}/I_{Raman} \quad (5)$$

The area averaged enhancement factor defined by the focal spot size is the standard most conservative approach [184]. This approach assumes that SERS is formed homogeneously across the focal spot size. In contrast, the local enhancement factor additionally accounts for the fraction of analyte molecules that forms the SERS signal. This fraction is typically very small, when the near-field is concentrated in a small hot spot. N_{SERS} is calculated using reported values for the monolayer packing density from benzene-thiol, $6.8 \cdot 10^{14}$ cm⁻², and the focal spot area [55].

N_{Raman} is calculated using the molecular weight and density of BET, 138.23 g/mol and 1.032 g/cm³, together with the focal volume of the incident laser spot. The SERS signal is obtained at an incident power of 2 mW and the normal Raman signal is obtained from pure analyte liquid at an increased incident power of 20 mW. Typical spectra for a SERS event and a Raman event are shown in the supporting information of manuscript (V).

For our crescent arrays and 10 nm gap arrays, we calculate an area averaged EF of roughly 1×10^6 . This value is not very large compared to other SERS substrates in the literature [120]. But one needs to keep in mind that the SERS signal originates only from a small fraction of molecules in the hot spot and thus the EF increases by the factor of molecules not contributing to the SERS signal. For crescent arrays, we assume that the SERS signal originates from an area within 5 nm of the crescent tip and thus from a factor of 1/25 of the focal spot area (2 hotspots per 250 nm period). This gives a local EF of 3×10^7 . For the 10 nm gap arrays, it is assumed, that the SERS signal originates from a small, roughly 1 nm wide strip of molecules at the gap opening, giving a factor of roughly 1/125 for one gap per period of 250 nm. This gives us a local EF of 1×10^8 , which is similar to the reported values for nanogap SERS substrates [120].

3.3 Simulations

3.3.1 Ballistic simulations

We use ballistic Monte Carlo simulations to analyze the cross section of the metal evaporation process onto prepatterned substrates. These simulations help predicting the evaporated geometry, with no need to perform multiple evaporations and cross sectional SEM images [185]. The evaporation process is simulated with a home-made code, implemented in matlab, which was originally developed by H. Solak. The model follows the trajectory and sticking of single particles in a two-dimensional field [186]. The geometry of the substrate is specified by the resist height and the gap size. The geometry is discretized with a quadratic mesh of 0.8 nm side length. The size of the particle impinging on the substrate is defined by one mesh cell. The particles are directed to the substrate at a specified angle from random positions. The movement of the particles is stopped at their first contact with the resist surface or with the uppermost sticking particle, i.e. occupied mesh cell. Subsequent particle movement allows simulating surface diffusion of the metal.

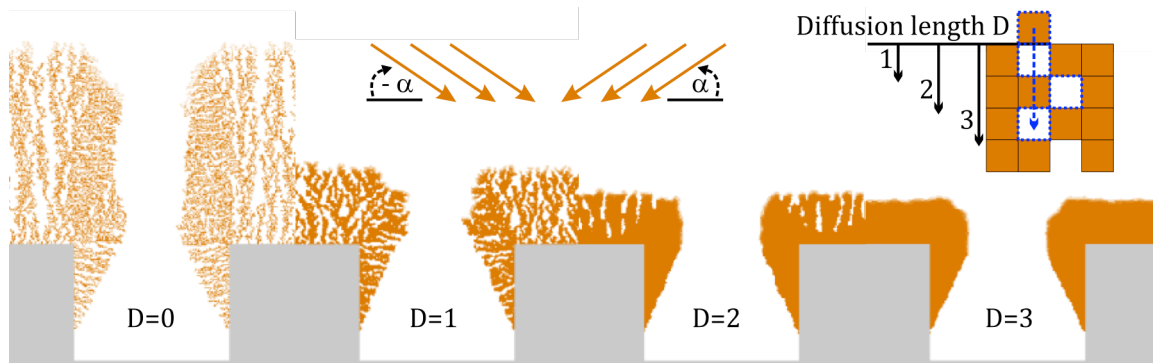


Figure 7. Ballistic simulations with varying diffusion parameter. The diffusion length D defines the allowed particle movement to fill empty pores underneath.

The importance of this diffusion length D is illustrated in Figure 7. Without the diffusion term, the particles would stick at their first contact with the layer, which leads to the extremely porous film shown in Figure 7 for the case of $D=0$. We thus allow the particles to move for a maximum of 3 cells, equal to 2.4 nm in distance, to fill empty cells in the particle assembly below. This leads to the formation of a homogeneous film, shown in Figure 7 for the case of $D=3$. Although the diffusion model does not reflect the materials diffusion coefficient, the results can well reproduce the cross section of the evaporated nanopattern and explain the formation of nanogap channels by shadowing effects. To describe the case of chromium, the distance of allowed particle movement is taken to be 1.6 nm ($D=2$), which verifies the obtained cross section well, shown in Figure 2 of manuscript (II).

3.3.2 Numerical simulations

Numerical simulations provide important insights into the near-field enhancement from resonant plasmon modes around the metal nanoparticles. While the near-field cannot be directly visualized in experiments with high resolution, the comparison between experiment and simulation is crucial in the description of the plasmon mode. Different simulation routines exist to simulate the electromagnetic field around metal nanoparticles by solving Maxwell's equations, as described in section 2.1. We use a full-field numerical method to solve Maxwell's equations with the Green's formalism, developed at the laboratory of Nanophotonics in EPFL [32]. The method is based on the solution of surface integral equations (SIE) and supports periodic boundary conditions, which is ideal for pattern arrays. The surface integral formalism allows for time-efficient calculation of complex nanopattern geometries and, at the same time, provides a precise determination of the electromagnetic field close to the metal surface. Generally, we compare the simulated far field of a nanopattern with experimental reflectance spectra. To match with the SERS signal intensity, the field around the nanopattern is calculated to identify the local field enhancement.

The simulation is carried out in a 3D unit cell consisting of only one array element, with periodic boundary conditions in the horizontal plane. The array element is discretized using a triangular mesh with a maximum side length of 15 nm and has a width of one period (typically 250 nm) and a depth of 100 nm. The geometry and the mesh are generated in Comsol. A parameter file is then generated containing the polarization, wavelength and wavevector of the incident planewave and the dielectric functions of assigned materials. The refractive index of the substrate glass and the photoresist HSQ is taken as 1.5 and 1.39 respectively [187]. The permittivities for silicon, PMMA and chromium are taken from an online database [70]. The permittivity for Au is interpolated using data from Johnson & Christy [188], and the refractive index of the surrounding medium is 1 (air).

In the first calculation loop, the surface current is obtained at each surface element defined by 3 mesh points. In the second loop, the electromagnetic field is integrated over the individual surface currents either at specified points in the far field or the near-field. To obtain a reflection spectrum, the scattered field is calculated at multiple positions 50 μm above the metal surface. The field amplitude is calculated and averaged for all points and referenced by the amplitude of the incident field. This is repeated for multiple wavelengths to obtain the full spectrum. To obtain a near-field map, the electromagnetic field is calculated at multiple points on a cross sectional plane through the nanopattern with a grid size of 1 nm. The near-field enhance-

ment E/E_0 is given by the amplitude of the local field, divided by the amplitude of the incident field. The phase of the near-field is obtained from the complex amplitude of the electric field. All post-processing calculations are performed in matlab.

3.4 Roughness contribution to SERS

In this thesis we correlate the SERS signal to the near-field enhancement produced around plasmonic nanopatterns. In order to do this, the origin of the SERS signal must be known reliably. In early SERS experiments, roughened noble metal films were utilized as substrates. These films have nm-spaced gaps between metal particles and crystallites, which can generate near-field enhancement at random positions. In this thesis we study the effect of minimal geometric changes in the nanopattern on the SERS signal. A roughness contribution to the SERS signal must therefore be minimized. The roughness of gold films is influenced both by the substrate and the evaporation process, and its contribution to the SERS signal is shown in Figure 8.

In the first experiment we test the gold roughness on SERS. We expose a 100 nm thick HSQ film with EUV light, without using an interference mask. This leads to a large area pattern, which is influenced by a Gaussian beam distribution with the highest doses in the center and the lowest ones in the outer corners. After gold deposition under normal incidence, we scan the roughness along the exposed area with a Veeco Dimension 3000 atomic force microscope (AFM). The roughness R_a is defined as the arithmetic average of the absolute values of the height levels recorded by the AFM tip within the scanned area. At the underexposed outer areas, the resist and gold roughness have a large mean value of 5 nm, which drops to 1 nm in the overexposed areas

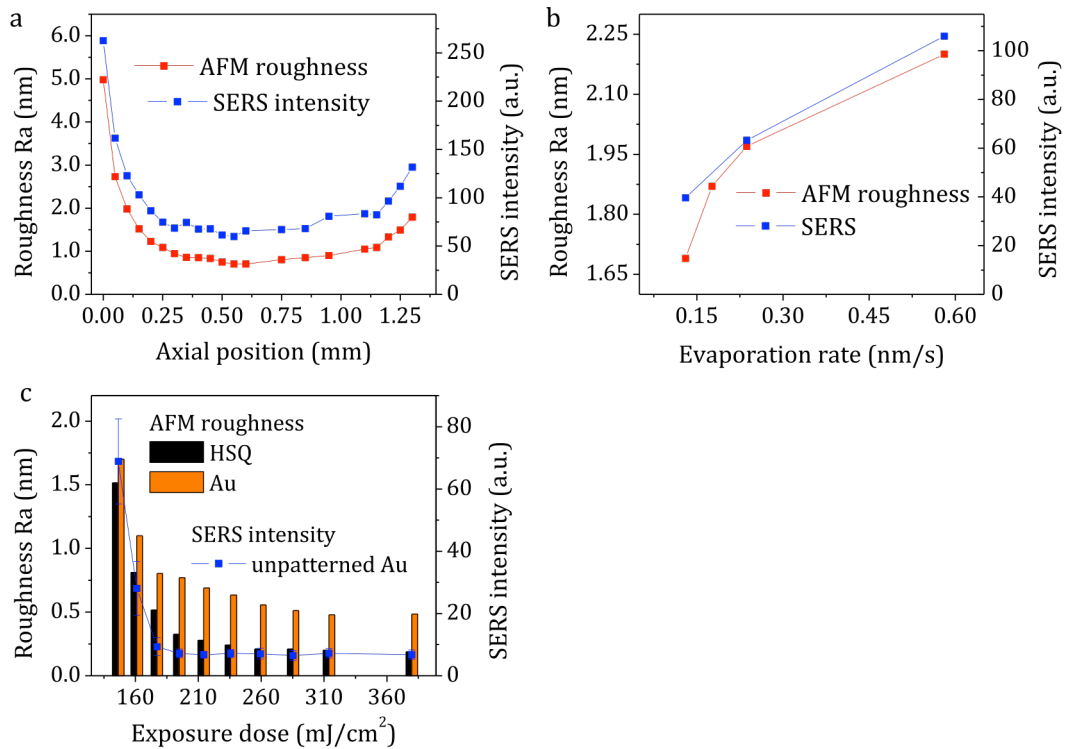


Figure 8. Gold Roughness influence on the SERS signal obtained on an unpatterned area. The gold roughness is influenced by (a) the resist roughness, (b) the gold evaporation rate and (c) the exposure dose.

in the center, shown in Figure 8a. The SERS intensity scales similar to the gold roughness with highest values at the rough outer areas. This shows that the gold roughness strongly influences the SERS signal and that there is an optimal dose range with a homogeneous SERS signal.

We also test how the gold evaporation rates influences the surface roughness of an unpatterned layer and the SERS signal contribution arising thereof. The roughness increases from 1.6 nm to 2.2 nm when the evaporation rate rises from 0.15 to 0.6 Å/s. Varying gold crystallite sizes can cause this roughness trend, when the deposition rate is above an optimal crystallization rate. Additionally, the pore density can also be increased at larger evaporation rates. These effects are however on the sub-nm level and cannot be detected in SEM images. As shown in Figure 8b the SERS signal scales proportionally with the increasing evaporation rate and gold roughness. We verify the influence of roughness using substrates fabricated by the same interference mask leading to line arrays and measure the roughness from both the HSQ layer and the gold layer at different exposure doses and outside the patterned array, see Figure 8c.

The experiments show clearly that the gold roughness scales with the HSQ roughness. We also determine a critical minimum dose of 200 mJ/cm² above which the roughness remains constant. This is also the minimal dose required for the SERS signal to be free from a detectable roughness contribution. Due to these observations, we conclude that the evaporation rate must be kept constant and the resist exposure dose must be above a critical minimum of 200 mJ/cm² to ensure constant gold roughness. Only with a constant gold roughness can the SERS background be minimized and the SERS signal used as a measure of the near-field enhancement.

Chapter 4 Results and discussion

This chapter discusses the main results obtained in the thesis. We intend to give a complete picture of the published results and explain how the publications relate to each other. We begin by summarizing important findings of the state of the art and then explain how our research choices have advanced the field. The interested reader is referred to publications (I) to 0, which form the body of this work, for further details.

4.1 Towards the ideal pattern by using angular evaporation

The generation of strong near-fields is the key ingredient for applications arising from plasmonic arrays such as surface enhanced spectroscopy. The prerequisite is the fabrication of noble metal particles that are much smaller than the wavelength of light. In this case, localized plasmon modes at the metal interface can be excited under normal incidence without the requirement for impedance matching necessary for the excitation of propagating surface plasmons. In the state of the art section, it was mentioned that large near-field enhancement is obtained from sharp metal edges, in nanogap spacings and in Fano-resonant patterns. With recently available fabrication techniques offering nanometer resolution, such as electron beam lithography, any particle shape can be realized from scratch. Thus the question is: what are the characteristics of an ideal pattern? We address this question from the following perspectives: near-field enhancement, control over the near-field, near-field homogeneity, reproducibility and simplicity of the fabrication.

To refer to the state of the art in Chapter 2, we give a summary over the existing plasmonic substrates. Roughened noble metal surfaces were among the first substrates to show the near-field based effect of SERS. By reverse engineering one has found that nanometer-sized gaps and grooves on the particulate metal film generate local near-field hot spots at random positions. Such substrates do not require lithography and thus are low cost, and can be produced over large areas. The possible near-field enhancement is however limited due to large scattering losses and the plasmon resonance can hardly be controlled to match a specific incident wavelength. Also, the thus obtained field enhancement is an average effect. When scanning locally across the surface, large signal inhomogeneities are observed. On the contrary, custom designed nanoparticles and nanoantennas enable to control the near-field at practically any desired incident wavelength. In fact, by choosing size, geometry and material of the particles, the plasmon resonance and hence the position of the near-field enhancement peak can be shifted from the UV to the infrared. Strongest near-field enhancement is obtained at sharp particle edges, where plasmons are confined in a small spot. Also few nanometer spacings between particles lead to extreme near-field enhancement in cases where good coupling to the plasmon modes is achieved. Then, the near-field is highly sensitive to few nanometer changes in the particle geometry or their spacing. Nanoparticle pattern with sharp points and nanogaps are ideal for experiments on isolated particles or antennas, but can lose their advantage in larger assemblies and environments. This limit originates from low reproducibility of particle-based pattern on the large scale,

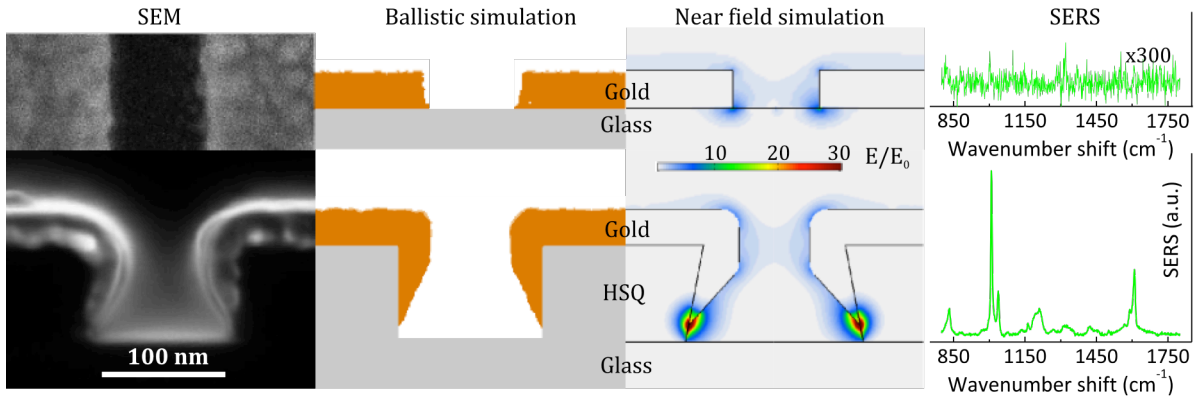


Figure 9. Comparison of linear gold arrays and crescent shaped gold arrays. The SEM images and ballistic simulations show the different cross section, near-field simulations and SERS spectra show the potential field enhancement.

based on the commonly used lithography technique. Local defects reduce the uniformity of the near-field and thus limit the control over the substrate. Moreover, high-resolution lithography based fabrication techniques are often not scalable to large area and cannot be fabricated economically enough for real applications.

What we would like to have is a method that combines large area efficiency as known from roughened films with high-resolution control over the local metallic nanostructure. Periodic arrays offer high homogeneities over large areas and can be fabricated cost effectively by scalable processes such as self-assembly, interference or nanoimprint lithography. Yet, utilizing these methods in combination with high-resolution pattern transfer, local defects may again disturb the near-field enhancement across the patterned area. Here we propose to combine the patterning process with a second fabrication step, angular evaporation, which adds high-resolution features to the otherwise low-resolution (250 nm periodicity) pattern with minimal local defects. We will show that this unique method enables to obtain homogeneous near-field enhancement over large areas. We give in Figure 9 an example of periodic arrays obtained by angular evaporation and compare the pattern with periodic arrays that are obtained under normal incidence evaporation. For this example, we choose the simplest form of periodic pattern, namely linear arrays, such as gratings.

Linear metal gratings with a period down to about 200 nm can be fabricated homogeneously over large areas by patterning a photoresist, followed by metal evaporation under normal incidence and liftoff of the resist pattern [99]. SEM image and simulated cross section (details are given in section 3.3.1) of such a grating with vertical sidewalls of the metal are shown in Figure 9, on the top left hand side. Such periodic arrays can support plasmon modes that are located at each individual line element. The resonance can be tuned by the grating linewidth. The near-field, as found by our simulations, is homogeneously distributed around the grating, and does not show hot spots with strong field enhancement. The absence of intense local field hot spots thus makes such linear metal grating not attractive for SERS experiments as it is seen from missing SERS peaks in Figure 9 on the upper right hand side. However, when we evaporate metal on a resist grating at glancing angles of $\pm 60^\circ$ from the surface normal, we can add sharp, high-resolution features to the otherwise same low-resolution grating. The metal that is deposited on the sidewall of the resist forms sharp tips, as shown in the cross section SEM image and ballistic simulations in Figure 9 on the lower left hand side. The resulting cross section takes the shape of

a concave half-moon clasping around the resist pattern, which is reminiscent of a crescent. In contrast to the linear metal grating, the sharp metal tips enable strong near-fields of the localized plasmon mode and hence high near-field enhancement. This appears also from the simulation shown in Figure 9. This near-field hot spot enables generating high quality SERS spectra as is demonstrated for example in Figure 9, on the right hand side.

Angular evaporation in combination with a resist pattern is thus a very powerful method to obtain metallic nanopatterns with sharp, high-resolution features, while starting from low-resolution structures. Despite the two-step process, the fabrication is not complicated, since a photoresist pattern can be used directly for angular evaporation without any further etching and liftoff. The metal deposition is self-aligned, which means that sharp metal tips are obtained independent on the grating linewidth while the cross section of the pattern keeps the shape of a crescent. The geometry of the crescent is solely defined by the grating linewidth, the evaporation angle and thickness, shown in Figure 3; details are given in section 3.1.2.

Apart from the sharp metal tips, we have also found the possibility to accurately fabricate crescents with few-nm spaced gaps. For continuous evaporations, the gap size decreases and one would expect the structures to coalesce eventually. Yet, we have observed that the spacing stabilizes below a gap size of 10 nm and the pattern grows only along the vertical axis. From ballistic simulations we have identified that the self-shadowing of the sidewalls leads to this self-limiting effect. Since the shadowing effect does not rely on highly defined pattern, our angular evaporation method can be implemented and operated without the need for high-resolution and costly methods such as EUV or electron-beam lithography. For sub-5 nm gaps, finally, the sidewalls coalesce at the places with the largest gold crystallites. Around 10 nm spacing and above, the gap size can be controlled reproducibly, and the deposition is not limited to a critical evaporation thickness. Both, the linear and the dot arrays can be used for angular evaporation and give similar results. For details of the crescent fabrication we refer to the experimental section 3.1, and the fabrication limits of sub-10 nm gap arrays are described in manuscript (II) and (III).

Generally, the technique of angular evaporation is extremely versatile in turning a low-resolution resist pattern into metal arrays with sharp metal tips and few-nanometer gaps. Herewith, the near-field is strongly enhanced compared to substrates that are obtained from the same resist layer by a direct pattern transfer like etching or liftoff, shown in Figure 9. The evaporation technique is scalable to large areas, except for the resist-patterning step, which is based on EUV interference lithography. The maximal pattern area in a single EUV exposure is one mm², which is relatively large for high-resolution techniques such as ebeam lithography, but rather small for practical applications.

For the thesis, the use of EUV lithography turned out to be an important asset thanks to its fast patterning of periodic arrays and the precise control over the resist linewidth by the exposure time. By just varying the duty cycle between 0.25 and 0.75 of the grating and controlling the thickness of the deposited metal a large variety of metal pattern could be realized. Hence, EUV lithography together with angular evaporation set the basis for studying a broad range of crescent shaped array pattern, which enabled us to gain a deep understanding of plasmonic modes in periodic structures.

In the following section, we discuss the reproducibility of the fabrication and the homogeneity of both the pattern shape and the SERS signal arising from the near-field enhancement and we depict the high versatility of such crescent arrays.

4.2 Controlled fabrication of crescent arrays

In the following, we show that the angular evaporation technique is scalable up to wafer-scale areas and that the evaporation enables an accurate reproduction of the crescent geometry on multiple samples. We have simultaneously evaporated 5 EUV patterned chips aligned across a 4-inch wafer, with the distribution shown in Figure 10a. Each of the 5 chips has multiple patterns consisting of dot arrays with exposure time controlled spacings from 70 nm to 150 nm. Although the chips have been exposed within the same EUV exposure batch, the linewidth for any specific pattern slightly varies by typically ± 5 nm as observed by investigating all the fields of all the 5 chips by SEM. This resist linewidth variation originates from minimal flux variations of the EUV. After the angular evaporation, the SEM inspection has been repeated to obtain the gap size of the metal pattern which is correlated one by one with the resist gap size in Figure 10a. We observe only little scattering of the data proving a highly consistent correlation between the gap size before and after evaporation.

Related to this consistent behavior of the evaporation, we find that also the SERS intensity follows the structural and dimensional changes of the pattern. In particular, this is important for our investigations of structures with gaps in the sub-10 nm regime, as shown below. Here, we would like to demonstrate this regular behavior by correlating the SERS signal to the gap size of linear nanogap arrays from 3 individual chips. The chips were aligned in the center and on both edges of a 4-inch wafer and where simultaneously coated by angular evaporation. Again, the exact gap size of the resist pattern and thus the gold nanogaps differ slightly but as shown in Figure 10a in a consistent way. We use self-assembled thiol monolayers as SERS analyte, to ensure a reproducible density of molecules at the metal surface. Thereby the SERS signal is merely correlated to the near-field enhancement of the pattern. Of course, the SERS signal can also be affected by a rough gold surface, but this disturbing effect has been minimized by controlling the EUV exposure dose and the metal evaporation rate, as explained in the method section 3.4.

The obtained SERS intensity is compared with the individually measured gap size of the gold nanopattern in Figure 10b. We observe, similar to Figure 10a that the data points scatter only slightly and that the SERS signal follows the same trend for varying gap sizes. This proves the accurate control we have on the form and structure of the nanostructures in particularly in the promising range below 15 nm. As we show below, this reproducibility and predictable corre-

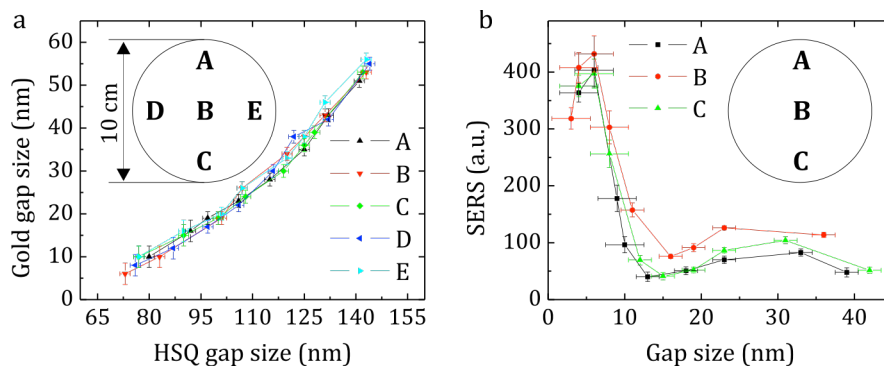


Figure 10. Pattern and SERS homogeneity across wafer scale array fabrication.

(a) The resist gap size and the gold array gap size are compared from patterns distributed across a full wafer. (b) The SERS signal for varying gold gap sizes is shown for pattern spread across a full wafer.

lation between the resist and the resulting metallic pattern is the key for the investigation of thickness, spacing and geometric dependencies on the optical properties and SERS performances of our structures. By making use of this versatile and powerful fabrication tool, we will show that a detailed understanding of the crescent array pattern is crucial for an ideal performance in plasmonic sensing.

We conclude this section by demonstrating the variable SERS performance of crescent arrays on array spacings for two different metal thicknesses, shown in Figure 11. Two distinct regimes can be identified, one for shorter and one for longer evaporation times, corresponding to thinner versus thicker metal capping. SEM images of the array cross section for both regimes are shown in Figure 11. Surprisingly, the gap size dependency on SERS is found to be opposite for the two regimes. While the SERS signal for thin crescent arrays increases with increasing gap sizes, the SERS signal for the thicker nanogap arrays increases with decreasing gap sizes. This counter-intuitive SERS behavior is intriguing and calls for detailed investigations. Its understanding is part of the results developed in the course of this thesis. What we now understand is that for thin metals the effective mode is related to the individual crescent shape, whereas for thicker capping layers the plasmon mode is related to the nanogap region. This will be carefully discussed in the coming sections.

In order to start the discussion, we would like to note that the SERS signals in the nanogap regime (i.e. thicker metal layer) are following our expectation since the near-field is known to increase for strongly coupled plasmon modes in few-nanometer gaps. But why did we not find this trend for thin crescent arrays? Even for gap sizes below 10 nm, as illustrated in Figure 11? Moreover, the increase of the SERS signal for larger spaced crescent arrays is not persistent, as we have found an optimum gap size of 60 nm, above which the SERS signal declines. Such an optimum gap size is also present in the nanogap regime for thick metal layers.

In the next two sections, we will answer these questions and will describe the underlying plasmon modes leading to the observed SERS trends and demonstrate possible applications that

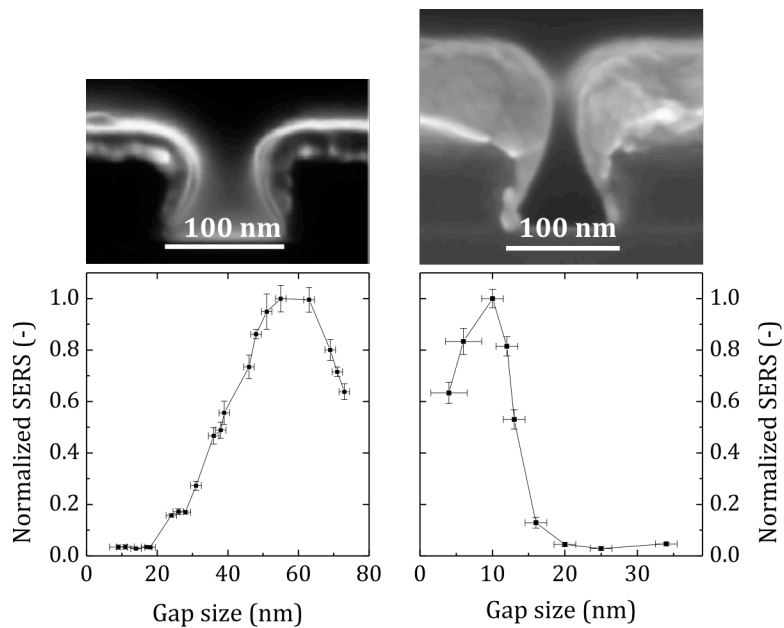


Figure 11. Opposing SERS dependency for crescent arrays with different metal thickness.

can arise from this. The details for the identification of the crescent plasmon mode are discussed in section 4.3. Applications as radiance sensor and reusable SERS sensor are discussed in section 4.6 and were published in the manuscripts (I) and (V), respectively. The plasmon mode of the nanogap arrays is discussed in section 4.4 and was published in the manuscripts (II), (III) and (IV).

The chapter will be concluded by a discussion of broadly applicable methods to optimize the near-field amplitude. The methods consist of minimizing the near-field damping from adhesion layers and maximizing the coupling efficiency with a reflective layer underneath. These methods are discussed in section 4.5 and were published in the manuscripts (V) and (VI).

4.3 Subradiant crescent mode - the limit of larger gap sizes

The answer to the previous question, why the SERS activity is declining for decreasing gap sizes of 30 nm thin crescent arrays, is found in Fano interferences. In Fano resonances, a dark mode couples to a broadband bright mode, which leads to an energy transfer within their spectral overlap and thus the possibility of coupling the dark mode to the incident field. In our array, the crescent plasmon mode is the subradiant, i.e. dark, mode that cannot couple to radiation by itself. The bright mode is given by light that funnels through the gap region nonresonantly and forms the radiative continuum. A sketch of the energy flow in a crescent Fano resonance is shown in Figure 12a.

As is shown below, this picture matches with the simulation and allows us to understand the experimental linear optical measurements (transmission and reflection) as well as the SERS signals, thus the near-field properties. In the following we are going to highlight the experiments and modeling performed on crescent arrays and will put our results into a broader context. For details we refer to the content of the attached manuscript (I), while the following should provide a comprehensive introduction to the topic.

To start, we like to refer to Figure 4 from section 3.2.1, where a characteristic reflection and transmission spectrum of a typical crescent array is shown. We observe a broad dip in re-

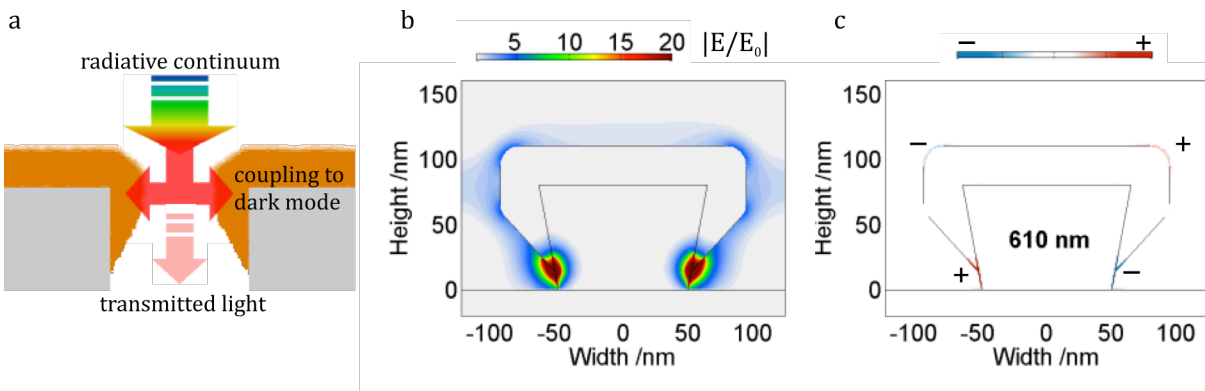


Figure 12. The subradiant crescent plasmon mode. (a) Ballistic simulation showing the cross section of crescent arrays. The arrows indicate the energy flow in the crescent Fano mode. (b) Near-field simulation showing the electromagnetic field hot spot. (c) Phase calculation showing the charge separation at the surface of the metal.

flection and a peak in transmission, which are indicating a plasmon resonance and thus a coupling to the incident field. The subradiant crescent mode can be excited because of an energy transfer from the nonresonantly tunneled light to the crescent dark mode and vice versa. The transmission peak originates from light reemission of the subradiant plasmon mode and the reflection dip originates from destructive interference of the reemitted light with the directly reflected light of the array. The subradiant crescent mode is a quadrupolar mode in the gap region, with a charge distribution between the crescent tip and the upper crescent edge at both metal sidewalls. The phase of the simulated near-field shows an opposite charge distribution on both metals, which is illustrated in Figure 12c. The near-field localizes at the sharp crescent tips and forms an intense hot spot due to the compression of the plasmon mode in a small area, seen in Figure 12b.

The Fano dip in reflection is highly dependent on the gap size and the metal thickness of the crescent array, which is shown in Figure 13. For small gap sizes below 10 nm, the reflection dip is close to zero and we measure and simulate a mere reflection similar to that of a flat gold film, illustrated Figure 13a and in Figure 4 of manuscript (I). When the gap size is opened to 70 nm, the far field dip magnitude increases considerably from zero to beyond 0.7 and the resonance position red shifts in the spectrum from 600 nm to 760 nm, which is shown in Figure 13a. For larger metal thickness of the crescent array, the Fano resonance red shifts with constant dip magnitude, which is illustrated by a shift from 580 nm to 800 nm for a thickness change from 20 nm to 60 nm in Figure 13b. For the understanding of this Fano resonance we separate the two effects into the resonance shift (i) and the magnitude shift (ii).

- (i) The resonance shift is found to originate from the crescent shape, in particular its height. The crescent height increases for larger gap sizes and for larger metal thickness, as shown by the geometric model in Equation (4). The larger crescent height implies that the plasmon mode of the crescent resonance has a larger mode volume, which red shifts the resonance.
- (ii) The reflection dip magnitude originates from the crescent gap size. The reason is found in the radiative continuum, represented by light funneling. For small gap sizes, light funneling is very weak and thus the dark mode cannot be excited. The nonresonant light funneling increases however for larger

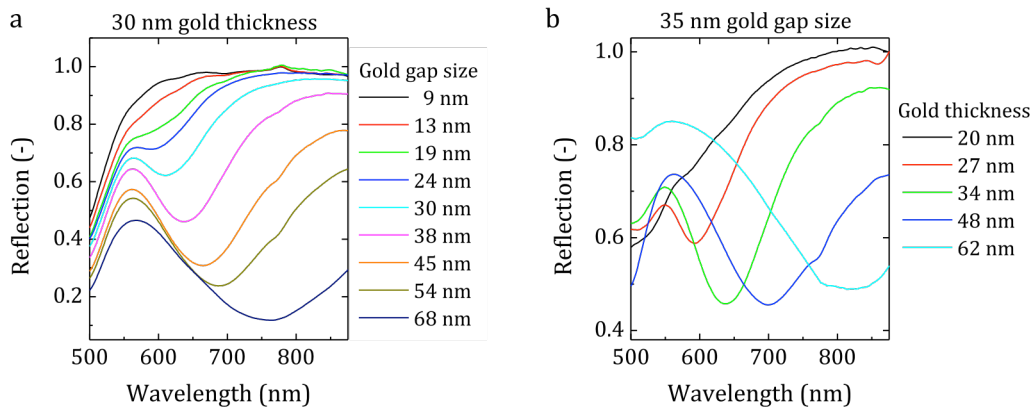


Figure 13. The Fano resonance in crescent arrays measured by its reflectance.
 (a) The crescent Fano resonance for varying gold gap size at a constant 30 nm metal thickness.
 (b) The crescent Fano resonance for varying gold thickness at a constant 35 nm gap size.

gap sizes and hence the dark mode can be efficiently excited, which is explained in detail in the published manuscript (I).

The Fano dip magnitude is the more important observable in our crescents arrays in connection to the near-field enhancement. The near-field only increases when the incident field is coupled to the dark mode, which is why we observe larger SERS signals for larger gap sizes, shown in Figure 11 on the left hand side. But why do we observe decreasing SERS signals above 60 nm gap sizes? To understand the coupling to Fano modes, a model was proposed by B. Gallinet based on the interplay between both radiative and nonradiative decay losses [189]. In our array, the radiative decay is the energy transferred from the radiative continuum to the subradiant crescent mode and vice versa. The nonradiative decay is given by the energy lost in the subradiant crescent mode by energy dissipation. The model introduces a critical coupling regime, where most energy can be stored in the dark mode. Above this critical regime, the radiative losses supersede the nonradiative losses and the near-field enhancement decreases, seen from the decreasing SERS signals above a gap size of 60 nm in Figure 11. The critical coupling regime is expected at a modulation damping of 0.25, which is exactly what we obtain from the reflection value at the highest SERS signal, illustrated in Figure 4 of manuscript (I). With this experiment, we have provided experimental evidence of the critical coupling regime in Fano modes, which is a general phenomenon and not only related to our crescent array pattern. This result was only possible due to the versatile tunability of our crescent arrays that allows us to tune both the resonance magnitude and the resonance position in a large range.

One of the main conclusions drawn from the manuscript (I) is that the Fano resonance dip in our crescent array is broadly tunable in terms of resonance position (from 600 nm to >950 nm) and dip magnitude (from almost 0 to 0.9). The near-field enhancement is maximal in the critical coupling regime, characterized by a reflection dip value of 0.25.

4.4 Gap plasmon mode – the limit of thick crescents

Let us recall that we have previously shown that due to the improved coupling to the incident field, the SERS signals increase for wider gap sizes, while no SERS was observed for 10 nm gap arrays with an evaporated metal thickness of only 30 nm, c.f. Figure 11. However, for crescent arrays with a metal layer thickness around 100 nm the SERS signal strongly increases for a decreasing gap size. The answer to this peculiar dependency on the metal layer thickness is related to the required length of a cavity to build up a plasmonic mode. The upper and the lower gap openings, i.e. the thickness of the evaporated metal layer, define this cavity. The gap plasmon mode is thus a Fabry-Perot mode that is entirely located in the gap region and the coupling to the incident field is solely defined by the gap geometry. This mode is different from nanogap enhancement in closely spaced nanoparticles, where the incident field first couples to the individual particle plasmon modes, which then form a strongly coupled mode in the gap spacing and enhance the near-field in the gap region.

The fundamental gap plasmon mode is given by the mode order one ($m=1$) and appears as a dipolar charge distribution with a phase change of π . Our investigations show that this mode requires a minimal gap channel length of 80 nm for gold; otherwise the gap plasmon cannot exist, which is shown in Figure 2 of manuscript (III). Higher order gap plasmon modes are possible, but would require even thicker layers, which would complicate the fabrication. Moreover, as

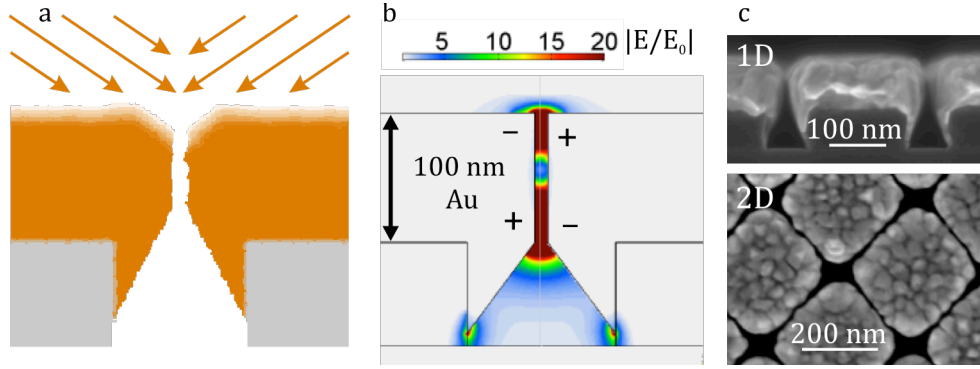


Figure 14. The gap plasmon mode. (a) Ballistic simulation showing the nanogap channel. (b) Near-field simulation showing the electromagnetic field hot spot and the charge distribution on the metal surface. (c) SEM images of 1D line arrays and 2D dot arrays.

higher order modes tend to lead to lower near-fields than the fundamental [138-140], no pattern in that regime has been fabricated, as the utilization of highest field enhancement is the focus of our work.

In manuscript (III), we have analyzed the near-field amplitude of gap plasmons by SERS in comparison with near-field simulations. We have studied the thickness and the gap size criterion, the coupling efficiency and the effect of the gap periodicity. The results are summarized below.

The thickness criterion is matched in near-field simulations, showing very weak enhancement for 10 nm spaced arrays with 30 nm layer thickness, and strong near-field enhancement for arrays with 100 nm layer thickness. The minimal layer thickness is the most important criterion for this gap plasmon mode and the gap size plays only the role in controlling the near-field amplitude for SERS. The optimal gap size of 10 nm for SERS experiments originates from the resonance matching condition of the gap plasmon mode with the excitation at 633 nm. The gap plasmon mode is characterized by a narrow dip in reflection. The gap plasmon resonance strongly redshifts for smaller gap sizes, i.e. from 580 nm to 720 nm for a gap size reduction from 30 nm to 7 nm, which is seen from simulations in Figure 1 of manuscript (III). When we excite the same crescent array at 785 nm, the optimum gap size is found at 5 nm, as a consequence of the better resonance matching at smaller gap sizes.

The coupling efficiency for exciting gap plasmons is very inefficient in 10 nm gap arrays, which is seen from the weak resonance magnitudes in the reflection spectra shown in Figure 3 of manuscript (III). This can be better understood from the fact that 96% of the pattern is composed of a flat gold film. We have found an efficient method to increase the coupling efficiency by tapering the small gap opening. In fact, we don't have to modify our nanogap fabrication to obtain tapered openings, but can merely excite the gap arrays from the rear side through the glass substrate. The gap region defined by two crescents has a flat opening on the front side and a tapered opening on the rear side of the array, which is seen in the SEM image and the ballistic simulations in Figure 14. By exciting the nanogap array from the tapered gap opening, the resonance magnitude increases 5-fold, shown in Figure 3 of manuscript (III). Similarly, we measure a 10-fold increased SERS signal compared to an excitation of the flat side. This corresponds to an increased near-field enhancement by a factor of 1.8, considering an $|E|^4$ dependency of the SERS signal.

The periodicity of the nanogap array influences the average near-field enhancement from the substrate. Contrary to this measured trend, we have found that the near-field enhancement per gap decreases for periods below 1 μm . This is concluded from the saturation of the average SERS signal for periodicities below 500 nm, which is shown in Figure 4 of manuscript (III). This effect originates from an interference of the individual gap plasmon modes leading to an inefficient coupling to the incident field. Such interference is possible for array spacings below the surface plasmon propagation length, which is roughly 3 μm for gold at a wavelength of 633 nm [190-192]. This result is interesting since it shows that the optimal packing density is not necessarily the one with the highest resolution.

One of the main conclusions drawn from the manuscripts (II) and (III) are that gold nanogap arrays require a minimum metal thickness of 80 nm to enable near-field enhancement in the gap channel. The gap plasmon resonance strongly redshifts for smaller gap sizes, meaning that the SERS enhancement is not necessarily maximal for the smallest gap size. The optimal period for gold nanogap arrays is 500 nm.

In the following, we demonstrate an alternative fabrication method for nanogap channels.

We have found an alternative technique to fabricate sub-10 nm gaps that does not require substrate tilting, which is discussed in manuscript (IV). Our angular evaporation method is considerably easier than other fabrication methods for sub-10 nm gap arrays, but substrate tilting might not be possible in many commercial evaporation tools. In the alternative method, we start from the same HSQ resist pattern and evaporate metal under normal incidence. Thereby, the metal layer on top of the resist not only increases in height, but also slightly broadens in width, due to surface diffusion and crystallite growth at the edges [193]. This implies that the elevated metal layer on top of the resist shadows the metal layer on the substrate level. The shadowing effect leads to a nanogap channel when the evaporated metal thickness exceeds the resist layer thickness, which is shown in the SEM images of Figure 15a-c. We have confirmed the nanochannels growth in ballistic simulations, shown in Figure 15d, and demonstrated the technique on various resist geometries, such as line, dot and kagome arrays, shown in Figures 1-4 of manuscript (IV).

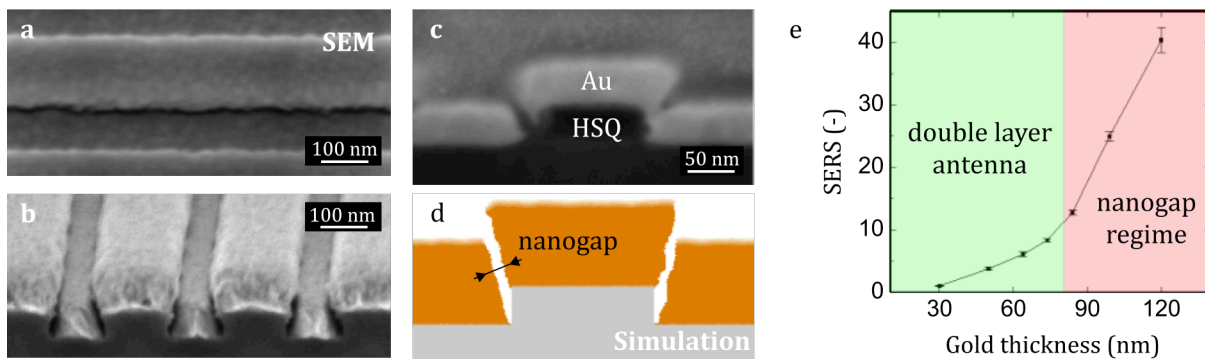


Figure 15. Double layer nanogap arrays. The obtained nanogap channels are seen in the SEM images: (a) tilted top view, (b) cross-section view and (c) Focused Ion Beam (FIB) cross-section cut. (d) The self-limited evaporation is verified in the ballistic simulations. (e) The SERS signal with increasing metal thickness showing the nanogap regime.

The critical parameter for this technique is the resist sidewall inclination. The nanogap channel only grows when the resist has a slight undercut or else both metal layers coalesce. The near-field enhancement of the double layer pattern is strongly influenced by the separation of both layers. For smaller separations, the near-field enhancement increases due to the coupling of image charges at both layers and peaks when the separation of both layers is below 10 nm. The measured SERS signals match with the simulations and increase continuously for smaller separations of the double layer pattern, which is illustrated in Figure 15e. Once a nanogap is formed for metal layers matching with the resist layer thickness, the SERS signal is boosted up to 40-fold compared to a separated double layer pattern, shown in Figure 15e and in Figure 3 of manuscript (IV).

One of the main conclusions drawn from the manuscript (IV) is that vertical nanogap channels can be fabricated in a one step evaporation under normal incidence. It is not only facile to implement, but also extremely low cost and yields a strong near-field enhancement.

4.5 Optimization of the near-field enhancement

4.5.1 Adhesion layer damping

In the previous sections, we have introduced a method to achieve strong near-field enhancement by controlling the geometry of the crescent array and found two operation regimes where either the subradiant crescent or the gap plasmon mode is excited. Apart from the metal geometry, the surrounding environment can also influence the near-field, such as the substrate and the adhesion layer. Such layers are often used to ensure the sticking of the metal on the silicon or the oxide surfaces. But it was already mentioned in several works, that such a layer interferes with the plasmon mode and reduces the near-field enhancement. The underlying mechanism involves plasmon resonance shifts, due to the modification of the surroundings permittivity, and near-field damping by absorbance in the adhesion material. Chromium is a widespread adhesion layer material, but also induces the strongest damping. Alternatives are discussed in the literature, such as using chromium oxide as adhesion material, which exhibits lower absorbance. The evaporation of oxidic adhesion layers is however considerably more complex and is not possible in many standard deposition tools.

In manuscript (V), we report a detailed analysis of the near-field damping for layer thicknesses varying between 0 nm and 7 nm for chromium, titanium and their oxides. As in all our

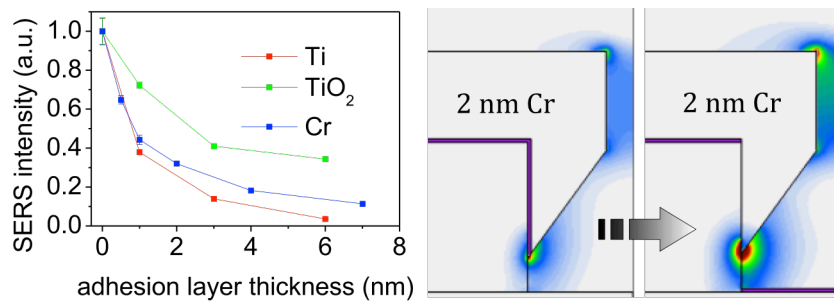


Figure 16. Modifying the adhesion layer such that the damping is minimal: small layer thickness and no overlap with the near-field hot spot.

work, the experimental findings were supported with thorough simulations. We observed and quantified the strong damping of the near-field amplitude by comparing the SERS activity of the crescent structures, which is shown in Figure 16 on the left hand side. This enabled us to confirm the importance of the materials absorbance when comparing the chromium and titanium layers with varying thickness. The SERS signal damping is found to become as low as a factor of 1.5 compared to patterns fabricated without an adhesion layer, when the adhesion layer thickness is reduced below 1 nm or changed to metal oxide.

Moreover, we have explored an alternative method, which can be applied to pure chromium evaporation and yet results in ultra low damping. This method is based on the modification of the adhesion layer geometry, so that it is not in contact with the near-field hot spots. Our angular evaporation method can be simply adapted to evaporate chromium under normal incidence. The adhesion layer is thereby not deposited on the resist sidewall and thus is not in contact with the near-field hot spots of the subradiant crescent mode. Both the simulated near-field enhancement and the measured SERS signal show a significant reduction of the damping factor, which is shown in Figure 16 on the right hand side. We have proved this concept by comparing the SERS damping of the subradiant crescent mode with the gap plasmon mode. The damping of the gap plasmon mode is considerably lower, since the near-field hot spot is entirely situated in the gap region and thus is not in contact with the adhesion layer per se, which is shown in Figure 5 of manuscript (V).

One of the main conclusion drawn from manuscript (V) is that metal adhesion layers can be realized without almost any signal loss by damping. It requires:

- (i) Adhesion layer thicknesses below 1 nm and
- (ii) Adhesion layer deposition without contact to the near-field hot spot

The latter requires a proper knowledge of the plasmonic modes, as is obtained here by combining the experimental with the modeled results. An artistic sketch of an “ideal” plasmonic structure, as developed in our work reported in manuscript (V), is shown in Figure 16.

4.5.2 Cavity resonance tuning

Another effective method for increasing the near-field amplitude is to improve the coupling efficiency of the plasmon mode. Previously, we have demonstrated the optimization of the pattern geometry and the excitation, to increase the coupling to plasmonic arrays. But nevertheless, part of the incident planewave is reflected from our crescent array and similarly, part of the incident light is transmitted through the crescent array. Hence, both the transmitted and reflected light seems to be lost for the excitation of plasmonic modes and cannot further enhance the near-field. In manuscript (VI), we have explored a substrate-based method for tuning the coupling efficiency by evaporating both a reflecting and a transparent layer on the substrate, before fabricating the crescent array. This layered substrate tunes both the amplitude and phase of the light that is transmitted through the crescent array and back reflected by the reflecting layer. This effect is illustrated in Figure 17, showing the involved fields and the design of the layered substrate below the plasmonic crescent array. Thus, the crescent array and the layered substrate form a Fabry-Perot cavity, which can be controlled by the spacing layer thickness. When the

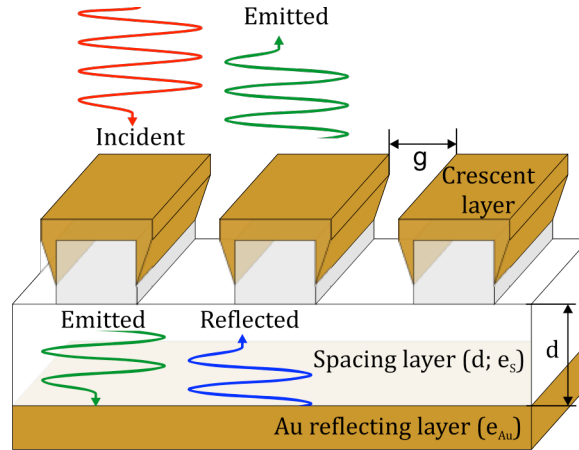


Figure 17. Tuning the coupling to the plasmonic array by a cavity below the crescent layer. The incident (red) field yields a plasmon emitted field (green) that interferes with the back-reflected (blue) field to yield near perfect trapping in the plasmonic array.

reflected light is out-of-phase with the plasmon emission, we reach near zero reflection and hence all the incident light is trapped in the layered crescent array.

Compared to the isolated crescent array on a glass substrate, the plasmon resonance of the layered structure is half as narrow, which is a result from the interference of the broad crescent resonance with the narrow cavity resonance. The plasmon resonance of the layer system can be tuned precisely by tuning either the spacer layer thickness or the gap size of the crescent array, which is demonstrated in Figure 2 and Figure 3 of the manuscript (VI). Doing so we achieved a modulation of the SERS signal by a factor in excess of 20, by simply changing the spacing thickness without modifying the crescent array itself. Additionally, the plasmon resonance position in our layered structure can be controlled by the angle of incidence, which is unique and originates from the dispersive cavity resonance. This is obviously a powerful approach, which adds versatility to practical applications that require precise resonance tuning, such as SERS.

The main conclusion drawn from manuscript (VI) is that layered substrates forming a Fabry-Perot cavity with the plasmonic layer are a simple and versatile method to control the resonance position and relative near-field enhancement, either by the spacer thickness of the incidence angle, with no need to tune the plasmonic pattern itself.

4.6 Applications arising from crescent arrays

4.6.1 Plasmon ruler based on radiance sensing

The gap size of our crescent array influences both the reflection magnitude and the SERS signal, as shown in section 4.3. Vice versa, one can detect gap size changes following either the SERS signal or the radiance of the plasmon resonance (i.e. the reflection or transmission magnitude), as sketched in Figure 18c. Since the SERS signal is an extremely localized effect prone to signal fluctuations (shown in Figure 11) and requires sophisticated microscope equipment, it is not the ideal technique to measure gap size changes. The radiance is however an averaged effect, which enable correlating the reflection magnitude to Ångström changes of the gap size that were induced by the EUV exposure dose for this purpose. Figure 18a illustrates the influence of the Fano

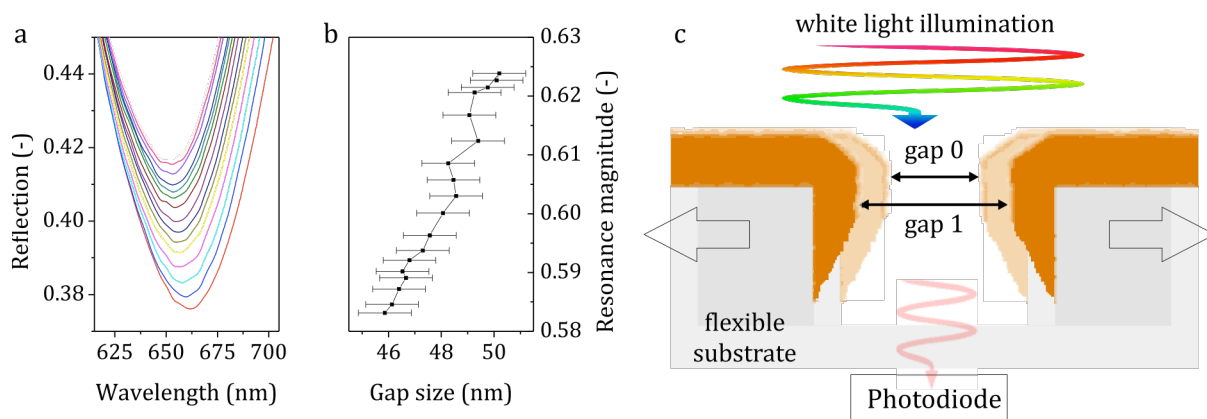


Figure 18. Design of a plasmon ruler with the radiance sensing principle. (a) The reflection spectrum for varying gap size of a crescent array. (b) The radiance, i.e. the reflection magnitude versus the gap size of a crescent array. The gap size is analyzed from SEM images. (c) Design of a plasmon ruler for the measurement of lateral displacement or torsion. The transmission through the gap array is measured with a photodiode.

resonance of crescent arrays with varying gap size. The gap size was measured by SEM image analysis beforehand and fitted for a calibration. Details of these experiments are given in the manuscript (I). We extract the magnitude of the reflection spectra at the resonance position and correlate this value with the array gap size, shown in Figure 18b.

From this experiment we obtain that a 1% change of the radiance corresponds to a variation of the gap size of roughly 6 Å, pointing to a sensing principle with sub-nanometer resolution. Such a plasmon radiance sensing method with Fano resonances can be implemented with a simple photodiode and could be applied for instance as a plasmon ruler [194, 195], to measure local displacement or torsion on the Ångström level. The sensor design is shown in Figure 18c and requires the fabrication of crescent arrays on a flexible and transparent substrate, i.e. polydimethyl-siloxane (PDMS).

4.6.2 Surface enhanced spectroscopy

Apart from sensing by the radiance, our crescent and nanogap arrays are indeed promising for surface enhanced spectroscopy because of (i) the ease of scalable large area fabrication, (ii) dense accumulation of near-field hot spots and (iii) high near-field homogeneity. The simple and yet controlled fabrication of sub-10 nm gaps is superior compared to other fabrication methods yielding sub-10 nm gaps [57, 121, 130, 131, 133-135], and at the same time, we can achieve high SERS signal homogeneity with deviations below 3%, shown in Figure 4 of the manuscript (II). This signal homogeneity is also confirmed by the polarization dependency of a linear gap array, with a modulation of the SERS signal of almost 100%, shown in the inset of Figure 4 in the manuscript (II).

For SERS experiments at different excitation wavelengths, we have fabricated crescent arrays from gold and silver. The gold crescent arrays have a good resonance overlap at SERS excitation wavelengths of 633 nm and 785 nm, which is shown in Figure 19a, but cannot be used at 532 nm due to the absorbance of gold arising from interband transitions [16]. Silver crescent

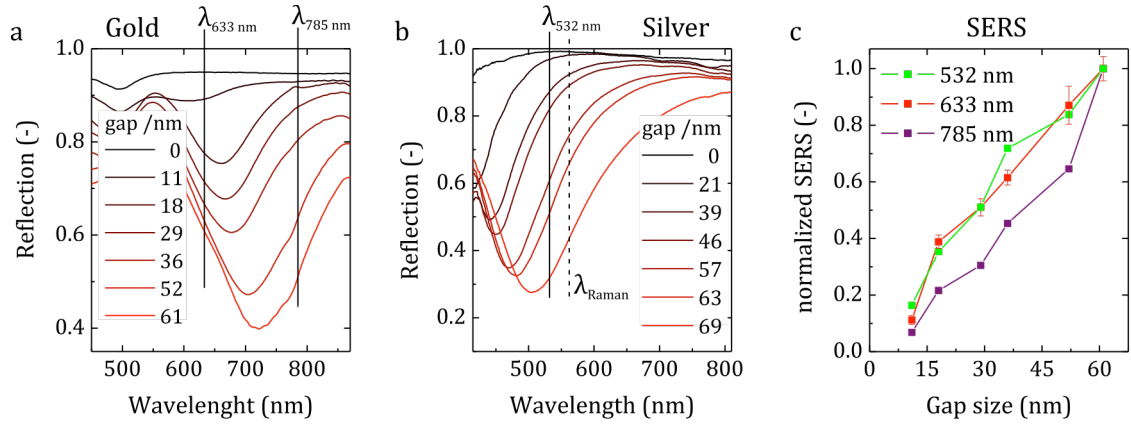


Figure 19. Crescent arrays for SERS experiments at different excitation wavelengths. (a) The plasmon resonance of a gold crescent array with 30 nm thickness and varying gap sizes. (b) The plasmon resonance of silver crescent arrays with 30 nm thickness and varying gap sizes. (c) SERS experiments at three excitation lines of 532 nm (on silver arrays), 633 nm and 785 nm (on gold arrays)

arrays on the contrary, induce 200 nm blueshifted Fano resonances in crescent arrays of the same size and thickness, which is shown in Figure 19b. The SERS signal dependency of all three SERS excitation wavelengths is shown in Figure 19c. The SERS signal increases for larger array gap sizes, which is in line with the larger resonance magnitude leading to higher near-field enhancement, explained in section 4.3. For gold crescent arrays at an excitation of 633 nm, we have calculated an averaged SERS enhancement factor of 1×10^6 and a local enhancement factor of 6×10^7 , when considering that the SERS signal is formed within 5 nm of the near-field hot spot, shown in section 3.2.2.

For 10 nm gap arrays with a gold thickness of 100 nm, we have calculated an average SERS enhancement factor of 1×10^6 and a local enhancement factor in the nanogap opening is calculated as 1×10^8 .

We have found that the crescent arrays can be reused repeatedly for SERS measurements, without deterioration of the enhancement factor, which is shown in Figure 20 with more details in manuscript (VII). The substrate is cleaned by ultraviolet (UV) exposure, with details given in the experimental section 3.2.2. We have applied the crescent arrays for measurements of differ-

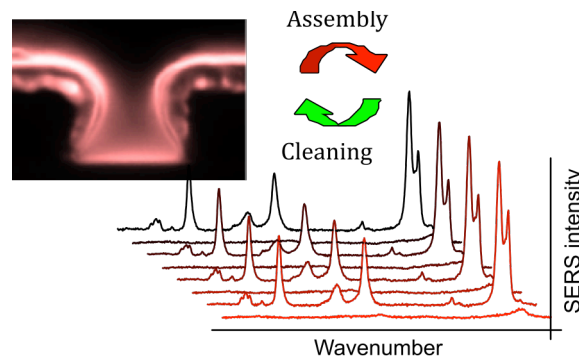


Figure 20. Reusable SERS sensing with crescent arrays. The substrate can be cleaned by UV exposure and reused for SERS experiments without deteriorating the enhancement factor.

ent thiol capped analytes on the same crescent array. In addition we have measured adsorption and oxidization kinetics during the layer formation and decomposition. We argue that with reusable SERS substrates, the absolute SERS signal can be quantified for conclusive studies in the determination of analyte concentration or packing density and the analysis of chemical SERS enhancement factors. Previously, SERS substrates were prone to irreproducible changes in the SERS enhancement factor after cleaning of the substrate [69-71]. We have shown that cleaning is also possible without deteriorating the near-field enhancement.

We have also identified a method to suppress the background peaks when measuring in solution, which is shown in Figure S3 of the published manuscript (III). By exciting the pattern from the rear side through a transparent substrate, the optical path overlaps only minimally with molecules in solution and hence their background Raman signal is less intense. Additionally, the tapered gap opening on the rear side of nanogap arrays improves the coupling efficiency and hence the near-field and SERS enhancement when the patterns are excited from the back-side, which was shown in section 4.4. This could be ideally applied in a fiber based sensor design.

To this end, we propose a sensor design where the crescent or the nanogap array is placed on a miniaturized probe at the end of a glass fiber tip, which is shown in Figure 21. Alternatively the crescent array could be bonded directly on the end of a fiber tip. This arrangement ensures a backside illumination of the array, while only molecules that diffuse into and through the crescent gaps are detected. At the same time, the background SERS signals from molecules or from the solvent diffusing along the top crescent surface are suppressed. By this, one can build a mobile SERS fiber probe that can be applied at remote locations and in solution. With our cleaning method based on UV exposure and washing, the fiber probe could also be made reusable without degradation of the near-field enhancement.

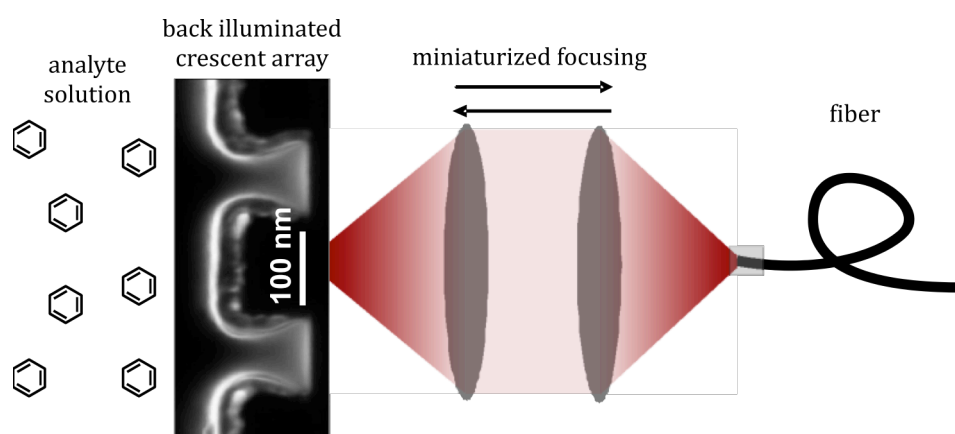


Figure 21. Design of a SERS fiber sensor under backside illumination of crescent or nanogap arrays.

Chapter 5 Conclusions

5.1 Achieved results

In this thesis, we have demonstrated the concept of angular evaporation for the improvement of near-field enhancement in periodic arrays. This evaporation technique offers a versatile and low cost routine to develop nanopatterns with sharp metal edges and controlled sub-10 nm gaps over large-area dimensions. We have fabricated complex patterns that typically require high-resolution lithography with a simple evaporation technique starting from a low-resolution resist pattern. With a potential method of wafer scale patterning, e.g. displacement Talbot lithography, the technique is applicable for mass production. Starting from a linear grating or nanodot resist pattern we reproducibly obtain metal crescent arrays with a large range of gap sizes and crescent shapes. We have identified that crescent arrays support both subradiant dark modes and gap plasmons. The plasmon modes strongly enhance the near-field either at the sharp crescent tips or in the gap region between two nanocrescents. The subradiant crescent mode leads to a Fano dip of the plasmon resonance in reflection and enhanced optical transmission through the array. Highest energy conservation and maximal near-field enhancement is proven to exist under critical coupling conditions of the subradiant mode to the incident field. This condition is met at a modulation damping value of 0.25 at the resonance position. We have proven that gap plasmons in 1D or 2D gold arrays are only supported above a minimum metal thickness of 80 nm. Such plasmons are Fabry-Perot type gap resonances and form a cavity mode between the upper and lower gap openings. Maximum near-field enhancement is found at the resonance position and when tapering the gap opening to optimize the coupling of the incidence field to the gap plasmon mode. We have shown for the first time, that highly periodic gold nanogap arrays can render the near-field enhancement in individual gaps inefficient, when gap plasmons begin to interfere at periods below 1 μm . This proves that the ideal period for maximum average near-field enhancement is not necessarily the smallest one.

Our concept of angular evaporation provides considerable technical improvements compared to other plasmonic substrates. We demonstrate reproducible fabrication of nanocrescent arrays over wafer scale area, only limited by the exposure area of the EUV lithography step. Owing to self-shadowing of the gap sidewalls, we also demonstrate reproducible sub-10 nm gap dimensions. This originates from the self-limiting fabrication leading to better uniformity of both the sharp crescent tips and the nanometer gap separations with only little defects. It is supported by the perfect SERS polarization dependency and extremely low SERS signal deviation of 3% over a linear array. We have demonstrated a method to minimize damping of the near-field caused by adhesion layers. The method is based on excluding the adhesion layer from the near-field hot spot together with a minimal layer thickness below 1 nm. Our angular evaporation concept is ideally suited for this; it uses different evaporation angles for the adhesion layer and thereby covers the substrate only partially. The near-field of the crescent arrays has been additionally improved by total absorption of the incident field. This was achieved by adding a reflecting layer and a spacing layer below the crescent pattern. By destructive interference, al-

most all the incident light was trapped in the crescent array and the SERS signal was modulated by a factor of 20. This method is powerful because it is purely substrate based and does not require modifying the plasmonic pattern. The arrays have proven itself robust against oxygen plasma and ultraviolet treatment, sonication and storage. This is demonstrated by the consistent near-field enhancement after numerous cycles of analyte deposition, SERS analysis and substrate cleaning.

Arising from large areas, from low cost substrates and their technical improvements, we have demonstrated several promising applications. The crescent arrays are found to be extremely sensitive to Ångström changes of the gap size, when measuring the magnitude of the reflection dip. This radiance based sensing can be simply realized by a photodiode, rather than by measuring a plasmon resonance shift requiring a spectrometer. Such a sensor can be used as plasmon ruler to detect small lateral displacements or torsion. The main applicability is however found in utilizing the near-field for excitation and emission enhancement. The large area crescent or nanogap arrays are both ideal substrates for SERS and fluorescence enhancement. The superior SERS signal homogeneity with less than 3% deviation is promising for practical applications, especially when both qualitative and quantitative analysis is required. We have calculated an average/or local SERS enhancement factor in excess of 1×10^6 / or 1×10^8 . Resonance matching with the excitation laser is a prerequisite for maximum enhancement factors. The plasmon resonance of the array can be tuned either by the gap size and metal thickness, or by the angle of incidence without changing the nanopattern geometry. The incidence angle tuning is unique for the layered substrate composed of a reflecting and a spacing layer, which induces mode dispersion of the crescent array. The tapered gap opening at the rear side of the nanogap array enables better coupling efficiency and thus higher SERS enhancement factors. We demonstrated that background SERS signals are reduced under the excitation from the rear side through a glass substrate, which is attractive for fiber coupled SERS sensor probes. The crescent array is extremely robust due to the clasp of metal around the resist. This is beneficial for reusable SERS experiments, where we found that the substrate can be reused with exactly the same near-field enhancement for multiple times. By this, we have demonstrated kinetic SERS analysis studies of a thiol layer self-assembly and its oxidation rate during UV exposure. The versatile geometry of the pattern array can also allow for a size-based selection of the analyte molecules. By controlling the gap size of the array, larger molecules are prevented from entering the gap region. Only smaller molecules that diffuse through the gap are detected by SERS, since the near-field hot spot is located inside the gap region or on the rear side of the gap.

5.2 Future developments

Up to now, the wafer scale fabrication of crescent and nanogap arrays is only possible with multiple EUV exposures. The EUV lithography was ideally suited for the analysis in this thesis thanks to its precise tunability of the duty cycle that results in reproducible fabrication and homogeneity over mm^2 large pattern. Due to the fact that only the angular evaporation is scalable, the EUV resist patterning must be replaced by another technique, which is able to cover wafer scale areas in a single exposure. Examples of such exposure techniques with resolution of 200-500 nm periods include self-assembly, standard (UV) photolithography, displacement Talbot lithography [196], (UV) laser interference [99] and nanoimprint lithography.

We have identified several opportunities for promising sensor devices and applications, with two of them already demonstrated in section 4.6. In SERS, the qualitative analysis of analyte molecules can be hindered when multiple analyte molecules and solvents create background peaks that overlap with the desired analyte peaks. To circumvent this, the background peaks must either be suppressed or the analyte molecules separated to allow for an individual detection. In our opinion, the linear crescent array could serve as a separation column. The crescent array encloses 1.8 mm long nanochannels where the analyte molecules could diffuse along and thereby undergo a size-based separation. After their separation, each analyte could be detected individually by scanning the SERS signal along the channel. Moreover, the HSQ resist and substrate inside the nanochannels could be functionalized to improve the separation of analyte molecules along the channels.

Transmission through nanometer channels leads to a giant near-field enhancement in small volumes [197]. We have performed preliminary experiments in the mid infrared wavelength regime (5 μm to 10 μm) and observed that light can penetrate through our 10 nm gap arrays made of gold. These are promising results to perform sensing experiments in the infrared, by placing analyte molecules into the nanogaps. Their infrared absorbance might be strongly enhanced by the near-field and small quantities could be measured with this method. It is planned to optimize the array geometry to support localized resonances in the infrared. Moreover, nanogap arrays have shown a near-field enhancement in the terahertz regime [197]. By modifying our fabrication technique to provide terahertz transmission through the nanogap arrays, we may contribute significantly to the currently blossoming field of terahertz sensing combined with near-field enhancement.

Crescent arrays are promising patterns to fabricate metamaterials, which was demonstrated by achieving broadband negative index of refraction in the visible range via numerical studies [110]. For this, a multilayer stacking of crescent arrays is necessary. The long-term objectives arising from negative index of refraction are applications in optical manipulation, cloaking, and flat optical components [198]. So far, negative index of refraction could not be shown in a large visible range experimentally and over large areas. In preliminary experiments, we have tested the possibility of stacking 2 to 4 gold crescent array layers. We have observed hybridized plasmon modes and a linked SERS modulation of the stacked layers, which is promising for future experiments. We have identified the importance of a homogeneous dielectric medium surrounding the crescents and the perfect alignment of the 1D crescent array layers. This can be circumvented by choosing 2D crescent arrays stacked on top of each other separated by transparent spacing layers obtained by spin coating, sputtering or depositions.

The generation of hot electrons currently receives a lot of attention, with the aim of harvesting the charges created by a plasmon's near-field [11]. The essential objective is to build a device that can collect the hot electrons in order to produce a photocurrent. The possibility to generate hot electrons in noble metals was shown experimentally by x-ray spectroscopy [199]. In an early publication [200], it was shown that the near-field could be read out electrically to build a photodetector, which is sensitive only at the plasmon resonance of the metal nanoparticle. Apart from this, the electric near-field was also used to induce photochemical processes that are controlled by exciting the plasmon mode [201]. If it were possible to increase the efficiency of the hot electron extraction, it would be possible to build a plasmonic solar cell [11]. We have shown several methods to increase the near-field enhancement around metal nanoparticles in this thesis. With our knowledge to achieve a homogeneous and reproducible near-field distribu-

tion across the patterned area, we have set a solid basis for plasmon energy harvesting devices. Apart from that, we have shown broadband tunability of the plasmon resonance from the UV to the near infrared by an appropriate choice of the array geometry and material. Moreover, our angular evaporation technique is suitable for low cost fabrication of large area patterns. Thereby, a patterned semiconductor array can replace the HSQ resist pattern to design a photoelectric cell. By using an Ti adhesion layer as the Schottky barrier, one could design a device for a controlled flow of the photocurrent [200]. This principle was already shown in earlier publications [202].

Chapter 6 Publications

(I) Critical coupling to crescent arrays and plasmon radiance sensing

Manuscript state

Published manuscript

Reference

B. Gallinet, T. Siegfried, H. Sigg, P. Nordlander, O. J. F. Martin, “*Plasmonic Radiance: Probing Structure at the Ångström Scale with Visible Light*”, Nano Letters **2012**, 13 (2), 497-503

Publication date: 28. December 2012

DOI: 10.1021/nl303896d

URL: <http://pubs.acs.org/doi/abs/10.1021/nl303896d>

Current citations: 20

Highlighted in Nature Materials:

- K. Tsakmakidis, “*Plasmonic Radiance*”, Nature Materials **2013**, 12, 4, 282

Author contribution

B. Gallinet developed the theory and the model of critical coupling to Fano modes. T. Siegfried fabricated the samples. T. Siegfried performed the experiments and crescent near-field simulations, leading to the verification of the model. B. Gallinet wrote the manuscript and T. Siegfried added the experimental part. B. Gallinet and T. Siegfried revised the manuscript. O. J. F. Martin supervised the project and corrected the manuscript. P. Nordlander and H. Sigg corrected the manuscript.

Conference contribution

T. Siegfried “*Fano coupling from line arrays of crescents*”, **poster** at Surface Plasmon Polariton (SPP6) in May **2013**, Ottawa, Canada

Published paper

Plasmonic Radiance: Probing Structure at the Ångström Scale with Visible Light

Benjamin Gallinet,[†] Thomas Siegfried,[‡] Hans Sigg,[‡] Peter Nordlander,[§] and Olivier J. F. Martin^{*,†}

[†]Nanophotonics and Metrology Laboratory, Swiss Federal Institute of Technology (EPFL), CH-1015 Lausanne, Switzerland

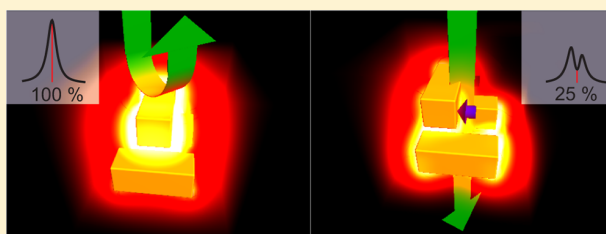
[‡]Laboratory for Micro. and Nanotechnology, Paul Scherrer Institut, 5232 Villigen PSI, Switzerland

[§]Department of Physics and Astronomy, M.S. 61 Laboratory for Nanophotonics, Rice University, Houston, Texas 77251-1892, United States

S Supporting Information

ABSTRACT: Plasmonic modes with long radiative lifetimes combine strong nanoscale light confinement with a narrow spectral line width carrying the signature of Fano resonances, making them very promising for nanophotonic applications such as sensing, lasing, and switching. Their coupling to incident radiation, also known as radiance, determines their optical properties and optimal use in applications. In this work, we theoretically and experimentally demonstrate that the radiance of a plasmonic mode can be classified into three different regimes. In the weak coupling regime, the line shape exhibits remarkable sensitivity to the dielectric environment. We show that geometrical displacements and deformations at the Ångström scale can be detected optically by measuring the radiance. In the intermediate regime, the electromagnetic energy stored in the mode is maximal, with large electric field enhancements that can be exploited in surface enhanced spectroscopy applications. In the strong coupling regime, the interaction can result in hybridized modes with tunable energies.

KEYWORDS: Fano resonances, electromagnetically induced transparency, plasmonic nanosensors, surface enhanced Raman scattering (SERS), extraordinary optical transmission



With their ability to concentrate light at a deep-subwavelength scale by excitation of surface plasmons, metallic nanostructures play a major role in current nanoscience.¹ In particular, optical tweezers,² antennas,^{3,4} lasers,⁵ photodetectors,⁶ or biochemical sensing platforms^{7,8} have been scaled down to the nanometer range. However, their performance are limited by the short lifetimes of surface plasmon resonances.⁹ Recently, it has been shown that the use of plasmonic modes with long radiative life times (subradiant modes) can drastically enhance the performance of nanophotonic devices.^{10–12} Their spectral response carry an asymmetric line shape with sharp spectral features, characteristic of Fano resonances.^{13–22} The coupling of subradiant modes to radiation, their radiance, is directly controlled by the geometrical configuration of the nanostructures,¹⁹ and also governs their optical response and the location and amplitude of light confinement.²⁰ Despite the fact that the use of subradiant modes for nanophotonic applications critically depends on the coupling strength, the choice of an optimal regime has so far never been addressed.

In this work, we use a universal model for interacting radiative and localized channels to investigate the radiance of a plasmonic mode. We demonstrate that the radiance of a plasmonic mode can be classified into three different regimes. In the weak coupling regime, the radiance of the mode is small and extremely sensitive to perturbations in the coupling. We

introduce a novel sensing concept, radiance sensing, which is based on the sensitivity of the radiance to the environment, rather than conventional plasmon sensing relying on the wavelength shift of plasmon modes.⁸ In the intermediate regime, the radiative damping is equal to the intrinsic damping, and the radiance does not depend strongly on the coupling. However for this critical coupling, the electromagnetic energy stored in the mode is maximal and associated to large electromagnetic field enhancements. For strong coupling, the optical response can result in two distinct and broad hybridized modes.²³ We illustrate these universal findings theoretically and experimentally on two very different plasmonic nanostructures. Specifically, we study a plasmonic nanostructure consisting of a dipolar nanorod antenna on top of two parallel nanorods supporting a nonradiative quadrupolar mode. The other specific example consists of subwavelength slits in a metallic film fabricated with extreme ultraviolet interference lithography (EUV–IL). In this system, the plasmon mode supported by the individual nanowires serves as the subradiant mode, and its radiance is controlled by changing the width of the gap. The facile tuning of the coupling in this nanostructure makes it

Received: October 23, 2012

Revised: December 19, 2012

Published: December 28, 2012



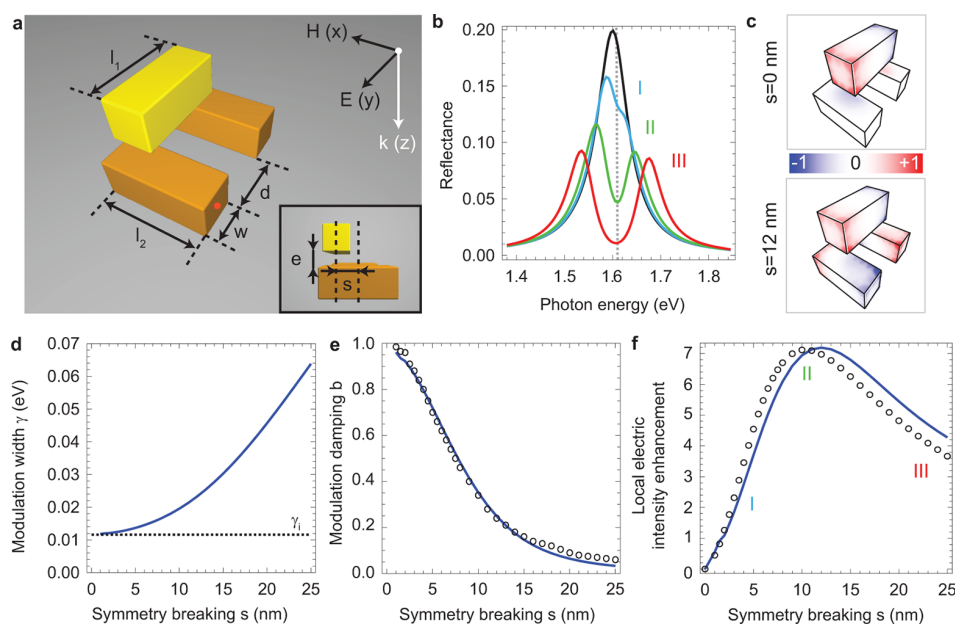


Figure 1. Symmetry breaking in a plasmonic nanostructure. (a) Schematic of a single nanostructure and definition of the geometrical parameters: $l_1 = l_2 = 100$ nm, $w = 40$ nm, $d = 60$ nm, $e = 20$ nm. (b) Reflectance of a two-dimensional array with period 500 nm in both x and y directions for various values of the symmetry breaking s . The permittivity of gold is interpolated from experimental data,²⁴ and the refractive index of the surrounding environment is 1.33 (water). The black, blue, red, and green curves correspond to $s = 0$ nm, $s = 5$ nm, $s = 12$ nm, and $s = 25$ nm, respectively. In the system with broken symmetry, the resonant excitation of the quadrupolar mode supported by the bottom nanoparticles induces a modulation of the reflectance spectrum. The symbols I, II, and III represent the three different coupling regimes. (c) Surface charge distribution at a resonant energy 1.61 eV for $s = 0$ nm and $s = 12$ nm, respectively. (d) Spectral width of the modulation as a function of the symmetry breaking. The solid blue and the dashed black lines represent the total and the intrinsic width, respectively. (e) Modulation damping b as a function of the symmetry breaking. The solid blue line corresponds to the ratio of the reflectance at a photon energy of 1.61 eV in the symmetry broken system ($s \neq 0$) to the reflectance in the symmetric system ($s = 0$) at the same energy. The black circles correspond to calculations using panel d and the expression of b in eq 2. In panels d and e, the modulation width and damping are fitted from eq 1 for $q = 0$. (f) Electric field intensity enhancement related to the quadrupolar mode at 1.61 eV as a function of the symmetry breaking. The solid blue line corresponds to a direct evaluation at 4 nm from the surface of the bottom bar, as shown by a red point in panel a. The black circles correspond to calculations using panel d and eq 3.

possible to reach all three levels of radiance. In the weak coupling regime, we show that radiance sensing enables the detection of gap widths at the sub-nanometer scale. Using surface-enhanced Raman scattering (SERS), we verify that the largest electric field enhancement occurs in the intermediate regime.

Figure 1a illustrates the geometry of a plasmonic nanostructure characterized by a Fano-resonant response.²⁵ Each unit cell consists of a metallic nanoparticle placed on top of two parallel metallic nanoparticles. The top nanoparticle supports a plasmonic mode with a dipolar distribution of charges and acts as an antenna for receiving and emitting light. The two bottom nanoparticles support a hybridized plasmonic mode with a quadrupolar distribution of charges. In the quasistatic approximation, the out-of-phase dipole moments of the quadrupolar mode forbids far-field radiation. In the symmetric configuration ($s = 0$), only the antenna mode can be excited by the homogeneous field of a plane wave. The spectra of the nanostructure array are calculated with a full-field numerical method based on the solution of surface integrals.^{26,27} As shown in the reflectance spectrum of Figure 1b, the antenna resonance appears as a Lorentzian centered around $\omega_a = 1.599$ eV with a spectral width of $\gamma_a = 0.040$ eV. A relative displacement s of the top antenna from the symmetric position allows the coupling of light into the quadrupolar mode resulting in an antiresonance (dip) of the reflectance (see Figure 1c). The resonance width γ of the quadrupolar mode is

given by the sum of two contributions: the intrinsic damping γ_i and the radiative contribution γ_c . For simplicity, in the following we will refer to the coupling between these two modes as γ_c although strictly speaking the radiative damping will depend both on the coupling and antenna properties. The intrinsic width γ_i is associated with nonradiative decay by the Joule effect in the metallic nanostructures and corresponds to the minimal value of the total spectral width γ . As the mode coupling is increased by symmetry breaking (increasing s , as shown in Figure 1d), the quadrupolar mode broadens, and the contribution of γ_c to the spectral width increases.

In the symmetry-broken configuration, the light impinging onto the system can follow two pathways: it is either directly scattered by the antenna or re-emitted after indirect excitation of the quadrupolar mode. The destructive interference between the direct and the indirect pathways yields a window of transparency, as a plasmonic equivalent to electromagnetically induced transparency.^{14,25} In the more general case where the antenna mode is detuned from the quadrupolar mode, both destructive and constructive interference can be observed. The resulting reflectance profile is modulated by an asymmetric line shape characteristic of Fano resonances.^{16,21,28,29} Around the resonance frequency of the quadrupolar mode ω_0 , the reflectance spectrum R is the product of the antenna reflectance R_a by the asymmetric modulation function:^{19,29}

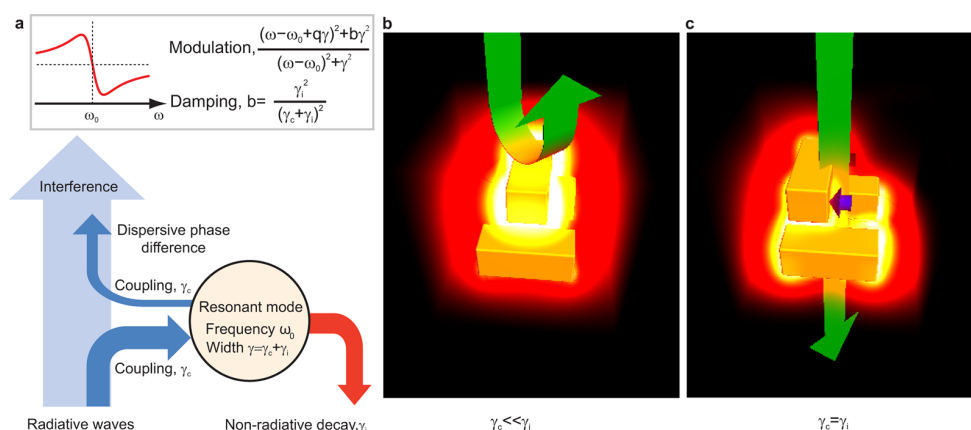


Figure 2. Fano interference and radiance sensors. (a) A mode of resonance frequency ω_0 is weakly coupled to a continuum of radiative waves with constant γ_c . The in-coupled energy is either lost by nonradiative decay with constant γ_i or recoupled to the continuum. The total resonance spectral width is $\gamma = \gamma_c + \gamma_i$. Due to destructive or constructive interference between the direct and the indirect pathways, the spectral response is modulated by an asymmetric line shape. The parameter q , known as the Fano parameter, describes the degree of asymmetry. Nonradiative decay prevents full interference, resulting in a modulation damping. The modulation damping parameter b is given by the ratio of the intrinsic width to the total width. (b) For low radiative coupling $\gamma_c \ll \gamma_i$, the resonant mode is weakly excited, corresponding to full reflectance in the plasmonic nanostructure. (c) For balanced lifetimes $\gamma_c = \gamma_i$, the resonant mode is fully excited, and transparency is observed. Only a nanometer-scale geometrical perturbation is necessary for this switching process, which can be used for the design of ultrasensitive nanosensors.

$$R = R_a \frac{(\omega - \omega_0 + q\gamma)^2 + b\gamma^2}{(\omega - \omega_0)^2 + \gamma^2} \quad (1)$$

where q and b describe the modulation asymmetry and modulation damping, respectively. In the case where the mode detuning is small compared to the antenna resonance width γ_a , the modulation is symmetric ($q = 0$), and the modulation damping b becomes the ratio of the reflectance at the minimum of the anti-resonance in the symmetry-broken configuration ($s \neq 0$) to the reference reflectance in the symmetric configuration ($s = 0$) at the same frequency: $R(\omega_0) = R_a(\omega_0)b$. As the mode coupling is increased, the modulation becomes more pronounced (see Figure 1e): the modulation damping ranges from 1 in the weak coupling regime ($\gamma_c \ll \gamma_i$) and decreases monotonically to 0 in the strong coupling regime ($\gamma_c \gg \gamma_i$). For weak coupling, the modulation amplitude is extremely sensitive to the symmetry breaking. A relative displacement of 12 nm of the antenna induces 75% variation of reflectance. However, the monotonic behavior of the modulation parameters in the far-field reflectance spectra does not appear in the near-field. In Figure 1f, the electric field intensity enhancement associated with the quadrupolar mode initially increases along with the modes coupling but reaches a maximum for a specific value of the mode coupling and then decreases. The same behavior is reproduced for an isolated structure (see Figure S1 in the Supporting Information).

The local near-field intensity enhancement depends on the total energy stored by the mode and the modal field distribution. As will be shown in the next subsection, the energy flow through a subradiant mode is the key parameter determining its radiance and role in Fano interference. Thus the results in Figure 1f allow us to classify the radiance of a subradiant mode into three distinct regimes: a weak coupling regime (I) where the mode energy increases monotonically with coupling; an intermediate regime (II) where the mode energy is maximal and the radiance is only weakly dependent on coupling; a strong coupling regime (III) where the mode excitation decreases with increasing coupling. The identification of energy transfer as the key parameter determining the

radiance of the subradiant mode provides crucial insight for the rational design of Fano-resonant structures for specific applications. For instance, in sensing applications, the system should be positioned in the weak coupling regime. As will be demonstrated below, the extreme sensitivity to geometrical perturbations is due to a reversal of the relative role of the radiative and nonradiative contributions to the total damping. In SERS applications, the system should be in the intermediate coupling regime where the electromagnetic energy stored in the subradiant mode is maximal.

To provide more insights into the interplay between radiative and nonradiative decay, we introduce a general model for coupling of radiative and localized channels (see Figure 2). The trade-off between radiative and nonradiative decays is a fundamental issue in quantum optics, in particular for the control of spontaneous emission,^{30–32} and we will explicitly investigate it in Fano-resonant systems. The localized channel is a spectrally narrow resonant mode, such as the quadrupolar mode in Figure 1. This mode is coupled to a continuum of radiative waves with constant γ_c (the role of the dipole antenna is only to enhance the coupling efficiency between the resonant mode and the continuum). The in-coupled energy is either lost by nonradiative decay with a damping rate γ_i or by reciprocity recoupled to the continuum with a rate γ_c . Due to the constructive and destructive interference between the continuum and the recoupled wave, the amplitude of the observed signal carries an asymmetric signature. The nonradiative and radiative lifetimes of the resonant mode are given by γ_i^{-1} and γ_c^{-1} , respectively. During this process of energy exchange between the continuum and the resonant mode, part of the light intensity is decayed nonradiatively, which prevents complete destructive and constructive interference. The portion of light intensity which does not contribute to the interference is the modulation damping and is given by the ratio of the intrinsic width to the total width (eq S38 in the Supporting Information):

$$b = \frac{\gamma_i^2}{(\gamma_c + \gamma_i)^2} \quad (2)$$

Let us now consider the electromagnetic energy storage in the resonant mode. In a conservative system ($\gamma_i = 0$) more energy would be stored in the mode with decreasing coupling. In a nonideal case, however, intrinsic losses introduce dissipation, so that energy accumulation in the mode is negligible for very weak coupling. In the weak coupling regime (I), the modulation depth rapidly evolves as the radiative channel opens up for the resonant mode. As the coupling increases, the in-coupled energy balances the intrinsic losses, and the energy storage in the mode reaches a maximum (coupling regime II). For stronger coupling (III), the radiative channel limits the energy stored in the mode which decreases. The electromagnetic energy stored in the resonant mode has the following behavior as a function of the coupling:

$$\text{stored energy} \propto \frac{\gamma_c}{(\gamma_c + \gamma_i)^2} \quad (3)$$

derived in the Supporting Information. The regime of high energy storage (II) occurs when the radiative and non-radiative losses exactly compensate each other ($\gamma_c = \gamma_i$), which is analogous to the impedance matching condition in the design of antennas.¹⁰ This condition which we will refer to as the critical coupling, corresponds to $b = 1/4$ and can thus be deduced from the far-field pattern. The quantitative relations between modulation damping and energy storage drawn from this model are valid for any linear wave-propagating system with coupled radiative and nonradiative channels. In particular, the decomposition into three coupling regimes and the corresponding behavior of the modulation damping parameter are very well reproduced in the plasmonic nanostructure of Figure 1. The extreme sensitivity of the plasmonic nanostructure to geometrical perturbations in the weakly interacting regime (I) stems from a transfer from low to full excitation of the resonant mode. During the process, light switches from total reflectance (see Figure 2b) to transparency (see Figure 2c).

The model system sketched in Figure 3a consisting of two coupled oscillators A and B, introduced as a mechanical analogue of Fano resonances,³³ provides a particularly simple and intuitive corroboration of the mechanisms described in our two-channel model. The oscillator A is forced and has a high damping constant γ_a modeling both radiative and nonradiative losses of the antenna mode, whereas the oscillator B has a low damping constant γ_i associated only to nonradiative losses. The equivalents of eqs 1, 2, and 3 for this system can be derived and expressed directly in the harmonic oscillator parameters (see the Supporting Information), which shows the universality of our approach. In Figure 3b, the two oscillators have different resonance frequencies, and the modulation is asymmetric.¹⁹ This more general case of destructive and constructive interference corresponds to $q \neq 0$ in eq 1. The presence of the resonant mode alters the intrinsic properties of the radiative channel, so that the spectral response is altered for strong coupling. In Figure 3c, the mode energy is equivalent to the amplitude of the oscillator B, which also increases as a function of the oscillator coupling and reaches a maximum when the coupling γ_c balances intrinsic losses γ_i . As the coupling increases, the width γ of the modulation becomes comparable to the width γ_a of the oscillator A. For strong coupling,

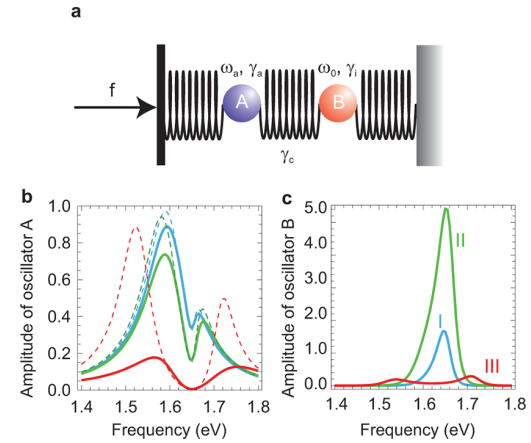


Figure 3. Mechanical analogue of Fano interference. (a) A forced oscillator A with frequency ω_a and large damping γ_a modeling a plasmon mode with both radiative and nonradiative losses, is coupled with constant γ_c to a free oscillator B with frequency ω_0 and low damping γ_i modeling a plasmon mode with nonradiative losses only. (b–c) Amplitude of the oscillators (b) A and (c) B as a function of the frequency, with $\hbar\omega_a = 1.599$ eV, $\hbar\gamma_a = 0.060$ eV, $\hbar\omega_0 = 1.650$ eV, and $\hbar\gamma_i = 0.012$ eV. The blue, green, and red curves correspond to $\hbar\gamma_c = 0.003$ eV, $\hbar\gamma_c = 0.009$ eV, and $\hbar\gamma_c = 0.082$ eV, respectively. The solid and dashed line correspond to the direct evaluation from the equations of motion and to the evaluation with eq 1, respectively.

splitting in the response of the oscillator B is observed, each individual resonance being a normal mode of the composite system, and the dip in the spectral response of oscillator A of the system is not Fano interference but just the sum of two Lorentzians centered on each hybridized mode.^{23,34,35} This limiting case is the classical analogue of Autler–Townes splitting.^{33,34,36}

As an experimental illustration of the model, the optical properties of plasmons in a sub-wavelength array of gold nanostructures were investigated as a function of the nearest-neighbor separation distance (see Figure 4). In this system, the radiative channel is given by the light directly transmitted through the slits. This forms a nonresonant radiative continuum, in contrast to what was the case for the nanostructure of Figure 1 where a resonant dipole antenna coupled to the radiative continuum acts as the immediate emitter–receptor. Here, the plasmon associated the individual wires plays the role of the resonant mode weakly coupled to radiation. Figure S2 of the Supporting Information shows that the plasmon mode is excited only for an electric field polarization perpendicular to the wires, and at the resonance frequency hot spots are observed at the edges of the nanowires. For very small slit openings, the plasmon mode is not efficiently excited, and the reflectance in Figure 4b is close to that of an infinite gold film. As the gap opens, the coupling of the plasmon mode to the radiative continuum increases. The destructive interference of light re-emitted by the plasmon mode with the directly reflected light results in a dip in the reflectance spectrum and enhanced transmission through the nanoslits.³⁷ With this interference process which is also the physical origin of extraordinary optical transmission,^{1,37} less light is reflected than the ratio of metal filling the unit cell (see Figure 4c).

The opening of the gap increases the amount of light entering the slit and as a consequence the coupling of the

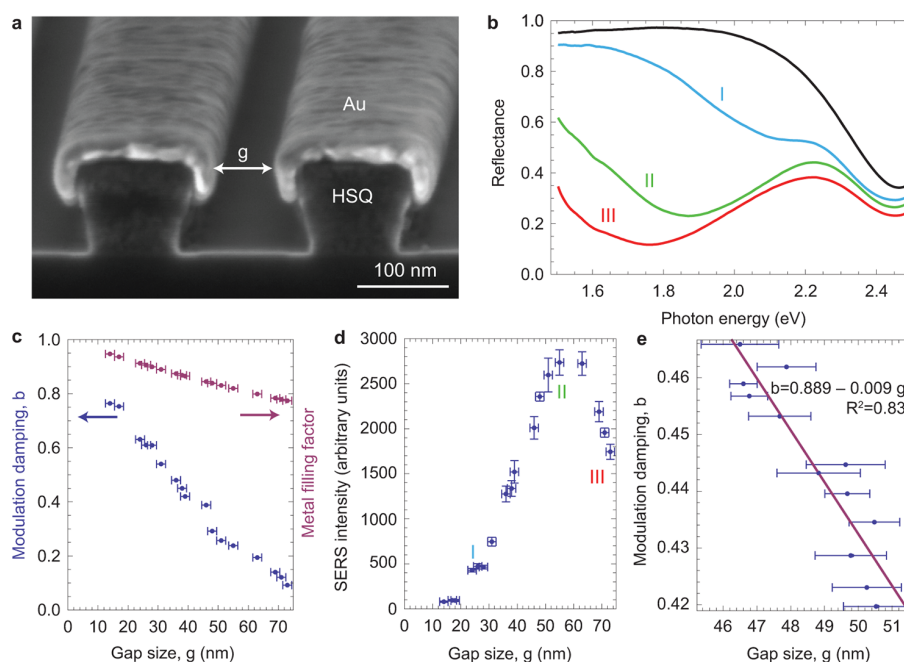


Figure 4. Control of slit opening in a sub-wavelength array of gold nanostructures. (a) Cross section scanning electron micrograph (SEM) of an array fabricated with extreme ultraviolet interference lithography and shadow evaporation. The underlying grating has a periodicity of 250 nm, a depth of 120 nm, and a spacing of 110 nm between two lines. The gold layer thickness is 38 nm. (b) Reflectance spectra for various values of the gap size. The black, blue, red, and green curves correspond to $g = 0$ nm, $g = 36$ nm, $g = 61$ nm, and $g = 75$ nm. A surface plasmon resonance is excited in the gap between two neighboring nanostructures. The interference of the gap plasmon with the directly reflected light yields a window of transmission. (c) Modulation damping as a function of the gap size g , compared to the metal filling factor defined as the ratio (period-gap)/period. (d) The surface enhanced Raman scattering (SERS) intensity of a benzenethiol monolayer excited at 633 nm, proportional to the fourth power of the electric field enhancement, is measured as a function of the gap size g . (e) Optical spectra are collected stepwise along a 600 μm long pattern with a gold layer thickness of 45 nm. Multiple SEM images are recorded along the same axis of the optical measurements to compare the average gap size to the modulation damping. Horizontal error bars correspond to the standard deviation of the average gap size measured with SEM over the area of illumination.

plasmon mode to the radiative continuum. The ratio of the nonradiative to the radiative decay rate of the plasmon mode decreases and as a consequence also the modulation damping (see Figure 4c). To probe the corresponding variation in near-field intensity, we measure the SERS response of molecules adsorbed at the surface of the sample, enhanced as a function of the fourth power of the electric field amplitude.^{8,38} In Figure 4d, the SERS signal from the array is measured as a function of the gap size. Similarly to the reflectance, the SERS signal strongly depends on the polarization.³⁹ A maximum is observed for a gap of 55 ± 1.5 nm, and the corresponding value of the modulation damping parameter is 0.24. This value is in very good agreement with our universal theoretical prediction of maximal energy storage for 1/4, confirming experimentally the validity of the existence of a critical coupling for optimal near-field enhancement. The modulation damping b is used here as direct quantitative indicator of the radiative decay rate. During the opening of the gap to full excitation of the plasmon mode (regime I), a change of 75% of the modulation damping is observed. In this regime, variations of the gap size measured with scanning electron microscopy (SEM) are probed optically by directly measuring the modulation damping: a linear fit of slope 0.009 nm^{-1} is obtained (see Figure 4e). The horizontal error bars correspond to the standard deviation of the gap size measured with SEM over the area of illumination, which can reach the sub-nanometer scale. In these cases, the distance from the average of the gap size to the trendline is comparable to the standard deviation. This implies that, by using the trendline as a

calibration curve, a measurement of the gap size at the sub-nanometer scale can be performed. With this method, the measurement is not limited by the spectral resolution of the apparatus.

Surface plasmon modes are extremely sensitive to perturbations of their radiance. The new concept of radiance sensing uses this advantage when the optical response of a subradiant mode switches from a nonresonant to a fully resonant situation. We now compare this approach to standard localized surface plasmon sensing, where the perturbation is monitored via a spectral shift of the resonance.^{7,8,12} For approaches where the shift is calculated by fitting the entire line shape to an analytical formula,^{12,19,20} the accuracy and stability of the fit in detecting a perturbation depends on the strength of the intensity variations of the line shape. In experimental measurements, the accuracy is determined by the signal-to-noise ratio, which also depends on the strength of the intensity variation at a fixed frequency. We therefore consider the strength of the intensity variations for a given displacement as the sensitivity of the system. Considering the system of Figure 1, a perturbation is applied to the interparticle distance so that a spectral shift of the subradiant mode is observed (Figure S3 of the Supporting Information). The sensitivity with respect to the antenna position in Figure S1 (controlling the radiance of the subradiant mode) is more than five times larger than the sensitivity with respect to the interparticle distance in Figure S3. This shows that radiance sensing is able to surpass the performance of standard localized surface plasmon sensing. In

Nano Letters

Letter

our particular experimentally fabricated gap array, radiance sensing has been used to detect geometrical displacements at the Ångström scale.

In conclusion, by analyzing the energy flow through a subradiant optical mode coupled to a radiative continuum, we have shown that the radiance of the subradiant mode is the key parameter determining its optical properties. We have demonstrated that the radiance can be classified as belonging to one of three different regimes: weak, intermediate, or strong interaction. This insight provides the key element of understanding needed for rational design of structures for optimal performance of a broad range of nano-optical devices such as nanoantennas,^{3,4,10} plasmonic lasers,^{40–42} infrared metamaterial,^{12,43} optomechanical,⁴⁴ nonlinear devices,^{45,46} and chemical and biological sensors.⁸ For the weak radiance situation, we have introduced a novel concept of sensing, radiance sensing, and experimentally show that this sensing approach allows for detection of Ångström sized geometrical displacements. The development of ultra sensitive sensors based on radiance sensing has significant potential in a wide range of applications, such as in molecular rulers^{11,47} for monitoring noninvasively chemical or biological processes, strain sensors,⁴⁸ for optical trapping and manipulation,^{2,49} or in combination with specific materials for indirect sensing (for instance the pH,⁵⁰ the presence of hydrogen, or the local temperature⁵¹).

■ ASSOCIATED CONTENT

S Supporting Information

Details of fabrication, optical and structural characterization, derivation of eqs 1, 2, and 3. This material is available free of charge via the Internet at <http://pubs.acs.org>.

■ AUTHOR INFORMATION

Corresponding Author

*E-mail: olivier.martin@epfl.ch.

Notes

The authors declare no competing financial interest.

■ ACKNOWLEDGMENTS

B.G. and O.J.F.M. acknowledge funding from CCMX–FanoSense. T.S. acknowledges funding from the Swiss Federal foundation. P.N. acknowledges funding from the Robert A. Welch Foundation (C-1222) and the Defense Threat Reduction Agency (HDTRA1-11-1-0040). B.G. would like to thank H. Giessen for stimulating discussions. T.S. would like to thank Y. Ekinici (PSI) and M. Vockenhuber (PSI) for their support. Part of this work was performed at the Swiss Light Source.

■ REFERENCES

- (1) Genet, C.; Ebbesen, T. W. Light in tiny holes. *Nature* **2007**, *445*, 39–46.
- (2) Juan, M. L.; Righini, M.; Quidant, R. Plasmon nano-optical tweezers. *Nat. Photonics* **2011**, *5*, 349–356.
- (3) Mühlschlegel, P.; Eisler, H. J.; Martin, O. J. F.; Hecht, B.; Pohl, D. W. Resonant optical antennas. *Science* **2005**, *308*, 1607–1609.
- (4) Novotny, L.; van Hulst, N. Antennas for light. *Nat. Photonics* **2011**, *5*, 83–90.
- (5) Berini, P.; De Leon, I. Surface plasmon-polariton amplifiers and lasers. *Nat. Photonics* **2012**, *6*, 16–24.
- (6) Knight, M. W.; Sobhani, H.; Nordlander, P.; Halas, N. J. Photodetection with Active Optical Antennas. *Science* **2011**, *332*, 702–704.
- (7) Anker, J. N.; Hall, W. P.; Lyandres, O.; Shah, N. C.; Zhao, J.; Van Duyne, R. P. Biosensing with plasmonic nanosensors. *Nat. Mater.* **2008**, *7*, 442–453.
- (8) Halas, N. J.; Lal, S.; Chang, W.-S.; Link, S.; Nordlander, P. Plasmons in Strongly Coupled Metallic Nanostructures. *Chem. Rev.* **2011**, *111*, 3913–3961.
- (9) Brongersma, M. L.; Shalaev, V. M. Applied Physics The Case for Plasmonics. *Science* **2010**, *328*, 440–441.
- (10) Seok, T. J.; Jamshidi, A.; Kim, M.; Dhuey, S.; Lakhani, A.; Choo, H.; Schuck, P. J.; Cabrini, S.; Schwartzberg, A. M.; Bokor, J.; Yablonovitch, E.; Wu, M. C. Radiation Engineering of Optical Antennas for Maximum Field Enhancement. *Nano Lett.* **2011**, *11*, 2606–2610.
- (11) Liu, N.; Hentschel, M.; Weiss, T.; Alivisatos, A. P.; Giessen, H. Three-Dimensional Plasmon Rulers. *Science* **2011**, *332*, 1407–1410.
- (12) Wu, C.; Khanikaev, A. B.; Adato, R.; Arju, N.; Yanik, A. A.; Altug, H.; Shvets, G. Fano-Resonant Asymmetric Metamaterials for Ultrasensitive Spectroscopy and Identification of Molecular Monolayers. *Nat. Mater.* **2012**, *11*, 69–75.
- (13) Christ, A.; Martin, O. J. F.; Ekinici, Y.; Gippius, N. A.; Tikhodeev, S. G. Symmetry Breaking in a Plasmonic Metamaterial at Optical Wavelength. *Nano Lett.* **2008**, *8*, 2171–2175.
- (14) Zhang, S.; Genov, D. A.; Wang, Y.; Liu, M.; Zhang, X. Plasmon-Induced Transparency in Metamaterials. *Phys. Rev. Lett.* **2008**, *101*, 047401.
- (15) Verellen, N.; Sonnefraud, Y.; Sobhani, H.; Hao, F.; Moshchalkov, V. V.; Van Dorpe, P.; Nordlander, P.; Maier, S. A. Fano Resonances in Individual Coherent Plasmonic Nanocavities. *Nano Lett.* **2009**, *9*, 1663–1667.
- (16) Ruan, Z.; Fan, S. Temporal Coupled Mode Theory for Fano Resonance in Light Scattering by a Single Obstacle. *J. Phys. Chem. C* **2010**, *114*, 7324–7329.
- (17) Luk'yanchuk, B.; Zheludev, N. I.; Maier, S. A.; Halas, N. J.; Nordlander, P.; Giessen, H.; Chong, C. T. The Fano Resonance in Plasmonic Nanostructures and Metamaterials. *Nat. Mater.* **2010**, *9*, 707–715.
- (18) Miroshnichenko, A. E.; Flach, S.; Kivshar, Y. S. Fano Resonances in Nanoscale Structures. *Rev. Mod. Phys.* **2010**, *82*, 2257–2298.
- (19) Gallinet, B.; Martin, O. J. F. Influence of Electromagnetic Interactions on the Line Shape of Plasmonic Fano Resonances. *ACS Nano* **2011**, *5*, 8999–9008.
- (20) Gallinet, B.; Martin, O. J. F. The Relation Between Near-field and Far-field Properties of Plasmonic Fano Resonances. *Opt. Express* **2011**, *19*, 22167–22175.
- (21) Giannini, V.; Francescato, Y.; Amrania, H.; Phillips, C. C.; Maier, S. A. Fano Resonances in Nanoscale Plasmonic Systems: A Parameter-Free Modeling Approach. *Nano Lett.* **2011**, *11*, 2835–2840.
- (22) Francescato, Y.; Giannini, V.; Maier, S. A. Plasmonic Systems Unveiled by Fano Resonances. *ACS Nano* **2012**, *6*, 1830–1838.
- (23) Prodan, E.; Radloff, C.; Halas, N.; Nordlander, P. A Hybridization Model for the Plasmon Response of Complex Nanostructures. *Science* **2003**, *302*, 419–422.
- (24) Johnson, P. B.; Christy, R. W. Optical-Constants of Noble-Metals. *Phys. Rev. B* **1972**, *6*, 4370.
- (25) Liu, N.; Langguth, L.; Weiss, T.; Kaestel, J.; Fleischhauer, M.; Pfau, T.; Giessen, H. Plasmonic Analogue of Electromagnetically Induced Transparency at the Drude Damping Limit. *Nat. Mater.* **2009**, *8*, 758–762.
- (26) Gallinet, B.; Martin, O. J. F. Scattering on Plasmonic Nanostructures Arrays Modeled with a Surface Integral Formulation. *Photonic Nanostruct.* **2010**, *8*, 278–284.
- (27) Gallinet, B.; Kern, A. M.; Martin, O. J. F. Accurate and Versatile Modeling of Electromagnetic Scattering on Periodic Nanostructures with a Surface Integral Approach. *J. Opt. Soc. Am. A* **2010**, *27*, 2261–2271.
- (28) Fano, U. Effects of Configuration Interaction on Intensities and Phase Shifts. *Phys. Rev.* **1961**, *124*, 1866.

Nano Letters

Letter

- (29) Gallinet, B.; Martin, O. J. F. Ab Initio Theory of Fano Resonances in Plasmonic Nanostructures and Metamaterials. *Phys. Rev. B* **2011**, *83*, 235427.
- (30) Thomas, M.; Greff t, J. J.; Carminati, R.; Arias-Gonzalez, J. R. Single-molecule spontaneous emission close to absorbing nanostructures. *Appl. Phys. Lett.* **2004**, *85*, 3863–3865.
- (31) Carminati, R.; Greff t, J. J.; Henkel, C.; Vigoureux, J. M. Radiative and non-radiative decay of a single molecule close to a metallic nanoparticle. *Opt. Commun.* **2006**, *261*, 368–375.
- (32) Kern, A. M.; Meixner, A. J.; Martin, O. J. F. Molecule-Dependant Plasmonic Enhancement of Fluorescence and Raman Scattering near Realistic Nanostructures. *ACS Nano* **2012**, *6*, 9828–9836.
- (33) Alzar, C. L. G.; Martinez, M. A. G.; Nussenzeig, P. Classical Analog of Electromagnetically Induced Transparency. *Am. J. Phys.* **2002**, *70*, 37–41.
- (34) Anisimov, P. M.; Dowling, J. P.; Sanders, B. C. Objectively Discerning Autler-Townes Splitting from Electromagnetically Induced Transparency. *Phys. Rev. Lett.* **2011**, *107*, 163604.
- (35) Liu, N.; Kaiser, S.; Giessen, H. Magnetoinductive and Electroinductive Coupling in Plasmonic Metamaterial Molecules. *Adv. Mater.* **2008**, *20*, 4521–4525.
- (36) Autler, S. H.; Townes, C. H. Stark effect in rapidly varying fields. *Phys. Rev.* **1955**, *100*, 703–722.
- (37) Pardo, F.; Bouchon, P.; Haidar, R.; Pelouard, J.-L. Light Funneling Mechanism Explained by Magnetoelectric Interference. *Phys. Rev. Lett.* **2011**, *107*, 093902.
- (38) Ye, J.; Wen, F.; Sobhani, H.; Lassiter, J. B.; Dorpe, P. V.; Nordlander, P.; Halas, N. J. Plasmonic Nanoclusters: Near Field Properties of the Fano Resonance Interrogated with SERS. *Nano Lett.* **2012**, *12*, 1660–1667.
- (39) Siegfried, T.; Ekinici, Y.; Solak, H. H.; Martin, O. J. F.; Sigg, H. Fabrication of sub-10 nm gap arrays over large areas for plasmonic sensors. *Appl. Phys. Lett.* **2011**, *99*, 263302.
- (40) Bergman, D. J.; Stockman, M. I. Surface Plasmon Amplification by Stimulated Emission of Radiation: Quantum Generation of Coherent Surface Plasmons in Nanosystems. *Phys. Rev. Lett.* **2003**, *90*, 027402.
- (41) Zheludev, N. I.; Prosvirnin, S. L.; Papasimakis, N.; Fedotov, V. A. Lasing Spaser. *Nat. Photonics* **2008**, *2*, 351–354.
- (42) Ma, R.-M.; Oulton, R. F.; Sorger, V. J.; Bartal, G.; Zhang, X. Room-temperature sub-diffraction-limited plasmon laser by total internal reflection. *Nat. Mater.* **2011**, *10*, 110–113.
- (43) Cubukcu, E.; Zhang, S.; Park, Y.-S.; Bartal, G.; Zhang, X. Split ring resonator sensors for infrared detection of single molecular monolayers. *Appl. Phys. Lett.* **2009**, *95*, 043113.
- (44) Weis, S.; Riviere, R.; Deleglise, S.; Gavartin, E.; Arcizet, O.; Schliesser, A.; Kippenberg, T. J. Optomechanically Induced Transparency. *Science* **2010**, *330*, 1520–1523.
- (45) Tuovinen, H.; Kauranen, M.; Jefimovs, K.; Vahimaa, P.; Vallius, T.; Turunen, J.; Tkachenko, N. V.; Lemmetyinen, H. Linear and second-order nonlinear optical properties of arrays of noncentrosymmetric gold nanoparticles. *J. Nonlinear Opt. Phys. Mater.* **2002**, *11*, 421–432.
- (46) Zhang, Y.; Grady, N. K.; Ayala-Orozco, C.; Halas, N. J. Three-Dimensional Nanostructures as Highly Efficient Generators of Second Harmonic Light. *Nano Lett.* **2011**, *11*, 5519–5523.
- (47) Sonnichsen, C.; Reinhard, B. M.; Liphardt, J.; Alivisatos, A. P. A molecular ruler based on plasmon coupling of single gold and silver nanoparticles. *Nat. Biotechnol.* **2005**, *23*, 741–745.
- (48) Pryce, I. M.; Aydin, K.; Kelaita, Y. A.; Briggs, R. M.; Atwater, H. A. Highly Strained Compliant Optical Metamaterials with Large Frequency Tunability. *Nano Lett.* **2010**, *10*, 4222–4227.
- (49) Zhang, W.; Huang, L.; Santschi, C.; Martin, O. J. F. Trapping and Sensing 10 nm Metal Nanoparticles Using Plasmonic Dipole Antennas. *Nano Lett.* **2010**, *10*, 1006–1011.
- (50) Nunes, S. P.; Behzad, A. R.; Hooghan, B.; Sougrat, R.; Karunakaran, M.; Pradeep, N.; Vainio, U.; Peinemann, K.-V. Switchable pH-Responsive Polymeric Membranes Prepared via Block Copolymer Micelle Assembly. *ACS Nano* **2011**, *5*, 3516–3522.
- (51) Langhammer, C.; Larsson, E. M.; Kasemo, B.; Zoric, I. Indirect Nanoplasmonic Sensing: Ultrasensitive Experimental Platform for Nanomaterials Science and Optical Nanocalorimetry. *Nano Lett.* **2010**, *10*, 3529–3538.

(II) Self-limiting nanogap fabrication by angular evaporation

Manuscript state

Published manuscript

Reference

T. Siegfried, Y. Ekinici, H. H. Solak, O. J. F. Martin, H. Sigg, "*Fabrication of sub-10 nm gap arrays over large areas for plasmonic sensors*", *Applied Physics Letters* **2011**, 99, 263302

Publication date: 27. December 2011

DOI: 10.1063/1.3672045

URL: <http://scitation.aip.org/content/aip/journal/apl/99/26/10.1063/1.3672045>

Current citations: 27

Author contribution

T. Siegfried fabricated the samples. T. Siegfried performed the experiments, analyzed and concluded the data. T. Siegfried wrote the manuscript. H. Sigg and O.J.F. Martin corrected the manuscript.

Conference contribution

T. Siegfried, "*High density fabrication of deterministic nanogap arrays*", **poster** at Surface Plasmon Polariton (SPP5) in May **2011**, Busan, South Korea

Published paper + Supporting information

APPLIED PHYSICS LETTERS 99, 263302 (2011)

Fabrication of sub-10 nm gap arrays over large areas for plasmonic sensors

T. Siegfried,^{1,a)} Y. Ekinici,^{1,2} H. H. Solak,³ O. J. F. Martin,⁴ and H. Sigg¹¹Laboratory for Micro- and Nanotechnology, Paul Scherrer Institut, 5232 Villigen-PSI, Switzerland²Department of Materials, Laboratory of Metal Physics and Technology, ETH Zurich, 8093 Zurich, Switzerland³Eulitha AG, 5232 Villigen PSI, Switzerland⁴Nanophotonics and Metrology Laboratory, EPFL, 1015 Lausanne, Switzerland

(Received 8 November 2011; accepted 3 December 2011; published online 27 December 2011)

We report a high-throughput method for the fabrication of metallic nanogap arrays with high-accuracy over large areas. This method, based on shadow evaporation and interference lithography, achieves sub-10 nm gap sizes with a high accuracy of ± 1.5 nm. Controlled fabrication is demonstrated over mm^2 areas and for periods of 250 nm. Experiments complemented with numerical simulations indicate that the formation of nanogaps is a robust, self-limiting process that can be applied to wafer-scale substrates. Surface-enhanced Raman scattering (SERS) experiments illustrate the potential for plasmonic sensing with an exceptionally low standard-deviation of the SERS signal below 3% and average enhancement factors exceeding 1×10^6 . © 2011 American Institute of Physics. [doi:10.1063/1.3672045]

Surface plasmon-based sensing techniques have generated substantial interest especially since the demonstration of single molecule sensitivity in 1997.^{1,2} This enhancement phenomenon relies on strongly confined electromagnetic fields generated by localized plasmons on metal nanostructures much smaller than the incident wavelength.^{3,4} However, surface enhanced (SE) spectroscopic techniques are not yet routinely used at the industrial level. This is due to poor signal reproducibility, moderate average enhancement factors, and high costs.⁵ To increase the signal enhancement, nanogap patterns are currently used: they produce extremely large electromagnetic fields for nano objects separated by a distance below 20 nm.⁶ Local enhancement factors up to $\sim 10^9$ have been reported with a one-dimensional (1D) nanogap pattern,⁷ enabling single molecule detection.⁸ The fabrication of nanogap arrays has been demonstrated with a variety of techniques. Electron-beam lithography (EBL) is used for direct writing⁹ or patterning of shadow masks for angular evaporation.^{10,11} With EBL, the pattern can be designed and realized with an exceptional degree of freedom. Due to proximity effects of the electron beam and limitations set by the photoresist liftoff, the resulting metal nanogap dimensions are limited to above roughly 10 nm and a metal layer thickness of below 30 nm.^{9,12} The serial writing process of EBL makes this technique unfavorable for the fabrication of large area and low-cost sensors. Other lithography-based techniques have been used, including molecular rulers^{13,14} or atomic layer deposition (ALD),⁷ as effective methods to tune the nanogap size even below 2 nm. This, however, involves complicated multistep fabrication processes and produces local defects, which are found to cause fluctuations of the surface-enhanced Raman scattering (SERS) enhancement across the sensing area⁷ or between different substrates.

In this letter, we report the fabrication of homogeneous sub-10 nm gap arrays with high surface densities and over large areas. The fabrication scheme for our nanogap arrays consists of only two stages, lithography and metal layer deposition.

In the first step, extreme ultraviolet interference lithography (EUV-IL) is used to provide a 1D line array on the substrate, which is typically float glass or silicon. Details of the EUV lithography, available at the Swiss Light Source, can be found elsewhere.¹⁵ This technique provides high resolution patterns over large areas and with high throughput. Briefly, a coherent beam with 13.5 nm wavelength is incident on a mask comprising two identical gratings. Beams diffracted by the gratings interfere to form high resolution patterns with dimensions below 10 nm half pitch.¹⁶ In our experiments, line patterns with a period of 250 nm were exposed into a 80 nm thick hydrogen silsesquioxane (HSQ) photoresist layer. In a single exposure, a $1.7 \times 0.6 \text{ mm}^2$ pattern was generated within a timeframe of 3 s–10 s, depending on the desired duty cycle. HSQ was then developed in a 25% tetra-methyl-ammonium-hydroxide (TMAH) solution for 60 s. After the exposure, HSQ is cross-linked to form a SiO_x network providing a chemically stable pattern that was used directly without further etching into the substrate.

In the second step, glancing angle deposition (GLAD) is used to thermally evaporate metal layers directly onto the photoresist pattern, as illustrated in Fig. 1. A similar process was

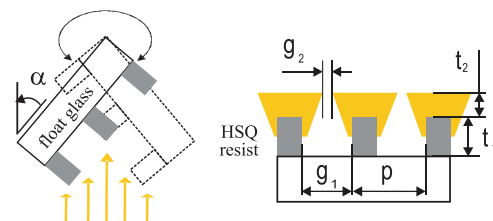


FIG. 1. (Color online) Scheme of the shadow evaporation process. The metal is evaporated iteratively from two sides of the surface.

^{a)}Author to whom correspondence should be addressed. Electronic mail: thomas.siegfried@psi.ch.

263302-2 Siegfried *et al.*Appl. Phys. Lett. **99**, 263302 (2011)

previously used to obtain metal nanowire arrays.^{17,18} However, sub-10 nm gap arrays with excellent homogeneity over large surfaces have not yet been reported. Gold and chromium, both of 99.99% purity, were deposited at angles α between 30° and 70° from the surface normal and with an azimuthal orientation perpendicular to the length of the nanowires (Fig. 1). Repeated cycles of ~ 4 nm metal layer deposition (at a rate of 0.3 nm/s) followed by flipping the substrate to the opposite direction (Fig. 1) were carried out until the final thickness was reached. Important for our experiment is the observation that the linear slope of the gap edge changes for a separation distance smaller than roughly 30 nm. Beyond this distance, the gap closes only slowly when additional metal is deposited (see, for example, Fig. 2(b)).

Ballistic Monte Carlo simulations¹⁹ were performed to analyze the geometry resulting from this GLAD process. Using a 2D home-made code, the trajectory and sticking of single metal particles with a 0.7 nm size were simulated. The particles were impinging on the surface from random positions under a specified angle. Similar to the experiment, the angle of the trajectory was flipped after a certain deposition time. Once a particle reached the uppermost surface, a diffusion length was introduced to model the further movement of the particle on the surface which controls the filling up of pores underneath.

In the first example, we have evaporated chromium. From the SEM images in Fig. 2(a), one can clearly see a columnar shaped layer growth that is known to result from angular evaporation and an exceptionally low diffusion length of the material.²⁰ Interestingly, no closure of the gap was observed, even for metal thicknesses exceeding 160 nm. Instead, self shadowing of the adjacent geometry seemed to prevent the gap from closing, making possible the realization of sub-10 nm gap sizes in a very reliable manner (see, for example, Fig. 2(b)). In the simulations, the diffusion length was set to 0, according to the small effective diffusion length of chromium. This assumption reproduced the experimen-

tally observed geometry and the columnar growth very well, as illustrated by comparing Figs. 2(b) and 2(c).

Gold was used as another example, which was selected for subsequent SERS studies due to its tunable plasmon resonance in the visible range, chemical inertness, and biocompatibility.²¹ As opposed to chromium, gold forms much larger grains during deposition (Figs. 3(a) and 3(b)) and does not form films with columnar texture thanks to a remarkably high diffusion length of the adatoms.²² Again, we observed an initial almost linear closing of the gap that gradually slowed down once the gap was below 30 nm. In the ballistic simulation, an effective diffusion length of 2.1 nm was used, to account for the surface diffusion. The simulated cross section reproduced the experimental geometry very well, as illustrated in Fig. 3(b). Furthermore, the simulation model was used to predict the size of the nanogap arrays and its dependence on the evaporation angle, gold layer thickness, and HSQ line width. Experimental control of the final gap size was obtained by varying the initial HSQ gap size. For Au gap sizes down to roughly 10 nm, we could obtain extremely high uniformity of the patterned area with an accuracy of ± 1.5 nm, as indicated in Fig. 3. This homogeneity was reduced for gap sizes below 10 nm, when crystallites from opposite sidewalls start randomly to coalesce.

Thanks to the shadowing effect, the formation of nanogaps was found to be self limited, enabling the control of the evaporation process accurately. In a typical evaporation process, up to 8 single substrate chips were coated simultaneously, covering a 4 in. substrate. With an appropriate low-cost lithography tool, e.g., displacement Talbot lithography²³ or laser interference lithography,²⁴ one could easily pattern and evaporate nanogap arrays over a full wafer, which was, however, not a part of this study.

The SERS enhancement provided by the fabricated nanogap arrays was evaluated using spectra recorded on a Horiba LabRam HR device (Fig. 4(a)). The excitation source was a 633 nm HeNe laser with 2 mW power collimated by a

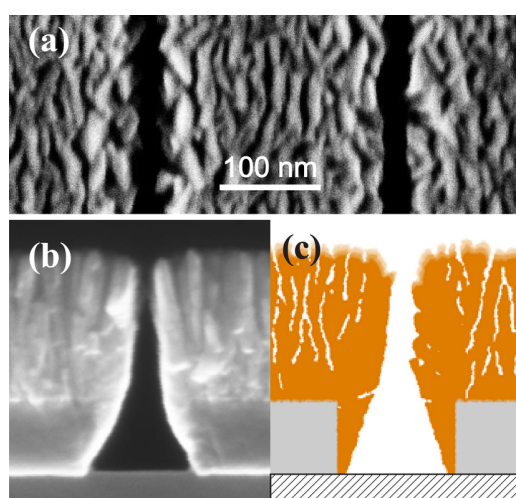


FIG. 2. (Color online) (a) Top view SEM and (b) cross sectional view of a cleaved chromium nanogap array compared with (c) ballistic simulation results. The 160 nm thick metal was evaporated at an angle of 55° from the surface normal. The resulting gap size is ~ 10 nm. The underlying pattern consists of the HSQ photoresist with a periodicity of 250 nm, a thickness of 80 nm, and a gap size of 110 nm. Silicon was used as a substrate.

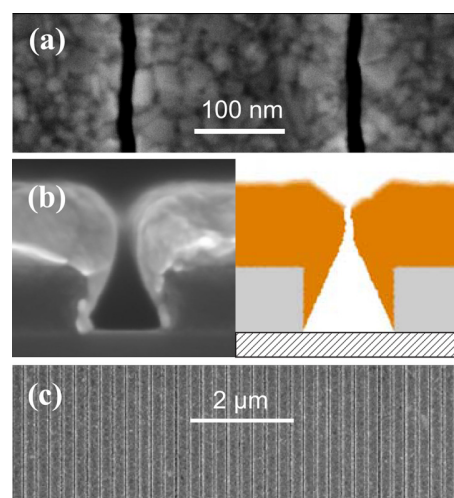


FIG. 3. (Color online) (a) and (c) Top view SEM and (b) cross sectional view of a cleaved gold nanogap array compared with ballistic simulation results. The 100 nm thick metal was evaporated at an angle of 60° from the surface normal. The resulting gap size is ~ 13 nm. The underlying pattern consists of the HSQ photoresist with a periodicity of 250 nm, a thickness of 80 nm, and a gap size of ~ 110 nm. Silicon was used as a substrate.

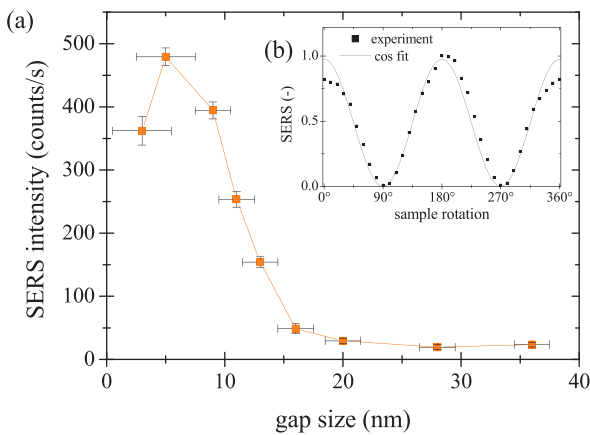


FIG. 4. (Color online) (a) SERS intensity for varying nanogap size. (b) SERS intensity as a function of the sample rotation for linearly polarized excitation. The sample consists of a nanogap array with a Au thickness of 100 nm. The excitation was at 633 nm and the SERS intensity corresponded to the 1008 cm^{-1} peak of a self assembled benzenethiol monolayer. Error bars correspond to the standard deviation of 16 spatially separated SERS measurements and quantitative analysis of SEM images across the patterned area.

50X (NA of 0.5) objective. The SERS intensity was found to increase strongly for gap sizes below 20 nm, as expected. Within the $500 \times 400\text{ }\mu\text{m}^2$ sensing area, the SERS signal was found to be highly reproducible with a standard deviation below 3%. For a 10 nm gap array, we have calculated an average enhancement factor of 1×10^6 , with Raman spectra recorded from an undiluted analyte solution.

For gap sizes below ~ 10 nm, the SERS intensity leveled out and decreased for gap sizes below ~ 5 nm, as illustrated in Fig. 4(a). This discrepancy from the expected trend can be explained by increasing the events of coalescing gap side-walls. This was not only found to reduce the overall SERS signal, but also to increase the areal standard deviation to roughly 6%.

The SERS intensity exhibited clear polarization dependence with maximal values for the electric field perpendicular to the nanogap expansion, as shown in the inset of Fig. 4(b). This large intensity ratio between s- and p-polarizations, indicates a well defined enhancement mechanism located within the nanogap and excludes the contributions from surface roughness.

In summary, we have fabricated sub-10 nm gap arrays with a simple, self-aligning, and easily scalable shadow evaporation technique. The formation of nanogaps was sup-

ported by simulations and could be realized with high homogeneity as observed both in SEM images and SERS measurements, with signal deviations below 3%. The potential use as a SERS sensor was demonstrated, with an average enhancement factor of 1×10^6 well reproducible over the entire patterned sensing area. Such patterns have great potential for numerous applications ranging from sensors to nanoliter vessels and nano-membranes.

The work was supported by the Swiss Federal Foundation. Part of this work was performed at the Swiss Light Source (SLS), PSI, Switzerland. We acknowledge the support of M. Vockenhuber for EUV lithography and P. Sahoo for preliminary experiments.

- ¹K. Kneipp, Y. Wang, H. Kneipp, L. T. Perelman, I. Itzkan, R. R. Dasari, and M. S. Feld, *Phys. Rev. Lett.* **78**, 1667 (1997).
- ²S. Nie and S. R. Emory, *Science* **275**, 1102 (1997).
- ³S. J. Tan, M. J. Campolongo, D. Luo, and W. Cheng, *Nat. Nanotechnol.* **6**, 268 (2011).
- ⁴M. Rycenga, C. M. Cobley, J. Zeng, W. Li, C. H. Moran, Q. Zhang, D. Qin, and Y. Xia, *Chem. Rev.* **111**, 3669 (2011).
- ⁵M. J. Natan, *Faraday Discuss.* **132**, 321 (2006).
- ⁶J. Zuloaga, E. Prodan, and P. Nordlander, *Nano Lett.* **9**, 887 (2009).
- ⁷H. Im, K. C. Bantz, N. C. Lindquist, C. L. Haynes, and S.-H. Oh, *Nano Lett.* **10**, 2231 (2010).
- ⁸A. Otto, *J. Raman Spectrosc.* **37**, 937 (2006).
- ⁹H. Duan, H. Hu, K. Kumar, Z. Shen, and J. K. W. Yang, *ACS Nano* **5**, 7593 (2011).
- ¹⁰W. Zhu, M. G. Banee, D. Wang, Y. Chu, and K. B. Crozier, *Small* **7**, 1761 (2010).
- ¹¹R. Stosch, F. Yaghobian, T. Weimann, R. J. C. Brown, M. J. T. Milton, and B. Güttler, *Nanotechnology* **22**, 105303 (2011).
- ¹²H. Duan, V. R. Manfrinato, J. K. W. Yang, D. Winston, B. M. Cord, and K. K. Berggren, *J. Vac. Sci. Technol. B* **28**, C6H11 (2010).
- ¹³G. S. McCarty, *Nano Lett.* **4**, 1391 (2004).
- ¹⁴R. Negishi, T. Hasegawa, K. Terabe, M. Aono, T. Ebihara, H. Tanaka, and T. Ogawa, *Appl. Phys. Lett.* **88**, 223111 (2006).
- ¹⁵V. Auzelyte, C. Dais, P. Farquet, D. Grutzmacher, L. J. Heyderman, F. Luo, S. Olliges, C. Padeste, P. K. Sahoo, T. Thomson *et al.*, *J. Micro/Nanolith. MEMS MOEMS* **8**, 021204 (2009).
- ¹⁶B. Päiväranta, A. Langner, E. Kirk, C. David, and Y. Ekinici, *Nanotechnology* **22**, 375302 (2011).
- ¹⁷V. Auzelyte, H. H. Solak, Y. Ekinici, R. MacKenzie, J. Vörös, S. Olliges, and R. Spolenak, *Microelectron. Eng.* **85**, 1131 (2008).
- ¹⁸J. G. Bai, W. H. Yeo, and J. H. Chung, *Lab Chip* **9**, 449 (2009).
- ¹⁹S. Müller-Pfeiffer, H. van Kranenburg, and J. C. Lodder, *Thin Solid Films* **213**, 143 (1992).
- ²⁰K. Naoto, E. Akinori, O. Kiyoshi, S. Ippai, S. Yuichi, and M. Shoji, *J. Vac. Sci. Technol. A* **19**, 153 (2001).
- ²¹M. Moskovits, *J. Raman Spectrosc.* **36**, 485 (2005).
- ²²T. Ishida, Y. Nakajima, J. Endo, D. Collard, and H. Fujita, *Nanotechnology* **20**, 065705 (2009).
- ²³H. H. Solak, C. Dais, and F. Clube, *Opt. Express* **19**, 10686 (2011).
- ²⁴C. Lu and R. H. Lipson, *Laser Photonics Rev.* **4**, 568 (2009).

(III) Near-field enhancement in nanogap resonators

Manuscript state

Published manuscript

Reference

T. Siegfried, Y. Ekinici, O. J. F. Martin, H. Sigg, "*Gap Plasmons and Near-Field Enhancement in Closely Packed Sub-10 nm Gap Resonators*", Nano Letters **2013**, 13 (11), 5449-5453.

Publication date: 10. October 2013

DOI: 10.1021/nl403030g

URL: <http://pubs.acs.org/doi/abs/10.1021/nl403030g>

Current citations: 0

Author contribution

T. Siegfried fabricated the samples. T. Siegfried performed the experiments and simulations, analyzed and concluded the data. T. Siegfried wrote the manuscript. H. Sigg helped in optimizing the story of the manuscript and corrected it. O.J.F. Martin corrected the manuscript.

Conference contribution

- T. Siegfried, "*Near-field enhancement in sub-10 nm gap arrays*", **oral** at Surface Plasmon Polariton (SPP6) in May **2013**, Ottawa, Canada
- T. Siegfried "*Periodic Nanogap Arrays for Surface Enhanced Spectroscopy: Modeling and Performance*", **oral** at SPS Meeting **2012**, Zurich, Switzerland

Published paper + Supporting information

Gap Plasmons and Near-Field Enhancement in Closely Packed Sub-10 nm Gap Resonators

Thomas Siegfried,^{*,†} Yasin Ekinici,[†] Olivier J. F. Martin,[‡] and Hans Sigg[†]

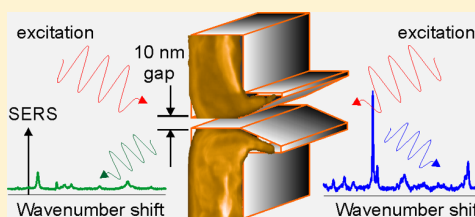
[†]Laboratory for Micro- and Nanotechnology, Paul Scherrer Institut, 5232 Villigen-PSI, Switzerland

[‡]Nanophotonics and Metrology Laboratory, EPFL, 1015 Lausanne, Switzerland

S Supporting Information

ABSTRACT: Pairs of metal nanoparticles with a sub-10 nm gap are an efficient way to achieve extreme near-field enhancement for sensing applications. We demonstrate an attractive alternative based on Fabry–Perot type nanogap resonators, where the resonance is defined by the gap width and vertical elongation instead of the particle geometry. We discuss the crucial design parameters for such gap plasmons to produce maximum near-field enhancement for surface-enhanced Raman scattering and show compatibility of the pattern processing with low-cost and low-resolution lithography. We find a minimum critical metal thickness of 80 nm and observe that the mode coupling from the far field increases by tapering the gap opening. We also show the saturation of the Raman signal for nanogap periodicities below 1 μm , demonstrating efficient funneling of light into such nanogap arrays.

KEYWORDS: Nanogap, gap plasmon, surface-enhanced Raman scattering, near-field enhancement, light funneling, Fabry–Perot



The generation of electromagnetic hot spots with extreme near-field enhancement is the prerequisite for plasmonic sensing applications, especially for detection down to the single molecule level.^{1–6} Few nanometer separations between noble metal nanoparticles are known to produce such extreme near-field enhancements and are thus often used to design nanostructures for practical applications.^{6–14} Commonly, the near-field is enhanced with decreasing gap size, with an ultimate limit of roughly 0.5 nm before charge recombination occurs through electron tunneling.^{15,16}

However, an effective sensing platform should not only aim at strong near-field localization but also provide efficient coupling to the incident field, good reproducibility of the nanostructures, and a high density of the hot spots. For nanoantenna patterns, such as arrays of closely spaced bowtie antenna, the coupling efficiency is primarily defined by the individual antenna plasmon resonance which can be slightly shifted by the coupling to the neighboring structures.¹⁵ Nanoantenna have been studied extensively and can be fabricated cost-effectively,^{17,18} but control over few-nanometer gap separations was so far only realized by electron beam lithography (EBL),^{9,10,15} electromigration,¹⁴ spacing layers,⁸ or shadow evaporation.^{12,13} Such nanometer-precise lithographic processes are extremely challenging and cost-intensive, while offering only low throughput and are limited to a small sensing area with only a few nanogaps (i.e., a low filling factor). A notable exception is nanosphere lithography offering wafer-size arrays of nanoparticles by direct assembly or angular evaporation;^{17,19} the tuning of the particle shape, metal layer thickness, and gap size is however limited.

Recently, strong near-field enhancement from nanometer slit arrays was demonstrated over large areas using scalable

processes such as atomic layer deposition^{11,20} (ALD) or glancing angular deposition²¹ (GLAD). Such slits support gap plasmons which are created by lateral electromagnetic coupling between two opposing metallic surfaces. The upper and lower boundary of the slit can lead to Fabry–Perot interferences similar to a metal–insulator–metal (MIM) waveguide.^{22–24}

Here, we present a comprehensive study of the geometry required to obtain nanogap resonators which exhibit strong near-field enhancement. In particular, we study the role of the gap size and gap elongation on the gap plasmon mode. We show that surface-enhanced Raman scattering (SERS) critically depends on the resonance matching of the incident field with the gap plasmon mode. Furthermore, increased coupling efficiency by funneling of the incident light through a tapered geometry is demonstrated. We finally show saturation of the SERS signal for nanogap densities higher than 1 μm^{-1} .

The periodic nanogap arrays in our study were fabricated in a simple one-step process combining EUV interference lithography^{25,26} and angular evaporation.²⁷ Precise control of gap sizes even below 10 nm was obtained for both 1D and 2D periodic arrays of different thicknesses, without the need of further fabrication steps such as lift-off and etching which would jeopardize sub-10 nm accuracy.²¹ The Au is evaporated at grazing angles onto a grating pattern of transparent HSQ photoresist, such that by shadowing the opposite grating sidewall an elongated vertical channel with nanometric width is obtained (schematic and details in Figure S1 of the Supporting Information).²¹ The gap size is primarily defined by the resist

Received: August 13, 2013

Revised: October 2, 2013

Published: October 10, 2013

mask dimensions, the angle of incidence, and the deposition thickness. For a given metal thickness, the gap size is varied by changing the duty cycle of the resist pattern with the exposure and development time. The resulting gap size can be predicted with a geometric model combined with an analytic factor and is additionally determined by the analysis of several top and cross sectional scanning electron microscope (SEM) images. Evaporating multiple substrates simultaneously, we find similar gap sizes deviating by only few nanometers and also that the measured SERS signal intensity does not vary by more than 15%. Although we use high-resolution lithography in this work, it should be emphasized that our approach only depends on the abrupt vertical sidewalls which can also be well-produced by low-cost nanosphere, nanoimprint, or laser interference lithography.^{17,28} A 1-nm-thick Cr layer evaporated under normal incidence forms an effective adhesion layer which does not affect the plasmonic performance of the system.²⁹ The cross-section and top-view SEM images of the obtained sub-10 nm gap arrays are shown in Figure 1a and b.

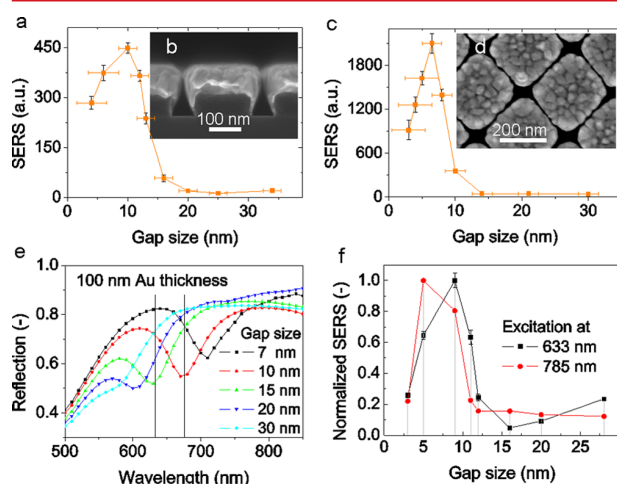


Figure 1. Gap plasmon modes and SERS intensity for varying nanogap sizes. Experimental SERS intensities for (a) 1D gratings with a period of 250 nm and (c) 2D nanodot arrays with a period of 280 nm. SEM micrographs of (b) the cross section of a 1D grating and (d) the top view of the 2D nanodot array with a Au thickness of the 95 nm and a gap size of roughly 10 nm. (e) Calculated gap plasmon modes for a 1D grating with varying gap sizes. The Raman excitation and detection wavelength are marked in the spectrum. (f) SERS intensity at excitation wavelengths of 633 and 785 nm for a 1D grating with varying gap sizes. The intensities correspond to the 1008 cm^{-1} peak of a self-assembled benzene-ethane-thiol monolayer. Error bars represent the standard deviation of 16 spatially separated SERS measurements and the analysis of multiple SEM images.

For nanogap sizes below 30 nm, the measured SERS intensity increases strongly for both 1D and 2D nanogap arrays, shown in Figure 1c and d, respectively. The SERS intensity for the 1D case is polarization-dependent with maximal intensity for the electric field aligned perpendicular (TM) to the gap.²¹ We find larger SERS signals from the 2D gap resonators, which could be attributed to better coupling efficiency of the 2D pattern mediated by the large hole in the crossing of two gaps (Figure 1d), compared to a 1D grating. Additionally, the 2D pattern is insensitive to the polarization, and the angular evaporation process is simplified by a continuous substrate rotation, while the 1D pattern requires frequent substrate

tilting. Gap plasmon modes are calculated with a full-field numerical method based on a surface integral formulation of Maxwell's equations.³⁰ Computed reflectance for nanogap resonators with varying gap sizes is shown in Figure 1e. The resonant plasmonic modes appear in reflection as a dip and are found to red-shift from 570 to 710 nm when the gap size is reduced from 30 to 7 nm. The SERS enhancement is found to peak at gap sizes for which the nanogap resonance overlaps with the excitation and detection wavelengths.³¹ In our experiments, this optimal gap size is at around 10 nm for an excitation wavelength of 633 nm. Interestingly, this optimal gap size shifts to 5 nm, when the same pattern is excited at 785 nm, as shown in Figure 1f and in good agreement with the calculated red-shift of the gap plasmon resonance for smaller gap sizes. Additionally, we observe a quenching of the resonance for gap sizes below 5 nm, when Au crystallites on opposing sidewalls start to intersect. Nanogap resonators are therefore prone to resonance matching since varying only the gap size controls the resonance wavelength. In contrast, the resonance of dipole antennas with nanometric gaps is mostly affected by the antenna size, but also by the gap size, which leads under resonance matching conditions to highest near-field enhancement where the antenna patterns are operated at the smallest gap.¹⁵

Let us now study the influence of the gap sidewall length on SERS by varying the Au layer thickness between 30 and 100 nm, Figure 2a and b, for a given nanogap size. Remarkably, with 10 nm gap arrays strong SERS signals appear only when the Au layer thickness is above 60 nm, Figure 2e. After a steep rise, the SERS intensity levels off around a thickness of 100 nm, suggesting that a minimum cavity length is required to allow for Fabry–Perot type gap plasmons. Indeed, we obtain by calculation that, for a 10 nm gap with 100 nm long sidewalls, the fundamental, lowest order Fabry–Perot mode is an antisymmetric MIM plasmon, Figure 2d. The fundamental mode of such a gap plasmon corresponds to a dipolar charge distribution at each metal sidewall with one node corresponding to a phase change of π .^{24,32} The longitudinal modal size of the fundamental MIM gap plasmon mode has been shown to range between 80 and 110 nm,^{22,32,33} in good agreement with the metal layer thickness onset for which we measure strong SERS enhancement. Below 80 nm metal thickness, gap plasmon modes cannot exist, and thus the observed near-field intensity in the gap region, Figure 2c, and the SERS signal are minimal.

During the angular evaporation, metal is also deposited onto the sidewall of the photoresist, producing the sharp metal apex visible in Figure 2b. For thin metal layers, this apex forms a crescent-like nano structure. Its resonance is found to be extremely sensitive to sub-Ångström changes of the gap opening and thus is a measure of the plasmon radiance.³⁴ For our case, the metal tapering enables an efficient coupling of the external field to the plasmon mode. It has been previously shown that gap plasmon modes can lead to highly localized near-field hotspots, but to achieve strong SERS enhancement this plasmonic mode must also be efficiently coupled to the incident field³⁴ and scatter back into the far-field.³⁵ For nanogap resonator arrays, the top surface consists mostly of a flat metal film with high reflectivity and therefore a low coupling efficiency. By tapering the opening of the nanogap region, the coupling of the incident field to the gap plasmon mode is enhanced and the incoming energy guided to the nanogap mode by adiabatic compression.^{36–39} To explore this

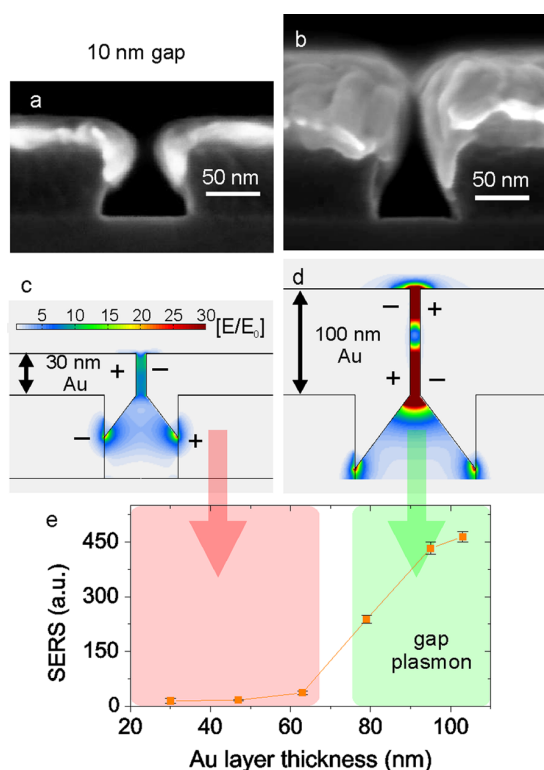


Figure 2. Gap plasmon modes at varying metal layer thickness. (a and b) Cross section SEM images; (c and d) simulated near-field maps at a wavelength of 650 nm for two different Au thicknesses of 30 and 100 nm. (e) SERS enhancement of a 10 nm gap arrays with varying Au metal thicknesses. The intensities correspond to the 1008 cm^{-1} Raman shift peak of a self-assembled benzene-ethane-thiol monolayer. Error bars represent the standard deviation of 16 spatially separated SERS measurements.

coupling effect, we compare in Figure 3 the SERS enhancement and visible to near-infrared reflection for a 100 nm thick pattern with 10 nm gaps that are excited either from the flat top or the tapered bottom side. We observe a 7-fold increase in the SERS intensity for excitation from the bottom side, compared to the top side, in Figure 3a. This increase of SERS enhancement is assigned to an improved coupling efficiency. The latter we estimate from the plasmonic radiance³⁴ obtained from the comparison of the top and bottom reflection as compared to a continuous Au film from an unpatterned area, Figure 3b. While we observe for the 10 nm gap structure a broadband absorption with 6% magnitude for top side excitation, a distinct resonance dip in reflection with 30% magnitude is observed when the pattern is excited from the bottom side. We cannot discuss the resonance position due to the broadband effect under top side excitation, but from the resonance magnitude we estimate a 5-fold increase in the coupling efficiency. This could ideally lead to a 25× increase in SERS intensity, while we only observe a gain of 7×. In comparison with the far-field simulations from Figure 1 the observed resonances are much broader and smaller in magnitude. We attribute this to gap size dispersions and roughness of the investigated structure. In agreement with the coupling model, the SERS intensity dependence on the gap size of the 100 nm thick pattern follows the same trend for either excitation side, with an optimum gap at about 10 nm. Hence,

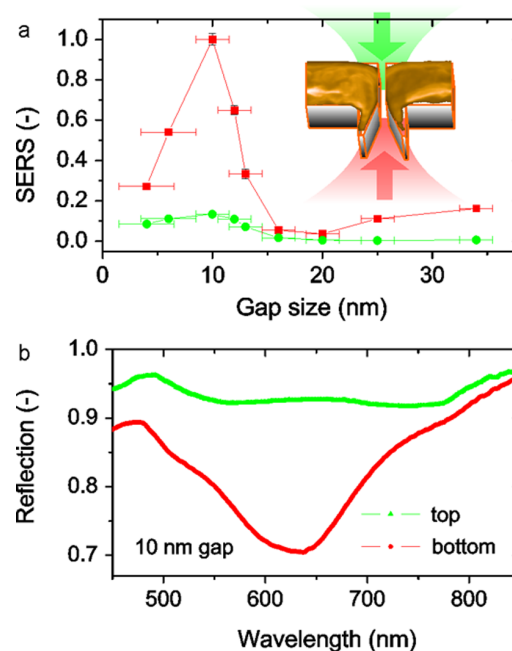


Figure 3. Influence of the excitation side of a 100 nm thick gap array on a glass substrate with excitation either from the top (green) or the bottom (red). (a) The SERS intensity of the 1008 cm^{-1} peak of a self-assembled benzene-ethane-thiol monolayer with varying gap sizes and (b) the pattern reflection of a 10 nm gap array. Error bars represent the standard deviation of 16 spatially separated SERS measurements and the analysis of multiple SEM images. The excitation, polarization, and integration times were kept constant for all measurements.

the same gap plasmon mode is excited from both sides, although more efficiently from the bottom side.

In the following, we compare the top with bottom side excitation scheme to a nanopattern enclosed in a liquid cell filled with ethanol. In this case, not only is the SERS intensity from the analyte monolayer for bottom side excitation improved by a factor of 10 compared to top side excitation, but also the background signal from the ethanol is suppressed by a factor of 2, as shown in Figure S3 of the Supporting Information. Taking into account that the optical path for bottom side excitation does not cross the analyte solution flowing on the top side of the structure, we can conclude that the SERS background is dominantly generated by molecules near or in the nanogap opening.

So far, we have discussed the enhancement factor of a slit array with 250 nm periodicity averaged over the excitation spot which is expected to be about $1.5\text{ }\mu\text{m}$ from $1.22\lambda_{\text{laser}}/\text{NA}$. The thus-obtained SERS intensities show a standard deviation below 4% across a patterned area of 0.5 mm^2 with a histogram given in Figure S2 of the Supporting Information. We calculate a surface averaged SERS enhancement factor of 10^6 for a 10 nm gap array under backside excitation, assuming that all molecules on the surface and in the focal spot contribute to the signal (details in the Supporting Information). This conservative enhancement factor is similar to values reported for nanogap resonators, although the local enhancement factor can be assumed larger,¹¹ whereby we do not know the exact number of molecules contributing to SERS. To investigate the SERS signal dependence associated with the number of illuminated slits, nanogap resonators are prepared with gap periodicities between

Nano Letters

Letter

15 μm and 250 nm using electron-beam lithography. By scanning the laser excitation spot across the gap, we can resolve the Raman signal from individual nanogaps, once the slits are well-separated; see inset in Figure 4. The average SERS signal is

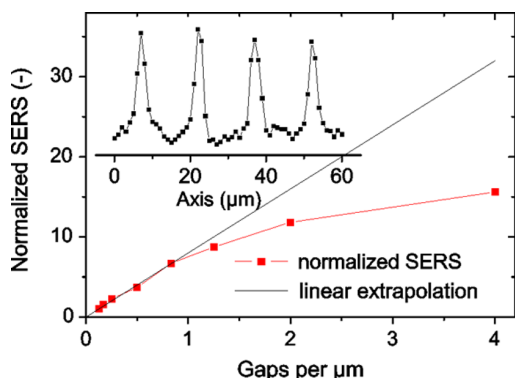


Figure 4. SERS intensity related to varying the nanogap periodicity. The gap arrays were fabricated with electron-beam lithography and angular evaporation. The SERS signal corresponds to the 1008 cm^{-1} Raman shift of a self-assembled benzene-ethane-thiol monolayer and was normalized to the intensity at a period of $8\text{ }\mu\text{m}$. The periodicity is expressed as the number of gaps per micrometers. For the average SERS signal, the focal spot was continuously deflected within a field of $20 \times 20\text{ }\mu\text{m}^2$ during the SERS signal integration of 5 s. The inset shows a SERS scan across four nanogaps with a period of $15\text{ }\mu\text{m}$, recorded without the laser focal spot deflection.

taken by integrating the Raman signal while scanning the laser beam over an area of $20 \times 20\text{ }\mu\text{m}^2$. We obtain a linear increase of the SERS intensity when plotted against the gap density up to a gap packing of almost 1 gap per μm that originates from the linear increase of molecules contributing to the SERS signal. Above 1 gap per μm , the average SERS intensity deviates from the linear trend and saturates for densities higher than about $2\text{ }\mu\text{m}^{-1}$, as seen in Figure 4. For high gap densities, the individual gap plasmon modes might interfere which decreases the optimal coupling efficiency of each individual gap plasmon. We assume that the SERS saturation results from inefficient coupling to the gap plasmon modes leading to a reduced near field intensity. From this we can immediately conclude that such nanogap arrays do not need to be denser than 1–2 slits per μm , which makes it possible to produce such structures by cheaper mass fabrication methods.²⁸ Disregarding the detailed mechanism leading to the funneling of light into the nanogaps, we like to mention that in extraordinary optical transmission (EOT) efficient funneling is observed up to the propagation length of surface plasmons of roughly $3\text{ }\mu\text{m}$ for Au at a wavelength of 633 nm .^{40–42} Interestingly, the width of the SERS signal recorded when scanning normal to the vertical direction of the slit is considerably larger (\pm factor of 2) than the expected $1.5\text{ }\mu\text{m}$, Figure 4; this could either be related to the above-mentioned collection mechanism or to the recently introduced magnetoelectric interference effect.⁴³ The latter model predicts that the energy flow, that is, the funneling of light, is described as the interference between evanescent and propagating fields. This effect thus predicts collection diameters related to the amplitude decay length of involved fields, which is larger than the intensity decay length typically by $2^{1/2}$.

In summary, nanogap resonator arrays enable strong near-field enhancement for SERS measurements and can be fabricated over large arrays with a scalable technique based

on interference lithography and angular evaporation, enabling accurate gap sizes below 10 nm . Such arrays represent an inexpensive alternative to nanoparticle based gap arrays requiring high-resolution lithography. Resonance matching with the excitation wavelength is shown to be crucial, as the resonance strongly depends on the gap size, the optimum gap being not necessarily the smallest one. Most importantly, gap plasmon modes require a minimal cavity length defined by the metal layer thickness (about 80 nm in our experiments) in order to allow for a standing wave Fabry–Perot mode. Another limitation comes from the coupling requirement to gap plasmon modes, as flat nanogap arrays can be highly reflective. We have measured a $10\times$ increase of the SERS intensity by tapering the backside of the array with a conical gap opening obtained as a byproduct of the angular evaporation. Additionally, suppression of solvent background signals is achieved under backside excitation. Finally, we observed saturation of the SERS intensity for nanogap periods below $1\text{ }\mu\text{m}$ because the incident field is distributed to multiple gap modes. We pinpoint the trade-off between highest average SERS enhancement and the demand for higher resolution lithography, at a period of about 500 nm , which is well achievable by low-cost lithography.²⁸

To conclude, nanogap resonator arrays offer substantial advantages for sensitive and reproducible sensing experiments and can be fabricated without high-resolution and cost-intensive lithography steps over wafer scale dimensions. The presented angular evaporation scheme is broadly applicable and leads to a self-limiting sub- 10 nm gap precision used for maximum near-field enhancement. Combined with a fiber-based SERS probe, molecules could be analyzed remotely, while background signals from surrounding molecules in solution are suppressed. Together with a sensor cleaning method, such a sensor probe can be made reusable without losing the signal enhancement factor.⁴⁴

■ ASSOCIATED CONTENT

Supporting Information

Schematic and fabrication details leading to sub- 10 nm gap arrays, experimental methods, and simulation details; SERS histogram of a 12 nm gap array and details of the enhancement factor calculation; SERS spectra recorded in a liquid cell under top and bottom excitation. This material is available free of charge via the Internet at <http://pubs.acs.org>.

■ AUTHOR INFORMATION

Corresponding Author

*E-mail: thomas.siegfried@psi.ch.

Notes

The authors declare no competing financial interest.

■ ACKNOWLEDGMENTS

T.S. would like to thank R. Ernst, for using his private Raman setup for measurements at 785 nm and the introduction to Tibetan art. This work was supported by the Swiss National Science Foundation (SNF). Part of this work was performed at the Swiss Light Source (SLS), Paul Scherrer Institute, Switzerland.

■ REFERENCES

- (1) Kneipp, K.; Wang, Y.; Kneipp, H.; Perelman, L. T.; Itzkan, I.; Dasari, R. R.; Feld, M. S. *Phys. Rev. Lett.* **1997**, *78* (9), 1667–1670.

Nano Letters

Letter

- (2) Bantz, K. C.; Meyer, A. F.; Wittenberg, N. J.; Im, H.; Kurtulus, O.; Lee, S. H.; Lindquist, N. C.; Oh, S.-H.; Haynes, C. L. *Phys. Chem. Chem. Phys.* **2011**, *13* (24), 11551–11567.
- (3) Halas, N. J.; Lal, S.; Chang, W.-S.; Link, S.; Nordlander, P. *Chem. Rev.* **2011**, *111* (6), 3913–3961.
- (4) Ye, J.; Wen, F.; Sobhani, H.; Lassiter, J. B.; Dorpe, P. V.; Nordlander, P.; Halas, N. J. *Nano Lett.* **2012**, *12* (3), 1660–1667.
- (5) Novotny, L.; Hecht, B. *Principles of Nano-Optics*; Cambridge University Press: New York, 2012.
- (6) Lindquist, N. C.; Nagpal, P.; McPeak, K. M.; Norris, D. J.; Oh, S.-H. *Rep. Prog. Phys.* **2012**, *75* (3), 036501.
- (7) Bora, M.; Fasenfest, B. J.; Behymer, E. M.; Chang, A. S. P.; Nguyen, H. T.; Britten, J. A.; Larson, C. C.; Chan, J. W.; Miles, R. R.; Bond, T. C. *Nano Lett.* **2010**, *10* (8), 2832–2837.
- (8) Ciraci, C.; Hill, R. T.; Mock, J. J.; Urzhumov, Y.; Fernandez-Dominguez, A. I.; Maier, S. A.; Pendry, J. B.; Chilkoti, A.; Smith, D. R. *Science* **2012**, *337* (6098), 1072–1074.
- (9) Duan, H.; Hu, H.; Kumar, K.; Shen, Z.; Yang, J. K. W. *ACS Nano* **2011**, *5* (9), 7593–7600.
- (10) Hatab, N. A.; Hsueh, C.-H.; Gaddis, A. L.; Retterer, S. T.; Li, J.-H.; Eres, G.; Zhang, Z.; Gu, B. *Nano Lett.* **2010**, *10* (12), 4952–4955.
- (11) Im, H.; Bantz, K. C.; Lindquist, N. C.; Haynes, C. L.; Oh, S.-H. *Nano Lett.* **2010**, *10* (6), 2231–2236.
- (12) Stosch, R.; Yaghobian, F.; Weimann, T.; Brown, R. J. C.; Milton, M. J. T.; Güttler, B. *Nanotechnology* **2011**, *22* (10), 105303.
- (13) Theiss, J.; Pavaskar, P.; Echternach, P. M.; Müller, R. E.; Cronin, S. B. *Nano Lett.* **2010**, *10* (8), 2749–2754.
- (14) Ward, D. R.; Huser, F.; Pauly, F.; Cuevas, J. C.; Natelson, D. *Nat. Nanotechnol.* **2010**, *5* (10), 732–736.
- (15) Duan, H.; Fernández-Domínguez, A. I.; Bosman, M.; Maier, S. A.; Yang, J. K. W. *Nano Lett.* **2012**, *12* (3), 1683–1689.
- (16) Zuloaga, J.; Prodan, E.; Nordlander, P. *Nano Lett.* **2009**, *9* (2), 887–891.
- (17) Haynes, C. L.; Van Duyne, R. P. *J. Phys. Chem. B* **2001**, *105* (24), 5599–5611.
- (18) Wen, X.; Xi, Z.; Jiao, X.; Yu, W.; Xue, G.; Zhang, D.; Lu, Y.; Wang, P.; Blair, S.; Ming, H. *Plasmonics* **2013**, *8* (2), 225–231.
- (19) Wang, H.; Levin, C. S.; Halas, N. J. *J. Am. Chem. Soc.* **2005**, *127* (43), 14992–14993.
- (20) Im, H.; Bantz, K. C.; Lee, S. H.; Johnson, T. W.; Haynes, C. L.; Oh, S.-H. *Adv. Mater.* **2013**, *25* (19), 2678–2685.
- (21) Siegfried, T.; Ekinici, Y.; Solak, H. H.; Martin, O. J. F.; Sigg, H. *Appl. Phys. Lett.* **2011**, *99* (26), 263302.
- (22) Søndergaard, T.; Siahpoush, V.; Jung, J. *Phys. Rev. B* **2012**, *86* (8), 085455.
- (23) Belotelov, V. I.; Kalish, A. N.; Zvezdin, A. K.; Gopal, A. V.; Vengurlekar, A. S. *J. Opt. Soc. Am. B* **2012**, *29* (3), 294–299.
- (24) Kern, J.; Großmann, S.; Tarakina, N. V.; Häckel, T.; Emmerling, M.; Kamp, M.; Huang, J.-S.; Biagioni, P.; Prangsma, J. C.; Hecht, B. *Nano Lett.* **2012**, *12* (11), 5504–5509.
- (25) Auzelyte, V.; Dais, C.; Farquet, P.; Grutzmacher, D.; Heyderman, L. J.; Luo, F.; Olliges, S.; Padeste, C.; Sahoo, P. K.; Thomson, T.; Turchanin, A.; David, C.; Solak, H. H. *J. Micro/Nanolithogr., MEMS MOEMS* **2009**, *8* (2), 021204–10.
- (26) Päivänranta, B.; Langner, A.; Kirk, E.; David, C.; Ekinici, Y. *Nanotechnology* **2011**, *22* (37), 375302.
- (27) Abelman, L.; Lodder, C. *Thin Solid Films* **1997**, *305* (1–2), 1–21.
- (28) Fucetola, C. P. *J. Vac. Sci. Technol., B* **2009**, *27* (6), 2958.
- (29) Siegfried, T.; Ekinici, Y.; Martin, O. J. F.; Sigg, H. *ACS Nano* **2013**, *7* (3), 2751–2757.
- (30) Gallinet, B.; Kern, A. M.; Martin, O. J. F. *J. Opt. Soc. Am. A* **2010**, *27* (10), 2261–2271.
- (31) Kern, A. M.; Meixner, A. J.; Martin, O. J. F. *ACS Nano* **2012**, *6* (11), 9828–9836.
- (32) Søndergaard, T.; Jung, J.; Bozhevolnyi, S. I.; Valle, G. D. *New J. Phys.* **2008**, *10* (10), 105008.
- (33) Jung, J.; Søndergaard, T.; Bozhevolnyi, S. I. *Phys. Rev. B* **2009**, *79* (3), 035401.
- (34) Gallinet, B.; Siegfried, T.; Sigg, H.; Nordlander, P.; Martin, O. J. F. *Nano Lett.* **2012**, *13* (2), 497–503.
- (35) Weihua, Z.; Fischer, H.; Schmid, T.; Zenobi, R.; Martin, O. J. F. *J. Phys. Chem. C* **2009**, *113* (33), 14672–14675.
- (36) Choo, H.; Kim, M.-K.; Staffaroni, M.; Seok, T. J.; Bokor, J.; Cabrini, S.; Schuck, P. J.; Wu, M. C.; Yablonovitch, E. *Nat. Photonics* **2012**, *6* (12), 838–844.
- (37) Ginzburg, P.; Arbel, D.; Orenstein, M. *Opt. Lett.* **2006**, *31* (22), 3288–3290.
- (38) Lindquist, N. C.; Johnson, T. W.; Nagpal, P.; Norris, D. J.; Oh, S.-H. *Sci. Rep.* **2013**, *3*, 1857.
- (39) Diwekar, M.; Davis, M.; Blair, S. *J. Nanophotonics* **2010**, *4* (1), 043504–043504-11.
- (40) Bravo-Abad, J.; Degiron, A.; Przybilla, F.; Genet, C.; Garcia-Vidal, F. J.; Martin-Moreno, L.; Ebbesen, T. W. *Nat. Phys.* **2006**, *2* (2), 120–123.
- (41) Fernández-Domínguez, A. I.; García-Vidal, F. J.; Martín-Moreno, L. *Phys. Rev. B* **2007**, *76* (23), 235430.
- (42) Kolomenski, A.; Kolomenskii, A.; Noel, J.; Peng, S.; Schuessler, H. *Appl. Opt.* **2009**, *48* (30), 5683–5691.
- (43) Pardo, F.; Bouchon, P.; Haidar, R.; Pelouard, J.-L. *Phys. Rev. Lett.* **2011**, *107* (9), 093902.
- (44) Siegfried, T.; Kind, M.; Terfort, A.; Martin, O. J. F.; Zharnikov, M.; Ballav, N.; Sigg, H. *J. Raman Spectrosc.* **2012**, *44* (2), 170–175.

SUPPORTING INFORMATION

Gap Plasmons and Near-Field Enhancement in Closely Packed Sub-10 nm Gap Resonators

Thomas Siegfried,[†] Yasin Ekinci,[†] Olivier J.F. Martin,[§] Hans Sigg[†]*

[†]Laboratory for Micro- and Nanotechnology, Paul Scherrer Institut, 5232 Villigen-PSI, Switzerland,

[§]Nanophotonics and Metrology Laboratory, EPFL, 1015 Lausanne, Switzerland

AUTHOR EMAIL ADDRESS thomas.siegfried@psi.ch

METHODS

Fabrication of the nanogap arrays

Line patterns with period 250 nm over an area of $0.6 \times 1.8 \text{ mm}^2$, as well as dot patterns with period 280 nm over an area of $300 \times 300 \text{ }\mu\text{m}^2$ were exposed by using extreme ultraviolet interference (EUV) lithography into an 80 nm hydrogen silsesquioxane (HSQ) film. The HSQ layer was developed for 60s in a 25 % tetra methyl ammonium hydroxide (TMAH) solution. Glancing angular deposition was then used directly to thermally evaporate an Au (99.99 % purity) layer onto HSQ at a base pressure of 2×10^{-6} mbar. A schematic of the evaporation process is shown in Figure S1. The substrate was aligned at an angle of 60° from the surface normal with an azimuthal orientation of the line pattern perpendicular to the gap extension.¹ During evaporation, the substrate was tilted to the opposite direction (-60°) after every 2 nm until the final thickness was reached. A modulation of the pattern gap size was achieved by changing the duty cycle of the photoresist pattern with constant evaporation process conditions. The 2D nanogap pattern was obtained by continuous rotation of a dot resist pattern that is tilted by an angle of

60° from the surface normal. Further details on the self-limiting shadowing process leading to sub-10 nm gaps are described elsewhere.¹

The patterns with varying periodicity between 15 μm and 250 nm were fabricated with electron beam lithography. We used a Vistec EBP5000 plus tool at 100 keV electron energy and exposed the line arrays with an aperture of 400 μm and a dose of 4000 $\mu\text{C cm}^{-2}$. The subsequent fabrication steps were the same as before.

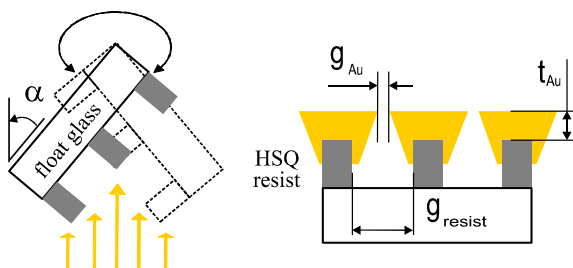


Figure S1. Schematic of the glancing angular deposition process. The nanogap pattern is defined by the gold gap size g_{Au} and the gold thickness t_{Au} and can be predicted from the evaporation angle α and the resist gap size g_{resist} .

Optical measurements

Reflection spectra were recorded with a Sentech FTP spectrometer connected to a Leica microscope. The incident path was polarized and focused to roughly 10 μm . The reference was taken at a continuous Au layer outside the patterned area on the same substrate.

The surface enhanced Raman scattering was performed on a Horiba LabRam HR with a grating resolution of 600 lines mm^{-1} . A Helium-Neon laser at 633 nm with an incident power of 2 mW was focused (50x, numerical aperture NA 0.5) and deflected within an area of 10*10 μm^2 to minimize photobleaching. The SERS intensities of all figures correspond to the Raman peak intensity at the 1008 cm^{-1} vibrational mode from a self assembled benzene-ethane-thiol (BET) monolayer, formed during 12 h immersion in a 1 mM solution. 16 spectra were taken over a patterned area of 300x800 μm^2 for

statistical evaluation. SERS spectra of a 12 nm gap under backside excitation are shown in Figure S2, along with a histogram of the intensities at a wavenumber shift of 1008 cm^{-1} .

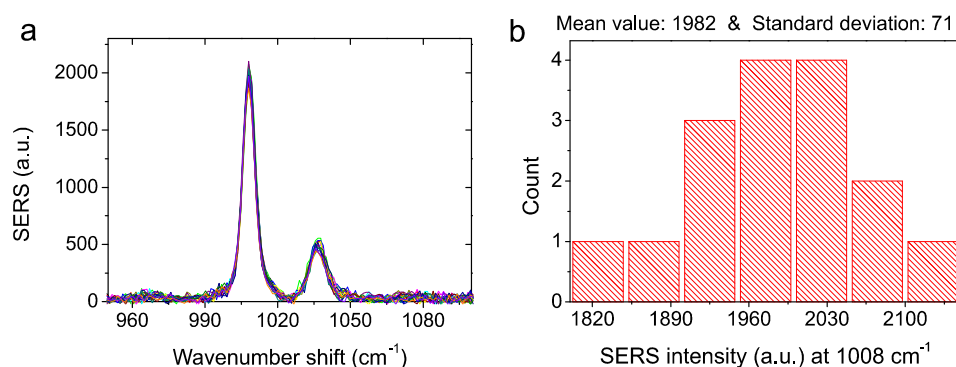


Figure S2. SERS spectra and histogram of 16 spatially separated measurements. The spectra are obtained from a 12 nm gap array with period 250 nm and under backside illumination.

The enhancement factor (EF) is calculated on the basis of the 1008 cm^{-1} peak intensity of BET recorded with an x50 (NA 0.5) objective. We use a conservative approach and calculate only the area averaged enhancement factor defined by the focal spot size, which does not take into account that SERS is obtained only from molecules in the hotspot region, $EF = (I_{\text{SERS}} \cdot N_{\text{Raman}}) / (I_{\text{Raman}} \cdot N_{\text{SERS}})$, where N is the number of molecules possibly contributing to the signal. N_{SERS} is calculated with reported values of the monolayer packing density from benzene-thiol, $6.8 \cdot 10^{14} \text{ cm}^{-2}$.² N_{Raman} is calculated via the molecular weight and density of BET, 138.23 g/mol and 1.032 g/ cm^3 . The SERS intensity is obtained from an analyte monolayer at an incident power of 2 mW and the normal Raman intensity is obtained from a pure analyte liquid at an incident power of 20 mW. For the 12 nm gap array from Figure S2 we calculate an area averaged EF of $1 \cdot 10^6$. Additionally one can assume a local EF, which is increased by the factor of molecules not contributing to the SERS signal. In the literature, the factor of the local EF was assumed to be roughly 100, when only a single strip of molecules at the opening of the nanogap contributes to the large majority of SERS.³ This would lead to a local EF of 10^8 for our 12 nm gap array under backside illumination, which is similar to reported values of nanogap SERS substrates.³

Numerical Simulation

The far-field spectra and corresponding near-field maps were calculated with a full-field numerical method based on the solution of surface integrals.⁴ The simulation of the nanogap array was carried out in a 3D unit cell with periodic boundary conditions along and across the gap plane. The structures were discretized using a triangular mesh with a maximum side length of 20 nm. The polarization of the electric field was set across the gap axis. The refractive index of the substrate glass and the photoresist HSQ was estimated with 1.5 and 1.39 respectively. The permittivity of Au was estimated with data from Johnson & Christy,⁵ and the refractive index of the surrounding medium was 1 (air).

SERS spectra recorded in a liquid cell under top and bottom excitation

To demonstrate sensing of a nanogap resonator array enclosed in a liquid cell, we have attached a 2 mm Polydimethylsiloxane (PMDS) spacing layer to our sensor array fabricated on a float glass array. The enclosed volume was filled with ethanol and closed with a cover slip to prevent evaporation, shown in Figure S3. The Au nanogap array was previously covered with a benzene-ethane-thiol monolayer acting as analyte, while the ethanol lead to the Raman background peaks. We do not expect additional Raman peaks i.e. from HSQ vibrational modes at wavenumber shifts below 600 cm^{-1} (Si-O-Si) and above 2200 cm^{-1} (Si-H²). In the following, we applied top side excitation and rear side excitation to the nanopattern. In this case, not only was the SERS intensity increased by a factor of 10, but also the background signal i.e. at 890 cm^{-1} from ethanol was suppressed by a factor of 2. Under the rear side excitation, the optical path does not cross the analyte solution flowing on the top side of the structure. The SERS background therefore must be related to molecules near the nanogap opening, where the incident field is focused and the gap plasmon near-field amplitude decays into free space.

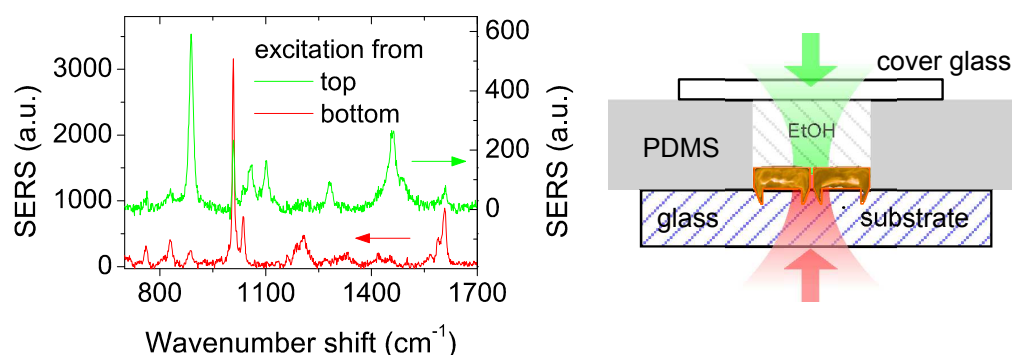


Figure S3. The influence of the excitation side on SERS for a 10 nm nanogap resonator array with 100 nm Au thickness. SERS spectra are recorded from a self assembled benzene-ethane-thiol monolayer on patterned chip enclosed in an ethanol filled liquid cell. The electric field is polarized across the gaps. The excitation and integration time was kept constant for both measurements.

References

1. Siegfried, T.; Ekinci, Y.; Solak, H. H.; Martin, O. J. F.; Sigg, H., Fabrication of Sub-10 nm Gap Arrays over Large Areas for Plasmonic Sensors. *Appl. Phys. Lett.* **2011**, 99, 263302.
2. Aggarwal, R. L.; Farrar, L. W.; Polla, D. L., Measurement of the absolute Stokes Raman cross sections of the longitudinal optical (LO) phonons of room-temperature GaP. *Solid State Commun.* **2009**, 149, 1330-1332.
3. Im, H.; Bantz, K. C.; Lindquist, N. C.; Haynes, C. L.; Oh, S.-H., Vertically Oriented Sub-10-nm Plasmonic Nanogap Arrays. *Nano Lett.* **2010**, 10, 2231-2236.
4. Gallinet, B.; Kern, A. M.; Martin, O. J. F., Accurate and Versatile Modeling of Electromagnetic Scattering on Periodic Nanostructures with a Surface Integral Approach. *J. Opt. Soc. Am. A* **2010**, 27, 2261-2271.
5. Johnson, P. B.; Christy, R. W., Optical Constants of the Noble Metals. *Phys. Rev. B* **1972**, 6, 4370-4379.

(IV) Double layer pattern with nanogap channels

Manuscript state

Submitted manuscript

Reference

T. Siegfried, L. Wang, Y. Ekinici, O. J. F. Martin, H. Sigg, "*Metal Double Layers with Sub-10 nm Channels*".

Submitted: 20.01.2014

Author contribution

T. Siegfried fabricated the samples. T. Siegfried performed the experiments and simulations, analyzed and concluded the data. T. Siegfried wrote the manuscript. L. Wang and Y. Ekinici proof-read the manuscript. H. Sigg and O.J.F. Martin corrected the manuscript.

Submitted paper + Supporting information

Metal Double Layers with Sub-10 nm Channels

Thomas Siegfried,[†] Li Wang,[‡] Yasin Ekinici,[†] Olivier J.F. Martin,[§] and Hans Sigg^{†,*}

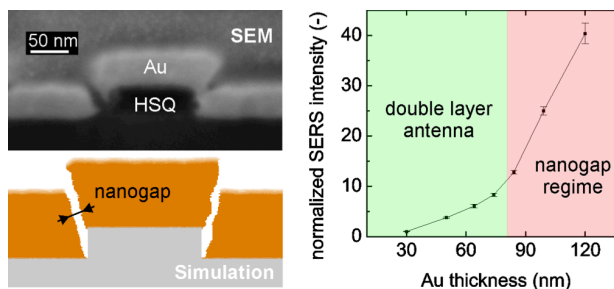
[†]Laboratory for Micro- and Nanotechnology, Paul Scherrer Institut, 5232 Villigen-PSI, Switzerland

[‡]Eulitha AG, 5232 Villigen PSI, Switzerland

[§]Nanophotonics and Metrology Laboratory, EPFL, 1015 Lausanne, Switzerland

ABSTRACT Double layer plasmonic nanostructures are fabricated by depositing metal at normal incidence onto various resist masks forming an antenna layer on top of the resist post and a hole layer on the substrate. Antenna plasmon resonances are found to couple to the hole layer, inducing image charges which enhance the near-field for small layer spacings. For continued evaporation above the resist height, a sub-10 nm gap channel develops thanks to a self-aligned process and a minimal undercut of the resist sidewall. For such double layers with nanogap channels, the average surface enhanced Raman scattering (SERS) intensity is improved by a factor in excess of 60 in comparison to a single layer antenna with the same dimensions. The proposed design principle is compatible with low-cost fabrication, is straightforward to implement and applicable over large areas. Moreover, it can be applied for any particular antenna shape to improve the signals in surface enhanced spectroscopy applications.

KEYWORDS: double layer, nanogap, SERS, antenna, coupled modes, surface plasmon, localized plasmon resonance, near-field



Surface-enhanced spectroscopy enables promising applications in various fields including medical sensing, single molecule detection and electromagnetic field characterization.¹⁻³ Its extraordinary sensitivity relies on the near-field enhancement within electromagnetic hotspots, which are generated by the resonant modes of the electrons oscillating at the surface of noble metal nanoparticles.⁴ In plasmonics, antenna geometries are commonly used due to their tunable plasmon resonance and efficient scattering to the far field enabling a good matching of the resonance with the excitation frequency and an efficient detection of the emitted waves, respectively.^{4, 5} Previously, antenna geometries were optimized to obtain strong near-field enhancement through, e.g. the exploration of sharp particle edges, leading to strong field localization, or the utilization of particle pairs with few-nm gaps, leading to strongly coupled modes.⁶⁻¹¹ Strong near-field enhancement was also obtained with Fano-resonant antenna geometries via the coupling to dark modes with suppressed absorption/scattering losses.¹²⁻¹⁴ Apart from tuning the antenna geometry, the near-field enhancement can also be improved by placing the antenna onto a reflective layer with controlled spacing.¹⁵⁻¹⁸ Thereby, not only the coupling to the antenna resonance is improved, but also the scattered field can be manipulated to steer the emission in the direction of detection.¹⁹⁻²² Additionally, localized surface plasmon modes (LSPR) can be coupled to propagating surface plasmon modes (SPP) at the reflective layer, which may further improve the coupling to the incident field.²³⁻²⁵ The total coupling efficiency of a particular antenna geometry used for surface enhanced spectroscopy is also related to the

density and surface coverage of the hot spots which in the above mentioned examples were often very small. Dense antenna arrays with high average surface-enhancement may thus be the better choice, provided low-cost fabrication over large areas using only a few standard processing steps become available.²⁶

Here we propose a straightforward single-step fabrication method to boost the near-field enhancement for various antenna patterns over large areas, by combining two established techniques, i.e. reflecting layers and nanogaps. Instead of isolated single layer (SL) antenna geometries, we utilize double layer (DL) antenna-hole pattern^{15, 17, 27} obtained by metal evaporation onto a patterned photoresist. The nanogaps are added to the pattern by prolonged evaporation of the metal layer. When the metallic layer extends above the photoresist layer, an elongated sub-10 nm wide gap channels is formed as is predicted by our ballistic simulations. Our experiments reveal the enhanced near-field in DL pattern due to coupling of the antenna mode to image charges generated in the hole layer, and we expand the advantage of DL pattern 2by combining them with the strong coupling in nanogaps.

RESULTS AND DISCUSSION

We start by comparing an isolated SL antenna pattern with a DL antenna of the same size. Isolated antennas are fabricated by etching, while the corresponding DL structures are obtained via a simple single-step evaporation onto the same resist pattern previously used as etching mask, without further lift-off or etching processes. For the DL pattern, the metal on top of the resist post acts as antenna and the metal

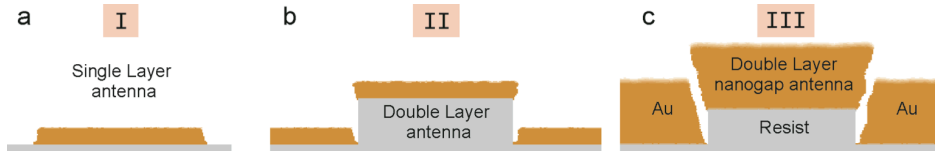


Figure 1. Ballistic simulation of the evaporated cross section for **a** single layer antenna (I) after mask liftoff, **b** double layer antenna pattern (II) separated by a resist post and **c** double layer pattern with a nanogap channel (III) for a metal layer thickness above the resist layer thickness.

film deposited on the substrate forms holes with shape of the inversed antenna and thus is representing the reflecting layer. The double layer separation is determined by the resist height minus the metal layer thickness. We use ballistic simulations^{8, 28} to illustrate the cross section of SL (regime I) and DL antennas (regime II), shown in Figure 1a and 1b. We observe that the evaporated metal layer not only grows vertically, but also slightly expands horizontally due to surface diffusion. The apparent undercut in the top metal layer and the resist post, leads to a shadowing of the metal layer that evolves at the substrate level. From this shadowing, a self-aligned nm spaced channel develops between the two metal layers as soon as the metal thickness deposited on the substrate exceeds the resist height (regime III), shown in Figure 1c. This channel is found to be the origin for boosting the SERS enhancement as will be demonstrated below.

Let us first clarify the difference between plasmon resonances of isolated antenna and of DL antenna. For their fabrication, we utilize extreme ultraviolet interference

lithography²⁹ (EUV) to yield triangular shaped antenna in a kagome array with a 700 nm lattice spacing.³⁰ The antenna thickness is 30 nm and much less than the height of the post which is 90 nm. The diameter of the antenna is varied between 100 nm and 200 nm by altering the exposure time. Thereby, the plasmon resonance is shifted from 600 nm to 770 nm as is shown from simulations using a surface integral approach (SIE)³¹ in Figure 2b. SL antennas are fabricated using patterned PMMA resist posts as the etch mask, while DL antenna of the same dimension are obtained by evaporation onto the same PMMA resist pattern. Both types of structures show a distinct resonance behavior with a peak in reflection for the isolated antenna pattern, Figure 2a, and a dip in reflection at the corresponding frequency for the DL antenna pattern, Figure 2c.

This reflection dip is verified by simulations (Figure 2d) and is explained by the lower metal layer acting as reflector. At resonance, the antenna couples to the incident field and induces a strong near-field at the metal/dielectric interface. This near-field is re-emitted into the far-field leading to a

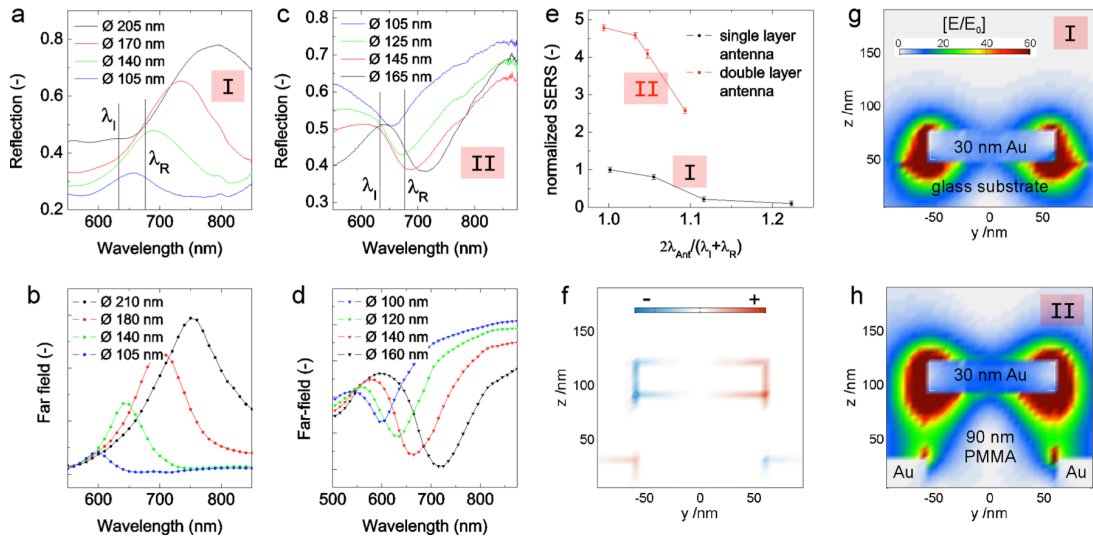


Figure 2. Comparison of a 30 nm thick Au single layer (SL, I) and double layer (DL, II) antenna pattern. The substrate is silicon and the 90 nm resist post is from PMMA. **a/c** Reflection spectra of triangular SL/DL pattern with varying effective diameter. The wavelengths of the 633 nm incident excitation λ_i and of the recorded Raman shift at 676 nm λ_R are marked. **b/d** Far-field simulation for an isolated SL/DL pattern with varying effective diameter. **e** SERS intensity of the 1008 cm^{-1} peak of a self assembled benzene-ethane-thiol monolayer normalized to the maximal intensity of the SL antenna and for varying relative resonance position. Error bars represent the standard deviation when mapping at 16 spatially separated spots. **f** Phase map of the near-field at resonance of a DL pattern covered by 30 nm Au film and **g/h** near-field map at resonance of a 30 nm covered SL/DL pattern with 120 nm diameter and 90 nm high PMMA resist post.

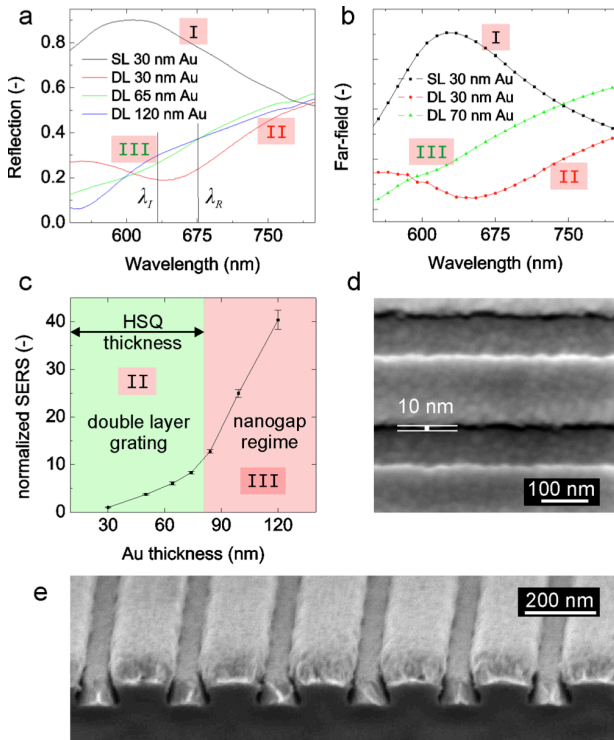


Figure 3. Double layer (DL) Au gratings at various metal layer thicknesses. The substrate is glass, the resist is of 90 nm HSQ and the grating period is 250 nm with a duty cycle of 0.5. **a** Reflection spectra. The wavelengths of the 633 nm incident excitation λ_i and of the recorded Raman shift at 676 nm λ_R are marked. The numbers I, II and III specify the pattern regime of SL, DL and DL antenna with nanogaps. **b** Far-field simulation. **c** SERS intensity of the 1008 cm^{-1} peak of a self assembled benzene-ethane-thiol monolayer normalized to the intensity of the 30 nm DL grating. Error bars represent the standard deviation when mapping 16 spatially separated spots. **d/e** Scanning electron micrograph (SEM) of a 120 nm thick gold metal DL. The substrate is tilted by 16° (**d**) and cleaved (**e**) to see the nanogap channel.

reflection maximum. When such an antenna is placed in front of a reflector, destructive interference of the light re-emitted by the antenna plasmon in backward direction and that emitted in forward and directly reflected by the metal film results in a dip in reflection. The antenna near-field enhancement is probed by SERS after decorating the metal surface with a self-assembled benzene-ethane-thiol monolayer. As expected, the SERS intensity has an optimum under resonance matching conditions with the incident excitation λ_i at 633 nm and the analyzed Raman wavelength λ_R at 676 nm, shown in Figure 2e. The SERS intensity for the DL pattern is as expected stronger by a factor of 5. This phenomenon has also been observed for antennas on top of a continuous reflecting layer.^{16, 17, 22, 32} From the simulated phase of the near-field we find image charges in the metal hole structure induced by the antenna on the resist post, as shown in Figure 2f. These image charges increase the near-field of the coupled antenna-hole mode above that one of the isolated antenna (Figure 2g and

2h), which in turn result in the enhanced SERS signals.

Next, we discuss the signal improvements from the narrow gap which is formed between the upper and lower metal layers at increased metal layer thickness. In the above used PMMA layers, the upper and lower metal levels are found to coalesce as soon the metal thickness exceeds the height of the posts because of an overcut of the resist sidewall.²⁹ The plasmon mode and near-field intensity thereby is quenched.³² The overcut of positive tone resists is characteristic in EUV lithography and results from absorption at the exposure wavelength of 13.5 nm, leading to lower doses at larger resist skin depths. In turn, when we switch to the negative tone resist hydrogen silsesquioxane (HSQ) a distinct undercut of the resist layers is obtained. This effect is found to be crucial for the generation of a self-aligned nanogap channel, as shown for grating structures with a period of 250 nm and a linewidth of 125 nm, Figure 3. Corresponding SL Au gratings are obtained using the same evaporated mask for a subsequent lift-off process.

We observe localized resonances in reflection for the individual grating lines at a wavelength of 600 nm for a 30 nm thick SL and with the electric field polarized perpendicular to the grating lines, c.f. Figure 3a. Similar to the antenna pattern in Figure 2, the reflection maximum inverts to a reflection dip, when we switch to a DL grating with same linewidth and layer thickness, as shown in Figure 3a. With increasing Au thickness, the localized plasmon resonance in the DL strongly broadens. This broadening is accurately described by the far-field simulations shown in Figure 3b and is ascribed to an increased coupling of the hole and antenna layer as the spacing decreases. In parallel, the SERS intensity is steadily increasing for smaller DL spacings (Figure 3c). We can relate the SERS signal to the antenna's near-field enhancement by accounting for the number density of contributing molecules: When the DL grating thickness is increased from 30 nm to 64 nm, the exposed surface area and hence the analyte number increases by roughly 1.4. At the same time, the SERS intensity gains by a factor of 6, c.f. Figure 3c, which we translate to a SERS activity enhancement of > 4 .

Above a metal thickness of 80 nm, the DL nanogap regime is formed, where we find vertically elongating nanogap channels, Figure 3d, as it was simulated in Figure 1. The formation of the DL nanogap channels is accompanied by a sharp increase in the SERS signal, which further rises for even longer channel lengths, Figure 3c. This gain in SERS results from strong localization of the plasmon mode in the nanochannel, which results in extremely high near-fields. We find a 40-fold increased SERS activity for the roughly 10 nm spaced DL grating (120 nm metal thickness) of elongated nanogap channels in comparison to a 50 nm spaced DL grating (30 nm metal thickness). We calculate an area averaged SERS enhancement factor (EF) of roughly 3×10^6 for the 120 nm thick Au DL grating by comparing the SERS intensity at monolayer analyte coverage to the Raman intensity of the liquid analyte. This average SERS EF value is similar to what we have previously reported on periodic sub-10 nm gap resonator

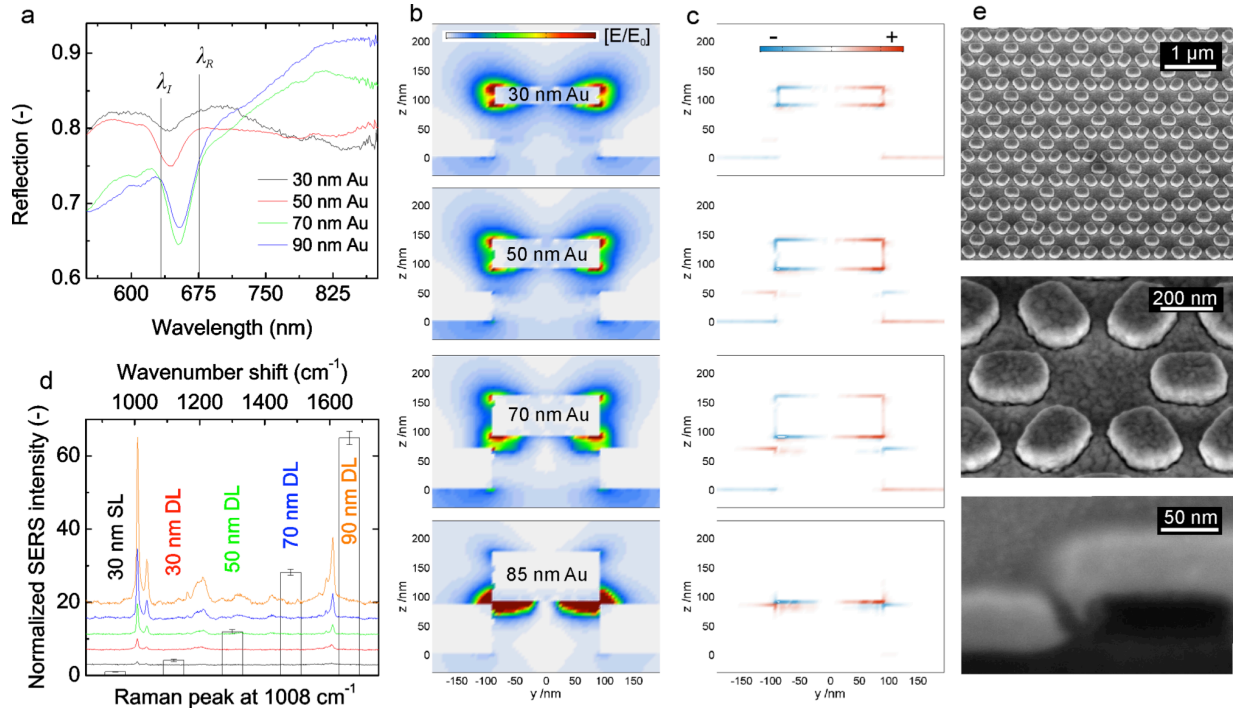


Figure 4. Double layer (DL) oval shaped antennas arranged in a hexagonal lattice, with increasing metal layer thickness and layer spacing, respectively. The substrate is silicon, the resist is 90 nm of HSQ, the antenna size is roughly 200x300 nm and the period is 700 nm. **a** Reflection spectra. The wavelengths of the 633 nm incident excitation λ_i and of the recorded Raman shift at 676 nm λ_R are marked. **b/c** Near-field intensity/ near-field phase plots for DL antenna with Au thickness between 30 nm and 90 nm. **d** SERS spectra (with arbitrary units) and the SERS intensity of the 1008 cm^{-1} peak of a self assembled benzene-ethane-thiol monolayer normalized to the intensity of the 30 nm single layer (SL) antenna pattern. Error bars represent the standard deviation when mapping 16 spatially separated spots. **e** SEM images of a 90 nm Au DL antenna pattern. The cross section SEM was cut by FIB and is recorded at an angle of 55°, hence the vertical axis is shrunk by a factor of roughly 0.6.

arrays.⁸ This hints that DL nanogap gratings can have a similar sensing efficiency as sub-10 nm gap arrays, although the fabrication of the DL pattern is considerably simpler to implement. Here we would also like to note that the DL nanogap fabrication is a robust process even for larger metal thicknesses leading to vertically elongated sub-10 nm gap channels. The high yield in accuracy over large areas is seen from SEM images (Figure 3d and 3e), and confirmed by the low SERS standard deviation of 3% for mapping across the patterned area (Figure 3c). Although we use a unique high resolution technique to fabricate our resist pattern, the DL evaporation process is also applicable to a resist pattern obtained from low-cost lithography, such as self-assembled nanospheres.³² The only requirement is that the resist sidewall needs to have an undercut to prevent coalescence of the two metal layers. In that case, the resist layer thickness can be used to adjust the gap size of the nanometer wide channels, which is shown in ballistic simulations in the Figure S1 of the Supporting Information.

In the next section, we expand the DL nanogap fabrication method to arbitrary antenna shapes to prove its general validity. This, we demonstrate on a kagome lattice of oval shaped antennas fabricated in an 80 nm thick HSQ layer, shown in Figure 4e. The antennas are sized 200x320

nm with a lattice spacing of 700 nm and result in LSPR peaks above 800 nm wavelengths for 30 nm thick isolated SL gold antennas (not shown). The reflection of the DL antenna pattern holds traces of the isolated SL resonance in the form of a broad reflection dip at wavelengths above 750 nm, as seen in Figure 4a and as has been discussed for the previous pattern. Additionally, we observe a weak but narrow dip at around 650 nm, which matches with the Raman excitation. With increasing metal thickness and hence reduced DL spacing, the resonance at 650 nm gains in magnitude, while the isolated antenna LSPR dip shifts to wavelengths above 750 nm. Based on this observation and in analogy with earlier results obtained for similar double layer geometries,²⁵ we attribute the resonance at 650 nm to a coupled mode consisting of the LSPR of the antenna and the continuous metal layer beneath. Since our simulation tool does not support kagome lattice boundary conditions, we could not reproduce the exact location of the resonance at 650 nm. Instead, we perform simulations for a rectangular arranged antenna-hole double layer pattern to illustrate the dependency of coupled modes on the spacing between both layers. From the near-field simulations for varying metal thickness, shown in Figure 4b, we find a coupled resonance at a wavelength of 690 nm (not shown) that leads to image

charges in the hole layer seen in the phase diagrams of Figure 4c. The coupling strength increases for small layer spacings, leading to extreme near-field enhancement in the gap region, c.f. the bottom image of Figure 4b. This dependence is nicely confirmed by SERS showing a 60-fold signal enhancement of the nanogap DL pattern coated by a 90 nm Au layer in comparison to the similarly shaped but only 30 nm thick SL antenna, shown in Figure 4d. For the 90 nm thick DL pattern, we obtain an area averaged SERS EF of $1 \cdot 10^7$, which is larger than the EF of the previously discussed grating DL pattern, in spite of the higher nanogap density in the latter. This extraordinary EF may be the result from improved coupling efficiency to the incident field, because of the distinct plasmon resonance, which matches so well with the SERS excitation, Figure 4a. For the grating DL pattern, only a broadband resonance is observed in reflection, c.f. Figure 3a.

CONCLUSION

We demonstrated a straightforward, single-step fabrication method for double layer antenna patterns with sub-10 nm spacing, where SERS is enhanced up to 60 fold in comparison to an isolated single layer antenna pattern. By direct metal evaporation onto a photoresist pattern, antenna-hole metal double layers were obtained, where the antenna plasmon mode can couple to image charges in the hole layer. A self-limiting sub-10 nm channel between both metal layers is found to develop for resist layers with an undercut. Such patterns combine the advantages of far-field coupling of antennas, the performance enhancement by light recycling in reflecting double layers and the extreme near-field enhancement in sub-10 nm gaps. The simple fabrication technique can be implemented for a broad range of patterns aiming at increasing the enhancement factor in surface enhanced spectroscopy with applications such as single molecule studies or other fields requiring extremely large and homogeneous field intensities over large areas.

METHODS

Fabrication of the pattern. Extreme ultraviolet interference lithography at the Swiss Light Source³³ is used to expose grating masks at a wavelength of 13.5 nm in 80-90 nm thick resist layers of hydrogen silsesquioxane (HSQ) or polymethyl-methacrylate (PMMA). Line pattern are obtained from a two-beam interference mask leading to a period of 250 nm over a patterned area of 1 mm^2 . Kagome pattern are obtained from a multibeam interference mask with a lattice spacing of 700 nm over a patterned area $100 \times 100 \mu\text{m}^2$.³⁰ HSQ is developed in a 25% tetra-methyl-ammonium-hydroxide (TMAH) solution for 60 s and PMMA is developed in a 20% isopropanol/water mixture for 45 s.

SL antenna pattern are obtained by etching into an Au layer. A glass substrate is evaporated with 1 nm Cr, 30 nm Au and again 25 nm Cr, before a 50 nm PMMA or HSQ layer is patterned. The resist pattern serves as a mask for the following reactive ion etching process based on Cl_2/CO_2 plasma to remove the 25 nm Cr layer. The obtained Cr

pattern then serves as a hard mask to remove the 30 nm Au layer by ion etching in Ar/SF_6 plasma. The Au antennas are then cleaned from the remaining Cr mask in a Cr etching bath.

SL gratings are obtained by evaporation through a PMMA/HSQ resist mask. 100 nm PMMA and 80 nm HSQ are spun on a glass wafer. After development of the top HSQ layer, the PMMA film is under etched in an O_2 plasma. The metal grating (1 nm Cr, 30 nm Au) is then evaporated thermally and the resist pattern is removed in an acetone bath under gentle sonication.

DL pattern are obtained by direct evaporation onto an 80 nm thick resist layer. The substrate was silicon and thermal evaporation was done at normal incidence with a 1 nm Cr adhesion layer, thereby minimizing near-field quenching.³⁴ Nanogap channels could only be obtained from HSQ layers, due to the apparent resist undercut, which prevents the coating of the resist sidewall and eventually suppresses the coalescence of the layers.

Optical measurements. Reflection spectra are recorded with a Sentech spectrometer connected to a Leica microscope. The incident field is focused through a 20x (0.45 NA) objective and is unpolarized for the kagome pattern and polarized for the grating pattern with the electric field across the lines. The reflection spectrum from a continuous Au layer on the same substrate served as the reference.

SERS experiments are performed on a Horiba LabRam HR with a grating resolution of $600 \text{ lines mm}^{-1}$. The excitation source (HeNe laser, 633 nm) with an incident power of 2 mW is focused (50x, 0.5 NA) and laterally deflected within an area of $10 \times 10 \mu\text{m}^2$ to suppress photobleaching. The incident field is linearly polarized with the electric field aligned across the grating lines. The average of 16 single spectra is taken over a patterned area of $800 \times 400 \mu\text{m}^2$ for the grating pattern and $80 \times 80 \mu\text{m}^2$ for the kagome pattern in order to allow for statistical evaluation. The SERS intensities correspond to the Raman peak of the 1008 cm^{-1} vibrational mode from a self-assembled benzene-ethane-thiol monolayer obtained by 12 h immersion in a 1 mM solution.

Numerical Simulations. Ballistic Monte Carlo simulations are performed to analyze the cross section of the metal evaporation process.²⁸ Using a 2D home-made code, the trajectory and sticking of single metal particles sized 0.5 nm are simulated. Particles are impinging under normal incidence from random positions. Once a particle reaches the uppermost surface, surface diffusion of particles is modeled with a diffusion length of 2 nm in order to fill empty pores within this distance.

The far-field spectra, near-field amplitude and phase maps are calculated with a full-field numerical method based on the solution of surface integral equations (SIE).³¹ The permittivities for Si, PMMA and Cr are taken from an online database.³⁵ The refractive index of glass and HSQ are estimated with 1.5 and 1.39 respectively,³⁶ the permittivity

of Au was estimated with values from Johnson & Christy,³⁷ and the surrounding medium was air. The antenna and grating geometries are discretized using a triangular mesh with a maximum side length of 20 nm. The simulation of the grating pattern is carried out in a 3D unit cell with periodic boundary conditions along the line plane of 100 nm depth and across the line plane of 250 nm width. The substrate is glass and the resist HSQ. The polarization of the electric field is set across the lines. The simulation of the isolated and DL pattern is carried out in a quadratic lattice with a period of 500 nm and periodic boundary conditions. While isolated antennas are discretized with a triangular shape, the DL pattern is approximated with a circular shape of corresponding diameter. The substrate is glass for the SL pattern and Si for the DL pattern with PMMA as the resist. The simulation of the DL oval antennas is carried out in a quadratic lattice with a period of 500 nm and periodic boundary conditions. The polarization of the electric field is set across the short axis of the antenna.

Conflict of Interest: The authors declare no competing financial interest.

Acknowledgement. We thank the Swiss National Science Foundation (SNF) for financial support. Part of this work was performed at the Swiss Light Source, Paul Scherrer Institute, Switzerland.

Supporting Information Available: Ballistic simulation of double layer pattern with varying resist thickness, showing the control over the gap size. This material is available free of charge via the Internet at <http://pubs.acs.org>.

REFERENCES AND NOTES

1. Qian, X.; Peng, X.-H.; Ansari, D. O.; Yin-Goen, Q.; Chen, G. Z.; Shin, D. M.; Yang, L.; Young, A. N.; Wang, M. D.; Nie, S., In vivo tumor targeting and spectroscopic detection with surface-enhanced Raman nanoparticle tags. *Nat Biotech* **2008**, 26, 83-90.
2. Kneipp, K.; Wang, Y.; Kneipp, H.; Perelman, L. T.; Itzkan, I.; Dasari, R. R.; Feld, M. S., Single molecule detection using surface-enhanced Raman scattering (SERS). *Phys Rev Lett* **1997**, 78, 1667-1670.
3. Bukasov, R.; Ali, T. A.; Nordlander, P.; Shumaker-Parry, J. S., Probing the Plasmonic Near-Field of Gold Nanocrescent Antennas. *ACS Nano* **2010**, 4, 6639-6650.
4. Halas, N. J.; Lal, S.; Chang, W.-S.; Link, S.; Nordlander, P., Plasmons in Strongly Coupled Metallic Nanostructures. *Chemical Reviews (Washington, DC, United States)* **2011**, 111, 3913-3961.
5. Le, F.; Brandl, D. W.; Urzhumov, Y. A.; Wang, H.; Kundu, J.; Halas, N. J.; Aizpurua, J.; Nordlander, P., Metallic Nanoparticle Arrays: A Common Substrate for Both Surface-Enhanced Raman Scattering and Surface-Enhanced Infrared Absorption. *ACS Nano* **2008**, 2, 707-718.
6. Zuloaga, J.; Prodan, E.; Nordlander, P., Quantum Description of the Plasmon Resonances of a Nanoparticle Dimer. *Nano Lett* **2009**, 9, 887-891.
7. Siegfried, T.; Ekinici, Y.; Martin, O. J. F.; Sigg, H., Gap Plasmons and Near-Field Enhancement in Closely Packed Sub-10 nm Gap Resonators. *Nano Lett* **2013**, 13, 5449-5453.
8. Siegfried, T.; Ekinici, Y.; Solak, H. H.; Martin, O. J. F.; Sigg, H., Fabrication of Sub-10 nm Gap Arrays over Large Areas for Plasmonic Sensors. *Appl Phys Lett* **2011**, 99, 263302.
9. Duan, H.; Hu, H.; Kumar, K.; Shen, Z.; Yang, J. K. W., Direct and Reliable Patterning of Plasmonic Nanostructures with Sub-10-nm Gaps. *ACS Nano* **2011**, 5, 7593-7600.
10. Theiss, J.; Pavaskar, P.; Echternach, P. M.; Muller, R. E.; Cronin, S. B., Plasmonic Nanoparticle Arrays with Nanometer Separation for High-Performance SERS Substrates. *Nano Lett* **2010**, 10, 2749-2754.
11. Chen, X.; Park, H.-R.; Pelton, M.; Piao, X.; Lindquist, N. C.; Im, H.; Kim, Y. J.; Ahn, J. S.; Ahn, K. J.; Park, N.; Kim, D.-S.; Oh, S.-H., Atomic layer lithography of wafer-scale nanogap arrays for extreme confinement of electromagnetic waves. *Nat Commun* **2013**, 4.
12. Ye, J.; Wen, F.; Sobhani, H.; Lassiter, J. B.; Dorpe, P. V.; Nordlander, P.; Halas, N. J., Plasmonic Nanoclusters: Near Field Properties of the Fano Resonance Interrogated with SERS. *Nano Lett* **2012**, 12, 1660-1667.
13. Gallinet, B.; Siegfried, T.; Sigg, H.; Nordlander, P.; Martin, O. J. F., Plasmonic Radiance: Probing Structure at the Ångström Scale with Visible Light. *Nano Lett* **2012**, 13, 497-503.
14. Luk'yanchuk, B.; Zheludev, N. I.; Maier, S. A.; Halas, N. J.; Nordlander, P.; Giessen, H.; Chong, C. T., The Fano resonance in plasmonic nanostructures and metamaterials. *Nat Mater* **2010**, 9, 707-715.
15. Min, Q.; Pang, Y.; Collins, D. J.; Kuklev, N. A.; Gottselig, K.; Steuerman, D. W.; Gordon, R., Substrate-based platform for boosting the surface-enhanced Raman of plasmonic nanoparticles. *Opt. Express* **2011**, 19, 1648-1655.
16. Seok, T. J.; Jamshidi, A.; Kim, M.; Dhuey, S.; Lakhani, A.; Choo, H.; Schuck, P. J.; Cabrini, S.; Schwartzberg, A. M.; Bokor, J.; Yablonovitch, E.; Wu, M. C., Radiation Engineering of Optical Antennas for Maximum Field Enhancement. *Nano Lett* **2011**, 11, 2606-2610.
17. Shoute, L. C. T., Multilayer Substrate-Mediated Tuning Resonance of Plasmon and SERS EF of Nanostructured Silver. *ChemPhysChem* **2010**, 11, 2539-2545.

18. Hou, Y.; Xu, J.; Zhang, X.; Yu, D., SERS on periodic arrays of coupled quadrate-holes and squares. *Nanotechnology* **2010**, 21, 195203.
19. Ahmed, A.; Gordon, R., Directivity Enhanced Raman Spectroscopy Using Nanoantennas. *Nano Lett* **2011**, 11, 1800-1803.
20. Ahmed, A.; Gordon, R., Single Molecule Directivity Enhanced Raman Scattering using Nanoantennas. *Nano Lett* **2012**, 12, 2625-2630.
21. Zhu, W.; Wang, D.; Crozier, K. B., Direct Observation of Beamed Raman Scattering. *Nano Lett* **2012**, 12, 6235-6243.
22. Wang, D.; Zhu, W.; Chu, Y.; Crozier, K. B., High Directivity Optical Antenna Substrates for Surface Enhanced Raman Scattering. *Adv Mater* **2012**, 24, 4376-4380.
23. Chu, Y.; Zhu, W.; Wang, D.; Crozier, K. B., Beamed Raman: directional excitation and emission enhancement in a plasmonic crystal double resonance SERS substrate. *Opt. Express* **2011**, 19, 20054-20068.
24. Christ, A.; Zentgraf, T.; Tikhodeev, S. G.; Gippius, N. A.; Martin, O. J. F.; Kuhl, J.; Giessen, H., Interaction between localized and delocalized surface plasmon polariton modes in a metallic photonic crystal. *physica status solidi (b)* **2006**, 243, 2344-2348.
25. Lévêque, G.; Martin, O. J. F., Optical interactions in a plasmonic particle coupled to a metallic film. *Opt. Express* **2006**, 14, 9971-9981.
26. Natan, M. J., Concluding Remarks Surface enhanced Raman scattering. *Faraday Discussions* **2006**, 132, 321-328.
27. Li, W.-D.; Ding, F.; Hu, J.; Chou, S. Y., Three-dimensional cavity nanoantenna coupled plasmonic nanodots for ultrahigh and uniform surface-enhanced Raman scattering over large area. *Opt. Express* **2011**, 19, 3925-3936.
28. Müller-Pfeiffer, S.; van Kranenburg, H.; Lodder, J. C., A two-dimensional Monte Carlo model for thin film growth by oblique evaporation: simulation of two-component systems for the example of Co-Cr. *Thin Solid Films* **1992**, 213, 143-153.
29. Auzelyte, V.; Dais, C.; Farquet, P.; Grutzmacher, D.; Heyderman, L. J.; Luo, F.; Olliges, S.; Padeste, C.; Sahoo, P. K.; Thomson, T.; Turchanin, A.; David, C.; Solak, H. H., Extreme ultraviolet interference lithography at the Paul Scherrer Institut. *Journal of Micro/Nanolithography, MEMS and MOEMS* **2009**, 8, 021204-10.
30. Wang, L.; Terhalle, B.; Guzenko, V. A.; Farhan, A.; Hojeij, M.; Ekinici, Y., Generation of high-resolution kagome lattice structures using extreme ultraviolet interference lithography. *Appl Phys Lett* **2012**, 101, 093104-5.
31. Gallinet, B.; Kern, A. M.; Martin, O. J. F., Accurate and Versatile Modeling of Electromagnetic Scattering on Periodic Nanostructures with a Surface Integral Approach. *Journal of the Optical Society of America A: Optics and Image Science* **2010**, 27, 2261-2271.
32. Wen, X.; Xi, Z.; Jiao, X.; Yu, W.; Xue, G.; Zhang, D.; Lu, Y.; Wang, P.; Blair, S.; Ming, H., Plasmonic Coupling Effect in Ag Nanocap-Nanohole Pairs for Surface-Enhanced Raman Scattering. *Plasmonics* **2013**, 8, 225-231.
33. Päivänranta, B.; Langner, A.; Kirk, E.; David, C.; Ekinici, Y., Sub-10 nm Patterning using EUV Interference Lithography. *Nanotechnology* **2011**, 22, 375302.
34. Siegfried, T.; Ekinici, Y.; Martin, O. J. F.; Sigg, H., Engineering Metal Adhesion Layers That Do Not Deteriorate Plasmon Resonances. *ACS Nano* **2013**, 7, 2751-2757.
35. Li, X.; Hu, H.; Li, D.; Shen, Z.; Xiong, Q.; Li, S.; Fan, H. J., Ordered Array of Gold Semishells on TiO₂ Spheres: An Ultrasensitive and Recyclable SERS Substrate. *Acs Appl Mater Inter* **2012**, 4, 2180-2185.
36. Yang, C.-C.; Chen, W.-C., The Structures and Properties of Hydrogen Silsesquioxane (HSQ) Films Produced by Thermal Curing. *J Mater Chem* **2002**, 12, 1138-1141.
37. Johnson, P. B.; Christy, R. W., Optical Constants of the Noble Metals. *Phys. Rev. B* **1972**, 6, 4370-4379.

SUPPORTING INFORMATION

Metal Double Layers with Sub-10 nm Channels

Thomas Siegfried,[†] Li Wang,[‡] Yasin Ekinici,[†] Olivier J.F. Martin,[§] and Hans Sigg^{*,†}

[†]Laboratory for Micro- and Nanotechnology, Paul Scherrer Institute, 5232 Villigen-PSI, Switzerland

[‡]Eulitha AG, Switzerland

[§]Nanophotonics and Metrology Laboratory, EPFL, 1015 Lausanne,
Switzerland

AUTHOR EMAIL ADDRESS hans.sigg@psi.ch

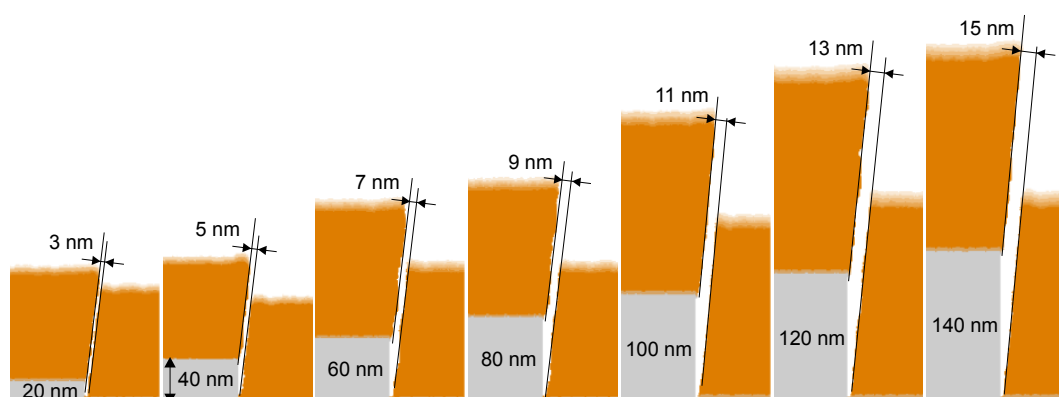


Figure S1. Ballistic simulations of the evaporated cross-section for double layer nanogap pattern of varying resist thickness. Particles movement and sticking is simulated under normal incidence evaporation conditions.

(V) Minimizing near-field damping by adhesion layers

Manuscript state

Published manuscript

Reference

T. Siegfried, Y. Ekinici, O. J. F. Martin, H. Sigg, “*Engineering Metal Adhesion Layers That Do Not Deteriorate Plasmon Resonances*”, ACS Nano **2013**, 7 (3), 2751-2757.

Publication date: 22. February 2013

DOI: 10.1021/nn4002006

URL: <http://pubs.acs.org/doi/full/10.1021/nn4002006>

Current citations: 7

Author contribution

T. Siegfried fabricated the samples. T. Siegfried performed the experiments and simulations, analyzed and concluded the data. T. Siegfried wrote the manuscript. H. Sigg and O.J.F. Martin corrected the manuscript.

Conference contribution

- T. Siegfried “*Minimizing Quenching of Plasmonic Sensors caused by Adhesion Layers*”, **oral** at CLEO **2012**, San Jose, USA
- T. Siegfried “*Intense quenching of SERS caused by Chromium adhesion layer*”, **oral** at Surface Plasmon Polariton (SPP5) in May **2011**, Busan, South Korea

Published paper + Supporting information

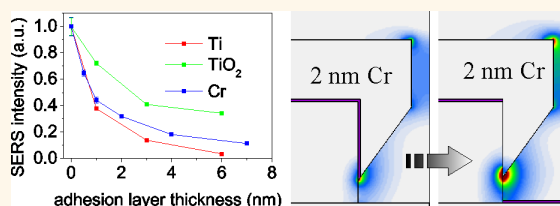
Engineering Metal Adhesion Layers That Do Not Deteriorate Plasmon Resonances

Thomas Siegfried,^{†,*} Yasin Ekinici,[†] Olivier J.F. Martin,^{*} and Hans Sigg[†]

[†]Laboratory for Micro- and Nanotechnology, Paul Scherrer Institute, 5232 Villigen-PSI, Switzerland and ^{*}Nanophotonics and Metrology Laboratory, EPFL, 1015 Lausanne, Switzerland

ABSTRACT Adhesion layers, required to stabilize metallic nanostructures, dramatically deteriorate the performances of plasmonic sensors, by severely damping the plasmon modes. In this article, we show that these detrimental effects critically depend on the overlap of the electromagnetic near-field of the resonant plasmon mode with the adhesion layer and can be minimized by careful engineering of the latter. We study the dependence of the geometrical parameters such as layer thickness and

shape on the near-field of localized plasmon resonances for traditional adhesion layers such as Cr, Ti, and TiO₂. Our experiments and simulations reveal a strong dependence of the damping on the layer thickness, in agreement with the exponential decay of the plasmon near-field. We developed a method to minimize the damping by selective deposition of thin adhesion layers (<1 nm) in a manner that prevents the layer to overlap with the hotspots of the plasmonic structure. Such a designed structure enables the use of standard Cr and Ti adhesion materials to fabricate robust plasmonic sensors without deteriorating their sensitivity.



KEYWORDS: adhesion layer · damping · surface-enhanced Raman scattering · near-field simulation · localized plasmon resonance · biosensors

Great amounts of numerical and experimental investigations have been devoted to boosting the signal of plasmonic sensors fabricated from noble metal nanoantennas with sharp edges or with gaps separated by a few nanometers.^{1–8} The field enhancement depends mainly on the ability to couple incident photons to localized surface plasmon modes. Such resonant modes are prone to damping by scattering and absorption in the metal and its surrounding materials, thus, limiting the achievable enhancement.⁹ By interference with sub-radiant modes, as in Fano resonant systems, radiative losses can be reduced, but not suppressed completely.^{10,11} In any case, the field enhancement is often severely reduced by the presence of adhesion layers. These layers are required to pin the noble metals to the substrate, particularly when the fabrication requires lift-off and sonication or when the applications demand high structural robustness.¹² Thanks to their broad availability and process compatibility with the evaporation of the noble metals, Cr and Ti are the

most commonly used adhesion materials, with typical thicknesses ranging between 1 and 10 nm.^{13–15} Although the existence of the adhesion layer is an important part of the plasmonic structure, its influence on the near and far field of the plasmonic modes is often neglected.^{9,16} The perturbation of the plasmon resonance can be derived from the real and imaginary parts of the adhesion materials dielectric function which affects the refractive index locally and introduces absorption. Under such circumstances, surface and localized surface plasmon resonances (SPR and LSPR) are red-shifted and broadened, leading to reduced signal sensitivities, caused by the reduced quality factor *Q* of the resonant mode.^{17–21} As a consequence, processes where high near-field amplitudes are needed, such as surface enhanced Raman scattering (SERS) and fluorescence,^{16,21–23} as well as particle trapping,²⁴ are weakened.

A route to reduce damping is the use of less absorptive adhesion materials such as Cr₂O₃, TiO₂,^{16,25} and ITO,²⁶ although these

* Address correspondence to thomas.siegfried@psi.ch.

Received for review January 14, 2013 and accepted February 22, 2013.

Published online February 22, 2013
10.1021/nn4002006

© 2013 American Chemical Society

oxides require more specialized preparation and equipment. Another alternative is the use of a self-assembled monolayer such as mercaptosilane, where the silane binds to oxidic surfaces and the thiol end group binds to noble metals.²⁷ The dielectric environment of the noble metal is found almost unaffected by such a monolayer, and thus, the induced plasmon resonance shift and near-field damping are minimal.^{9,21} Unfortunately, the utilization of molecular adhesion layers has severe drawbacks as it requires additional fabrication steps either in wet²¹ or dry⁹ conditions and the layers may not withstand oxygen plasma or ultraviolet ozone (UVO) cleaning steps indispensable for reusable plasmonic sensors.¹²

In this work, we systematically investigate the damping effect of adhesion layers on the near field enhancement of Au nanostructures. We provide a nanometer precise study of the thickness dependency of metal and metal oxide adhesion layers on the near- and far-field properties of plasmonic nanostructures using SERS and reflection spectroscopy. Additionally, we propose and demonstrate a method to minimize plasmon damping of adhesion layers by excluding the adhesion material from the hotspot (region with the highest near-field enhancement). We further verify for a broad range of Au grating gap sizes and adhesion layer thicknesses that damping is mostly dependent on the overlap between the near-field hotspot and the adhesion layer. Comparison with simulations provides deeper insight into the damping mechanism of adhesion layers and demonstrates how thin adhesion layers can be made without deteriorating their bonding properties. These different strategies enable the realization of plasmonic nanostructures that include metal adhesion layers and do not suffer from damping.

RESULTS AND DISCUSSION

To study the influence of adhesion layers on the performance of plasmonic structures, we utilize periodic nanogap arrays. These were fabricated in a single-step lithography and angular evaporation process. One-dimensional gratings of photoresists with various thicknesses and duty cycles were obtained reproducibly over large areas and with high throughput using extreme ultraviolet interference lithography (EUV-IL).²⁸ Hydrogen silsesquioxane (HSQ) was used as photoresist, which is converted into SiO₂ upon exposure and development. The adhesion layer and noble metal were evaporated successively onto the photoresist under glancing angles. The substrate was repeatedly tilted to the opposite angle, as shown in Figure 1a, to homogeneously cover the photoresist and controllably reduce the size of the gap.²⁹ With this technique, we fabricated nanogap patterns with variable thicknesses and gap sizes, with the cross section shown in Figure 1b.

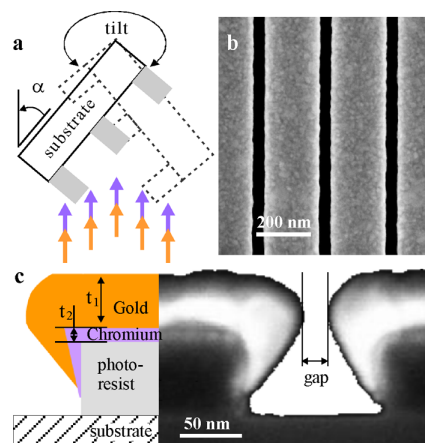


Figure 1. (a) Schematic description of the angular evaporation method, resulting in periodic nanogap arrays. (b) Top view scanning electron micrograph (SEM) and (c) schematic view and SEM of the cross section of the nanogap arrays with the adhesion and gold layers. The pattern is characterized by the gold thickness t_1 , the adhesion layer thickness t_2 and the pattern gap size. The cross section is reminiscent of a crescent.

The thus obtained nanostructures consist of an array of crescent shaped line gratings. This configuration, as we will show later, facilitates the generation of strong electromagnetic fields near the crescent tips when the incident light field couples resonantly to the gap-mode of the periodic array.¹⁰ Our nanometer precise and widely adjustable evaporation technique allowed us to study the damping effect of several adhesion layer parameters. The near-field amplitude was quantified using the SERS signal intensity. Thanks to our gentle fabrication process, adhesion layer free patterning was also possible, which we attribute to the clasping of the evaporated gold around the photoresist grating.

The far- and near-field response of our nanogap pattern are simulated for adhesion layers of various thicknesses using a 3D finite element method based on the surface integral solution of Maxwell's equations.^{30,31} The far-field spectra in reflection for increasing Cr adhesion layer thicknesses are shown in Figure 2a. The distinctive dip at 680 nm wavelength is attributed to the resonant excitation of the plasmon gap mode, similar to enhanced optical transmission (EOT).^{32,33} This resonance exhibits a red-shift with increasing Cr layer thickness, while its amplitude strongly decreases. The second reflection minimum below 500 nm is attributed to the absorbing interband transitions of gold.

At the resonance wavelength of 680 nm, localized plasmons produce a strong near-field at the metal tips of the crescent pattern, as is visible in Figure 2b. The amplitude of this hotspot near the sharp crescent tips significantly decreases for increasing adhesion layer thickness, whereas the near-field in the upper gap region seems not at all affected by the adhesion layer. This suggests that the amplitude of the near-field

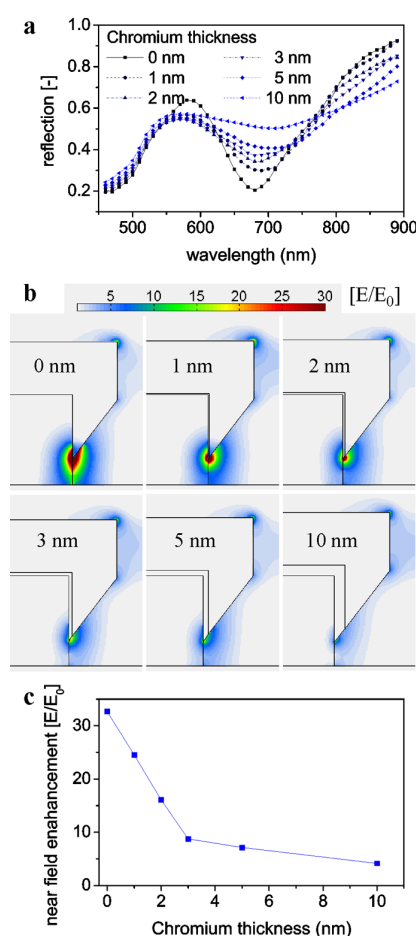


Figure 2. Simulations of the far- and near-field for increasing adhesion layer thicknesses of the crescent pattern with 50 nm Au gap and a period of 250 nm. (a) Far-field reflection spectra, (b) near-field amplitude maps of the crescent array calculated at a wavelength of 680 nm and (c) near-field enhancement, E/E_0 , within 5 nm of the crescent tips. The complex refractive indices (n , k) at a wavelength of 680 nm for the 80 nm high photoresist pattern, the Cr with thickness between 0 and 10 nm and the 50 nm Au layer were taken to be (1.39, 0), (3.07, 3.36), and (0.135, 3.88), respectively. The substrate was silicon (3.81, 0.0024). The polarization of the electric field is set across the gaps.

is locally weakened, while the plasmonic mode of the crescent pattern is nearly not altered. We will show that the origin of this phenomenon is the close contact between the electrical field at the hotspot and the adhesion layer. The dependence on the adhesion layer thickness of the damping of the electrical field at the hotspot is shown in Figure 2c. The damping increases strongly with the adhesion layer thickness, resulting in a dramatic loss of the near-field enhancement by a factor of 5 already for a 3 nm thick adhesion layer. This near-field damping on the layer thickness is congruent to what we observe in the SERS measurements, shown below.

The corresponding experiments were performed for adhesion layers made of Cr, Ti and TiO_2 . The Au was

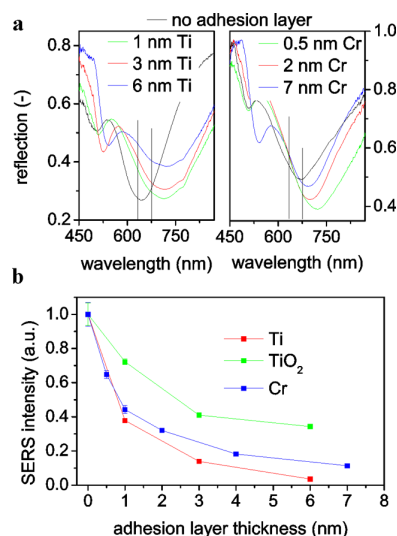


Figure 3. Dependence of the adhesion layer thickness on (a) the reflection spectra for Ti and Cr coatings and (b) the SERS intensity for Ti, TiO_2 and Cr coatings. The laser excitation wavelength at 633 nm and the recorded SERS wavelength at 676 nm, corresponding to a Raman shift of 1008 cm^{-1} , are marked in the reflection spectra. The SERS signal is recorded from a self-assembled benzene–ethane–thiol monolayer deposited on a line array of 50 nm thick Au approximately 40 nm wide gaps. The polarization of the electric field is set across the gaps. Error bars, often smaller than the icon size, represent the standard deviation for 16 spatially separated SERS measurements.

always evaporated in parallel for each sample series of varying thicknesses, to minimize the influence of metal roughness deviations. Reflection spectra are shown for Ti and Cr in Figure 3a and indicate a 70 nm resonance red-shift, independent of the Ti layer thickness, and a roughly 30 nm red-shift for Cr, slightly changing with the thickness. The resonance broadens and its amplitude decreases with increasing Ti and Cr layer thicknesses, in agreement with the simulation on Cr shown in Figure 2a. The observed blue-shift for increasing the Cr adhesion layer thickness is attributed to an Au gap size reduction of about 5 nm observed when the adhesion layer thickness is increased from 0 to 7 nm. The deviation between Ti and Cr with no adhesion layer could be attributed to a partial liftoff of the Au grating in the Cr sample, caused by weak bonding.

Figure 3b shows the SERS signal intensity dependence on the layer thickness for the three investigated adhesion materials: Ti, TiO_2 , and Cr. It is also compared to the near-field decay averaged around the full Au surface. The samples were prepared with a monolayer of benzene–ethane–thiol and were excited and measured at a wavelength of 633 and 676 nm, respectively, corresponding to a Raman shift of 1008 cm^{-1} . We observe indeed a strong reduction of the SERS intensity for adhesion layer thicknesses up to 3 nm. For thicker layers, this damping of SERS levels off,

especially for the Cr adhesion coating. To quantify the strength of the SERS damping, the evolution of the normalized intensity I/I_0 on the adhesion layer thickness is fitted with a power law of the form $(1 + x/nm)^{-a}$, where x is the adhesion layer thickness in nanometers and the exponent a describes the damping rate. An exponent of roughly 0.5 was found for TiO_2 , 1 for Cr and roughly 1.5 for Ti. Details of the fitting procedure are given in the Supporting Information, Figure S3. For an adhesion layer thickness of about 6 nm, the SERS intensity was damped by a factor of 2.5 for TiO_2 , by 10 for Cr and by 25 for Ti.

As expected, the damping is the smallest for TiO_2 , since this material has negligible absorption at this wavelength. The residual damping of $a = 0.5$ is in part attributed to an incomplete Ti oxidation during evaporation under partial oxygen pressure. The SERS damping is considerably stronger for the metals, because of their large absorption coefficients related to the complex refractive index, $n + ik$. The SERS signal can also decay because of a shift of the resonance, in which case the plasmonic mode is less effectively coupled to the external excitation.^{22,34} For Ti and TiO_2 , the induced red-shift was around 70 nm, while for Cr, we have observed a red-shift of only 30 nm, shown in Figure 3a and additionally in Figure S1 of the Supporting Information. This may explain the stronger damping of Ti despite its smaller absorption coefficient. In fact, as shown in Figure 3a, the overlap of the excitation and Raman scattering wavelength with the resonance wavelength is best for the sample without an adhesion layer and better for Cr adhesion layers compared to Ti.

The sharp decrease of SERS intensity for adhesion layer thicknesses up to about 3 nm is attributed to the spatial extension of the confined plasmons. The near-field generated by plasmons decays exponentially with the distance from the metal surface and typical decay lengths in metals are in the order of up to 10 nm.³⁵ Hence, when the adhesion material is located within this plasmon decay length, the damping is strongest. The reduced slope of SERS damping for increasing adhesion layer thicknesses mimics the exponential decay of the plasmon near-field. Conversely, when the adhesion layer remains away from any hotspot, the damping should be minimized, as will be demonstrated below.

Modeling the expected SERS damping with a power scaling of $|E/E_0|^4$, the slope of the experimentally observed SERS damping is found to be smaller compared to the computed decay of the near-field enhancement from Figure 2c. We attribute this behavior to the idealized geometry used in the computation with a point-shaped hotspot, while the real geometry is prone to roughness and corner rounding that spatially expands the hotspot region. In fact, we will demonstrate in the next paragraph that damping is avoided

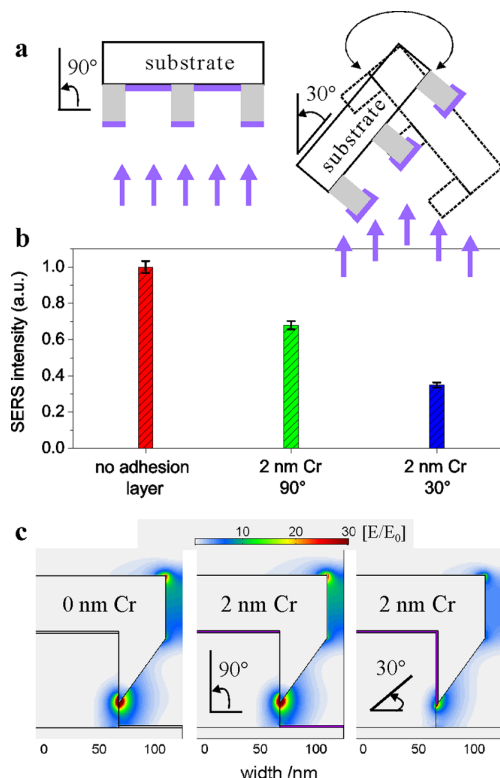


Figure 4. Comparison of SERS signals for vertically and sideward directed Cr layer deposition. (a) Sample orientation for deposition. (b) Observed SERS damping and (c) simulated near-field amplitude maps for a gold crescent array with a 0 nm Cr and 2 nm Cr adhesion layers (drawn in purple) evaporated under 90° and 30° incidence, calculated at a wavelength of 680 nm. The normalized SERS intensities correspond to the 1008 cm^{-1} peak obtained from a self-assembled benzene–ethane–thiol monolayer. The polarization of the electric field as in all other experiments is set across the gaps. Error bars represent the standard deviation for 16 spatially separated SERS measurements. The gold thickness for the periodic pattern was 50 nm and the gap size 30 nm.

when the hotspot is not in direct contact with the adhesion layer.

By changing the evaporation angle for the adhesion material, we could control the contact areas between the adhesion and the Au layers and thus were able to correlate contact area with damping. In the previously discussed experiments, the adhesion material was evaporated at the same angle of 30° at which the shadow evaporation of Au was performed. This enabled the adhesion layer to fully cover the photoresist grating, including the top and the sidewalls. Evaporating the adhesion layer under normal incidence, however, prevents material deposition on the sidewalls of the resist. In a series of experiments with 2 nm thick Cr layers evaporated under 30° and 90°, we observed that the damping of SERS intensity can indeed be strongly reduced by a factor of 2, as shown in Figure 4a.

Since the plasmonic hotspot is located at the crescent tips, as seen in Figure 2b, we attribute the strong

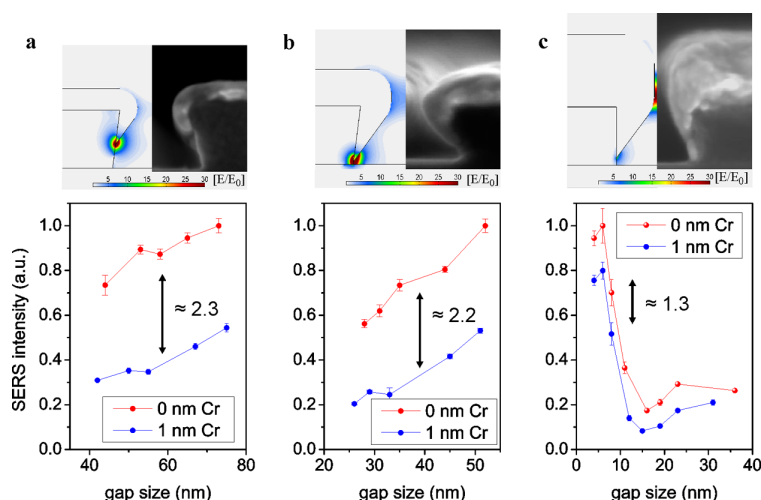


Figure 5. SERS damping for varying gap sizes and metal layer thicknesses of (a) 30 nm, (b) 50 nm, and (c) 80 nm. The Cr was evaporated under $\pm 30^\circ$ from the surface normal. Near-field amplitude maps are compared with cross section scanning electron micrograph images to relate fabrication parameters to the location of hotspots. The polarization of the electric field is set across the gaps. The normalized SERS intensities correspond to the 1008 cm^{-1} peak of a self-assembled benzene–ethane–thiol monolayer. Error bars represent the standard deviation for 16 individual SERS measurements taken at different locations on the substrate.

SERS improvement to the exclusion of the adhesion material from that tip. Simulations performed in conjunction to the experiments show the strongly reduced field (E/E_0) when the adhesion layer is located at the sidewall of the photoresist (Figure 4c, right panel) compared to the case without contact (Figure 4c, center panel). The near-fields and the plasmon resonances (not shown) for the no- and the distant adhesion layer cases are, however, very similar. Compared to the no-adhesion layer case, the average near-field enhancement (averaged over 5 nm around the hot spot) for the sidewall adhesion layer is about a factor of 3. The SERS damping is less than we would expect from the simple $|E/E_0|^4$ scaling, which we again attribute to the idealized simulation with no roughness and corner rounding. The observed SERS damping, when the adhesion layer is evaporated under 90° , is attributed to an imperfect 90° alignment of the sample during evaporation and the deposition of Cr onto the Si substrate, where it may come into contact with the hotspot, as can be seen from Figure 5b.

The simulations and experiments show that an appropriate adhesion layer design derived from the knowledge of the near-field distribution enables minimizing damping. The finding can also be extended to other nanopatterns requiring lift-off where additional underetching into the adhesion layer and the substrate can reduce the overlap of the adhesion layer with the near-field hot spot, thereby lowering damping.³⁶

In our experiments, the durability of the pattern is conserved for both evaporation angles, as long as the adhesion layer remains in contact with portions of the Au interface. This has been verified by treating the different substrates in an ultrasonic bath for several

minutes without observing any changes in the SERS intensity. Without an adhesion layer, as shown in Figure 3b, the SERS standard deviation within the tested pattern was observed to be larger than 7%, while it was well below 3% for all the other samples. Intense washing of the substrate and sonication induced a partial lift-off of the Au layer from the photoresist grating when no adhesion layer was used. Remarkably, the pattern did not lift-off for an adhesion layer thickness as thin as 0.5 nm, which was proven by consistent SERS signals for sonication times exceeding 20 min. The same pattern could also withstand several successive cleaning runs without losing the SERS enhancement.¹² For those experiments, the analyte was removed by 20 min exposure to an Ultraviolet source followed by redeposition of the analyte monolayer. These additional experiments are shown in Figure S2 of the Supporting Information.

We have validated our findings for a broader range of pattern gap sizes and metal Au thicknesses: in all cases, the overlap between the adhesion layer and the plasmons electromagnetic field is found to dominate the damping factor. We have analyzed the damping of SERS intensities for a variety of pattern gap sizes and gold thicknesses. In Figure 5, we compare the SERS signal damping between zero and 1 nm Cr layer for Au thicknesses of 30, 50, and 80 nm and for gap sizes between sub-10 and 75 nm. The gap size of the pattern was set by changing the photoresist duty cycle.

The SERS damping was found to be independent of the nanogap size but depends on the thickness of the Au layer. For Au thicknesses between 30 and 50 nm, the damping is roughly 2.2, while it is 1.3 for 80 nm. This behavior is congruent with simulations showing that

the position of the hotspot does not depend on the gap size but changes its locations from the tip to the nanogap region when the Au thickness becomes larger than about 70 nm, *cf.* comparison between Figure 5a and 5b to 5c. The damping rate of 1.3 is smaller due to the reduced overlap of adhesion layer and hotspot. For the 80 nm thick Au layers and gap sizes below 15 nm, the SERS intensity increases strongly due to stronger coupling between the crescents forming a nanogap channel.²⁹

CONCLUSION

We have systematically investigated the geometric constraints associated with adhesion layers such as thickness and overlap with the hotspots and found a route to minimize the near-field damping of localized plasmon resonances. The near-field damping has been quantified by simulations and SERS experiments. The damping has been attributed to the absorption in the adhesion layer, leading to the reduction of the field amplitude, broadening and red shifting up to 70 nm of the resonance wavelength. We find that adhesion

layers with a thickness well below 1 nm maintain their adhesive properties, while significantly reducing the damping of the SERS intensity. Outstandingly, the exclusion of the adhesion layer from the proximity of the near-field hotspot reduces damping to a level that was previously only obtained by using metal oxides or monolayers of self-assembled mercaptosilanes. Hence, near-field simulations to locate the hotspots precisely and correspondingly adapted evaporation schemes or underetching of metal adhesion layers into the substrate are the key to realize plasmonic nanostructures with negligible impact on the plasmon resonances. This finding can also be extended to other nanopatterns requiring lift-off, where additional underetching into the adhesion layer and substrate can reduce the overlap of the adhesion layer with the near-field hotspot thereby lowering damping.³⁶

To conclude, we could demonstrate that traditional metal adhesion layers with a thickness below 1 nm and deposited with minimal contact to the near-field hotspots produce robust plasmonic nanostructures without deteriorating their performance.

METHODS

Fabrication of Nanogap Arrays. Extreme ultraviolet interference lithography at the Swiss Light Source²⁸ was used to create line patterns with a period of 250 nm and a height of 80 nm over an area of 1 mm² using hydrogen silsesquioxane (HSQ) resist. Glancing angular deposition³⁷ was used to thermally evaporate the adhesion material and subsequently Au (99.99% purity, purchased from Balzers) layer directly onto the photoresist at a base pressure of 2×10^{-6} mbar. The substrate was aligned at an angle of 30° from the surface plane with an azimuthal orientation of the line pattern perpendicular to the gap expansion (Figure 1a). During evaporation, the substrate was tilted to the mirrored direction (−30°) after every deposited 2 nm, until the final thickness was reached. The adhesion materials Cr and Ti (both 99.99% purity, purchased from Sigma Aldrich) were evaporated at the same angle (30°/−30°) as is the Au or, when specified, evaporation has taken place under normal incidence. TiO₂ was evaporated using the Ti source at a partial oxygen pressure of 5 mbar. The Au was evaporated in parallel for the investigation of sample sequences with varying adhesion layer parameter, to help the accuracy of the evaluation and minimize the influence of metal roughness deviations. The gap size was set by the duty cycle of the photoresist pattern while keeping the evaporated thickness constant. Further details on the fabrication process of the sub-20 nm gap pattern have been reported elsewhere.²⁹ The adhesion layers were deposited accurately (nm precision of thickness) by placing a quartz balance sensor close to the evaporation source. Thereby, the monitored thickness had to be scaled by 1/3 to factor in the $t \sim x^2$ dependency of the layer thickness t compared to the distance x from the evaporation source.

Optical Measurements. Reflection spectra were recorded with a spatial resolution of about 10 μm using a commercial spectrometer (Sentech FTP) flanged to a microscope (Leica). The incident light was polarized such that the electric field was aligned across the nanogaps. The reflection spectrum obtained from the continuous Au layer on the same substrate served as reference.

The surface-enhanced Raman scattering experiments were performed on a Horiba LabRam HR with a grating resolution of 600 lines mm^{−1}. The excitation source (HeNe laser, 633 nm) with an incident power of 2 mW was focused (50 \times , numerical

aperture NA 0.5) and laterally deflected within an area of $10 \times 10 \mu\text{m}^2$ of the nanogap pattern to suppress photobleaching. The incident light was linearly polarized with the electric field aligned across the gaps. The average of 16 single spectra was taken over a patterned area of $300 \times 300 \mu\text{m}^2$ in order to allow for statistical evaluation. The SERS intensities depicted in all figures correspond to the Raman peak of the 1008 cm^{−1} vibrational mode from a self-assembled benzene–ethane–thiol monolayer obtained by 12 h immersion in a 1 mM solution.

Numerical Simulation. The far-field spectra and near-field maps were calculated with a full-field numerical method based on the solution of the surface integral.³⁰ The simulation of the crescent grating array was carried out in a 3D unit cell with periodic boundary conditions along and across the gap plane. The polarization of the electric field was set across the gap axis. The permittivities for the Si substrate and Cr were approximated with bulk values taken from SOPRA;³⁸ it is however noted that bulk values can become unreliable for nanometer layer thicknesses. The refractive index of the photoresist HSQ was assumed to be 1.39;³⁹ the permittivity of Au was taken from Johnson and Christy,⁴⁰ and the surrounding medium was air.

Conflict of Interest: The authors declare no competing financial interest.

Acknowledgment. We thank the Swiss National Science Foundation (SNF) for financial support. Part of this work was performed at the Swiss Light Source (SLS), Paul Scherrer Institute, Switzerland.

Supporting Information Available: Cr and TiO₂ reflection spectra; the pattern SERS stability against sonication and UV cleaning; details of the SERS fitting procedure. This material is available free of charge via the Internet at <http://pubs.acs.org>.

REFERENCES AND NOTES

- Cialla, D.; März, A.; Böhme, R.; Theil, F.; Weber, K.; Schmitt, M.; Popp, J. Surface-Enhanced Raman Spectroscopy (SERS): Progress and Trends. *Anal. Bioanal. Chem.* **2012**, *403*, 27–54.
- Biagioni, P.; Huang, J.-S.; Hecht, B. Nanoantennas for Visible and Infrared Radiation. *Rep. Prog. Phys.* **2012**, *75*, 024402.

3. Zuloaga, J.; Prodan, E.; Nordlander, P. Quantum Description of the Plasmon Resonances of a Nanoparticle Dimer. *Nano Lett.* **2009**, *9*, 887–891.
4. Duan, H.; Hu, H.; Kumar, K.; Shen, Z.; Yang, J. K. W. Direct and Reliable Patterning of Plasmonic Nanostructures with Sub-10-nm Gaps. *ACS Nano* **2011**, *5*, 7593–7600.
5. Feichtner, T.; Selig, O.; Kiunke, M.; Hecht, B. Evolutionary Optimization of Optical Antennas. *Phys. Rev. Lett.* **2012**, *109*, 127701.
6. Lindquist, N. C.; Nagpal, P.; McPeak, K. M.; Norris, D. J.; Oh, S.-H. Engineering Metallic Nanostructures for Plasmonics and Nanophotonics. *Rep. Prog. Phys.* **2012**, *75*, 036501.
7. Lindquist, N. C.; Nagpal, P.; Lesuffleur, A.; Norris, D. J.; Oh, S.-H. Three-Dimensional Plasmonic Nanofocusing. *Nano Lett.* **2010**, *10*, 1369–1373.
8. Nagpal, P.; Lindquist, N. C.; Oh, S.-H.; Norris, D. J. Ultra-smooth Patterned Metals for Plasmonics and Metamaterials. *Science* **2009**, *325*, 594–597.
9. Habteyes, T. G.; Dhuey, S.; Wood, E.; Gargas, D.; Cabrini, S.; Schuck, P. J.; Alivisatos, A. P.; Leone, S. R. Metallic Adhesion Layer Induced Plasmon Damping and Molecular Linker as a Nondamping Alternative. *ACS Nano* **2012**, *6*, 5702–5709.
10. Gallinet, B.; Siegfried, T.; Sigg, H.; Nordlander, P.; Martin, O. J. F. Plasmonic Radiance: Probing Structure at the Ångström Scale with Visible Light. *Nano Lett.* **2012**, *13*, 497–503.
11. Ye, J.; Wen, F.; Sobhani, H.; Lassiter, J. B.; Dorpe, P. V.; Nordlander, P.; Halas, N. J. Plasmonic Nanoclusters: Near Field Properties of the Fano Resonance Interrogated with SERS. *Nano Lett.* **2012**, *12*, 1660–1667.
12. Siegfried, T.; Kind, M.; Terfort, A.; Martin, O. J. F.; Zharnikov, M.; Ballav, N.; Sigg, H. Reusable Plasmonic Substrates Fabricated by Interference Lithography: a Platform for Systematic Sensing Studies. *J. Raman Spectrosc.* **2012**, *44*, 170–175.
13. Abdelsalam, M.; Bartlett, P. N.; Russell, A. E.; Baumberg, J. J.; Calvo, E. J.; Tognalli, N. G.; Fainstein, A. Quantitative Electrochemical SERS of Flavon at a Structured Silver Surface. *Langmuir* **2008**, *24*, 7018–7023.
14. Fromm, D. P.; Sundaramurthy, A.; Schuck, P. J.; Kino, G.; Moerner, W. E. Gap-Dependent Optical Coupling of Single Bowtie Nanoantennas Resonant in the Visible. *Nano Lett.* **2004**, *4*, 957–961.
15. Cui, B.; Clime, L.; Li, K.; Veres, B. Fabrication of Large Area Nanoprism Arrays and their Application for Surface Enhanced Raman Spectroscopy. *Nanotechnology* **2008**, *19*, 145302.
16. Aouani, H.; Wenger, J.; Gérard, D.; Rigneault, H.; Devaux, E.; Ebbesen, T. W.; Mahdavi, F.; Xu, T.; Blair, S. Crucial Role of the Adhesion Layer on the Plasmonic Fluorescence Enhancement. *ACS Nano* **2009**, *3*, 2043–2048.
17. Barchiesi, D.; Macías, D.; Belmar-Letellier, L.; van Labeke, D.; Lamy de la Chapelle, M.; Toury, T.; Kremer, E.; Moreau, L.; Grosge, T. Plasmonics: Influence of the Intermediate (or Stick) Layer on the Efficiency of Sensors. *Appl. Phys. B: Lasers Opt.* **2008**, *93*, 177–181.
18. Najiminaini, M.; Vasefi, F.; Kaminska, B.; Carson, J. J. L. Optical Resonance Transmission Properties of Nano-Hole Arrays in a Gold Film: Effect of Adhesion Layer. *Opt. Express* **2011**, *19*, 26186–26197.
19. Sexton, B. A.; Feltis, B. N.; Davis, T. J. Characterisation of Gold Surface Plasmon Resonance Sensor Substrates. *Sens. Actuators, A* **2008**, *141*, 471–475.
20. Lahiri, B.; Dylewicz, R.; De La Rue, R. M.; Johnson, N. P. Impact of Titanium Adhesion Layers on the Response of Arrays of Metallic Split-Ring Resonators (SRRs). *Opt. Express* **2010**, *18*, 11202–11208.
21. Lamy de la Chapelle, M.; Shen, H.; Guillot, N.; Frémaux, B.; Guelorget, B.; Toury, T. New Gold Nanoparticles Adhesion Process Opening the Way of Improved and Highly Sensitive Plasmonics Technologies. *Plasmonics* **2012**, 1–5.
22. Kern, A. M.; Meixner, A. J.; Martin, O. J. F. Molecule-Dependent Plasmonic Enhancement of Fluorescence and Raman Scattering near Realistic Nanostructures. *ACS Nano* **2012**, *6*, 9828–9836.
23. Djaker, N.; Hostein, R.; Devaux, E.; Ebbesen, T. W.; Rigneault, H.; Wenger, J. Surface Enhanced Raman Scattering on a Single Nanometric Aperture. *J. Phys. Chem. C* **2010**, *114*, 16250–16256.
24. Roxworthy, B. J.; Toussaint, K. C. Plasmonic Nanotweezers: Strong Influence of Adhesion Layer and Nanostructure Orientation on Trapping Performance. *Opt. Express* **2012**, *20*, 9591–9603.
25. Jiao, X.; Goeckeritz, J.; Blair, S. Oldham, M., Localization of Near-Field Resonances in Bowtie Antennae: Influence of Adhesion Layers. *Plasmonics* **2009**, *4*, 37–50.
26. Jeppesen, C.; Mortensen, N. A.; Kristensen, A. The Effect of Ti and ITO Adhesion Layers on Gold Split-ring Resonators. *Appl. Phys. Lett.* **2010**, *97*, 263103.
27. Goss, C. A.; Charych, D. H.; Majda, M. Application of (3-Mercaptopropyl)trimethoxysilane as a Molecular Adhesive in the Fabrication of Vapor-Deposited Gold Electrodes on Glass Substrates. *Anal. Chem.* **1991**, *63*, 85–88.
28. Päivänranta, B.; Langner, A.; Kirk, E.; David, C.; Ekinci, Y. Sub-10 nm Patterning using EUV Interference Lithography. *Nanotechnology* **2011**, *22*, 375302.
29. Siegfried, T.; Ekinci, Y.; Solak, H. H.; Martin, O. J. F.; Sigg, H. Fabrication of Sub-10 nm Gap Arrays over Large Areas for Plasmonic Sensors. *Appl. Phys. Lett.* **2011**, *99*, 263302.
30. Gallinet, B.; Kern, A. M.; Martin, O. J. F. Accurate and Versatile Modeling of Electromagnetic Scattering on Periodic Nanostructures with a Surface Integral Approach. *J. Opt. Soc. Am. A* **2010**, *27*, 2261–2271.
31. Gallinet, B.; Martin, O. J. F. Scattering on Plasmonic Nanostructures Arrays Modeled with a Surface Integral Formulation. *Photonics Nanostruct. Fundam. Appl.* **2010**, *8*, 278–284.
32. Ebbesen, T. W.; Lezec, H. J.; Ghaemi, H. F.; Thio, T.; Wolff, P. A. Extraordinary Optical Transmission through Sub-wavelength Hole Arrays. *Nature* **1998**, *391*, 667–669.
33. Wu, S.; Wang, Q.-j.; Yin, X.-g.; Li, J.-q.; Zhu, D.; Liu, S.-q.; Zhu, Y.-y. Enhanced Optical Transmission: Role of the Localized Surface Plasmon. *Appl. Phys. Lett.* **2008**, *93*, 101113.
34. McFarland, A. D.; Young, M. A.; Dieringer, J. A.; Van Duyne, R. P. Wavelength-Scanned Surface-Enhanced Raman Excitation Spectroscopy. *J. Phys. Chem. B* **2005**, *109*, 11279–11285.
35. Barnes, W. L.; Dereux, A.; Ebbesen, T. W. Surface Plasmon Subwavelength Optics. *Nature* **2003**, *424*, 824–830.
36. Otte, M. A.; Estavez, M. C.; Carrascosa, L. G.; Gonzalez-Guerrero, A. B.; Lechuga, L. M.; Sepalveda, B. Improved Biosensing Capability with Novel Suspended Nanodisks. *J. Phys. Chem. C* **2011**, *115*, 5344–5351.
37. Abelmann, L.; Lodder, C. Oblique Evaporation and Surface Diffusion. *Thin Solid Films* **1997**, *305*, 1–21.
38. Sopra, refraction indices database. www.refractiveindex.info.
39. Yang, C.-C.; Chen, W.-C. The Structures and Properties of Hydrogen Silsesquioxane (HSQ) Films Produced by Thermal Curing. *J. Mater. Chem.* **2002**, *12*, 1138–1141.
40. Johnson, P. B.; Christy, R. W. Optical Constants of the Noble Metals. *Phys. Rev. B* **1972**, *6*, 4370–4379.

Supporting Information to the Manuscript

Engineering Metal Adhesion Layers that Do Not Deteriorate Plasmon Resonances

Thomas Siegfried^{†}, Yasin Ekinci[†], Olivier J.F. Martin[§], and Hans Sigg[†]*

[†]Laboratory for Micro- and Nanotechnology, Paul Scherrer Institut, 5232 Villigen-PSI, Switzerland,

[§]Nanophotonics and Metrology Laboratory, EPFL, 1015 Lausanne, Switzerland

AUTHOR EMAIL ADDRESS thomas.siegfried@psi.ch

In analogy with Fig. 3a of the manuscript, the reflection spectra for varying adhesion layer thicknesses are shown in Fig. S1 for other adhesion materials: Cr and TiO₂. The plasmon resonance, seen as a dip around 650 nm, is red-shifted by about 60 nm when introducing TiO₂ adhesion layers and this shift is constant for different layer thicknesses. Note that the small dips around 530 nm are artifacts from referencing the spectra with the reflection from an unpatterned Au area of the same substrate.

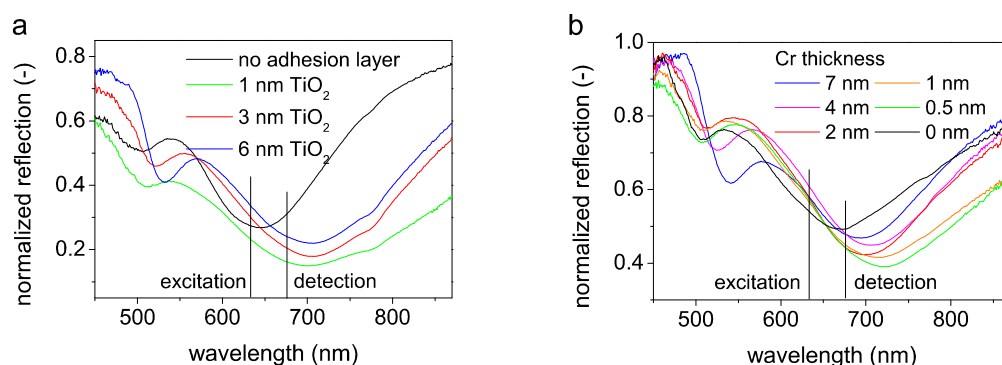


Figure S1. Reflection spectra for Au nanogap arrays with increasing adhesion layer thickness. **a** For TiO_2 and **b** for Cr as adhesion material. The Au thickness of both periodic patterns was 50 nm and the Au gap size was 40 nm. The Raman excitation wavelength at 633 nm and the detection SERS wavelength at 676 nm, corresponding to a wavelength shift of 1008 cm^{-1} , are indicated in the graphs.

The magnitude of the resonance decreases for increasing adhesion layer thicknesses, similar to Fig. 3a with Ti as adhesion material. When Cr is used as adhesion layer, the red-shift is reduced to about 30 nm together with a reduction of the resonance magnitude for increasing adhesion layer thicknesses. Additionally the resonance position slightly blue-shifts for increasing adhesion layer thicknesses. This blue-shift is attributed to an induced Au gap size reduction of about 5 nm when the adhesion layer thickness is increased from 0 nm to 7 nm.

The pattern stability with a 0.5 nm thick only Cr adhesion layer is shown in Fig. S2. Sonication is applied as well as ultraviolet ozone cleaning to remove the adsorbed molecules at the gold interface.

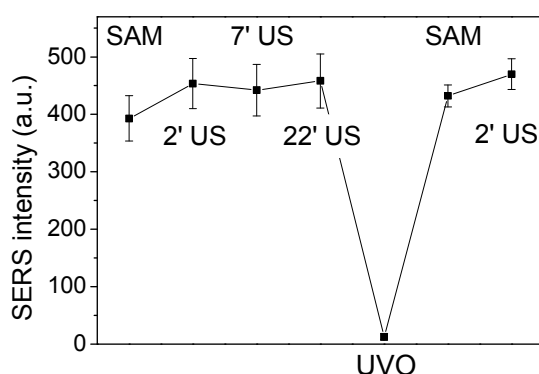


Figure S2. Pattern stabilized by a 0.5 nm thick Cr adhesion layer evaporated under 90°. The SERS intensity is measured after several exposures to an ethanol ultrasonic bath (US) and for one cycle of cleaning and reforming the benzene-ethane-thiol monolayer. The substrate was cleaned by 20 min ultraviolet ozone exposure (UVO) and repeated rinsing in ethanol. The thiol monolayer was formed during 1 h in a 5 mM benzene-ethane-thiol solution followed by ethanol rinsing (SAM). The Au thickness of the periodic pattern was 50 nm and the Au gap size was 40 nm. The normalized SERS intensities correspond to the 1008 cm^{-1} peak of a self assembled benzene-ethane-thiol monolayer. Error bars represent the standard deviation for 16 spatially separated SERS measurements.

The SERS intensity was found unchanged after sonication time of for up to 22 minutes. Moreover, the sensor could be cleaned and reused without losing SERS enhancement. Without the adhesion layer, the Au wire grating partially lifted off from the photoresist pattern and the SERS intensity became strongly irreproducible.

The fitting parameters for the damping rates of varying adhesion layer thicknesses are given in Fig. S3. All SERS measurements were normalized to the SERS intensity at 0 nm adhesion layer thickness. Excellent agreement of the fitted curve with the experimental data was found for Cr and Ti, as well as

for TiO₂.

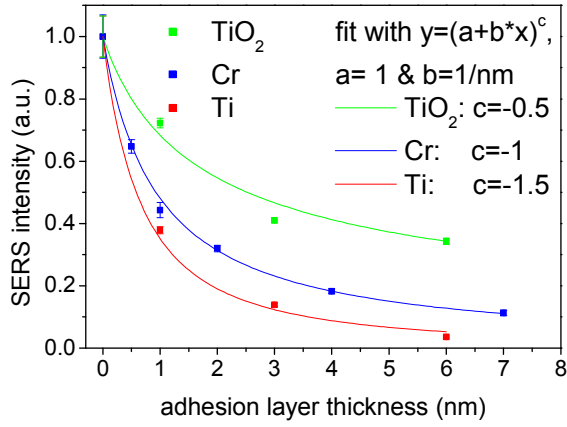


Figure S3. SERS intensity for Titanium, Titanium oxide and Chromium as adhesion material. The experimental data are fitted with the power law dependence $(1+x/\text{nm})^{-a}$, where x is the layer thickness in nm and a the exponent describing the damping. a was fitted with 0.5 for TiO₂, 1 for Cr and 1.5 for Ti. The normalized intensities correspond to the 1008 cm⁻¹ Raman peak of a self-assembled benzene-ethane-thiol monolayer. Error bars represent the standard deviation of 16 spatially separated SERS measurements. The gold thickness for the periodic pattern was 50 nm and the gap size was 40 nm.

(VI) Cavity controlled SERS tuning with layered crescent arrays

Manuscript state

Submitted manuscript

Reference

S. Dutta-Gupta*, T. Siegfried*, Y. Ekinici, H. Sigg, O. J. F. Martin “*Cavity-Controlled Perfect Absorption in Plasmonic Crescent Arrays Can Command the Raman Enhancement*”.

*equal contribution

Submission date: 12.02.2014

Author contribution

T. Siegfried fabricated the samples. T. Siegfried and S. Dutta-Gupta performed the experiments and simulations. T. Siegfried and S. Dutta-Gupta analyzed and concluded the data. S. Dutta-Gupta wrote the manuscript draft. S. Dutta-Gupta and T. Siegfried wrote the final manuscript and made the figures. H. Sigg and O.J.F. Martin corrected the manuscript.

Submitted paper + Supporting information

Cavity-Controlled Perfect Absorption in Plasmonic Crescent Arrays Can Command the Raman Enhancement

Shourya Dutta-Gupta,^{§,¶} Thomas Siegfried,^{†,¶} Yasin Ekinci,[†] Hans Sigg,[†] and Olivier J. F. Martin^{§,*}

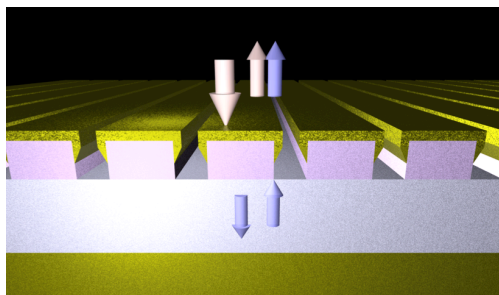
[§]Nanophotonics and Metrology Laboratory, EPFL, 1015 Lausanne, Switzerland

[†]Laboratory for Micro- and Nanotechnology, Paul Scherrer Institut, 5232 Villigen-PSI, Switzerland

[¶]Authors contributed equally

*Correspondence to: olivier.martin@epfl.ch

ABSTRACT Plasmonic substrates incorporating nanostructured metal layers have been successfully exploited for enhancing the SERS signals from analyte molecules. Large signals are obtained when the near-field of the plasmonic structure is strongly enhanced as well as efficiently coupled to the incident light. However, in most structures the coupling between the incident light and the near-field is not optimal because the fabrication parameters, such as the size or the gap of the nanostructures, have to be controlled in the order of a few nanometers. Here, we demonstrate a generic method to obtain optimally performing SERS substrates tunable over a broad spectral range, without the need to modify the plasmonic pattern. Our design



consists of a plasmonic crescent array placed on top of a spacer with a reflecting layer underneath. Together, the plasmonic structure and the reflecting layer form a Fabry-Perot cavity. Appropriate control of the reflectivity at the SERS excitation and emission wavelengths is demonstrated via tuning the spacer thickness (i.e. the cavity length), and the gap of the crescent array. With this, the SERS signal is modulated by a factor in excess of 20. The experimentally obtained SERS intensities demonstrate the optimal SERS operation regime when it is plotted against the reflectance at both the excitation and emission wavelengths. This layered plasmonic structure is capable of angle dependent tuning of the resonance, offering additional control for optimization in practical applications without having to modify the plasmonic substrate at all.

KEYWORDS: Plasmonics, perfect absorption, cavity tuning, SERS, interference, critical coupling, crescent array.

Plasmonic substrates with nanostructures have been successfully exploited for a wide variety of applications in the past few decades.¹⁻³ Local field enhancement in such structures is the key to improve the signals in processes like surface enhanced Raman scattering (SERS),⁴⁻¹¹ infrared absorption (SEIRA)¹²⁻¹⁴ and fluorescence (SEF).¹⁵⁻¹⁸ More specifically, the enhancement obtained in SERS can be as high as 10^9 allowing the detection of single molecules located in the hotspots.⁸⁻¹¹ In spite of the high signal intensities, the major drawback of SERS evolving from isolated nanostructures is their lack of reproducibility, rendering practical applications less feasible.⁵ Therefore, ample emphasis has been placed towards the development of large area and uniform SERS substrates which do not suffer from similar limitations.⁶ Examples of such techniques include extreme UV lithography, nanosphere lithography and nanoimprint lithography that have been optimized for the fabrication of wafer scale SERS substrates.^{6, 19-21}

Yet, in realistic situations only part of the incident light is coupled into the near-field of the plasmonic structures, which limits the total SERS enhancement.²² To improve the coupling to light, a generic approach is demonstrated for transforming array-based SERS substrates into perfect absorbers of incident light, leading to an optimized SERS performance. This is achieved by exploiting a critical coupling configuration where a dielectric spacer with a

reflective layer is used as the underlying substrate.²³⁻²⁸ Such critical coupling structures have been used for making perfectly absorbing substrates with just a 5 nm thick absorbing layer.²⁷ In our critical coupling configuration, the reflective layer ensures zero transmission of light and the spacer with an appropriate thickness enables complete destructive interference amongst the different reflected planewaves from the various interfaces. Thus, when the reflection and the transmission are simultaneously zero, all the incident light must be absorbed by the structure. Although alternative ways of developing plasmonic perfect absorbers exist, for example via near-field coupling, such methods result in the formation of hybridized plasmon modes, which make the control of the resonance positions difficult without altering the structure.^{23, 29}

We will show, that the interference in these plasmonic crescent arrays can be controlled using either the gap of the array, which modifies the complex transmission and reflection coefficients,³⁰ or the spacer thickness, which controls the phase difference between the planewaves propagating forth and back in the cavity. We also relate the SERS enhancement to the planewave reflectivity at the laser excitation and Raman shifted wavelengths and illustrate the dispersive character of the resonance of the composite structure.

MATERIALS AND METHODS

Numerical simulation. The far-field spectra and the near-field amplitude are calculated with a full-field numerical method based on the solution of surface integrals.³¹ The crescent arrays and the layered substrate are simulated in a 3D unit cell with periodic boundary conditions along and across the gap plane. A triangular mesh with a maximum side length of 10 nm is used to discretize one crescent. The polarization of the electric field is set across the gap. The reflecting layer is made of gold and the spacing layer is glass. The refractive index of the glass and the HSQ photoresist is estimated with 1.5 and 1.39 respectively. The dielectric function of gold used in the simulations is taken from Johnson and Christy.³² The refractive index of the surrounding medium is 1 (air).

Fabrication of the crescent arrays. Line array patterns with a period of 250 nm are obtained by extreme ultraviolet interference (EUV) lithography in an 80 nm thick hydrogen silsesquioxane (HSQ) film and over an area of $0.6 \times 1.8 \text{ mm}^2$. HSQ is developed in 25% tetra methyl ammonium hydroxide (TMAH) for 60 s. Gold (Balzers, 99.99 % purity) is thermally evaporated on HSQ at a glancing angle of 60° from the surface normal. The substrate is aligned at an azimuthal orientation of the line array perpendicular to the gap expansion. The substrate is repeatedly tilted to the opposite direction ($\pm 60^\circ$) after every 2 nm of evaporated metal. The crescent spacing is set by the resist duty cycle, which is controlled by the EUV exposure time.

Reflection measurement. The normal incidence reflection measurements were performed using an inverted optical microscope (Olympus IX-71) coupled to a spectrometer (Jobin Yvon Horiba Triax 550). The sample was illuminated using a halogen light source focused onto the sample using a 20x objective (NA 0.2). The illumination was such that the angle of incidence was below 2° . The reflected light was collected using the same objective and analyzed using a spectrometer. The reflected intensity was normalized to the reflection from a silver mirror. Reflectivity as a function of wavelength and incidence angle was measured using a home-made prism-based setup as described by Farhang *et al.*³³ Again, the spectrally resolved reflected intensity was normalized with the reflectivity of a silver film (thickness 100 nm).

Raman measurement. Surface enhanced Raman scattering is measured at an excitation wavelength of 633 nm on samples coated with a self assembled benzene-ethane-thiol (BET) monolayer, formed during 12 h immersion in a 1 mM solution. The reported SERS intensities relate to the Raman peak intensity at the 1008 cm^{-1} vibrational mode of BET. Raman peak intensities from alternative modes are noted in the text. We use a Horiba LabRam HR instrument with a spectral resolution of 1 cm^{-1} . An incident power of 2 mW is focused (50x, numerical aperture NA 0.5) and deflected within an area of $10 \times 10 \text{ }\mu\text{m}^2$ to minimize photobleaching. 16 spectra were taken over an area of $300 \times 800 \text{ }\mu\text{m}^2$ for signal averaging and the calculation of signal deviation.

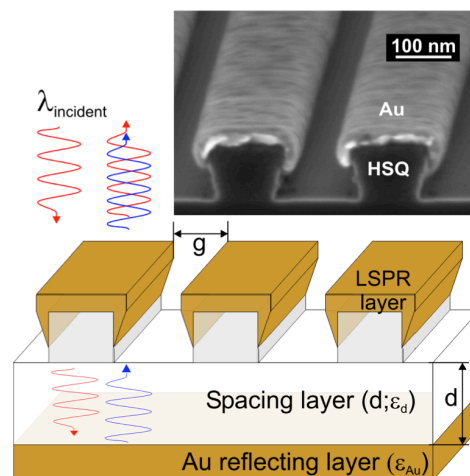


Figure 1. Schematic of the layered geometry. The structure is defined by a spacer layer with thickness d , and a crescent layer with a gap g . The inset shows a SEM image of an isolated crescent array.

RESULTS AND DISCUSSION

A schematic illustration and a representative SEM image of the fabricated structure used to demonstrate perfect absorption of light for SERS substrates are shown in Fig. 1. The structure consists of a periodic crescent array (period 250 nm, thickness 30 nm and gap size g 10 nm - 70 nm) placed on top of a spacer (thickness d = 100 nm - 700 nm) and a reflective gold layer (thickness 70 nm). The crescent array is fabricated using EUV lithography followed by angular evaporation, with details given in the experimental section and published elsewhere.^{6, 19} A chromium adhesion layer is applied between all layers to ensure the structure's stability. Near-field damping by the chromium is suppressed by a minimal layer thickness of 1 nm evaporated at normal incidence to avoid direct contact with the plasmonic near-field hot spot.³⁴

When the structure is illuminated with a planewave at normal incidence, the 70 nm thick reflective layer ensures near zero transmission over the here employed spectral range. The reflectivity from the layered structure, as is known for a multilayer Fabry Perot (FP) cavity, is governed by constructive or destructive interference between the various planewaves reflected from the different interfaces. As compared to a standard FP cavity, our system is complicated due to the presence of the resonant plasmonic crescent layer, which adds a phase shift that modifies the spectral position of destructive interference. This additional phase shift can take values between 0 and π depending on the spectral overlap of the standard FP cavity and the plasmon resonance.

The interference is thus controlled by the thickness of the spacer, *and* the gap and the thickness of the crescent array. In this manner it is possible to choose a set of system parameters that achieve perfect destructive interference of the reflected planewaves at a given wavelength. At this wavelength all the incident energy is absorbed by the

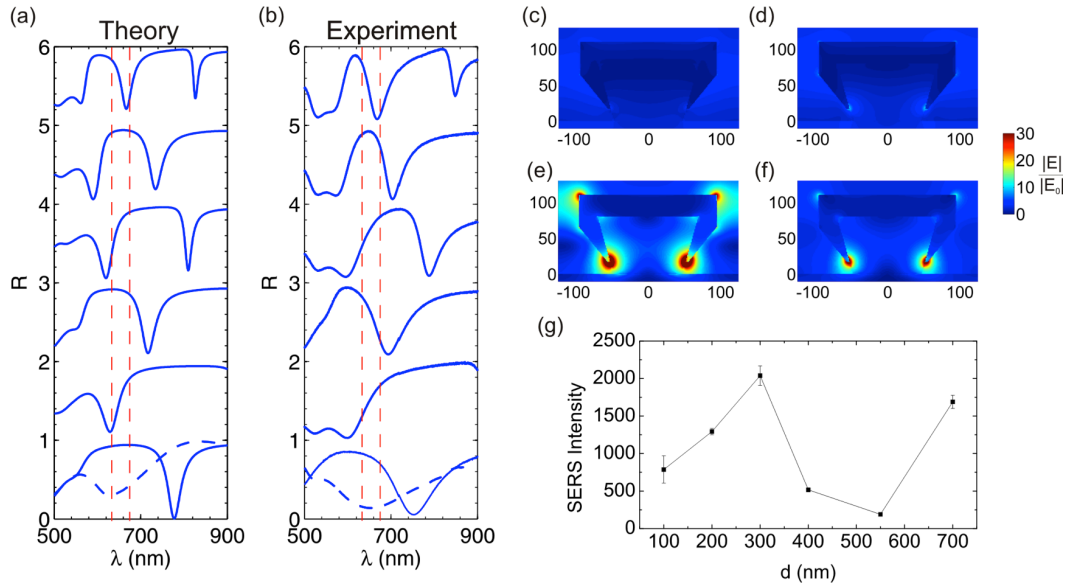


Figure 2. (a) Simulated and (b) experimentally measured reflection spectra for normal incidence for a crescent gap size of $g = 62$ nm and various spacer thicknesses d (from bottom to top: 100 nm, 200 nm, 300 nm, 400 nm, 550 nm and 700 nm). The dashed lines show the response of crescent arrays placed on top of a glass substrate without a reflecting layer underneath. (c) - (f) Near-field amplitude enhancement plotted in the x-y plane for a structure with $g = 62$ nm at $\lambda = 633$ nm and $\lambda = 676$ nm. Spacer thickness is $d = 100$ nm ((c) and (d)), and $d = 200$ nm ((e) and (f)), respectively. (g) SERS intensity variation as a function of the spacer thickness d for a structure with $g = 62$ nm.

plasmonic pattern and the continuous layer underneath as dictated by energy conservation, i.e. $A = I - R - T$. If such a reflection minimum coincides with the plasmon resonance, the energy of the incident wave will be absorbed largely by the plasmonic structure yielding strong enhancement at its hotspot. In the following we refer to the resonance of the complete structure, formed by the coupling of the FP cavity and the plasmonic crescent resonance, unless otherwise mentioned.

Figures 2 (a) and (b) show the numerically calculated and experimentally measured reflection spectra from crescent arrays without the underlying reflecting layer (dashed lines) and from arrays with varying spacer thicknesses from $d = 100$ nm to 700 nm. The structures are illuminated by a planewave at normal incidence, which is polarized across the gap of the crescent array. We only chose spacer thicknesses larger than 100 nm, thus preventing the formation of new hybridized plasmon modes by coupling to image charges in the subjacent gold layer.^{35, 36}

Numerical simulations were performed using a periodic surface integral equation method with structural dimensions as extracted from SEM analyzes of the fabricated patterns.³¹ The reflection spectra of the crescent array without the reflecting layer shows a broad reflection minimum, which we associated with the fundamental plasmon mode of the crescents. The minimum originates from the destructive interference between the directly reflected light and the light scattered by this resonant mode, as demonstrated by Gallinet *et al.*³⁰ The half-width at half-maximum of the crescent

plasmon mode is found to be about 150 nm, which provides a significant wavelength window, in which critical coupling of light to the structure can be applied. In contrast to the rather broad plasmon resonance observed for the pattern without a cavity, the FP reflection minima are steep and easily tunable by the spacer thickness, as shown in Fig. 2 (a) and (b). Under appropriate conditions, the reflectivity at resonance can be reduced below 5%, such that more than 95% of the light is absorbed by the structure with a 60 nm gap. Without the spacer and the reflecting layers, only about 70% of the incident light is absorbed by the otherwise identical structure with a 60 nm gap shown by the modeling.

To experimentally validate that near perfect absorption leads to an enhanced near-field, we carry out SERS measurements originating from a self-assembled analyte monolayer of benzene-ethane-thiol. The two wavelengths of primary interest for our experiments are 633 nm and 676 nm, corresponding to the excitation and the Stokes shifted Raman line of the analyte at 1008 cm^{-1} . Enhancing the near-field at either or both the excitation/observation wavelength is achieved by controlling the resonance position via the spacer thickness. Figures 2 (c) - (f) show the simulated electric field plots at the two different wavelengths (633 nm and 676 nm) for two different spacer thicknesses (100 nm and 200 nm). We observe that the crescent array with the underlying spacer of 100 nm is off-resonance, while the array with the 200 nm spacer is near-resonance at both wavelengths of interest. Correspondingly, the near-field of the 100 nm spacer, c.f. Fig. 2 (c) and (d), is significantly lower as compared to the 200 nm spacer, with a maximum near-field enhancement of $\times 45$ at the

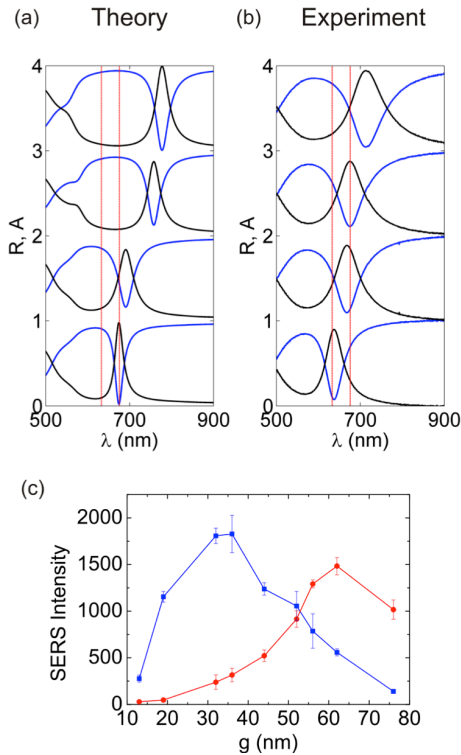


Figure 3. (a) Simulated and (b) experimentally measured reflection (blue) and absorption (black) spectra under normal incidence for $g = 36$ nm, 40 nm, 48 nm and 62 nm (from bottom to top) and a fixed $d = 100$ nm. The red lines indicate 633 nm and 676 nm. (c) SERS intensity as a function of gap size for $d = 100$ nm (blue) and $d = 200$ nm (red).

hotspot of the plasmon mode. The experimental validation of this observation by SERS reveals a modulated signal when varying the spacer thickness, see Fig. 2 (g). The modulation contrast exceeds 95% (ratio between the minimum and maximum > 20), which conclusively proves that the near-field is strongly enhanced when the critical coupling condition is satisfied.

In the following, we show that the gap of the crescent array enables us to adjust the complex amplitude of the reflected planewave, thereby providing a second handle for controlling the absorption of light and thus the coupling strength. Figure 3 (a) and (b) show the simulated and the experimentally measured reflection spectra for crescents placed on the substrate with the 100 nm spacer for gaps between $g = 36$ nm and $g = 62$ nm. A significant red shift of the reflection resonance is observed on increasing the gap. The full set of experimentally measured reflection spectra from samples with gaps varying from 13 nm to 80 nm (spacer $d = 100$ nm) is given in Fig. S1. We observe that a change of the gap for constant spacer, alike the changes of the spacer thickness for constant gap size, results in a shift of the reflection dip. Figure 3 (c) compares the SERS intensity dependence on the gap sizes g in the range between 10 nm and 80 nm for two spacer thicknesses d of 100 nm and 200 nm. The optimal gap size with maximal SERS signal is found

for $g = 36$ nm in case of the 100 nm spacer and for $g = 62$ nm in case of the 200 nm spacer. This shift from $g = 36$ nm to $g = 62$ nm thus assists to recover the optimal resonance matching with the SERS excitation and emission wavelengths. In reverse, by changing the underlying spacer thickness similar optimal SERS enhancement are obtained for various gaps. Such a handle on the gap size for optimal SERS signals opens up numerous possibilities in the sensing of complex biological samples. For example, most biological samples contain significant contaminants, which require a purification step prior to the use of an analytical measurement tool. However, the structure proposed here intrinsically provides a route for size-based exclusion of unwanted contaminants depending on the nanogap employed. Only molecules that can diffuse through the gap of the crescent array are detected by SERS, since the near-field hot spot is located on the rear side at the sharp crescent tip.³⁴

In the following, we correlate the far field response, i.e. the reflection strength, to the corresponding SERS intensities. In most reported cases, the SERS signal is correlated to the extinction at the mean wavelength of the excitation and emission.³⁷ However, in our nearly perfectly absorbing structure such a scheme breaks down, due to the resonance width being comparable to the wavelength difference between the excitation and emission wavelengths. Under conditions where the excitation (or emission) wavelength is in resonance while the emission (or excitation) at the Stoke shifted wavelength is off resonance, the SERS intensity may thus be weakened. We can identify such events from the large scatter of SERS signals when plotted against the median reflectance at both the excitation and detection wavelengths, shown in Figure S2. Instead, we correlate the SERS to the reflectivity at both the excitation and the emission wavelength and thus, the connection of the SERS intensity to both the emission and excitation enhancement becomes evident.

The 2D map shown in Figure 4 (a) summarizes the normalized SERS intensity for all spacers d (between 100 nm and 700 nm) and all crescent gap sizes g (between 10 nm and 80 nm) plotted against the reflectivity at the excitation (x-axis) and emission wavelength (y-axis). The plot is generated using three Raman lines (800 cm^{-1} , 1000 cm^{-1} and 1600 cm^{-1}) corresponding to the emission wavelength at 667 nm, 676 nm and 705 nm, respectively. The intensities are normalized to the maximal intensity for each of the lines. We observe that the regions of high SERS intensities - colored green and red in Fig. 4 (a) - are surrounded by regions of low SERS intensities (blue regions, Fig. 4 (a)). Low SERS intensities are found when either the excitation or the emission is off resonance defined by $R_{\text{em}} > 0.8$ or $R_{\text{ex}} > 0.8$). When the reflectivity at the excitation (λ_{ex}) and emission (λ_{em}) wavelengths is in the range between 0.2 and 0.75, the detected SERS signal is high irrespective of the actual gap or spacer. Since the reflectivity is only low when a resonance is near λ_{ex} and λ_{em} , the occurrence of strong SERS elusively supports our here proposed mechanism that the near-field is enhanced due to the near total absorption. Figure S3 shows the SERS maps as a function of reflectivity for each of the three Raman lines. It is clear that each pair of excitation and emission

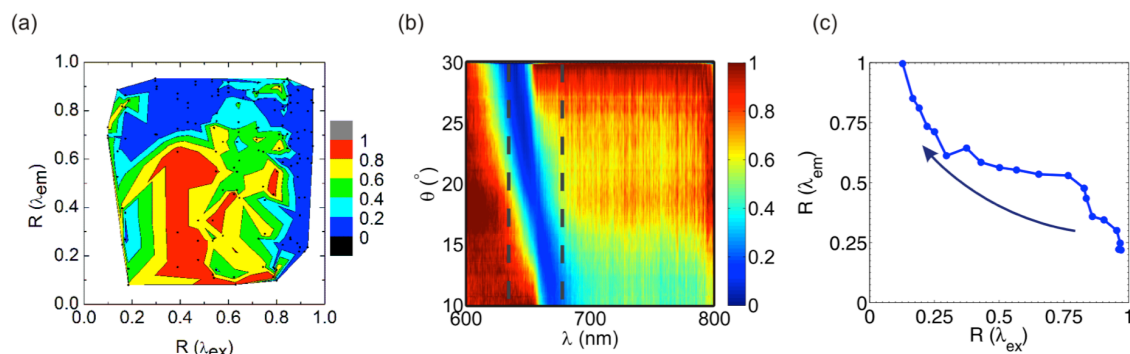


Figure 4. (a) Normalized SERS signal as a function of reflectivity at excitation and emission wavelengths. Three different Raman lines (800 cm^{-1} , 1008 cm^{-1} and 1600 cm^{-1}) are used for computing this map. The SERS signal is normalized to the maximum signal for each Raman line. Black dots indicate the measured signals. (b) Reflectivity measured as a function of the angle of incidence θ and λ for a spacer thickness $d = 700\text{ nm}$ and a crescent gap size $g = 62\text{ nm}$. The dashed black lines indicate our typical incident and emitted Raman wavelength of 633 nm and 676 nm . (c) Trace of the reflectivity at excitation ($\lambda = 633\text{ nm}$) and emission ($\lambda = 676\text{ nm}$) wavelengths for a 62 nm gap when changing the angle of incidence from 10° to 30° in steps of 1° . The arrow indicates the direction of increasing angle of incidence. The spacer thickness is 700 nm .

wavelengths corresponding to a given Raman line provide very similar results. From theory, the calculated SERS enhancement ($|E_{ex}|^2|E_{em}|^2$) as a function of the reflectivity at the excitation and emission wavelengths indeed matters. In Figure S3 (a), the calculated near-field enhancement at both wavelengths is plotted in a 2D map for simulated arrays with different spacer thicknesses ($d = 100\text{ nm} - 700\text{ nm}$) and gaps ($g = 50\text{ nm}$ and 60 nm). A good agreement is observed between the numerically calculated and the experimentally measured SERS maps.

Knowing that the system resonance condition is governed by the FP cavity, the angle of incidence - analogous to the spacer thickness discussed before - provides a control of the phase difference between the reflected planewaves. This behavior is unique for our cavity based structure because crescent arrays, or antennas in general, without a reflecting layer support only non-dispersive localized modes. Figure 4 (b) shows a dispersion curve, with the experimental reflectivity plotted against the angle of incidence and wavelength, for a crescent array with gap $g = 62\text{ nm}$ and a spacer of $d = 700\text{ nm}$. We observe a 60 nm blue shift upon changing the angle of incidence from 10° to 30° . The resonance shift of the reflectivity at the here-applied excitation and emission wavelengths is shown in Fig. 4 (c). For a 10° angle of incidence, the structure is off-resonance because R_{ex} exceeds 0.8 , which, according to Fig. 4 (a) is when the SERS signals are low. Changing the angle of incidence from 10° to 20° , the resonance crosses the excitation wavelength, and again from the analogy with Fig. 4 (a), a high SERS intensity is expected. This case thus represents a ‘SERS on’ state. Further increase in the angle of incidence would generate again a ‘SERS off’ state. We expect that this simple angular control will give an additional degree of freedom for optimizing plasmonic structures for SERS measurements, e.g. by changing the incidence angle in situ under the microscope.

CONCLUSION

We have proposed and validated a generic method for making plasmonic structures perfect absorbers of light by modifying the underlying substrate to include a spacer and a reflecting layer. The presence of the reflecting layer ensures zero transmission whereas the spacer controls the nature of interference, destructive or constructive, between the reflected plane waves. This technique does not modify the character of the near-field distribution of the plasmonic structure but merely alters the field enhancement at a given wavelength. SERS signal variations in excess of 20 are demonstrated depending on the spacer thickness. We have identified the optimal SERS operating regime, when the reflectivity at both the excitation and emission wavelengths is in the range between 0.2 and 0.75 . Finally, we illustrated that the dispersive nature of the modes allows for angle controlled full tuning of SERS enhancement.

Conflict of Interest: The authors declare no competing financial interest.

Acknowledgement. This work was supported by the Swiss National Science Foundation (SNF) (projects 200021_125326 and CR23I2_147279). Part of this work was performed at the Swiss Light Source (SLS), Paul Scherrer Institute, Switzerland.

Supporting Information Available: Fabrication details, characterization methods and numerical simulation details; Reflection spectra for varying gap sizes and constant spacer thickness; SERS dependency as a function of the midpoint of the excitation and detection wavelength; Theoretical 2D SERS map; Measured 2D SERS map for all three Raman lines. This material is available free of charge via the Internet at <http://pubs.acs.org>.

REFERENCES AND NOTES

- 1 Brolo, A. G., Plasmonics for future biosensors. *Nature Photonics* **2012**, 6, 709-713.
- 2 Gramotnev, D. K.; Bozhevolnyi, S. I., Plasmonics beyond the diffraction limit. *Nature Photonics* **4**, 83-91.
- 3 Schuller, J. A.; Barnard, E. S.; Cai, W. S.; Jun, Y. C.; White, J. S.; Brongersma, M. L., Plasmonics for extreme light concentration and manipulation. *Nature Materials* **2010**, 9, 193-204.
- 4 Kern, A. M.; Meixner, A. J.; Martin, O. J. F., Molecule-Dependent Plasmonic Enhancement of Fluorescence and Raman Scattering near Realistic Nanostructures. *ACS Nano* **2012**, 6, 9828-9836.
- 5 Natan, M. J., Concluding Remarks Surface enhanced Raman scattering. *Faraday Discussions* **2006**, 132, 321-328.
- 6 Siegfried, T.; Kind, M.; Terfort, A.; Martin, O. J. F.; Zhamikov, M.; Ballav, N.; Sigg, H., Reusable Plasmonic Substrates Fabricated by Interference Lithography: a Platform for Systematic Sensing Studies. *J. Raman Spectrosc.* **2012**, 44, 170-175.
- 7 Zhang, W.; Fischer, H.; Schmid, T.; Zenobi, R.; Martin, O. J. F., Mode-Selective Surface-Enhanced Raman Spectroscopy Using Nanofabricated Plasmonic Dipole Antennas. *The Journal of Physical Chemistry C* **2009**, 113, 14672-14675.
- 8 Le Ru, E. C.; Meyer, M.; Etchegoin, P. G., Proof of Single-Molecule Sensitivity in Surface Enhanced Raman Scattering (SERS) by Means of a Two-Analyte Technique. *The Journal of Physical Chemistry B* **2006**, 110, 1944-1948.
- 9 Kneipp, K.; Wang, Y.; Kneipp, H.; Perelman, L. T.; Itzkan, I.; Dasari, R. R.; Feld, M. S., Single Molecule Detection Using Surface-Enhanced Raman Scattering (SERS). *Physical Review Letters* **1997**, 78, 1667-1670.
- 10 Nie, S.; Emory, S. R., Probing Single Molecules and Single Nanoparticles by Surface-Enhanced Raman Scattering. *Science* **1997**, 275, 1102-1106.
- 11 Xu, H.; Bjerneld, E. J.; Käll, M.; Börjesson, L., Spectroscopy of Single Hemoglobin Molecules by Surface Enhanced Raman Scattering. *Physical Review Letters* **1999**, 83, 4357-4360.
- 12 Adato, R.; Altug, H., In-situ ultra-sensitive infrared absorption spectroscopy of biomolecule interactions in real time with plasmonic nanoantennas. *Nature Communication* **2013**, 4.
- 13 Hoffmann, J. M.; Yin, X.; Richter, J.; Hartung, A.; Maß, T. W. W.; Taubner, T., Low-Cost Infrared Resonant Structures for Surface-Enhanced Infrared Absorption Spectroscopy in the Fingerprint Region from 3 to 13 μm . *The Journal of Physical Chemistry C* **2013**, 117, 11311-11316.
- 14 Neubrech, F.; Pucci, A.; Cornelius, T. W.; Karim, S.; García-Etxarri, A.; Aizpurua, J., Resonant Plasmonic and Vibrational Coupling in a Tailored Nanoantenna for Infrared Detection. *Physical Review Letters* **2008**, 101, 157403.
- 15 Aslan, K.; Gryczynski, I.; Malicka, J.; Matveeva, E.; Lakowicz, J. R.; Geddes, C. D., Metal-enhanced fluorescence: an emerging tool in biotechnology. *Current Opinion in Biotechnology* **2005**, 16, 55-62.
- 16 Emmanuel, F.; Samuel, G., Surface enhanced fluorescence. *Journal of Physics D: Applied Physics* **2008**, 41, 013001.
- 17 Lakowicz, J. R., Radiative decay engineering 5: metal-enhanced fluorescence and plasmon emission. *Analytical Biochemistry* **2005**, 337, 171-194.
- 18 Ray, K.; Badugu, R.; Lakowicz, J. R., Metal-Enhanced Fluorescence from CdTe Nanocrystals: A Single-Molecule Fluorescence Study. *Journal of the American Chemical Society* **2006**, 128, 8998-8999.
- 19 Siegfried, T.; Ekinici, Y.; Solak, H. H.; Martin, O. J. F.; Sigg, H., Fabrication of Sub-10 nm Gap Arrays over Large Areas for Plasmonic Sensors. *Appl Phys Lett* **2011**, 99, 263302.
- 20 Haynes, C. L.; Van Duyne, R. P., Nanosphere Lithography: A Versatile Nanofabrication Tool for Studies of Size-Dependent Nanoparticle Optics. *The Journal of Physical Chemistry B* **2001**, 105, 5599-5611.
- 21 Guo, L. J., Nanoimprint lithography: Methods and material requirements. *Adv Mater* **2007**, 19, 495-513.
- 22 Siegfried, T.; Ekinici, Y.; Martin, O. J.; Sigg, H., Gap Plasmons and Near-Field Enhancement in Closely Packed Sub-10 nm Gap Resonators. *Nano Lett* **2013**, 13, 5449-53.
- 23 Ameling, R.; Giessen, H., Microcavity plasmonics: strong coupling of photonic cavities and plasmons. *Laser & Photonics Reviews* **2013**, 7, 141-169.
- 24 Dutta Gupta, S., Strong-interaction mediated critical coupling at two distinct frequencies. *Optics Letters* **2007**, 32, 1483-1485.
- 25 Hedayati, M. K.; Javaherirahim, M.; Mozooni, B.; Abdelaziz, R.; Tavassolizadeh, A.; Chakravadhanula, V. S. K.; Zaporozhtchenko, V.; Strunkus, T.; Faupel, F.; Elbahri, M., Perfect Plasmonic Absorber: Design of a Perfect Black Absorber at Visible Frequencies Using Plasmonic Metamaterials. *Advanced Materials* **2011**, 23, 5409-5409.
- 26 Subimal, D.; Shourya Dutta, G.; Banerji, J.; Gupta, S. D., Critical coupling at oblique incidence. *Journal of Optics A: Pure and Applied Optics* **2007**, 9, 555.
- 27 Tischler, J. R.; Bradley, M. S.; Bulovi, V., Critically coupled resonators in vertical geometry using a planar mirror and a 5 nm thick absorbing film. *Optics Letters* **2006**, 31, 2045-2047.
- 28 Ameling, R.; Langguth, L.; Hentschel, M.; Mesch, M.; Braun, P. V.; Giessen, H., Cavity-enhanced localized plasmon resonance sensing. *Applied Physics Letters* **2010**, 97, -.

- 29 Liu, N.; Mesch, M.; Weiss, T.; Hentschel, M.; Giessen, H., Infrared Perfect Absorber and Its Application As Plasmonic Sensor. *Nano Letters* **2010**, 10, 2342-2348.
- 30 Gallinet, B.; Siegfried, T.; Sigg, H.; Nordlander, P.; Martin, O. J. F., Plasmonic Radiance: Probing Structure at the Ångström Scale with Visible Light. *Nano Lett* **2012**, 13, 497-503.
- 31 Gallinet, B.; Kern, A. M.; Martin, O. J. F., Accurate and Versatile Modeling of Electromagnetic Scattering on Periodic Nanostructures with a Surface Integral Approach. *Journal of the Optical Society of America A: Optics and Image Science* **2010**, 27, 2261-2271.
- 32 Johnson, P. B.; Christy, R. W., Optical Constants of the Noble Metals. *Physical Review B* **1972**, 6, 4370-4379.
- 33 Farhang, A.; Abasahl, B.; Dutta-Gupta, S.; Lovera, A.; Mandracci, P.; Descrovi, E.; Martin, O. J. F., Broadband wide-angle dispersion measurements: Instrumental setup, alignment, and pitfalls. *Review of Scientific Instruments* **2013**, 84, -.
- 34 Siegfried, T.; Ekinci, Y.; Martin, O. J. F.; Sigg, H., Engineering Metal Adhesion Layers That Do Not Deteriorate Plasmon Resonances. *ACS Nano* **2013**, 7, 2751-2757.
- 35 Lévêque, G.; Martin, O. J. F., Optical interactions in a plasmonic particle coupled to a metallic film. *Optics Express* **2006**, 14, 9971-9981.
- 36 Farhang, A.; Siegfried, T.; Ekinci, Y.; Sigg, H.; Martin, O. J. F., Large-scale sub-100 nm compound plasmonic grating arrays to control the interaction between localized and propagating plasmons. *NANOP* **2014**, 8, 083897-083897.
- 37 Kleinman, S. L.; Sharma, B.; Blaber, M. G.; Henry, A.-I.; Valley, N.; Freeman, R. G.; Natan, M. J.; Schatz, G. C.; Van Duyne, R. P., Structure Enhancement Factor Relationships in Single Gold Nanoantennas by Surface-Enhanced Raman Excitation Spectroscopy. *Journal of the American Chemical Society* **2012**, 135, 301-308.

SUPPORTING INFORMATION

Cavity-Controlled Perfect Absorption in Plasmonic Crescent Arrays Can
Command the Raman Enhancement

Shourya Dutta-Gupta^{§,#}, Thomas Siegfried^{†,#}, Yasin Ekinici[†], Hans Sigg[†] and Olivier J. F. Martin^{§,}*

[§]Nanophotonics and Metrology Laboratory, EPFL, 1015 Lausanne, Switzerland

[†]Laboratory for Micro- and Nanotechnology, Paul Scherrer Institut, 5232 Villigen-PSI, Switzerland

*Corresponding author email: olivier.martin@epfl.ch

[#] Authors contributed equally

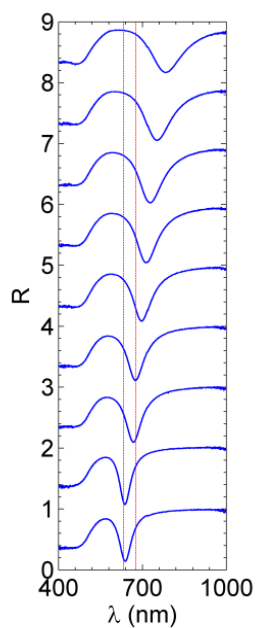


Fig S1. Experimental reflection spectra at normally incident for various gaps (from bottom to top: $g = 13, 19, 32, 36, 44, 52, 56, 62$ and 76 nm) for a constant spacer thickness of 100 nm. The red vertical lines indicate $\lambda = 633$ nm and $\lambda = 676$ nm.

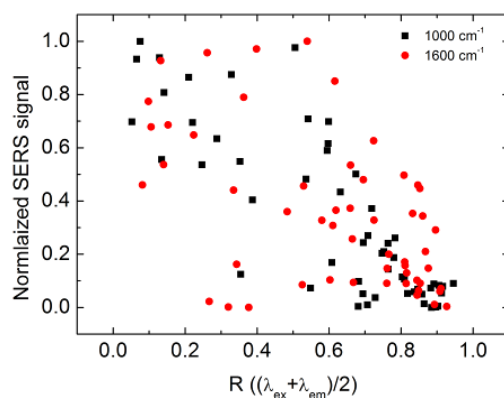


Fig S2. Normalized SERS intensity as a function of reflectivity at the midpoint between the excitation and emission wavelengths. A fixed excitation wavelength of 633 nm was used.

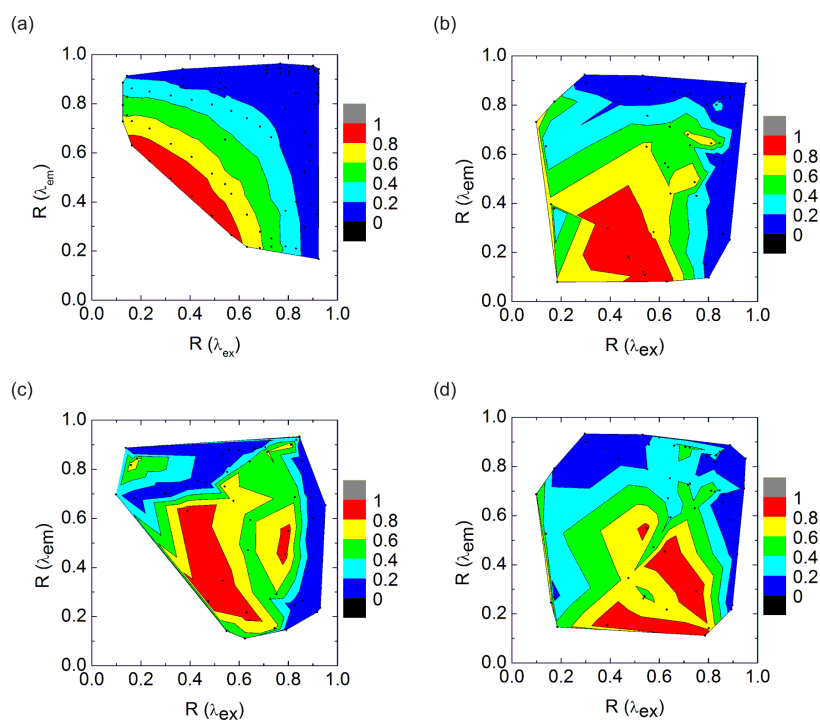


Fig S3. (a) Theoretically calculated SERS map as a function of reflectivity at excitation and emission wavelengths taking the three Raman lines into account. (b), (c) and (d) SERS maps as a function of reflectivity at the excitation and emission wavelengths for Raman lines at 800 cm^{-1} , 1000 cm^{-1} and 1600 cm^{-1} , respectively.

(VII) Reusable plasmonic substrates

Manuscript state

Published manuscript

Reference

T. Siegfried, M. Kind, A. Terfort, O. J. F. Martin, M. Zharnikov, N. Ballav, H Sigg, “Reusable plasmonic substrates fabricated by interference lithography: a platform for reliable sensing studies”, *Journal of Raman Spectroscopy* **2012**, 44 (2), 170-175.

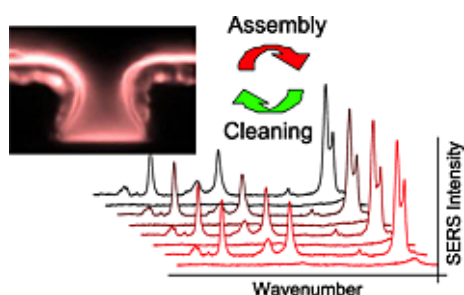
Publication date: 31. August 2012

DOI: 10.1002/jrs.4163

URL: <http://onlinelibrary.wiley.com/doi/10.1002/jrs.4163/abstract>

Current citations: 4

Table of Contents entry



Periodic, nanoslit-based gold substrates fabricated by EUV interference lithography provide excellent reproducibility in the SERS enhancement and, additionally, reusability of the substrate. The outstanding capabilities were demonstrated using monomolecular films of thiols and open a powerful platform for an analytical tool or for advanced SERS studies for the investigation of chemical enhancement effects, surface selection rules and molecular alignment.

Author contribution

T. Siegfried fabricated the samples. T. Siegfried performed the experiments, analyzed and concluded the data. M. Kind simulated the Raman spectra. T. Siegfried created the figures and wrote the manuscript draft. N. Ballav corrected the manuscript.

Conference contribution

T. Siegfried, “Plasmonic nanogap arrays for a deterministic sensor performance by EUV lithography”, **oral** at SPS meeting in June **2011**, in Lausanne, Switzerland

Published paper & Supporting information

Research article

Received: 2 April 2012

Revised: 11 July 2012

Accepted: 11 July 2012

Published online in Wiley Online Library: 31 August 2012

(wileyonlinelibrary.com) DOI 10.1002/jrs.4163

Reusable plasmonic substrates fabricated by interference lithography: a platform for systematic sensing studies

Thomas Siegfried,^a Martin Kind,^b Andreas Terfort,^b Olivier J. F. Martin,^c Michael Zharnikov,^d Nirmalya Ballav^{e*} and Hans Sigg^{a*}

Surface-enhanced Raman scattering (SERS) has become increasingly popular in the scientific and industrial communities because of its analytical capabilities and potential to study fundamentals in plasmonics. Although under certain conditions extremely high sensitivity is possible, the practical use of SERS is frequently limited by instability and poor reproducibility of the enhancement factor. For analytical applications or for comparative measurements to enable the distinction between electromagnetic and chemical enhancement, the development of standardized and recyclable SERS substrates, having uniform and persistent performance, is proposed. To this end, we have fabricated periodic nanoslit arrays using extreme ultraviolet lithography that provide average large (2×10^6) and homogeneous SERS enhancement factors with a spot-to-spot variability of less than 3%. In addition, they are reusable without any degradation or loss of enhancement. The fabrication of such arrays consists of two steps only, lithographic patterning followed by metal evaporation. Both processes may be performed over areas of several square mm on any planar substrate. The sensor capabilities were demonstrated by substrates with monomolecular films of several different thiols. The concept of reusable SERS substrates may open a powerful platform within an analytical tool and in particular for systematic SERS studies for the investigation of fundamental parameters such as chemical enhancement, surface selection rules, and molecular alignment. Copyright © 2012 John Wiley & Sons, Ltd.

Supporting information may be found in the online version of this article.

Keywords: surface-enhanced Raman scattering; reusability; reproducibility, nanofabrication; analytical tool

Introduction

Thanks to its strong signal enhancement in the vicinity of metal nanostructures, surface-enhanced Raman scattering (SERS) is emerging as one of the most prominent plasmonic sensing techniques.^[1–3] Because of the increased sensitivity in the detection of characteristic vibrational modes associated with a specific (surface-adsorbed) analyte, SERS has established itself as a label-free detection technique that may be applied to almost any adsorbate down to concentrations of a single molecule. A large variety of SERS-active substrates, such as roughened or patterned metallic surfaces and nanoparticle-based systems have been fabricated.^[3–6] Among these substrates, Au-based and Ag-based nanostructures with sharp edges (so called 'hot-spots') are preferred because of their biocompatibility^[7] and their extremely high electromagnetic fields arising from the excitation of local surface plasmon resonances. However, such 'hot-spots' associated with rough or nanoparticle-based substrates are randomly distributed at the nano scale such that these substrates frequently respond in an irreproducible way.^[8] This lack of control renders such substrates rather useless for systematic studies and the characterization of molecular assemblies.^[9]

In fact, an ideal analytical platform for cost-effective and reproducible measurements would ideally consist of a reusable and standardized substrate. Subsequently, one could identify and separate fundamental parameters such as the chemical enhancement from a systematic study of different adsorbed species and physical surroundings using the SAME substrate. Of course, this

approach requires an effective cleaning procedure and robust substrates, so that the substrate sensitivity is not altered during repeated cycles of use.^[10] Substrate reusability has previously been reported with the use of random particle-based or self-ordered array substrates^[11] and protective oxide layers^[12] that can prevent metal contamination and also strongly reduce the enhancement factor. Custom tunability of the plasmon resonance is however limited in these substrates and also the spot to spot deviation is found to be well above 12%.^[11,13]

* Correspondence to: Hans Sigg, Laboratory for Micro- and Nanotechnology, Paul Scherrer Institut, 5232 Villigen, Switzerland.
E-mail: hans.sigg@psi.ch

* Nirmalya Ballav, Department of Chemistry, Indian Institute of Science Education and Research, 411 021 Pune, India.
E-mail: nbhallav@iiserpune.ac.in

a Laboratory for Micro- and Nanotechnology Paul Scherrer Institut, 5232, Villigen, Switzerland

b Institut für Anorganische und Analytische Chemie, Goethe-Universität Frankfurt 60438, Frankfurt, Germany

c Nanophotonics and Metrology Laboratory EPFL, 1015 Lausanne, Switzerland

d Angewandte Physikalische Chemie, Universität Heidelberg, 69120 Heidelberg, Germany

e Department of Chemistry, Indian Institute of Science Education and Research, 411 021 Pune, India

A suitable way to meet the demand for high signal strength and reproducibility is lithography combined with sophisticated pattern design.^[14,15] Electron-beam lithography is especially attractive because of its flexibility and ultimate lateral resolution allowing fabrication of complex nanopatterns.^[16] However, the serial writing process of e-beam lithography makes this method economically unattractive. The combination of the precision of e-beam lithography with parallel, large-scale fabrication methods of nanopatterns employing extreme ultraviolet (EUV) interference lithography is proposed as the winning approach. It offers high-resolution patterning with a half-pitch down to about 10 nm.^[17] We fabricated nanoslit-based Au substrates exhibiting a high and reproducible SERS signal enhancement over several mm² while withstanding multiple cleaning cycles. To quantify the reusability of this new substrate, we chose thiol-anchored chemisorbed monolayers as the analyte. We observed a vanishing dependence of the thiol adsorption probability on the metal substrate upon repeated cleaning cycles. The constant successive SERS signals prove that the cleaning is neither altering nor modifying the geometry of the nanoslits. No noticeable changes in the enhancement factor were observed after several successive cleaning/self-assembly cycles.

Experimental

Materials and preparation

All solvents and chemicals were purchased from Sigma-Aldrich GmbH and used without further purification. The studied self-assembled monolayer (SAM) precursor molecules biphenylthiol (BP0), 4,4'-terphenyl-4-thiol (TP0), 4,4'-terphenyl methanethiol (TP1), and 4,4'-perfluoroterphenyl methanethiol (FTP1) were custom-synthesized following the published protocols.^[18,19] SAM layers were formed by immersion of freshly patterned or cleaned plasmonic sensor substrates into a 1 mM solution of the respective precursor in tetrahydrofuran (THF) for >1 h at room temperature. After immersion, the samples were carefully rinsed with pure THF, distilled water and ethanol, and blown dry in a nitrogen stream.

Nanofabrication of nanoslit substrates

The nanocavity substrates were fabricated using shadow evaporation of gold (99.99% purity, purchased from Balzers) on the prepatterned layer of photoresist (hydrogen silsesquioxane, HSQ) on float glass chips. The 80-nm-thick HSQ film was exposed using EUV interference lithography^[20] at the Swiss Light Source to form a line pattern with period 250 nm over one mm². Although this technique is rather unique, it has its main advantages in the exposure time (roughly 4 s) for the high resolution pattern of large areas (mm²). The HSQ layer was developed for 60 s in a 25% tetramethylammonium hydroxide solution and used without further liftoff treatments. Gold and chromium (1 nm acting as adhesion layer) were thermally evaporated at an angle of 60° from the surface normal and with an azimuthal orientation perpendicular to the nanoslits. The base pressure was 4 × 10⁻⁶ mbar. Further details on the fabrication process can be taken from the literature.^[21]

Instrumentation

Reflection spectra were recorded on a Sentech FTP advanced spectrometer attached to a Zeiss optical microscope with a 20-fold objective. The spectra were normalized with a reference

spectrum on the same substrate at a continuous gold layer without the nanoslit pattern to account for metal thickness and roughness effects. Because nanoslit arrays are highly polarization dependent, the incident light was polarized, that the electric field was perpendicular to the nanogap expansion. For opposite polarization the pattern exhibits no resonance and subsequently no SERS enhancement.^[21] Raman spectra were taken on a Horiba LabRam HR with a grating resolution of 600 lines mm⁻¹. The excitation source was a HeNe laser operating at 633 nm and the incident laser power was fixed at 2 mW. The system was equipped with a constantly rotating laser spot that reflected the beam within an area of 10 × 10 μm², further minimizing substrate degradation and photobleaching of the analyte to a maximal level of 10% during 100 s of illumination. The laser was focused onto the dried substrate with an Olympus ×50 long distance objective (numerical aperture, NA 0.5). An integration time of only 1 s was sufficient to obtain high quality Raman spectra and 16 spectra were taken over a patterned area of 600 × 300 μm² for statistical evaluation. Baseline corrections were carried out to correct the optical background signal from the substrate. The SERS intensity of all subsequent figures corresponds to the highest Raman peak intensity around 1600 cm⁻¹ of the analytes and is normalized for comparison of different species.

Substrate cleaning

The substrates were cleaned using an ultraviolet ozone (UVO) cleaner 42 from Jelight Company, Inc. The typical illumination time was 20 min for BP0, TP0, and FTP1, and 30 min for TP1. The distance between the substrate and lamp was 15 mm with an irradiation power of 0.28 W cm⁻². After illumination, the substrates were thoroughly washed in THF, ethanol, and distilled water to remove the remaining contaminants and blown dry in a nitrogen stream.

Raman spectra simulation

Density functional theory calculations of the Raman spectra: the calculations were performed at the Center for Scientific Computing (CSC) of the Goethe University Frankfurt using the GAUSSIAN 09 program package.^[22] The optimal functional (Becke, three-parameter, Lee–Yang–Parr) and basis set (6-311G*) was selected by comparing the conventional Raman spectra of BP0 (recorded with a Renishaw RM-1000 micro-Raman spectrometer at the department of geosciences/geography of the Goethe University of Frankfurt) with the calculated spectra. This combination was used thereafter for the calculation of the Raman spectra of all other thiol molecules investigated in this study. The calculated spectra were used to aid the band assignment of the SERS peaks. The wavenumbers in all calculated spectra were scaled by a factor of 0.975 to further account for overestimated energies of the respective vibrational modes.

Results and discussion

Gold was used as the active plasmonic material, because this noble metal does not form protective surface oxide layers and can be cleaned reproducibly (see below). The geometry of the pattern (Fig. 1) was designed in such a way that the energy of the plasmon resonance was in between the excitation line and the detected Raman signal, as shown in Fig. 1(c). Such configuration is known to provide the highest SERS enhancements.^[23] In a previous study

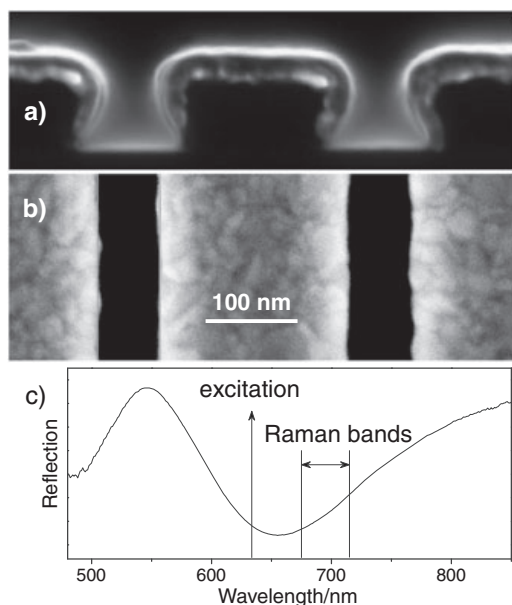


Figure 1. (a) Cross-section and (b) top-view scanning electron microscopy images of the EUV fabricated nanoslit pattern. The pattern is written in HSQ photoresist (80 nm thickness) and has a periodicity of 250 nm. The lines are covered by Au (35 nm thickness) serving as active metal. The gap size between the Au lines is 60 nm. (c) Normalized optical reflection spectrum of a typical nanoslit pattern with an incident polarization of the electric field perpendicular to the gap expansion. The Raman excitation wavelength is 633 nm while the detected bands are wavelength shifted by 1100–1700 cm^{-1} .

it was shown that the nanogap dimension strongly alters the electric near-field intensity of the pattern and the strength of the SERS enhancement.^[21]

As a representative test system for SERS experiments, we have selected a series of arene-based monomolecular films with a thiol headgroup as a suitable anchor for the Au substrate. The thus obtained self-assembled monolayers (SAMs) form a well-defined and homogeneous molecular adsorbate, providing a good platform for monitoring the SERS performance of our nanoslit substrate. In addition, SAMs are frequently used as building blocks of sensors and nanoscale assemblies, and are of great interest for lithography, nanofabrication, and organic electronics on their own.^[24,25]

The SAM precursors under study are biphenylthiol (BP0), 4,4'-terphenyl-4-thiol (TP0), 4,4'-terphenyl methanethiol (TP1), and 4,4'-perfluoroterphenyl methanethiol (FTP1) (see Fig. 2). All these molecules have been previously shown to form well-ordered, densely packed and contamination-free SAMs on thermally evaporated Au thin film substrates – as in the present study.^[18,26,27]

Surface-enhanced Raman scattering spectra of the target SAMs on the nanoslit substrate are presented in Fig. 3(a). The spectra were recorded successively (system after system) on the same substrate area, with the following substrate cleaning step in between each measurement: the SAM-covered substrate was exposed to ultraviolet light, which generated chemically active ozone species. It is well-known that the SAM constituents are decomposed upon such a treatment while the thiolate headgroups (S–Au) become sulphonates ($\text{SO}_3\text{--Au}$), which are weakly bond to the substrate. The resulting physisorbed species can then be easily removed with a solvent rinsing procedure or exchanged for another SAM precursor upon immersion into the solution

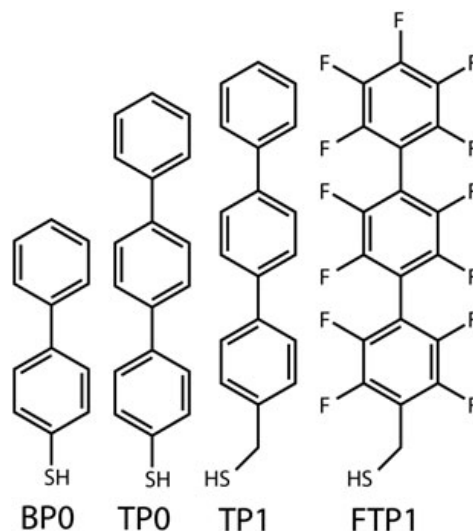


Figure 2. Structure of the SAM precursors used in this study, along with the respective abbreviations.

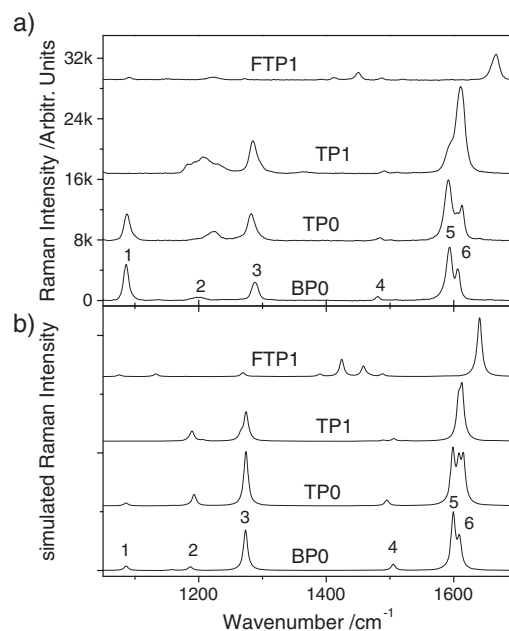


Figure 3. Comparison of (a) typical experimental SERS spectra of the monomolecular films with (b) the simulated spectra of the isolated SAM precursors. A baseline correction was applied to the experimental spectra and normalized intensities were applied to the simulated spectra.

containing these moieties.^[28] This guarantees the reusability of the substrate, shown in Fig. 5, if the gold morphology is not altered during ultraviolet irradiation.

The SERS spectra in Fig. 3(a) possess a very high signal-to-noise ratio, exhibiting intense characteristic vibration modes of the target molecular assemblies. In the case of BP0, TP0, and TP1, the spectra are dominated by the ring breathing modes at $\sim 1280\text{ cm}^{-1}$ and 1600 cm^{-1} , with the latter mode consisting of three components related to the individual rings. These peaks are accompanied by weaker features at $\sim 1200\text{ cm}^{-1}$ and 1500 cm^{-1} associated with the bending modes of the CH bond. In addition, in the spectra of BP0

and TP0, there is a relatively strong peak at $\sim 1080\text{ cm}^{-1}$ that can be assigned to the stretching mode (ν_{CS} of the S–C(ring) bond.^[29] Expectedly, this mode only exists if there is no substituent between the S atom and the phenyl ring – but not for TP1/Au and FTP1/Au.

The difference in the distribution of the spectral weight within the ν_{CC} mode (1600 cm^{-1}) for the BP0/TP0 and TP1 cases is presumably related to the enhancement of the contribution of the bottom ring (see Fig. 3) for BP0 and TP0 because this moiety is in direct neighborhood to the S atom, which has a higher polarizability than a C atom ($-\text{CH}_2$ group of TP1). For FTP1, the appearance of the corresponding ring breathing modes at higher wavenumbers (around 1450 cm^{-1} and 1665 cm^{-1}) indicates a clear signature of the aromatic ring substitution by strong electron withdrawing fluorine atoms.^[26]

The vibrational modes of the experimental SERS spectra were confirmed by theoretical simulations of the isolated SAM precursors. The obtained simulated spectra are presented in Fig. 3(b). Excellent agreement of most peak positions and relative intensities between the experimental and simulated spectra was found for all the studied systems, which is additionally illustrated in Table 1 by a detailed comparison of the peak positions and intensities for the BP0 case (and additionally in Fig. S1 and Table S1 for all other precursors). Surface selection rules can play an important role in weakening of Raman bands because of an unfavorable local field polarization and molecular alignment.^[8,30,31]

Comparison of surface-enhanced Raman spectra with conventional Raman spectra of the investigated substances has showed no noteworthy changes in the relative intensities of the vibrational bands. Interestingly, there is a strong additional amplification (by a factor of ~ 20) of the ν_{CS} stretching mode for the SERS system compared with the theory of neat Raman, occurring also for TP0. This amplification stems presumably from a change in the molecule polarizability and from particular high influence of the chemical enhancement in the ν_{CS} case. The latter enhancement could be associated with the charge transfer upon the formation of the substrate–S anchor and with the respective change in the electronic configuration of the C(ring)–S bond.^[32] Note that the S–H bending mode exhibited in the simulated spectra at about 920 cm^{-1} (not shown) was not observed in the experiments, thereby proving the expected abstraction of H and covalent attachment of the SAM precursors to the substrate via the thiolate (S–Au) bond.

Figure 4 compares the Raman spectra of patterned and unpatterned areas, and a normal Raman spectrum of the precursor TP1 solution in THF. While the normal Raman spectrum is strongly dominated by the solvent peaks (914 , 1030 , 1240 , and 1480 cm^{-1}),

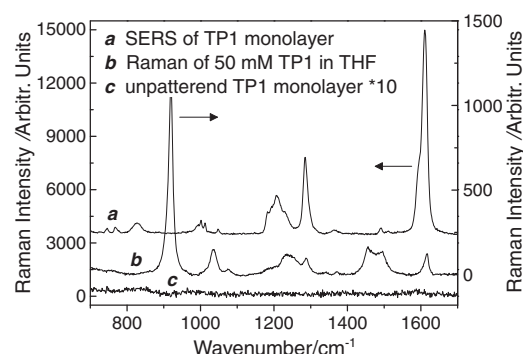


Figure 4. SERS spectra for a TP1 monolayer (a) at a patterned and (c) unpatterned Au substrate. (b) Normal Raman spectrum of a 50-mM TP1 solution in THF. The normal Raman was recorded with an $\times 10$ (NA 0.2) objective at a tenfold increased intensity (20 mW). A baseline correction was applied to all spectra.

the ν_{CC} mode of TP1 at 1609 cm^{-1} is clearly separated. Significantly, no SERS peaks could be detected from unpatterned areas of the same substrate (separated $10\text{ }\mu\text{m}$ from the pattern) covered by the SAMs, even with tenfold higher excitation intensity. This observation leads to the conclusion that the SERS 'hot-spots' are located solely at the nanoslit arrays and surface roughness does not contribute to their generation. In a previous publication we have shown the polarization dependency of the SERS signal on nanogap arrays.^[21] Full signal was obtained when the electric field is perpendicular to the nanogap expansion (TE), while no SERS signal could be found for the TM mode. Despite ambiguities for the determination of SERS enhancement factors, we have calculated an average enhancement factor following a conservative routine described in the literature.^[33] The enhancement factor was calculated on the basis of the 1609 cm^{-1} peak of TP1, with SERS spectra recorded with an $\times 50$ (NA 0.5) objective and normal Raman spectra recorded with an $\times 10$ (NA 0.25) objective from a 50 mM solution at tenfold increased excitation intensity. The monolayer packing density was expected to be similar to benzenethiol, $6.8 \times 10^{14}\text{ cm}^{-2}$,^[34] and leads to a precursor density of 3.2×10^6 for the SERS measurement, considering a laser spot size of $0.8\text{ }\mu\text{m}$. Considering a focal volume of 10.6 pL , the molecule density of the normal Raman measurement was calculated to be 3.2×10^8 . Together with the area integrated Raman peaks of 190 for the normal Raman spectrum and 290 000 for the SERS spectra, an area average enhancement factor of 2×10^6 was obtained.

Table 1. Wavenumber positions (WN), relative intensities, and assignments of the Raman peaks for the BP0 case. Experimentally determined values (exp.) are compared with the simulation results (sim.)

Nr.	exp. WN/ cm^{-1}	exp. Intensity	sim. WN/ cm^{-1}	sim. Intensity	Assignment
1	1084	s	1086	7	ν_{CS} , β_{CH} ^a
2	1198	w, broad	1187	6	β_{CH}
3	1286	m	1273	69	ν_{CC} , β_{CH}
4	1480	w	1480	11	β_{CH}
5	1593	s	1599	100	ν_{CC} , β_{CH}
6	1605	m	1609	52	ν_{CC} , β_{CH}

^av are stretching modes and β are in-plane bending modes. Signal strength: s, strong; m, medium; w, weak.

Cleaning and reusing SERS substrates

The dynamics of the self-assembly and cleaning steps was monitored to understand and optimize the substrate performance. During the self-assembly step, a logarithmic growth of the SERS intensity with immersion time was found, as illustrated in Fig. 5(a) by the example of TP0 (left panel). Assuming that the SERS intensity scales predominately linear with the number density of chemisorbed molecules (only valid for up to monolayer coverage and while EM and chemical enhancement are constant), we conclude that the formation of the monomolecular film was completed after 4 min. Longer immersion (up to 24 h) did not result in a change of the SERS intensity and respectively the molecular coverage (a structural rearrangement or alignment was however

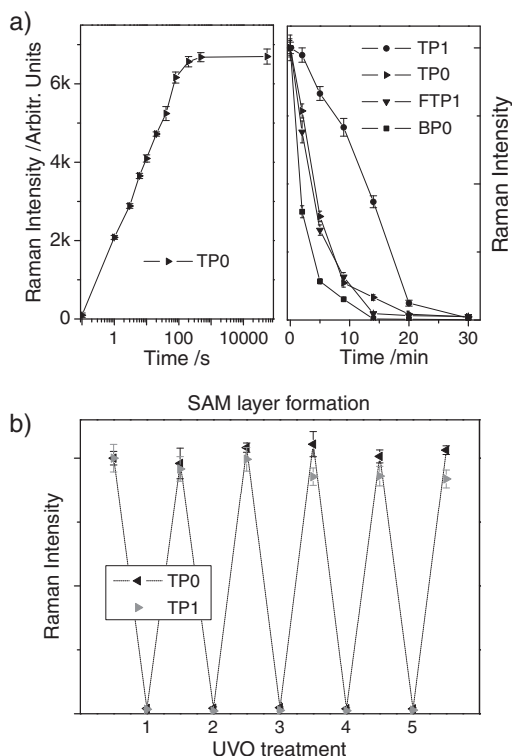


Figure 5. (a) SERS intensity of the strongest peak of the ν_{CC} mode around $\sim 1600\text{ cm}^{-1}$ during the formation of the TP0 SAM on the nanoslit substrate (left panel) and for all precursors during UVO cleaning of the SAM covered substrate (right panel). The data points were recorded *ex situ*. (b) SERS intensity of the ν_{CC} mode around $\sim 1600\text{ cm}^{-1}$ for the molecules TP0 and TP1 during repeated cycles of substrate cleaning and monolayer reformation using the exact same pattern. Error bars correspond to the standard deviation of 16 spatially separated Raman measurements.

possible). Note that the intensity of the observed peaks, i.e. the SERS enhancement, was highly reproducible over the entire patterned substrate area; we have found an excellent standard deviation of below 3% throughout all measurements from the recorded spectra of 16 spatially separated regions on the sensor.

The recorded dynamics of the substrate cleaning process exhibited an exponential decay of the SERS intensity, as seen in Fig. 5(a) (right panel) with full spectra given in Figs S2 and S3. After 20 min of treatment, the detectable SERS intensities were well below 3% of the original value. Among the used molecules, only TP1 differed in the cleaning dynamics, with a longer time necessary for the cleaning, which could be caused by the especially tight molecular packing for this particular system^[27] hindering the penetration of the reactive ozone species to the thiolate-substrate interface. The SERS spectra of cleaned substrates (Fig. 5(b)) prove that all SAM constituents and their fragments could be removed from the substrate, which makes the sensor reusable for SERS measurements on further molecular films of different analytes, in case the pattern morphology is not influenced by the cleaning process.

In the following, we demonstrate the reusability of the nanoslit substrate, shown in Fig. 5(b). By alternating the self-assembly and the UVO cleaning steps on exactly the same substrate, we observed that it could withstand at least six cycles without any noticeable change in the obtained SERS spectra. The SERS peaks around 1600 cm^{-1} were compared for the SAM layers of TP0 and TP1

during repeated cleaning and assembly cycles, shown in Fig. 5(b) with full spectra given in Figs S4 and S5. In particular, the substrate used for the TP0 showed an excellent persistence of the average SERS enhancement with a deviation after each cleaning/self-assembly step below 3%. Building on these results, one could expect a reusable substrate for many more than the analyzed six cycles. This excellent reusability also indicates that the metal surface is not altered and contaminated during repeated cleaning steps so that the adsorbed molecules can still be well ordered and assemble with a similar packing density as for the pristine gold substrate. We think that thiols are one of the difficult cases in the sense of SERS substrate reusability because of the strong bonding and the easiness to cleave the S–C bond in the course of the cleaning procedure (the substrate will then be passivated with atomic sulphur). We believe that the reusability of the presented SERS-active substrates will be equally high in the case of weakly bound adsorbates, but cannot exclude that specific problems can arise for some of these systems.

Similar signal stability was also obtained for TP1, although there was a slight decrease observed after the third cycle. This decrease could be related to heating of the substrate during the UVO exposure, leading to microscopic changes in the metal morphology. Scanning electron microscopy images taken before and after the cleaning steps could however not reveal changes in the nanogap dimension. Note that to ensure a complete detachment of TP1, the UVO exposure time had to be 10 min longer than that for TP0, producing additional heating of the substrate. This can probably be compensated by external cooling, which however was not investigated in the present study. We do not claim that the demonstrated reusability is the exclusive property of our pattern design. We are, however, not aware of such a clear demonstration of the reusability for other nanostructured SERS pattern, such as the commercial Klarite pattern.^[10]

Conclusions

In summary, using EUV interference lithography, we prepared Au-templated nanoslit patterned substrates over mm^2 large area in a two-step process, which were used for SERS measurements on molecular adsorbate assemblies. The substrates exhibited high SERS enhancement ($\sim 2 \times 10^6$) enabling the acquisition of high-quality Raman spectra of monomolecular films. The average enhancement factor possesses a high homogeneity (less than 3% deviation). Finally, no noticeable changes in the enhancement factor after several successive cleaning/self-assembly cycles were observed. All these features make the designed nanoslit-based substrate an ideal platform for an analytical tool or for advanced SERS experiments. In particular, because of the reusability and persisting characteristics, the electromagnetic enhancement can be kept constant while the chemical enhancement,^[35] the influence of molecular alignment,^[36] and surface selection rules^[8] can be studied experimentally upon the adsorption of custom-designed molecules.

Acknowledgements

This work has been financially supported by the Swiss Federal foundation. Part of this work was performed at the Swiss Light Source. We acknowledge the support of Y. Ekinici (PSI) and H. Solak (Eulitha AG). N.B. thanks T. A. Jung (PSI) for the support and helpful discussions. M. K. thanks A. B. Woodland (Frankfurt) for his help with recording a Raman spectrum of BP0.

Supporting information

Supporting information may be found in the online version of this article.

References

- [1] K. Kneipp, Y. Wang, H. Kneipp, L. T. Perelman, I. Itzkan, R. R. Dasari, M. S. Feld, *Phys. Rev. Lett.* **1997**, *78*, 1667.
- [2] M. Rycenga, C. M. Cobley, J. Zeng, W. Li, C. H. Moran, Q. Zhang, D. Qin, Y. Xia, *Chem. Rev.* **2011**, *111*, 3669.
- [3] K. A. Willets, R. P. Van Duyne, in *Annual Review of Physical Chemistry*, Vol. 58, **2007**, pp. 267.
- [4] Y. Zhu, R. A. Dluhy, Y. Zhao, *Sensor Actuat B-Chem.* **2011**, *157*, 42.
- [5] H. Wang, C. S. Levin, N. J. Halas, *J. Am. Chem. Soc.* **2005**, *127*, 14992.
- [6] H. Ko, S. Singamaneni, V. V. Tsukruk, *Small* **2008**, *4*, 1576.
- [7] M. Moskovits, *J. Raman Spectrosc.* **2005**, *36*, 485.
- [8] E. C. Le Ru, S. A. Meyer, C. Artur, P. G. Etchegoin, J. Grand, P. Lang, F. Maurel, *Chem. Commun.* **2011**, *47*, 3903–3905.
- [9] M. J. Natan, *Faraday Discuss.* **2006**, *132*, 321.
- [10] S. Sadate, *Opt. Eng.* **2010**, *49*, 106501.
- [11] X. Li, H. Hu, D. Li, Z. Shen, Q. Xiong, S. Li, H. J. Fan, *ACS Appl. Mater. Interfaces* **2012**, *4*, 2180.
- [12] S. M. Mahurin, J. John, M. J. Sepaniak, S. Dai, *Appl. Spectrosc.* **2011**, *65*, 417.
- [13] G. Sinha, L. E. Depero, I. Alessandri, *ACS Appl. Mater. Interfaces* **2011**, *3*, 2557.
- [14] U. S. Dinis, F. C. Yaw, A. Agarwal, M. Olivo, *Biosens. Bioelectron.* **2011**, *26*, 1987.
- [15] D. Cialla, A. März, R. Böhme, F. Theil, K. Weber, M. Schmitt, J. Popp, *Anal. Bioanal. Chem.* **2011**, *403*, 1.
- [16] H. Duan, H. Hu, K. Kumar, Z. Shen, J. K. W. Yang, *ACS Nano* **2011**, *5*, 7593.
- [17] B. Päiväranta, A. Langner, E. Kirk, C. David, Y. Ekinci, *Nanotechnology* **2011**, *22*, 375302.
- [18] H. J. Himmel, A. Terfort, C. Wöll, *J. Am. Chem. Soc.* **1998**, *120*, 12069.
- [19] B. Schüpbach, M. Bolte, M. Zharnikov, A. Terfort, *Eur. J. Org. Chem.* **2010**, *16*, 3041.
- [20] V. Auzelyte, C. Dais, P. Farquet, D. Grutzmacher, L. J. Heyderman, F. Luo, S. Olliges, C. Padeste, P. K. Sahoo, T. Thomson, A. Turchanin, C. David, H. H. Solak, *J. Micro-Nanolith. Mem.* **2009**, *8*, 021204.
- [21] T. Siegfried, Y. Ekinci, H. H. Solak, O. J. F. Martin, H. Sigg, *Appl. Phys. Lett.* **2011**, *99*, 263302.
- [22] M. J. Frisch, G. W. Trucks, H. B. Schlegel, G. E. Scuseria, M. A. Robb, J. R. Cheeseman, G. Scalmani, V. Barone, B. Mennucci, G. A. Petersson, H. Nakatsuji, M. Caricato, X. Li, H. P. Hratchian, A. F. Izmaylov, J. Bloino, G. Zheng, J. L. Sonnenberg, M. Hada, M. Ehara, K. Toyota, R. Fukuda, J. Hasegawa, M. Ishida, T. Nakajima, Y. Honda, O. Kitao, H. Nakai, T. Vreven, J. A. Montgomery, J. E. Peralta, F. Ogliaro, M. Bearpark, J. J. Heyd, E. Brothers, K. N. Kudin, V. N. Staroverov, R. Kobayashi, J. Normand, K. Raghavachari, A. Rendell, J. C. Burant, S. S. Iyengar, J. Tomasi, M. Cossi, N. Rega, J. M. Millam, M. Klene, J. E. Knox, J. B. Cross, V. Bakken, C. Adamo, J. Jaramillo, R. Gomperts, R. E. Stratmann, O. Yazyev, A. J. Austin, R. Cammi, C. Pomelli, J. W. Ochterski, R. L. Martin, K. Morokuma, V. G. Zakrzewski, G. A. Voth, P. Salvador, J. J. Dannenberg, S. Dapprich, A. D. Daniels, Ö. Farkas, J. B. Foresman, J. V. Ortiz, J. Cioslowski, D. J. Fox, in *Gaussian 09, Revision A.02*, Gaussian, Inc., Wallingford CT, **2009**.
- [23] Z. Weihua, H. Fischer, T. Schmid, R. Zenobi, O. J. F. Martin, *J. Phys. Chem. C* **2009**, *113*, 14672.
- [24] M. Kind, C. Woll, *Prog. Surf. Sci.* **2009**, *84*, 230.
- [25] J. C. Love, L. A. Estroff, J. K. Kriebel, R. G. Nuzzo, G. M. Whitesides, *Chem. Rev.* **2005**, *105*, 1103.
- [26] F. Chesneau, B. Schupbach, K. Szelagowska-Kunstman, N. Ballav, P. Cyganik, A. Terfort, M. Zharnikov, *Phys. Chem. Chem. Phys.* **2010**, *12*, 12123.
- [27] A. Shaporenko, M. Brunnbauer, A. Terfort, M. Grunze, M. Zharnikov, *J. Phys. Chem. B* **2004**, *108*, 14462.
- [28] T. Winkler, N. Ballav, H. Thomas, M. Zharnikov, A. Terfort, *Angew. Chem. Int. Ed.* **2008**, *47*, 7238.
- [29] H. G. M. Edwards, A. F. Johnson, I. R. Lewis, D. J. Maitland, N. Webb, *J. Mol. Struct.* **1992**, *268*, 363.
- [30] E. C. Le Ru, M. Meyer, E. Blackie, P. G. Etchegoin, *J. Raman Spectrosc.* **2008**, *39*, 1127.
- [31] M. Moskovits, *J. Chem. Phys.* **1982**, *77*, 4408.
- [32] A. T. Zayak, Y. S. Hu, H. Choo, J. Bokor, S. Cabrini, P. J. Schuck, J. B. Neaton, *Phys. Rev. Lett.* **2011**, *106*, 083003.
- [33] D. Bhandari, S. M. Wells, A. Polemi, I. I. Kravchenko, K. L. Shuford, M. J. Sepaniak, *J. Raman Spectrosc.* **2008**, *42*, 1916.
- [34] R. L. Aggarwal, L. W. Farrar, E. D. Diebold, D. L. Polla, *J. Raman Spectrosc.* **2009**, *40*, 1331.
- [35] A. Barhoumi, D. Zhang, N. J. Halas, *J. Am. Chem. Soc.* **2008**, *130*, 14040.
- [36] S. M. Morton, L. Jensen, *J. Am. Chem. Soc.* **2009**, *131*, 4090.

Supporting Information

Reusable plasmonic substrates fabricated by interference lithography: a platform for systematic sensing studies

Thomas Siegfried, Martin Kind, Andreas Terfort, Olivier J. F. Martin, Michael Zharnikov, Nirmalya Ballav and Hans Sigg

1. Raman assignments

Figure S1, similar to the manuscript, is shown for comparison of the Raman spectra with the Raman peak assignments of all molecules, given in Table S1.

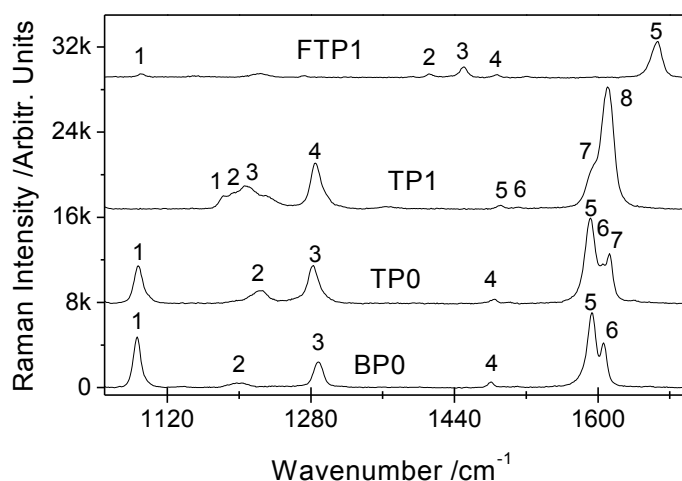


Figure S1. Experimental SERS spectra of the monomolecular films. A baseline correction has been applied.

Table S1. Positions, relative intensities, and assignments of the Raman peaks for the a) BP0, b) TP0, c) TP1 and d) FTP1 case.

a) BP0

Nr.	exp. WN /cm-1	exp.: I/a.u.	sim. WN /cm-1	sim. I/%	assignment
1	1084	s	1086	7	ν_{CS} , δ_{CH}
2	1198	w, broad	1187	6	δ_{CH}
3	1286	m	1273	69	ν_{CC} , δ_{CH}
4	1480	w	1480	11	δ_{CH}
5	1593	s	1599	100	ν_{CC} , δ_{CH}
6	1605	m	1609	52	ν_{CC} , δ_{CH}

b) TP0

Nr.	exp. WN /cm ⁻¹	exp.: I/a.u.	sim. WN /cm ⁻¹	sim. I/%	assignment
1	1087	m	1086	3	ν_{CS} , δ_{CC} , ν_{CH}
2	1223	m	1195	12	δ_{CH}
3	1281	m	1274	60	ν_{CC} , δ_{CH}
4	1483	w	1495	7	δ_{CH}
5	1590	s	1598	62	ν_{CC} , δ_{CH}
6	1604	m	1608	43	ν_{CC} , δ_{CH}
7	1612	s	1615	50	ν_{CC} , δ_{CH}

c) TP1

Nr.	exp. WN /cm ⁻¹	exp.: I/a.u.	sim. WN /cm ⁻¹	sim. I/%	assignment
1	1181	s	1184	2	δ_{CH}
2	1192	m	1190	19	δ_{CH}
3	1206	w	1206	2	ν_{CS} , ν_{CC} , τ_{CH}
4	1284	w	1274	50	ν_{CC} , δ_{CH}
5	1490	m	1506	5	δ_{CH}
6	1510	m	1525	1	ν_{CC} , δ_{CH}
7	1594	m	1608	75	ν_{CC} , δ_{CH}
8	1609	m	1613	100	ν_{CC} , δ_{CH}

d) FTP1

Nr.	exp. WN /cm ⁻¹	exp.: I/a.u.	sim. WN /cm ⁻¹	sim. I/%	assignment
1	1088	w	1076	5	ν_{CC} , ν_{CF} , τ_{CH2} , δ_{CSH}
2	1411	m	1424	30	ν_{CC} , ν_{CF}
3	1451	m	1458	18	ν_{CC} , ν_{CF}
4	1486	w	1488	5	ν_{CC}
5	1666	s	1641	100	ν_{CC} , δ_{CF}

Experimentally determined values (exp.) are compared to the simulation results (sim.). ν are stretching modes, δ are in-plane bending modes, γ are wagging modes and τ are twist modes. Signal strength: s=strong, m=medium, and w=weak.

2. Raman spectra

UVO cleaning: spectra are shown for TP0 (Figure S2) and TP1 (Figure S3)

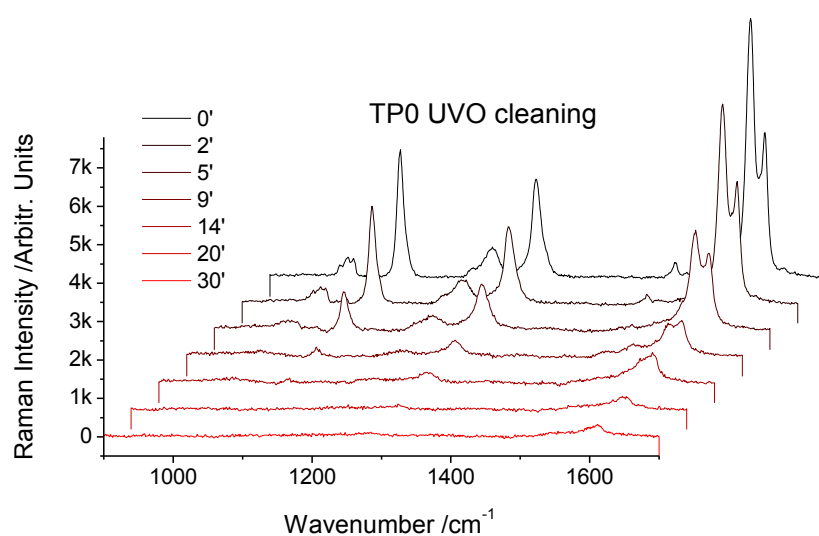


Figure S2. Raman spectra during the UVO cleaning of a monomolecular TP0 film. A baseline correction has been applied to all spectra.

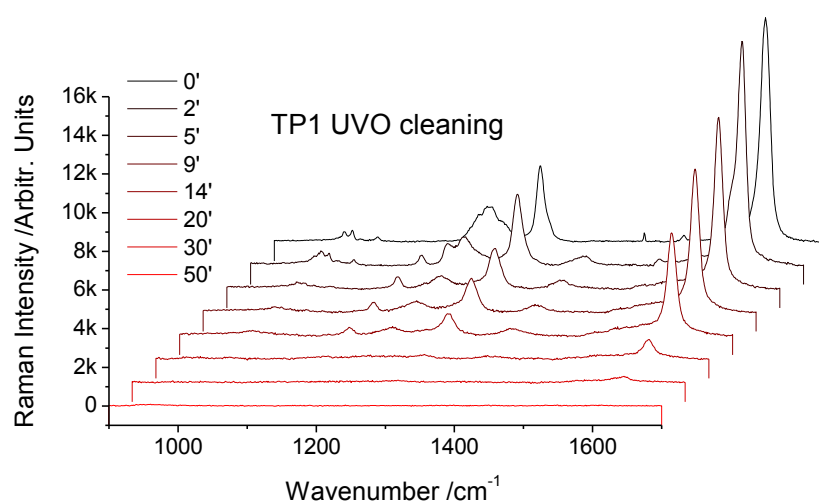


Figure S3. Raman spectra during the UVO cleaning of a monomolecular TP1 film. A baseline correction has been applied to all spectra.

Substrate Reusability: spectra are shown for TP0 (Figure S4) and TP1 (Figure S5)

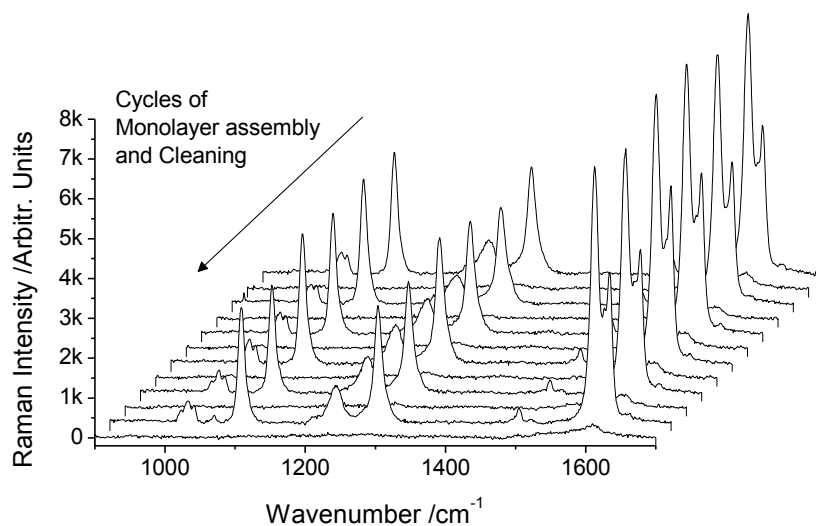


Figure S4. Raman spectra during the UVO cleaning of a monomolecular TP0 film. A baseline correction has been applied to all spectra.

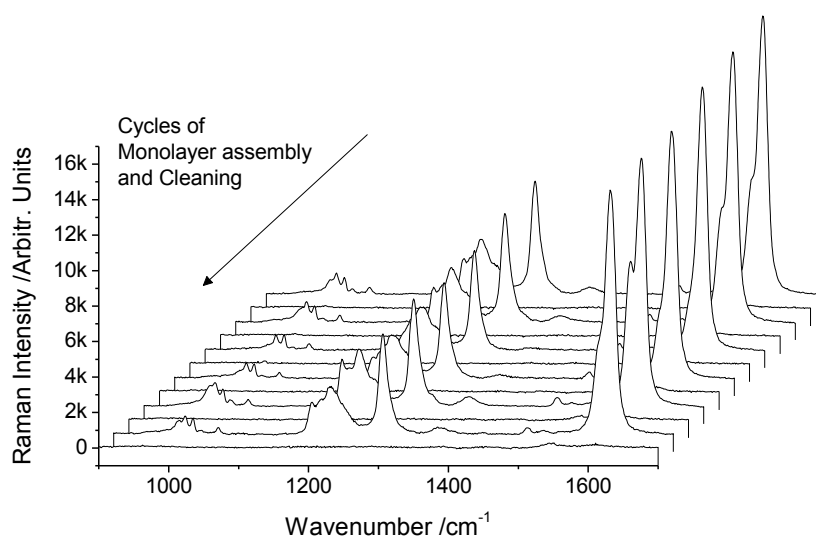


Figure S5. Raman spectra during the UVO cleaning of a monomolecular TP1 film. A baseline correction has been applied to all spectra.

- [1] Oshikane, Y.; Kataoka, T.; Okuda, M.; Hara, S.; Inoue, H.; Nakano, M., "Observation of nanostructure by scanning near-field optical microscope with small sphere probe." *Sci Technol Adv Mat* **2007**, *8* (3), 181-185.
- [2] Nagahara, S.; Takahata, K.; Nakagawa, S.; Murakami, T.; Takeda, K.; Nakamura, S.; Ueki, M.; Satake, M.; Ema, T.; Fujise, H.; Yonemitsu, H.; Seino, Y.; Nakagawa, S.; Asano, M.; Kitamura, Y.; Uchiyama, T.; Mimotogi, S.; Tominaga, M., "Resist process control for 32-nm logic node and beyond with NA > 1.30 immersion exposure tool." *Advances in Resist Materials and Processing Technology* **2009**, 7273.
- [3] Pan, L.; Park, Y.; Xiong, Y.; Ulin-Avila, E.; Wang, Y.; Zeng, L.; Xiong, S.; Rho, J.; Sun, C.; Bogy, D. B.; Zhang, X., "Maskless Plasmonic Lithography at 22 nm Resolution." *Sci. Rep.* **2011**, *1*, 175.
- [4] Haes, A. J.; Haynes, C. L.; McFarland, A. D.; Schatz, G. C.; Van Duyne, R. R.; Zou, S. L., "Plasmonic materials for surface-enhanced sensing and spectroscopy." *Mrs Bull* **2005**, *30* (5), 368-375.
- [5] Anker, J. N.; Hall, W. P.; Lyandres, O.; Shah, N. C.; Zhao, J.; Van Duyne, R. P., "Biosensing with plasmonic nanosensors." *Nat Mater* **2008**, *7* (6), 442-453.
- [6] Atwater, H. A.; Polman, A., "Plasmonics for improved photovoltaic devices." *Nat Mater* **2010**, *9* (3), 205-13.
- [7] The British Museum. (2013, 01.12.13). "Lycurgus Cup". Available: http://www.britishmuseum.org/explore/highlights/highlight_objects/pe_mla/t/the_lycurgus_cup.aspx
- [8] Freestone, I.; Meeks, N.; Sax, M.; Higgitt, C., "The Lycurgus Cup - A Roman nanotechnology." *Gold Bull* **2007**, *40* (4), 270-277.
- [9] Kern, A. M.; Martin, O. J. F., "Modeling near-field properties of plasmonic nanoparticles: a surface integral approach." *Plasmonics: Nanoimaging, Nanofabrication, and Their Applications V* **2009**, 7395, 739518.
- [10] Aroca, R. F., "Plasmon enhanced spectroscopy." *Phys Chem Chem Phys* **2013**, *15* (15), 5355-63.
- [11] Chalabi, H.; Brongersma, M. L., "Plasmonics: Harvest season for hot electrons." *Nat Nanotechnol* **2013**, *8* (4), 229-30.
- [12] Jain, S.; Hirst, D. G.; O'Sullivan, J. M., "Gold nanoparticles as novel agents for cancer therapy." *Br J Radiol* **2012**, *85* (1010), 101-13.
- [13] Neumann, O.; Feronti, C.; Neumann, A. D.; Dong, A.; Schell, K.; Lu, B.; Kim, E.; Quinn, M.; Thompson, S.; Grady, N.; Nordlander, P.; Oden, M.; Halas, N. J., "Compact solar autoclave based on steam generation using broadband light-harvesting nanoparticles." *Proc Natl Acad Sci U S A* **2013**, *110* (29), 11677-81.
- [14] Barnes, W. L., "Comparing experiment and theory in plasmonics." **2009**, *11* (11), 114002.
- [15] Barnes, W. L.; Dereux, A.; Ebbesen, T. W., "Surface plasmon subwavelength optics." *Nature* **2003**, *424* (6950), 824-30.
- [16] Biagioni, P.; Huang, J.-S.; Hecht, B., "Nanoantennas for Visible and Infrared Radiation." *Rep Prog Phys* **2012**, *75* (2), 024402.
- [17] Etchegoin, P. G.; Le Ru, E. C., "Basic Electromagnetic Theory of SERS": Wiley-VCH Verlag GmbH & Co. KGaA, **2010**.
- [18] Sönnichsen, C.; Franzl, T.; Wilk, T.; von Plessen, G.; Feldmann, J.; Wilson, O.; Mulvaney, P., "Drastic Reduction of Plasmon Damping in Gold Nanorods." *Phys Rev Lett* **2002**, *88* (7), 077402.
- [19] Hillenbrand, R.; Keilmann, F.; Hanarp, P.; Sutherland, D. S.; Aizpurua, J., "Coherent imaging of nanoscale plasmon patterns with a carbon nanotube optical probe." *Appl Phys Lett* **2003**, *83* (2), 368-370.

- [20] Vesseur, E. J. R.; Aizpurua, J.; Coenen, T.; Reyes-Coronado, A.; Batson, P. E.; Polman, A., "Plasmonic excitation and manipulation with an electron beam." *Mrs Bull* **2012**, 37 (8), 752-760.
- [21] Bosman, M.; Ye, E.; Tan, S. F.; Nijhuis, C. A.; Yang, J. K. W.; Marty, R.; Mlayah, A.; Arbouet, A.; Girard, C.; Han, M. Y., "Surface Plasmon Damping Quantified with an Electron Nanoprobe." *Sci Rep-Uk* **2013**, 3, 1312.
- [22] Myroshnychenko, V.; Nelayah, J.; Adamo, G.; Geuquet, N.; Rodriguez-Fernandez, J.; Pastoriza-Santos, I.; MacDonald, K. F.; Henrard, L.; Liz-Marzan, L. M.; Zheludev, N. I.; Kociak, M.; de Abajo, F. J. G., "Plasmon Spectroscopy and Imaging of Individual Gold Nanodecahedra: A Combined Optical Microscopy, Cathodoluminescence, and Electron Energy-Loss Spectroscopy Study." *Nano Lett* **2012**, 12 (8), 4172-4180.
- [23] Nicoletti, O.; de la Pena, F.; Leary, R. K.; Holland, D. J.; Ducati, C.; Midgley, P. A., "Three-dimensional imaging of localized surface plasmon resonances of metal nanoparticles." *Nature* **2013**, 502 (7469), 80.
- [24] Kane, Y., "Numerical solution of initial boundary value problems involving maxwell's equations in isotropic media." *Antennas and Propagation, IEEE Transactions on* **1966**, 14 (3), 302-307.
- [25] Etchegoin, P. G.; Le Ru, E. C.; Meyer, M., "An analytic model for the optical properties of gold." *J Chem Phys* **2006**, 125 (16), 164705.
- [26] Kern, A., "Realistic Modeling of 3D Plasmonic Systems: A Surface Integral Equation Approach," PhD thesis, Institut de microtechnique, EPFL, Lausanne, **2011**.
- [27] P.Monk, "*Finite Element Methods for Maxwell's Equations*": Oxford U. Press, **2003**.
- [28] Kottmann, J. P.; Martin, O. J. F., "Accurate solution of the volume integral equation for high-permittivity scatterers." *Ieee T Antenn Propag* **2000**, 48 (11), 1719-1726.
- [29] Hohenester, U.; Krenn, J., "Surface plasmon resonances of single and coupled metallic nanoparticles: A boundary integral method approach." *Phys Rev B* **2005**, 72 (19), 195429.
- [30] Kern, A. M.; Martin, O. J. F., "Surface integral formulation for 3D simulations of plasmonic and high permittivity nanostructures." *Journal of the Optical Society of America A: Optics and Image Science, and Vision* **2009**, 26 (4), 732-740.
- [31] Rodríguez-Oliveros, R.; Sánchez-Gil, J. A., "Localized surface-plasmon resonances on single and coupled nanoparticles through surface integral equations for flexible surfaces." *Opt. Express* **2011**, 19 (13), 12208-12219.
- [32] Gallinet, B.; Kern, A. M.; Martin, O. J. F., "Accurate and Versatile Modeling of Electromagnetic Scattering on Periodic Nanostructures with a Surface Integral Approach." *Journal of the Optical Society of America A: Optics and Image Science* **2010**, 27 (10), 2261-2271.
- [33] Kneipp, K.; Wang, Y.; Kneipp, H.; Perelman, L. T.; Itzkan, I.; Dasari, R. R.; Feld, M. S., "Single molecule detection using surface-enhanced Raman scattering (SERS)." *Phys Rev Lett* **1997**, 78 (9), 1667-1670.
- [34] Nie, S.; Emory, S. R., "Probing single molecules and single nanoparticles by surface-enhanced Raman scattering." *Science* **1997**, 275 (5303), 1102-1106.
- [35] Homola, J.; Yee, S. S.; Gauglitz, G., "Surface plasmon resonance sensors: review." *Sensors and Actuators, B: Chemical* **1999**, 54 (1), 3-15.
- [36] Haynes, C. L.; McFarland, A. D.; Zhao, L.; Van Duyne, R. P.; Schatz, G. C.; Gunnarsson, L.; Prikulis, J.; Kasemo, B.; Käll, M., "Nanoparticle Optics: The Importance of Radiative Dipole Coupling in Two-Dimensional Nanoparticle Arrays." *The Journal of Physical Chemistry B* **2003**, 107 (30), 7337-7342.
- [37] Le Ru, E. C.; Meyer, M.; Etchegoin, P. G., "Proof of single-molecule sensitivity in surface enhanced Raman scattering (SERS) by means of a two-analyte technique." *The journal of physical chemistry. B* **2006**, 110 (4), 1944-8.
- [38] Mahajan, S.; Cole, R. M.; Speed, J. D.; Pelfrey, S. H.; Russell, A. E.; Bartlett, P. N.; Barnett, S. M.; Baumberg, J. J., "Understanding the Surface-Enhanced Raman Spectroscopy Background." *The Journal of Physical Chemistry C* **2009**, 114 (16), 7242-7250.
- [39] Qin, L.; Zou, S.; Xue, C.; Atkinson, A.; Schatz, G. C.; Mirkin, C. A., "Designing, fabricating, and imaging Raman hot spots." **2006**, 103 (36), 13300-13303.

- [40] Tripp, R. A.; Dluhy, R. A.; Zhao, Y., "Novel nanostructures for SERS biosensing." *Nano Today* **2008**, 3 (3-4), 31-37.
- [41] Rycenga, M.; Cobley, C. M.; Zeng, J.; Li, W.; Moran, C. H.; Zhang, Q.; Qin, D.; Xia, Y., "Controlling the Synthesis and Assembly of Silver Nanostructures for Plasmonic Applications." *Chemical Reviews* **2011**, 111 (6), 3669-3712.
- [42] Willets, K. A.; Van Duyne, R. P., "Localized surface plasmon resonance spectroscopy and sensing." *Annual Review of Physical Chemistry* **2007**, 58, 267-297.
- [43] Aslan, K.; Gryczynski, I.; Malicka, J.; Matveeva, E.; Lakowicz, J. R.; Geddes, C. D., "Metal-enhanced fluorescence: an emerging tool in biotechnology." *Current Opinion in Biotechnology* **2005**, 16 (1), 55-62.
- [44] Anger, P.; Bharadwaj, P.; Novotny, L., "Enhancement and Quenching of Single-Molecule Fluorescence." *Phys Rev Lett* **2006**, 96 (11), 113002.
- [45] Aizpurua, J.; Taubner, T.; García de Abajo, F. J.; Brehm, M.; Hillenbrand, R., "Substrate-enhanced infrared near-fieldspectroscopy." *Opt. Express* **2008**, 16 (3), 1529-1545.
- [46] Le, F.; Brandl, D. W.; Urzhumov, Y. A.; Wang, H.; Kundu, J.; Halas, N. J.; Aizpurua, J.; Nordlander, P., "Metallic Nanoparticle Arrays: A Common Substrate for Both Surface-Enhanced Raman Scattering and Surface-Enhanced Infrared Absorption." *ACS Nano* **2008**, 2 (4), 707-718.
- [47] Ko, H.; Singamaneni, S.; Tsukruk, V. V., "Nanostructured Surfaces and Assemblies as SERS Media." *Small* **2008**, 4 (10), 1576-1599.
- [48] Sugawa, K.; Tamura, T.; Tahara, H.; Yamaguchi, D.; Akiyama, T.; Otsuki, J.; Kusaka, Y.; Fukuda, N.; Ushijima, H., "Metal-Enhanced Fluorescence Platforms Based on Plasmonic Ordered Copper Arrays: Wavelength Dependence of Quenching and Enhancement Effects." *ACS Nano* **2013**, 7 (11), 9997-10010.
- [49] Bardhan, R.; Grady, N. K.; Cole, J. R.; Joshi, A.; Halas, N. J., "Fluorescence enhancement by Au nanostructures: nanoshells and nanorods." *ACS Nano* **2009**, 3 (3), 744-52.
- [50] Jensen, L.; Aikens, C. M.; Schatz, G. C., "Electronic structure methods for studying surface-enhanced Raman scattering." *Chem Soc Rev* **2008**, 37 (5), 1061-1073.
- [51] Zayak, A. T.; Hu, Y. S.; Choo, H.; Bokor, J.; Cabrini, S.; Schuck, P. J.; Neaton, J. B., "Chemical Raman Enhancement of Organic Adsorbates on Metal Surfaces." *Phys Rev Lett* **2011**, 106 (8), 083003.
- [52] Natan, M. J., "Concluding Remarks Surface enhanced Raman scattering." *Faraday Discussions* **2006**, 132, 321-328.
- [53] Haynes, C. L.; Van Duyne, R. P., "Plasmon-Sampled Surface-Enhanced Raman Excitation Spectroscopy." *The Journal of Physical Chemistry B* **2003**, 107 (30), 7426-7433.
- [54] McFarland, A. D.; Young, M. A.; Dieringer, J. A.; Van Duyne, R. P., "Wavelength-Scanned Surface-Enhanced Raman Excitation Spectroscopy." *The Journal of Physical Chemistry B* **2005**, 109 (22), 11279-11285.
- [55] Aggarwal, R. L.; Farrar, L. W.; Polla, D. L., "Measurement of the absolute Stokes Raman cross sections of the longitudinal optical (LO) phonons of room-temperature GaP." *Solid State Commun* **2009**, 149 (33), 1330-1332.
- [56] Zhu, Y.; Dluhy, R. A.; Zhao, Y., "Development of silver nanorod array based fiber optic probes for SERS detection." *Sensors and Actuators B: Chemical* **2011**, 157 (1), 42-50.
- [57] Wang, H.; Levin, C. S.; Halas, N. J., "Nanosphere Arrays with Controlled Sub-10-nm Gaps as Surface-Enhanced Raman Spectroscopy Substrates." *Journal of the American Chemical Society* **2005**, 127 (43), 14992-14993.
- [58] Hu, W.; Zou, S., "Proposed Substrates for Reproducible Surface-Enhanced Raman Scattering Detection." *The Journal of Physical Chemistry C* **2011**, 115 (11), 4523-4532.
- [59] Le Ru, E. C.; Meyer, S. A.; Artur, C.; Etchegoin, P. G.; Grand, J.; Lang, P.; Maurel, F., "Experimental demonstration of surface selection rules for SERS on flat metallic surfaces." *Chem Commun* **2011**, 47 (13).
- [60] Mahurin, S. M.; John, J.; Sepaniak, M. J.; Dai, S., "A reusable surface-enhanced Raman scattering (SERS) substrate prepared by atomic layer deposition of alumina on a multi-layer gold and silver film." *Applied Spectroscopy* **2011**, 65 (4), 417-422.

- [61] Fan, M.; Andrade, G. F. S.; Brolo, A. G., "A review on the fabrication of substrates for surface enhanced Raman spectroscopy and their applications in analytical chemistry." *Anal Chim Acta* **2011**, 693 (1-2), 7-25.
- [62] Stoddart, P.; White, D., "Optical fibre SERS sensors." *Analytical and Bioanalytical Chemistry* **2009**, 394 (7), 1761-1774.
- [63] Gessner, R.; Rösch, P.; Kiefer, W.; Popp, J., "Raman spectroscopy investigation of biological materials by use of etched and silver coated glass fiber tips." *Biopolymers* **2002**, 67 (4-5), 327-330.
- [64] Deiss, F.; Sojic, N.; White, D.; Stoddart, P., "Nanostructured optical fibre arrays for high-density biochemical sensing and remote imaging." *Analytical and Bioanalytical Chemistry* **2010**, 396 (1), 53-71.
- [65] Ge, Rosch, P.; Petry, R.; Schmitt, M.; Strehle, M. A.; Kiefer, W.; Popp, J., "The application of a SERS fiber probe for the investigation of sensitive biological samples." *Analyst* **2004**, 129 (12), 1193-1199.
- [66] Raiber, K.; Terfort, A.; Benndorf, C.; Krings, N.; Strehblow, H.-H., "Removal of self-assembled monolayers of alkanethiolates on gold by plasma cleaning." *Surface Science* **2005**, 595 (1-3), 56-63.
- [67] Bhalla, V.; Carrara, S.; Stagni, C.; Samorì, B., "Chip cleaning and regeneration for electrochemical sensor arrays." *Thin Solid Films* **2010**, 518 (12), 3360-3366.
- [68] Mirsaleh-Kohan, N.; Bass, A. D.; Sanche, L., "X-ray Photoelectron Spectroscopy Analysis of Gold Surfaces after Removal of Thiolated DNA Oligomers by Ultraviolet/Ozone Treatment." *Langmuir* **2009**, 26 (9), 6508-6514.
- [69] Sadate, S., "Recycling of surface-enhanced Raman substrates by ultraviolet cleaning." *Opt. Eng.* **2010**, 49 (10), 106501.
- [70] Li, X.; Hu, H.; Li, D.; Shen, Z.; Xiong, Q.; Li, S.; Fan, H. J., "Ordered Array of Gold Semishells on TiO₂ Spheres: An Ultrasensitive and Recyclable SERS Substrate." *Acs Appl Mater Inter* **2012**, 4 (4), 2180-2185.
- [71] Sinha, G.; Depero, L. E.; Alessandri, I., "Recyclable SERS Substrates Based on Au-Coated ZnO Nanorods." *Acs Appl Mater Inter* **2011**, 3 (7), 2557-2563.
- [72] Mahurin, S. M.; John, J.; Sepaniak, M. J.; Dai, S., "A Reusable Surface-Enhanced Raman Scattering (SERS) Substrate Prepared by Atomic Layer Deposition of Alumina on a Multi-Layer Gold and Silver Film." *Appl. Spectrosc.* **2011**, 65 (4), 417-422.
- [73] Li, J. F.; Huang, Y. F.; Ding, Y.; Yang, Z. L.; Li, S. B.; Zhou, X. S.; Fan, F. R.; Zhang, W.; Zhou, Z. Y.; WuDe, Y.; Ren, B.; Wang, Z. L.; Tian, Z. Q., "Shell-isolated nanoparticle-enhanced Raman spectroscopy." *Nature* **2010**, 464 (7287), 392-395.
- [74] Rodriguez-Lorenzo, L.; Alvarez-Puebla, R. A.; de Abajo, F. J. G.; Liz-Marzan, L. M., "Surface Enhanced Raman Scattering Using Star-Shaped Gold Colloidal Nanoparticles." *J Phys Chem C* **2010**, 114 (16), 7336-7340.
- [75] Vigdeman, L.; Zubarev, E. R., "Starfruit-Shaped Gold Nanorods and Nanowires: Synthesis and SERS Characterization." *Langmuir* **2012**, 28 (24), 9034-9040.
- [76] Dickerson, E. B.; Dreaden, E. C.; Huang, X.; El-Sayed, I. H.; Chu, H.; Pushpanketh, S.; McDonald, J. F.; El-Sayed, M. A., "Gold nanorod assisted near-infrared plasmonic photothermal therapy (PPTT) of squamous cell carcinoma in mice." *Cancer Lett* **2008**, 269 (1), 57-66.
- [77] Auffan, M.; Rose, J.; Bottero, J. Y.; Lowry, G. V.; Jolivet, J. P.; Wiesner, M. R., "Towards a definition of inorganic nanoparticles from an environmental, health and safety perspective." *Nat Nanotechnol* **2009**, 4 (10), 634-41.
- [78] Nel, A. E.; Madler, L.; Velegol, D.; Xia, T.; Hoek, E. M.; Somasundaran, P.; Klaessig, F.; Castranova, V.; Thompson, M., "Understanding biophysicochemical interactions at the nano-bio interface." *Nat Mater* **2009**, 8 (7), 543-57.
- [79] Haynes, C. L.; Van Duyne, R. P., "Nanosphere Lithography: A Versatile Nanofabrication Tool for Studies of Size-Dependent Nanoparticle Optics." *The Journal of Physical Chemistry B* **2001**, 105 (24), 5599-5611.
- [80] Wen, X.; Xi, Z.; Jiao, X.; Yu, W.; Xue, G.; Zhang, D.; Lu, Y.; Wang, P.; Blair, S.; Ming, H., "Plasmonic Coupling Effect in Ag Nanocap-Nanohole Pairs for Surface-Enhanced Raman Scattering." *Plasmonics* **2013**, 8 (2), 225-231.

- [81] Hatab, N. A.; Hsueh, C.-H.; Gaddis, A. L.; Retterer, S. T.; Li, J.-H.; Eres, G.; Zhang, Z.; Gu, B., "Free-Standing Optical Gold Bowtie Nanoantenna with Variable Gap Size for Enhanced Raman Spectroscopy." *Nano Lett* **2010**, *10* (12), 4952-4955.
- [82] Jiao, X.; Goeckeritz, J.; Blair, S.; Oldham, M., "Localization of Near-Field Resonances in Bowtie Antennae: Influence of Adhesion Layers." *Plasmonics* **2009**, *4* (1), 37-50.
- [83] Corrigan, T. D.; Kolb, P. W.; Sushkov, A. B.; Drew, H. D.; Schmadel, D. C.; Phaneuf, R. J., "Optical plasmonic resonances in split-ring resonator structures: an improved LC model." *Opt Express* **2008**, *16* (24), 19850-64.
- [84] Unger, A.; Rietzler, U.; Berger, R.; Kreiter, M., "Sensitivity of Crescent-Shaped Metal Nanoparticles to Attachment of Dielectric Colloids." *Nano Lett* **2009**, *9* (6), 2311-2315.
- [85] Unger, A.; Kreiter, M., "Analyzing the Performance of Plasmonic Resonators for Dielectric Sensing." *The Journal of Physical Chemistry C* **2009**, *113* (28), 12243-12251.
- [86] Vogel, N.; Fischer, J.; Mohammadi, R.; Retsch, M.; Butt, H. J.; Landfester, K.; Weiss, C. K.; Kreiter, M., "Plasmon Hybridization in Stacked Double Crescents Arrays Fabricated by Colloidal Lithography." *Nano Lett* **2011**, *11* (2), 446-454.
- [87] Sherry, L. J.; Chang, S. H.; Schatz, G. C.; Van Duyne, R. P.; Wiley, B. J.; Xia, Y. N., "Localized surface plasmon resonance spectroscopy of single silver nanocubes." *Nano Lett* **2005**, *5* (10), 2034-2038.
- [88] Fischer, H.; Martin, O. J. F., "Engineering the optical response of plasmonic nanoantennas." *Opt Express* **2008**, *16* (12), 9144-9154.
- [89] Gu, Y.; Li, J.; Martin, O. J. F.; Gong, Q., "Controlling plasmonic resonances in binary metallic nanostructures." *J Appl Phys* **2010**, *107* (11), 114313.
- [90] Lindquist, N. C.; Nagpal, P.; McPeak, K. M.; Norris, D. J.; Oh, S.-H., "Engineering metallic nanostructures for plasmonics and nanophotonics." *Rep. Prog. Phys.* **2012**, *75* (3), 036501.
- [91] Sannomiya, T.; Sahoo, P. K.; Mahcicek, D. I.; Solak, H. H.; Hafner, C.; Grieshaber, D.; Vörös, J., "Biosensing by Densely Packed and Optically Coupled Plasmonic Particle Arrays." *Small* **2009**, *5* (16), 1889-1896.
- [92] Murray, W. A.; Barnes, W. L., "Plasmonic Materials." *Adv Mater* **2007**, *19* (22), 3771-3782.
- [93] Baumberg, J. J.; Kelf, T. A.; Sugawara, Y.; Cintra, S.; Abdelsalam, M. E.; Bartlett, P. N.; Russell, A. E., "Angle-Resolved Surface-Enhanced Raman Scattering on Metallic Nanostructured Plasmonic Crystals." *Nano Lett* **2005**, *5* (11), 2262-2267.
- [94] Duan, H.; Hu, H.; Kumar, K.; Shen, Z.; Yang, J. K. W., "Direct and Reliable Patterning of Plasmonic Nanostructures with Sub-10-nm Gaps." *ACS Nano* **2011**, *5* (9), 7593-7600.
- [95] Driskell, J. D.; Shanmukh, S.; Liu, Y.; Chaney, S. B.; Tang, X. J.; Zhao, Y. P.; Dluhy, R. A., "The Use of Aligned Silver Nanorod Arrays Prepared by Oblique Angle Deposition as Surface Enhanced Raman Scattering Substrates." *The Journal of Physical Chemistry C* **2008**, *112* (4), 895-901.
- [96] Liu, Y. J.; Chu, H. Y.; Zhao, Y. P., "Silver Nanorod Array Substrates Fabricated by Oblique Angle Deposition: Morphological, Optical, and SERS Characterizations." *The Journal of Physical Chemistry C* **2010**, *114* (18), 8176-8183.
- [97] Ye, D. X.; et al., "Growth of uniformly aligned nanorod arrays by oblique angle deposition with two-phase substrate rotation." **2004**, *15* (7), 817.
- [98] Zhao, Y.; Li, S.; Chaney, S.; Shanmukh, S.; Fan, J.; Dluhy, R.; Kisaalita, W., "Designing nanostructures for sensor applications." *Journal of Electronic Materials* **2006**, *35* (5), 846-851.
- [99] Fucetola, C. P., "Low-cost interference lithography." *J. Vac. Sci. Technol. B* **2009**, *27* (6), 2958.
- [100] Solak, H. H., "Nanolithography with coherent extreme ultraviolet light." *J Phys D Appl Phys* **2006**, *39* (10), R171-R188.
- [101] Guo, L. J., "Nanoimprint lithography: Methods and material requirements." *Adv Mater* **2007**, *19* (4), 495-513.
- [102] Zhu, J.; Ren, Y. J., "Negative curvature dependent plasmonic coupling and local field enhancement of crescent silver nanostructure." *J Nanopart Res* **2012**, *14* (12).

- [103] Wang, Y. F.; Zhou, W. J.; Liu, A. J.; Chen, W.; Fu, F. Y.; Yan, X. Y.; Jiang, B.; Xue, Q. K.; Zheng, W. H., "Optical properties of the crescent and coherent applications." *Opt Express* **2011**, 19 (9), 8303-8311.
- [104] Aubry, A.; Lei, D. Y.; Maier, S. A.; Pendry, J. B., "Broadband plasmonic device concentrating the energy at the nanoscale: The crescent-shaped cylinder." *Phys Rev B* **2010**, 82 (12), 125430.
- [105] Aubry, A.; Lei, D. Y.; Fernández-Domínguez, A. I.; Sonnefraud, Y.; Maier, S. A.; Pendry, J. B., "Plasmonic Light-Harvesting Devices over the Whole Visible Spectrum." *Nano Lett* **2010**, 10 (7), 2574-2579.
- [106] Luo, Y.; Lei, D. Y.; Maier, S. A.; Pendry, J. B., "Broadband Light Harvesting Nanostructures Robust to Edge Bluntness." *Phys Rev Lett* **2012**, 108 (2), 023901.
- [107] Atre, A. C.; García-Etxarri, A.; Alaeian, H.; Dionne, J. A., "Toward high-efficiency solar upconversion with plasmonic nanostructures." **2012**, 14 (2), 024008.
- [108] Shen, Y.; Liu, M.; Li, J.; Chen, X.; Xu, H.-X.; Zhu, Q.; Wang, X.; Jin, C., "Extraordinary Transmission of Three-Dimensional Crescent-like Holes Arrays." *Plasmonics* **2012**, 7 (2), 221-227.
- [109] Nidal, A.; Mohamed, O., "A Crescent Shaped Split Ring Resonator to Form a New Metamaterial." *International Journal of Engineering and Technology* **2012**, 2 (10), 1702-1706.
- [110] Atre, A. C.; García-Etxarri, A.; Alaeian, H.; Dionne, J. A., "A Broadband Negative Index Metamaterial at Optical Frequencies." *Adv Opt Mater* **2013**, 1 (4), 327-333.
- [111] Shumaker-Parry, J. S.; Rochholz, H.; Kreiter, M., "Fabrication of Crescent-Shaped Optical Antennas." *Adv Mater* **2005**, 17 (17), 2131-2134.
- [112] Wu, L. Y.; Ross, B. M.; Lee, L. P., "Optical Properties of the Crescent-Shaped Nanohole Antenna." *Nano Lett* **2009**, 9 (5), 1956-1961.
- [113] Su, K. H.; Wei, Q. H.; Zhang, X.; Mock, J. J.; Smith, D. R.; Schultz, S., "Interparticle coupling effects on plasmon resonances of nanogold particles." *Nano Lett* **2003**, 3 (8), 1087-1090.
- [114] Zuloaga, J.; Prodan, E.; Nordlander, P., "Quantum Description of the Plasmon Resonances of a Nanoparticle Dimer." *Nano Lett* **2009**, 9 (2), 887-891.
- [115] Ward, D. R.; Huser, F.; Pauly, F.; Cuevas, J. C.; Natelson, D., "Optical rectification and field enhancement in a plasmonic nanogap." *Nat Nano* **2010**, 5 (10), 732-736.
- [116] Duan, H.; Fernández-Domínguez, A. I.; Bosman, M.; Maier, S. A.; Yang, J. K. W., "Nanoplasmonics: Classical down to the Nanometer Scale." *Nano Lett* **2012**, 12 (3), 1683-1689.
- [117] Duan, H.; Manfrinato, V. R.; Yang, J. K. W.; Winston, D.; Cord, B. M.; Berggren, K. K., "Metrology for electron-beam lithography and resist contrast at the sub-10 nm scale." *Journal of Vacuum Science & Technology B: Microelectronics and Nanometer Structures* **2010**, 28 (6), 11.
- [118] Bora, M.; Fasenfest, B. J.; Behymer, E. M.; Chang, A. S. P.; Nguyen, H. T.; Britten, J. A.; Larson, C. C.; Chan, J. W.; Miles, R. R.; Bond, T. C., "Plasmon Resonant Cavities in Vertical Nanowire Arrays." *Nano Lett* **2010**, 10 (8), 2832-2837.
- [119] Ciraci, C.; Hill, R. T.; Mock, J. J.; Urzhumov, Y.; Fernandez-Dominguez, A. I.; Maier, S. A.; Pendry, J. B.; Chilkoti, A.; Smith, D. R., "Probing the Ultimate Limits of Plasmonic Enhancement." *Science* **2012**, 337 (6098), 1072-1074.
- [120] Im, H.; Bantz, K. C.; Lindquist, N. C.; Haynes, C. L.; Oh, S.-H., "Vertically Oriented Sub-10-nm Plasmonic Nanogap Arrays." *Nano Lett* **2010**, 10 (6), 2231-2236.
- [121] Stosch, R.; Yaghobian, F.; Weimann, T.; Brown, R. J. C.; Milton, M. J. T.; Güttler, B., "Lithographical gap-size engineered nanoarrays for surface-enhanced Raman probing of biomarkers." *Nanotechnology* **2011**, 22 (10), 105303.
- [122] Theiss, J.; Pavaskar, P.; Echternach, P. M.; Muller, R. E.; Cronin, S. B., "Plasmonic Nanoparticle Arrays with Nanometer Separation for High-Performance SERS Substrates." *Nano Lett* **2010**, 10 (8), 2749-2754.
- [123] Cialla, D.; März, A.; Böhme, R.; Theil, F.; Weber, K.; Schmitt, M.; Popp, J., "Surface-Enhanced Raman Spectroscopy (SERS): Progress and Trends." *Analytical and Bioanalytical Chemistry* **2012**, 403 (1), 27-54.

- [124] Feichtner, T.; Selig, O.; Kiunke, M.; Hecht, B., "Evolutionary Optimization of Optical Antennas." *Phys Rev Lett* **2012**, *109* (12), 127701.
- [125] Nagpal, P.; Lindquist, N. C.; Oh, S.-H.; Norris, D. J., "Ultrasooth Patterned Metals for Plasmonics and Metamaterials." *Science* **2009**, *325* (5940), 594-597.
- [126] Im, H.; Bantz, K. C.; Lee, S. H.; Johnson, T. W.; Haynes, C. L.; Oh, S.-H., "Self-Assembled Plasmonic Nanoring Cavity Arrays for SERS and LSPR Biosensing." *Advanced Materials (Weinheim, Germany)* **2013**, *25* (19), 2678-2685.
- [127] Otto, A., "On the significance of Shalaev's 'hot spots' in ensemble and single-molecule SERS by adsorbates on metallic films at the percolation threshold." *Journal of Raman Spectroscopy* **2006**, *37* (9), 937-947.
- [128] Liu, K.; Avouris, P.; Bucchignano, J.; Martel, R.; Sun, S.; Michl, J., "Simple fabrication scheme for sub-10 nm electrode gaps using electron-beam lithography." *Appl Phys Lett* **2002**, *80* (5), 865.
- [129] Zhu, W.; Banaee, M. G.; Wang, D.; Chu, Y.; Crozier, K. B., "Lithographically Fabricated Optical Antennas with Gaps Well Below 10 nm." *Small* **2010**, *7* (13), 1761-1766.
- [130] Dirk, S. M.; Howell, S. W.; Zmuda, S.; Childs, K.; Blain, M.; Simonson, R. J.; Wheeler, D. R., "Novel one-dimensional nanogap created with standard optical lithography and evaporation procedures." *Nanotechnology* **2005**, *16* (10), 1983-1985.
- [131] Kanda, A.; Wada, M.; Hamamoto, Y.; Ootuka, Y., "Simple and controlled fabrication of nanoscale gaps using double-angle evaporation." *Physica E: Low-Dimensional Systems and Nanostructures* **2005**, *29* (3-4), 707-711.
- [132] Bai, J. G.; Yeo, W. H.; Chung, J. H., "Nanostructured biosensing platform - Shadow edge lithography for high-throughput nanofabrication." *Lab on a Chip - Miniaturisation for Chemistry and Biology* **2009**, *9* (3), 449-455.
- [133] Yu, H. Y.; Ah, C. S.; Baek, I. B.; Kim, A.; Yang, J. H.; Ahn, C. G.; Park, C. W.; Kim, B. H., "Nanogap array fabrication using doubly clamped freestanding silicon nanowires and angle evaporations." *Etri J* **2009**, *31* (4), 351-356.
- [134] De Poortere, E. P.; Stormer, H. L.; Huang, L. M.; Wind, S. J.; O'Brien, S.; Huang, M.; Hone, J., "Single-walled carbon nanotubes as shadow masks for nanogap fabrication." *Appl Phys Lett* **2006**, *88* (14), 143124-3.
- [135] Hadeed, F. O.; Durkan, C., "Controlled fabrication of 1-2 nm nanogaps by electromigration in gold and gold-palladium nanowires." *Appl Phys Lett* **2007**, *91* (12), 123120-3.
- [136] McCarty, G. S., "Molecular Lithography for Wafer-Scale Fabrication of Molecular Junctions." *Nano Lett* **2004**, *4* (8), 1391-1394.
- [137] Negishi, R.; Hasegawa, T.; Terabe, K.; Aono, M.; Ebihara, T.; Tanaka, H.; Ogawa, T., "Fabrication of nanoscale gaps using a combination of self-assembled molecular and electron beam lithographic techniques." *Appl Phys Lett* **2006**, *88* (22), 223111-3.
- [138] Søndergaard, T.; Siahpoush, V.; Jung, J., "Coupling light into and out from the surface plasmon polaritons of a nanometer-thin metal film with a metal nanostrip." *Phys Rev B* **2012**, *86* (8), 085455.
- [139] Belotelov, V. I.; Kalish, A. N.; Zvezdin, A. K.; Gopal, A. V.; Vengurlekar, A. S., "Fabry Perot plasmonic structures for nanophotonics." *Journal of the Optical Society of America B: Optical Physics* **2012**, *29* (3), 294-299.
- [140] Kern, J.; Großmann, S.; Tarakina, N. V.; Häckel, T.; Emmerling, M.; Kamp, M.; Huang, J.-S.; Biagioni, P.; Prangsma, J. C.; Hecht, B., "Atomic-Scale Confinement of Resonant Optical Fields." *Nano Lett* **2012**, *12* (11), 5504-5509.
- [141] Luk'yanchuk, B.; Zheludev, N. I.; Maier, S. A.; Halas, N. J.; Nordlander, P.; Giessen, H.; Chong, C. T., "The Fano resonance in plasmonic nanostructures and metamaterials." *Nat Mater* **2010**, *9* (9), 707-715.
- [142] Ye, J.; Wen, F.; Sobhani, H.; Lassiter, J. B.; Dorpe, P. V.; Nordlander, P.; Halas, N. J., "Plasmonic Nanoclusters: Near Field Properties of the Fano Resonance Interrogated with SERS." *Nano Lett* **2012**, *12* (3), 1660-1667.
- [143] Gallinet, B.; Martin, O. J. F., "Ab initio theory of Fano resonances in plasmonic nanostructures and metamaterials." *Phys Rev B* **2011**, *83* (23), 235427.
- [144] Gallinet, B.; Martin, O. J. F., "Ab initio engineering of Fano resonances." *Plasmonics: Metallic Nanostructures and Their Optical Properties IX* **2011**, 8096.

- [145] Gallinet, B.; Martin, O. J. F., "Analytical Description of Fano Resonances in Plasmonic Nanostructures." *Fourth International Workshop on Theoretical and Computational Nanophotonics (Tacona-Photonics 2011)* **2011**, 1398.
- [146] Gallinet, B.; Martin, O. J. F., "Relation between near-field and far-field properties of plasmonic Fano resonances." *Opt Express* **2011**, 19 (22), 22167-22175.
- [147] Svedendahl, M.; Kall, M., "Fano Interference between Localized Plasmons and Interface Reflections." *ACS Nano* **2012**, 6 (8), 7533-7539.
- [148] Min, Q.; Pang, Y.; Collins, D. J.; Kuklev, N. A.; Gottselig, K.; Steuerman, D. W.; Gordon, R., "Substrate-based platform for boosting the surface-enhanced Raman of plasmonic nanoparticles." *Opt. Express* **2011**, 19 (2), 1648-1655.
- [149] Seok, T. J.; Jamshidi, A.; Kim, M.; Dhuey, S.; Lakhani, A.; Choo, H.; Schuck, P. J.; Cabrini, S.; Schwartzberg, A. M.; Bokor, J.; Yablonovitch, E.; Wu, M. C., "Radiation Engineering of Optical Antennas for Maximum Field Enhancement." *Nano Lett* **2011**, 11 (7), 2606-2610.
- [150] Shoute, L. C. T., "Multilayer Substrate-Mediated Tuning Resonance of Plasmon and SERS EF of Nanostructured Silver." *ChemPhysChem* **2010**, 11 (12), 2539-2545.
- [151] Hou, Y.; Xu, J.; Zhang, X.; Yu, D., "SERS on periodic arrays of coupled quadrate-holes and squares." *Nanotechnology* **2010**, 21 (19), 195203.
- [152] Ahmed, A.; Gordon, R., "Directivity Enhanced Raman Spectroscopy Using Nanoantennas." *Nano Lett* **2011**, 11 (4), 1800-1803.
- [153] Ahmed, A.; Gordon, R., "Single Molecule Directivity Enhanced Raman Scattering using Nanoantennas." *Nano Lett* **2012**, 12 (5), 2625-2630.
- [154] Zhu, W.; Wang, D.; Crozier, K. B., "Direct Observation of Beamed Raman Scattering." *Nano Lett* **2012**, 12 (12), 6235-6243.
- [155] Wang, D.; Zhu, W.; Chu, Y.; Crozier, K. B., "High Directivity Optical Antenna Substrates for Surface Enhanced Raman Scattering." *Adv Mater* **2012**, 24 (32), 4376-4380.
- [156] Chu, Y.; Zhu, W.; Wang, D.; Crozier, K. B., "Beamed Raman: directional excitation and emission enhancement in a plasmonic crystal double resonance SERS substrate." *Opt. Express* **2011**, 19 (21), 20054-20068.
- [157] Lodewijks, K.; Ryken, J.; Van Roy, W.; Borghs, G.; Lagae, L.; Van Dorpe, P., "Tuning the Fano Resonance Between Localized and Propagating Surface Plasmon Resonances for Refractive Index Sensing Applications." *Plasmonics* **2013**, 8 (3), 1379-1385.
- [158] Christ, A.; Zentgraf, T.; Tikhodeev, S. G.; Gippius, N. A.; Martin, O. J. F.; Kuhl, J.; Giessen, H., "Interaction between localized and delocalized surface plasmon polariton modes in a metallic photonic crystal." *physica status solidi (b)* **2006**, 243 (10), 2344-2348.
- [159] L  v  que, G.; Martin, O. J. F., "Optical interactions in a plasmonic particle coupled to a metallic film." *Opt. Express* **2006**, 14 (21), 9971-9981.
- [160] Chu, Y. Z.; Banaee, M. G.; Crozier, K. B., "Double-Resonance Plasmon Substrates for Surface-Enhanced Raman Scattering with Enhancement at Excitation and Stokes Frequencies." *ACS Nano* **2010**, 4 (5), 2804-2810.
- [161] Habteyes, T. G.; Dhuey, S.; Wood, E.; Gargas, D.; Cabrini, S.; Schuck, P. J.; Alivisatos, A. P.; Leone, S. R., "Metallic Adhesion Layer Induced Plasmon Damping and Molecular Linker as a Nondamping Alternative." *ACS Nano* **2012**, 6 (6), 5702-5709.
- [162] Dawson, P.; Alexander, K. B.; Thompson, J. R.; Haas, J. W.; Ferrell, T. L., "Influence of Metal Grain-Size on Surface-Enhanced Raman-Scattering." *Phys Rev B* **1991**, 44 (12), 6372-6381.
- [163] Nagpal, P.; Lindquist, N. C.; Oh, S. H.; Norris, D. J., "Ultrasmooth Patterned Metals for Plasmonics and Metamaterials." *Science* **2009**, 325 (5940), 594-597.
- [164] West, P. R.; Ishii, S.; Naik, G. V.; Emani, N. K.; Shalae, V. M.; Boltasseva, A., "Searching for better plasmonic materials." *Laser Photonics Rev* **2010**, 4 (6), 795-808.
- [165] Abdelsalam, M.; Bartlett, P. N.; Russell, A. E.; Baumberg, J. J.; Calvo, E. J.; Tognalli, N. G.; Fainstein, A., "Quantitative Electrochemical SERS of Flavin at a Structured Silver Surface." *Langmuir* **2008**, 24 (13), 7018-7023.
- [166] Fromm, D. P.; Sundaramurthy, A.; Schuck, P. J.; Kino, G.; Moerner, W. E., "Gap-Dependent Optical Coupling of Single Bowtie Nanoantennas Resonant in the Visible." *Nano Lett* **2004**, 4 (5), 957-961.

- [167] Cui, B.; Clime, L.; Li, K.; Veres, B., "Fabrication of Large Area Nanoprism Arrays and their Application for Surface Enhanced Raman Spectroscopy." *Nanotechnology* **2008**, *19* (14), 145302.
- [168] Aouani, H.; Wenger, J.; Gèrard, D.; Rigneault, H.; Devaux, E.; Ebbesen, T. W.; Mahdavi, F.; Xu, T.; Blair, S., "Crucial Role of the Adhesion Layer on the Plasmonic Fluorescence Enhancement." *ACS Nano* **2009**, *3* (7), 2043-2048.
- [169] Barchiesi, D.; Macías, D.; Belmar-Letellier, L.; van Labeke, D.; Lamy de la Chapelle, M.; Toury, T.; Kremer, E.; Moreau, L.; Grosjes, T., "Plasmonics: Influence of the Intermediate (or Stick) Layer on the Efficiency of Sensors." *Applied Physics B: Lasers and Optics* **2008**, *93* (1), 177-181.
- [170] Najiminaini, M.; Vasefi, F.; Kaminska, B.; Carson, J. J. L., "Optical Resonance Transmission Properties of Nano-hole Arrays in a Gold Film: Effect of Adhesion Layer." *Opt. Express* **2011**, *19* (27), 26186-26197.
- [171] Sexton, B. A.; Feltis, B. N.; Davis, T. J., "Characterisation of Gold Surface Plasmon Resonance Sensor Substrates." *Sensors and Actuators, A: Physical* **2008**, *141* (2), 471-475.
- [172] Lahiri, B.; Dylewicz, R.; De La Rue, R. M.; Johnson, N. P., "Impact of Titanium Adhesion Layers on the Response of Arrays of Metallic Split-Ring Resonators (SRRs)." *Opt. Express* **2010**, *18* (11), 11202-11208.
- [173] Lamy de la Chapelle, M.; Shen, H.; Guillot, N.; Frémaux, B.; Guelorget, B.; Toury, T., "New Gold Nanoparticles Adhesion Process Opening the Way of Improved and Highly Sensitive Plasmonics Technologies." *Plasmonics* **2012**, *8* (2), 411-415.
- [174] Kern, A. M.; Meixner, A. J.; Martin, O. J. F., "Molecule-Dependent Plasmonic Enhancement of Fluorescence and Raman Scattering near Realistic Nanostructures." *ACS Nano* **2012**, *6* (11), 9828-9836.
- [175] Djaker, N.; Hostein, R.; Devaux, E.; Ebbesen, T. W.; Rigneault, H.; Wenger, J., "Surface Enhanced Raman Scattering on a Single Nanometric Aperture." *J Phys Chem C* **2010**, *114* (39), 16250-16256.
- [176] Roxworthy, B. J.; Toussaint, K. C., "Plasmonic Nanotweezers: Strong Influence of Adhesion Layer and Nanostructure Orientation on Trapping Performance." *Opt. Express* **2012**, *20* (9), 9591-9603.
- [177] Jeppesen, C.; Mortensen, N. A.; Kristensen, A., "The Effect of Ti and ITO Adhesion Layers on Gold Split-ring Resonators." *Appl Phys Lett* **2010**, *97* (26), 263103-3.
- [178] Goss, C. A.; Charych, D. H.; Majda, M., "Application of (3-mercaptopropyl)-trimethoxysilane as a Molecular Adhesive in the Fabrication of Vapor-deposited Gold Electrodes on Glass Substrates." *Analytical Chemistry* **1991**, *63* (1), 85-88.
- [179] Auzelyte, V.; Dais, C.; Farquet, P.; Grutzmacher, D.; Heyderman, L. J.; Luo, F.; Olliges, S.; Padeste, C.; Sahoo, P. K.; Thomson, T.; Turchanin, A.; David, C.; Solak, H. H., "Extreme ultraviolet interference lithography at the Paul Scherrer Institut." *Journal of Micro/Nanolithography, MEMS and MOEMS* **2009**, *8* (2), 021204-10.
- [180] Ito, T.; Okazaki, S., "Pushing the limits of lithography." *Nature* **2000**, *406* (6799), 1027-1031.
- [181] Paul Scherrer Institute. (2013, 01.12.13). "Extreme Ultraviolet Interference Lithography". Available: <http://www.psi.ch/sls/xil/>
- [182] Wang, L.; Terhalle, B.; Guzenko, V. A.; Farhan, A.; Hojeij, M.; Ekinci, Y., "Generation of high-resolution kagome lattice structures using extreme ultraviolet interference lithography." *Appl Phys Lett* **2012**, *101* (9), 093104-5.
- [183] He, Y.; Fu, J.; Zhao, Y., "Oblique angle deposition and its applications in plasmonics." *Frontiers of Physics* **2013**, *9* (1), 47-59.
- [184] Le Ru, E. C.; Blackie, E.; Meyer, M.; Etchegoin, P. G., "Surface Enhanced Raman Scattering Enhancement Factors: A Comprehensive Study." *The Journal of Physical Chemistry C* **2007**, *111* (37), 13794-13803.
- [185] Zhou, X. D.; Liu, K. Y.; Knoll, W.; Quan, C. G.; Zhang, N., "3D Profile Simulation of Metal Nanostructures Obtained by Closely Packed Nanosphere Lithography." *Plasmonics* **2010**, *5* (2), 141-148.

- [186] Müller-Pfeiffer, S.; van Kranenburg, H.; Lodder, J. C., "A two-dimensional Monte Carlo model for thin film growth by oblique evaporation: simulation of two-component systems for the example of Co-Cr." *Thin Solid Films* **1992**, *213* (1), 143-153.
- [187] Yang, C.-C.; Chen, W.-C., "The Structures and Properties of Hydrogen Silsesquioxane (HSQ) Films Produced by Thermal Curing." *J Mater Chem* **2002**, *12* (4), 1138-1141.
- [188] Johnson, P. B.; Christy, R. W., "Optical Constants of the Noble Metals." *Phys. Rev. B* **1972**, *6* (12), 4370-4379.
- [189] Gallinet, B.; Siegfried, T.; Sigg, H.; Nordlander, P.; Martin, O. J. F., "Plasmonic Radiance: Probing Structure at the Ångström Scale with Visible Light." *Nano Lett* **2012**, *13* (2), 497-503.
- [190] Bravo-Abad, J.; Degiron, A.; Przybilla, F.; Genet, C.; Garcia-Vidal, F. J.; Martin-Moreno, L.; Ebbesen, T. W., "How light emerges from an illuminated array of subwavelength holes." *Nat. Phys.* **2006**, *2* (2), 120-123.
- [191] Fernández-Domínguez, A. I.; García-Vidal, F. J.; Martín-Moreno, L., "Resonant transmission of light through finite arrays of slits." *Physical Review B* **2007**, *76* (23), 235430.
- [192] Kolomenski, A.; Kolomenskii, A.; Noel, J.; Peng, S.; Schuessler, H., "Propagation length of surface plasmons in a metal film with roughness." *Appl. Opt.* **2009**, *48* (30), 5683-5691.
- [193] Tadashi, I.; et al., "Real-time transmission electron microscope observation of gold nanoclusters diffusing into silicon at room temperature." *Nanotechnology* **2009**, *20* (6), 065705.
- [194] Liu, N.; Hentschel, M.; Weiss, T.; Alivisatos, A. P.; Giessen, H., "Three-Dimensional Plasmon Rulers." *Science* **2011**, *332* (6036), 1407-1410.
- [195] Teperik, T. V.; Nordlander, P.; Aizpurua, J.; Borisov, A. G., "Robust Subnanometric Plasmon Ruler by Rescaling of the Nonlocal Optical Response." *Phys Rev Lett* **2013**, *110* (26).
- [196] Solak, H. H.; Dais, C.; Clube, F., "Displacement Talbot lithography: a new method for high-resolution patterning of large areas." *Opt. Express* **2011**, *19* (11), 10686-10691.
- [197] Chen, X. S.; Park, H. R.; Pelton, M.; Piao, X. J.; Lindquist, N. C.; Im, H.; Kim, Y. J.; Ahn, J. S.; Ahn, K. J.; Park, N.; Kim, D. S.; Oh, S. H., "Atomic layer lithography of wafer-scale nanogap arrays for extreme confinement of electromagnetic waves." *Nat Commun* **2013**, *4*, 2361.
- [198] Billings, L., "Exotic optics: Metamaterial world." *Nature* **2013**, *500* (7461), 138-40.
- [199] Sa, J.; Tagliabue, G.; Friedli, P.; Szlachetko, J.; Rittmann-Frank, M. H.; Santomauro, F. G.; Milne, C. J.; Sigg, H., "Direct observation of charge separation on Au localized surface plasmons." *Energy & Environmental Science* **2013**, *6* (12), 3584-3588.
- [200] Knight, M. W.; Sobhani, H.; Nordlander, P.; Halas, N. J., "Photodetection with Active Optical Antennas." *Science* **2011**, *332* (6030), 702-704.
- [201] Mubeen, S.; Lee, J.; Singh, N.; Kramer, S.; Stucky, G. D.; Moskovits, M., "An autonomous photosynthetic device in which all charge carriers derive from surface plasmons." *Nat Nanotechnol* **2013**, *8* (4), 247-251.
- [202] Giugni, A.; Torre, B.; Toma, A.; Francardi, M.; Malerba, M.; Alabastri, A.; Proietti Zaccaria, R.; Stockman, M. I.; Di Fabrizio, E., "Hot-electron nanoscopy using adiabatic compression of surface plasmons." *Nat Nano* **2013**, *8* (11), 845-852.

Acknowledgements

Conducting my PhD thesis at PSI in Switzerland was a wonderful experience and I like to acknowledge the people that have contributed and inspired me during to this nice time.

First of all, I would like to thank Hans Sigg for giving me the opportunity to come to PSI and work in this inspiring environment. His support and effort to extend my physical approach to fundamental research, while coming from an engineering background, helped me a lot in achieving the results and manuscripts that have assembled during the time. Thank you as well for the freedom and trust I had in following my ideas and designing the experiments. I further like to thank Olivier Martin for his support of my project and the welcoming in his group at the Nanophotonics and Metrology Laboratory at EPFL. His great interest and contribution to the work has led to many fruitful discussions and improved manuscripts being able to publish in high impact journals.

I thank Harun Solak for initiating and getting the SNF project funded, as well as his initial support and the essentials for the ballistic simulation code. To this end, I'm also grateful to Pratap Sahoo for his preliminary experiments on nanogap arrays.

I thank Yasin Ekinici for the support at the XIL-II beamline that allowed me to flexibly plan my exposures, and his pushing interest in the project. I thank Michaela Vockenhuber for her warm welcoming at the XIL-II beamline and her steady assistance in solving all technical challenges. I thank Stefan Stutz for the mechanical realization of experimental equipment and his collegial friendship. I thank Benjamin Gallinet for his support with the SIE simulations and the discussions leading to the essence of crescent Fano resonances. I thank Shourya Dutta-Gupta for his support and the discussions on cavity resonances and total absorption. I acknowledge the help of the following people, without order, that have helped me to conduct my research: Anja Weber, Vitaliy Guzenko, Mohamad Hojeij, Konrad Vogelsang, Celestino Padeste, Arnold Lücke, Christian Spreu, Eugen Deckardt, Rolf Schelldorfer, Thomas Neiger and David Desscan. I'm also grateful to Edith Meisel, Pierette Paulou and Cathy Buchs for generating such a nice atmosphere in the groups and reminding us of the important dates and obligations. I thank Richard Ernst for an inspiring day after inviting me to use his private Raman equipment, reactivating the coffee machine and the introduction to Tibetan art.

I also thank the rest of the LMN and NAM members for making the time memorable and fun, in particular: Elena, Peter, Stephan, Richard, Arne and Ismo for the relaxing coffee breaks and many funny evenings; Richard and Phillip for the fun in making PhD hats and ordering presents; Andrea, Krishnan, Shourya and Benjamin for the evenings in Satellite and during conferences; the Aare swimming team; the running team; the ODRA 100 roommates; the OASE team for the excellent lunch breaks; Jens & Anja, Stephan, Arne and Igor for the numerous outdoor activities and evenings that have helped to clear the mind.

I'm grateful to my family for the support in my steps and the visits to Switzerland, when I didn't have the time to return home.

Last but not least, I particularly thank my girlfriend Mavluda for her unconditional support of me going abroad, the forgivingness when my time was limited and the extensive travelling to meet with each other. The times were rough, but the nature in Switzerland and France has paid us back.

Zürich, 18.12.2013

Curriculum vitae

CONTACT INFORMATION

Email siegfried.ts@gmail.com

PERSONAL INFORMATION

Name Siegfried, Thomas Gerd

Born 13. November 1983, Regensburg, Germany

EMPLOYMENT HISTORY

2008 Bayer Technology Services, Caojing, China. Research assistant on “*Low temperature synthesis using micro reaction technology*”.

2008 Chinese Academy of Science, Beijing, China. Research assistant on “*Cobalt oxide nanoparticle synthesis*”.

EDUCATION

2010-2014 **Ph.D.** candidate at the Paul Scherrer Institute (PSI), under the supervision of Prof. O.J.F. Martin at the Swiss Federal Institute of Technology Lausanne (EPFL). Thesis title: “*Near-field enhancement in plasmonic arrays*”.

2009 Karlsruhe Institute of Technology (KIT), Germany. Research assistant on “*Molecular dynamics calculations of gas transport in Carbon nanotube forests*”.

2005-2009 **Diplom** in chemical and bioengineering (Dipl. Ing. Univ.). Friedrich Alexander University Erlangen, Germany. Thesis title: “*Analysis of early stage particle precipitation processes using Hyper Rayleigh Scattering and Absorption spectroscopy*”.

2003-2005 Technical University of Munich, Germany. Undergraduate in chemical engineering.

2003 Abitur, Albertus-Magnus Gymnasium Regensburg, Germany

2000-2001 Judson Senior High School, Texas, USA

ACADEMIC WORK EXPERIENCE

2011-present Peer-reviewing activity for Applied Physics Letters, Applied Physics: A and Optical Engineering.

2011-present ILab, Paul Scherrer Institute. Teaching and experimentation with school classes in vacuum science, sound wave science and spectroscopy.

2006-2007 Friedrich Alexander University. Teaching and laboratory assistant for “Particle laser diffraction” tutorial.

T. Siegfried, Y. Ekinici, O. J. F. Martin, H. Sigg, "*Periodic Crescent Arrays as Uniform and Versatile Plasmonic Substrates*", under preparation

S. Dutta-Gupta*, **T. Siegfried***, Y. Ekinici, H. Sigg, O. J. F. Martin "Cavity-Controlled Perfect Absorption in Plasmonic Crescent Arrays Can Command the Raman Enhancement", submitted Feb 2014.

T. Siegfried, L. Wang, Y. Ekinici, O. J. F. Martin, H. Sigg, "*Metal Double Layers with Sub-10 nm Channels*", submitted Jan 2014.

T. Siegfried, Y. Ekinici, O. J. F. Martin, H. Sigg, "*Gap Plasmons and Near-Field Enhancement in Closely Packed Sub-10 nm Gap Resonators*", Nano Letters **2013**, 13 (11), 5449-5453. DOI: <http://dx.doi.org/10.1021/nl403030g>

T. Siegfried, Y. Ekinici, O. J. F. Martin, H. Sigg, "*Engineering Metal Adhesion Layers That Do Not Deteriorate Plasmon Resonances*", ACS Nano **2013**, 7 (3), 2751-2757. DOI: <http://dx.doi.org/10.1021/nn4002006>

A. Farhang, **T. Siegfried**, Y. Ekinici, H. Sigg, O. J. F. Martin, "Large-scale sub-100 nm compound plasmonic grating arrays to control the interaction between localized and propagating plasmons", Journal of Nanophotonics **2013**, 8 (1), 083897-083897. DOI: <http://dx.doi.org/10.1117/1.JNP.8.083897>

K. Thyagarajan, **T. Siegfried**, H. Sigg, and O. J. F. Martin, "Surface second harmonic generation from sub-10 nm gap plasmonic gratings" in Nonlinear Optics **2013**, paper NM2A.2. DOI: <http://dx.doi.org/10.1364/NLO.2013.NM2A.2>

B. Gallinet, **T. Siegfried**, H. Sigg, P. Nordlander, O. J. F. Martin, "*Plasmonic Radiance: Probing Structure at the Ångström Scale with Visible Light*", Nano Letters **2012**, 13 (2), 497-503. DOI: <http://dx.doi.org/10.1021/nl303896d>

B. Gallinet, A. Lovera, **T. Siegfried**, H. Sigg, O. J. F. Martin, "*Fano resonant plasmonic systems: Functioning principles and applications*", AIP Conference Proceedings **2012**, 1475, 18-20. DOI: <http://dx.doi.org/10.1063/1.4750081>

T. Siegfried, M. Kind, A. Terfort, O. J. F. Martin, M. Zharnikov, N. Ballav, H Sigg, "*Reusable plasmonic substrates fabricated by interference lithography: a platform for reliable sensing studies*", Journal of Raman Spectroscopy **2012**, 44 (2), 170-175. DOI: <http://dx.doi.org/10.1002/jrs.4163>

T. Siegfried, Y. Ekinici, H. H. Solak, O. J. F. Martin, H. Sigg, "*Fabrication of sub-10 nm gap arrays over large areas for plasmonic sensors*", Applied Physics Letters **2011**, 99 (26), 263302. DOI: <http://dx.doi.org/10.1063/1.3672045>

Conference contributions

T. Siegfried, "*Near-field enhancement in sub-10 nm gap arrays*",
oral presentation at Surface Plasmon Polariton (SPP6) in May **2013**, Ottawa, Canada

T. Siegfried, "*Fano coupling from line arrays of crescents*",
poster presentation at Surface Plasmon Polariton (SPP6) in May **2013**, Ottawa, Canada

T. Siegfried, "*Minimizing Quenching of Plasmonic Sensors caused by Adhesion Layers*",
oral presentation at CLEO **2012**, San Jose, USA

T. Siegfried, "*Large Area Periodic Nanogap Arrays for Raman and Fluorescence Enhancement: Modeling and Performance*", **oral presentation** at CLEO in May **2012**, San Jose, USA

T. Siegfried, "*Hidden Fano resonances enable crescent type SERS enhancement*",
oral presentation at Frontiers of Plasmonics in April **2012**, Chengdu, China

T. Siegfried, "*Periodic Nanogap Arrays for Surface Enhanced Spectroscopy: Modeling and Performance*", **oral presentation** at SPS Meeting **2012**, Zurich, Switzerland

T. Siegfried, "*Plasmonic nanogap arrays for a deterministic sensor performance by EUV lithography*", **oral presentation** at SPS meeting in June **2011**, Lausanne, Switzerland

T. Siegfried, "*Intense quenching of SERS caused by Chromium adhesion layer*",
oral presentation at Surface Plasmon Polariton (SPP5) in May **2011**, Busan, South Korea

T. Siegfried, "*High density fabrication of deterministic nanogap arrays*",
poster presentation at Surface Plasmon Polariton (SPP5) in May **2011**, Busan, South Korea